Various Aspects of Astroparticle Physics and the Implications for Dark Matter Searches

Dissertation
zur
Erlangung des Doktorgrades (Dr. rer. nat.)
der
Mathematisch-Naturwissenschaftlichen Fakultät
der
Rheinischen Friedrich-Wilhelms-Universität Bonn

von
Annika Buchholz (geb. Reinert)
aus
Bonn

Bonn, December 2019

Angefertigt mit Genehmigung der Mathematisch-Naturwissenschaftlichen Fakultät der Rheinischen Friedrich-Wilhelms-Universität Bonn.

1. Gutachter:	Prof. Herbert Dreiner, PhD
2. Gutachter:	Prof. Dr. Manuel Drees
Tag der Promotion:	20.03.2020
Erscheinungsjahr:	2020

To my Parents

Summary

Cosmic rays offer an opportunity to search for dark matter, if the latter decays or annihilates into standard model particles. In the first part of this work, we address an excess that was claimed to be seen in the cosmic ray antiproton spectrum. Carefully evaluating the uncertainties of the analysis as well as their correlations, we show that the significance hardly exceeds 1σ. In the absence of an anomaly, we derive limits on the dark matter annihilation cross section that disfavor thermal WIMPs below roughly 500 GeV.

To go further, we question the general setup of typical homogeneous diffusion models. We point out that the measured e^+ and $e^\pm$ spectrum at TeV energies are consistent with the astrophysical background prediction, if energy losses are not relevant. We propose alternative models of cosmic ray propagation that capture these properties, and discuss the consistency with various astrophysical measurements. It turns out that secondary $e^\pm$ at TeV energy require short escape time $\lesssim 0.1$ Myr. We show that this implies that the cosmic rays at these energies have seen an average density of interstellar matter of a few particles per cm^3. This number is so far consistent with observations, but requires further investigation, e.g. through starlight extinction maps or γ-ray surveys.

In the last part we look at four explicit models of dark matter with a small coupling to the visible sector through the electromagnetic interaction, namely through a dark photon portal or through an electric or magnetic dipole moment. The small couplings prohibit thermalization with the standard model sector in the early universe, such that typical constraints for dark matter masses in the keV range are avoided. Instead, the dark matter may have been produced through annihilations and decay of standard model particles into the dark sector, so-called 'freeze-in' production. The parameters that reproduce the observed relic abundance can partially be constrained by stellar cooling arguments and upcoming direct detection experiments.

List of Publications

1. J.H. Chang, R. Essig, and A. Reinert, *Light(ly)-coupled Dark Matter in the keV Range: Freeze-In and Constraints*. arXiv:1911.03389[hep-ph]
2. K. Blum and A. Reinert, *Cosmic ray $e\pm$ at high energy*.
   Published in: **EPJ Web Conf. 208 (2019) 04001**.
3. A. Reinert and M. W. Winkler, *A Precision Search for WIMPs with Charged Cosmic Rays*.
   Published in: **JCAP 1801 (2018) no. 01, 055**, arXiv:1712.00002 [astro-ph.HE].
4. D. Dercks, H. Dreiner, M. E. Krauss, T. Opferkuch, and A. Reinert, *R-Parity Violation at the LHC*. Published in: **Eur. Phys. J. C 77 (2017) no. 12, 856**, arXiv:1706.09418 [hep-ph].
5. R. Kappl and A. Reinert, *Secondary Cosmic Positrons in an Inhomogeneous Diffusion Model*.
   Published in: **Phys. Dark Univ. 16 (2017) 71**, arXiv:1609.01300 [astro-ph.HE].
6. R. Kappl, M. Winkler, and A. Reinert, *Antiprotons reloaded*.
   Published in: **JCAP 1510 (2015) no. 10, 034**, arXiv:1506.04145 [astro-ph.HE].

The work presented in this thesis contains results from the publications 1, 2, and 3.

Acknowledgements

First of all, I want to express my deep gratitude to Herbi Dreiner, who encouraged me to work in this field and to pursue my own ideas. He always has an open ear for questions and problems of any kind and supported me in many ways. Another special thanks goes to Manuel Drees, for co-reviewing my thesis and his passionate interest in scientific discussions from which I benefited greatly. I further thank Cristiano Porciani and Ulrich Jaehde, who I am very happy to have on the committee for my PhD defense.

I also want to thank my collaborators: First of all, Martin Winkler and Rolf Kappl who sparked my interest in the open questions in cosmic ray physics. They supported me a lot in the early stages of my PhD and taught me how the scientific life works. I am very grateful to my other collaborators: Kfir Blum, Jae Hyeok Chang, Rouven Essig, Daniel Dercks, Manuel Krauss, Toby Opferkuch, and of course Herbi. I learned many good things from all of you and very much enjoyed our vivid discussions. I also want to thank Nadav Outmezguine, Lorenzo Ubaldi, Andreas Trautner, Dominik Köhler and Saurabh Nangia for many exiting and helpful discussions about miscellaneous ideas within and beyond physics. I further thank my careful proofreaders.

My visit at Tel Aviv University was very fruitful and inspiring for my research and I am very grateful to Tomer Volansky and his group. They did not only host me, but adopted me from the first day on such that I could benefit a lot from the discussions and collaborations that started there. I also want to thank Yuval Grossman for teaching me Hebrew and for many enthusiastic discussions about physics.

In the past years, I had a very good time at the Bethe Center for Theoretical Physics in Bonn, thanks to the good atmosphere among the students and researchers, and lastly also thanks to Petra Weiß, Patricia Zündorf and Christa Börsch, without whom the BCTP would not be what it is.

I am very grateful for the support I received through the Cusanuswerk. Finally, I want to thank my family, who set the seeds for my fascination for physics, was always interested in my work, and supported me greatly.

Contents

CHAPTER 1

Introduction

Throughout the history of humanity, people have been fascinated by the night sky, as well as questions about the fundamental principles of Nature. We know today, the phenomena on the unimaginably large scales of the Universe and on the small scales of elementary particle physics are significantly related. Still, a number of essential questions remain unanswered.

As we will explain later in more detail, one of these open questions arose from a closer look into the sky that revealed an anomalous gravitational force, possibly due to a yet undiscovered matter component. If this is the case, this type of matter seems to be dark in the sense that there is no (strong) interaction with light as it has not been seen with optical instruments. For more than half a century, a big effort has gone into probing and explaining the nature of dark matter, but no clear signal has been found.

From the history of the Universe, the relic abundance of various particle species can be derived and the predictions of the standard cosmological model have been successfully confirmed. If the dark matter was produced by any comparable mechanism, there must be some kind of interaction between the dark and the 'Standard Model' (of particle physics) sector. Although it is conceivable that the dark sector is completely decoupled from the baryonic matter component, this scenario is hard to explore. Thus, we focus on the case with interactions between the dark and the Standard Model particles.

In this work, we investigate two different aspects that arise from these couplings. The first one is the potential exploration of dark matter through indirect detection, so we study charged cosmic rays and their astrophysical backgrounds. Second, we consider explicit models of dark matter that is weakly coupled to the electromagnetic field and discuss the production and constraints.

To begin with, we want to investigate the origin and propagation of cosmic rays. If dark matter particles in our galaxy annihilate or decay to Standard Model particles, the flux of these cosmic rays would be enhanced. For a clear signal to background discrimination, the Standard Model astrophysical component has to be well understood. This turns out to be an open problem. Still, a huge number of papers have been written that claim to explain cosmic ray measurements with dark matter models. We want to address and question these interpretations from two different sides.

In the first part, Chap. 2, we analyze the effect of various uncertainties and their correlations in the derivation of the cosmic ray flux. From the literature, data on the production cross sections are collected and parameterized. We propose a simple analytic model to account for low energy effects that come from the Sun. Taking all uncertainties together reveals that the excess that was claimed to be seen in the antiproton spectrum [1] is not significant. As a consequence, we can present limits on the annihilation cross section of dark matter.

In the second part, Chap. 3, we scrutinize the commonly used class of propagation models in more detail. We collect and analyze various astrophysical observations that are sensitive to temporal and spatial propagation scales. It turns out there is evidence for the propagation timescale to be much

smaller than typically assumed, with radical consequences: The cosmic rays measured in the solar neighborhood may have been produced recently (on galactic timescales) and may at high energies be dominated by a local source. We draw a self-consistent picture in which the measured positrons as well as the antiprotons match the astrophysical background prediction, and are not due to pulsars or dark matter.

In the last part, Chap. 4, we take a look at explicit models of dark matter interacting with the visible sector via the electromagnetic interaction. One possibility to realize this is the so-called dark photon portal, where the dark matter is coupled to a dark photon, which is the gauge boson of an additional U(1) gauge symmetry. The dark photon is kinetically mixed with the Standard Model photon, giving rise to interactions between dark matter and charged Standard Model particles. The dark matter may be a fermion of spin-$1/2$ or a boson of spin 0. We further consider dark matter with a possible electric or magnetic dipole moment. These effective dimension five operators could be induced from new charged particles at a higher mass scale. We discuss the possible production of these particles in the early universe. If the couplings to the Standard Model are small, constraints from the effective number of relativistic degrees of freedom are evaded and dark matter can be produced through the freeze-in mechanism. However, in the low keV-range, the models are constrained by stellar cooling arguments. We determine these constraints and further discuss the detection prospects through electron recoils in direct detection experiments.

In Chap. 5 we give an overall conclusion. In the remaining part of this chapter, an overview is given of the structure of our galaxy and of the evidence, models, and detection techniques for dark matter.

1.1 General Aspects of Astrophysics

In this section, an overview is given of our galaxy and its structure, and of the origin and transport of cosmic rays.

1.1.1 The Galaxy and the Solar Neighborhood

A galaxy is a collection of gravitationally bound stars, gas, dust and other stellar objects. Our galaxy, the Milky Way, is a barred spiral galaxy with $O(10^{11})$ stars. In the center, it has the strong radio source, Sagittarius A*, which is widely considered to be a supermassive black hole [2]. Roughly 3 kpc around the center is a spherical, very dense region which is called the bulge. The spiral arms of the galaxy are located in a disc of radius $\sim$ 20 kpc and the spherical dark halo extends up to at least $\sim$ 50 kpc. The galactic disc has a thickness of $50 - 150$ pc.

The solar system is located on the inner edge of the Orion arm at a distance of $\sim$ 8.5 kpc from the galactic center [3], orbiting at a speed of roughly 220 km/s. It is located in the so-called local bubble, which is an underdense region with a particle number density of less than $0.01/\text{cm}^3$ that extends by $\sim$ 100 pc [4–6]. The reason for the underdensity is probably an old supernova in this area that blew away the interstellar medium. Outside of the local bubble, there are some very dense regions like molecular clouds, in which the average number density can reach hundreds or thousands of particles cm^{-3} [7].

1.1.2 Galactic Cosmic Rays

Cosmic rays are energetic particles that move through outer space. The main component are protons ($\sim 90\%$), followed by the nuclei of helium and heavier elements. Roughly 1% are electrons[1] and an even smaller fraction consists of antimatter like positrons or antiprotons.

High energy cosmic rays hitting the Earth's atmosphere cause shower cascades that can be detected by ground based experiments. However, low energy particles are missed and the identification of the incoming particle type is difficult, as the cascade properties hardly depend on the incoming particle's internal properties but more in it's momentum. Alternatively, there are balloon or space-borne experiments that detect cosmic rays directly. In the MeV to low TeV-range, the latter detector type is the most useful one. However, the charged particles with kinetic energies below 1 GeV are deflected by the solar magnetic field, such that they cannot enter the heliosphere and the flux in the vicinity of the Earth is suppressed. The modeling of this effect is called solar modulation and will be discussed in Sec. 2.2.2.

To interpret the measured cosmic ray data, two main aspects have to be understood: the cosmic ray sources and their propagation in the galaxy.

The Origin of Cosmic Rays

According to their production mechanism, cosmic rays are divided into the two categories of primary and secondary origin.

Primary cosmic rays are produced in astrophysical sources, mainly supernova remnants (SNR) [8]. After the explosion of a supernova, its shock front expands, accelerating roughly 10% of the interstellar medium it passes over. The acceleration mechanisms are not fully understood. The most common model is called Fermi-acceleration and results in a spectrum of cosmic rays that scales with energy, E, like E^{-2} [9]. There are ongoing investigations to study deviations of this spectral slope, as well as to test its dependence on the particle species [10]. In general, protons are accelerated more efficiently compared to electrons, since the protons have a higher interaction cross section with the particles in the shock front. Furthermore, electrons suffer energy losses before escaping from the source. Supposedly, there is a large amount of cosmic ray electrons with energies in the few MeV range, but as our experiments are not sensitive to the latter, we detect many more cosmic ray protons than electrons [11].

Apart from these established primary cosmic ray sources, more speculative primary sources are discussed in the literature. The most relevant ones are pulsar wind nebulae (PWN) and dark matter annihilation or decay products. Pulsars are known to have a strong electromagnetic field in which electron-positron pairs are produced. However, the flux amplitude and spectral properties of the resulting cosmic rays are unknown. Typically, the spectrum is set to a power law with an exponential cutoff and fit to the observed data. However, recent γ-ray measurements by the High-Altitude Water Cherenkov Observatory (HAWC) revealed that the PWN contribution to the local cosmic ray flux seems to be negligible [12]. They investigate the spatial distribution of synchrotron emission around two pulsars and find that cosmic ray transport is not efficient enough for a significant number of electrons and positrons to reach the solar neighborhood. We will elaborate more on this measurement in Sec. 3.2.3.

The spectrum of cosmic rays that could be produced from dark matter annihilations or decay is strongly model dependent. It certainly has a sharp cutoff at the energy that corresponds to the dark

[1] We will explain this apparent charge asymmetry in the next section.

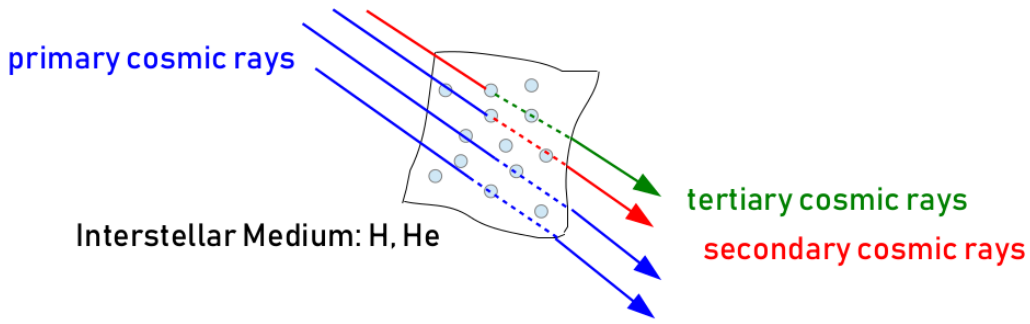

Figure 1.1: The production of secondary cosmic rays. Primary cosmic rays (blue) scatter inelastically off hydrogen or helium in the interstellar medium (light blue dots) and transform into secondary cosmic rays (red). The latter may again scatter, producing tertiary cosmic rays (green).

matter mass and further depends on the annihilation or decay products. If heavy quarks or gauge bosons are produced, their cascade decay results in lighter cosmic rays with a smooth energy distribution. In contrast, if the produced particles are stable (e.g. proton-antiproton pairs), a sharp peak is expected to be observed around the dark matter mass. If the exotically produced particles are leptons, their spectral distribution is smoothed by the energy losses they suffer during cosmic ray transport.

The non-observation of any of these features allows us to derive constraints on the dark matter-Standard Model interaction cross sections. Note, however, that these constraints strongly depend on the propagation model. The reason is the following: Dark matter is mainly produced in the galactic center and the halo. The bigger the size of the zone from which cosmic rays can reach the solar neighborhood, the more signal is expected and the stronger are the resulting limits. Unfortunately, it is hard to constrain the size of the propagation halo from astrophysical observations, as will be discussed in the next section.

The origin of secondary cosmic rays is much better understood. When primary particles[2] scatter off hydrogen or helium of the interstellar medium (ISM), new cosmic rays are produced, see Fig. 1.1. These are called secondary. Their source term can be derived from the primary fluxes Φ_i and the scattering cross sections σ. The latter are measured in the laboratory and will be discussed in detail in Sec. 2.3. The local spectrum of the primary cosmic rays is measured by various experiments. γ-ray observations indicate that the primary proton spectrum does not vary by more than a factor of $O(1)$ within the next 2-12 kpc (depending on the direction) up to energies of some hundreds of GeV [13]. With these ingredients, the secondary source term Q_s can be computed by summing over the contributions from all relevant primary particles i, and the constituents of the ISM, hydrogen and helium, j =H,He [8]

$$Q_s(T) = 4\pi \sum_{i,j} \rho_j \int_T^\infty \mathrm{d}T_i \Phi_i(T_i) \frac{\mathrm{d}\sigma_{ij\to s}(T_i, T)}{\mathrm{d}T} \,. \tag{1.1}$$

Here, the ISM density has the components $\rho_\mathrm{H} \approx 0.9 m_p$ cm^{-3} and $\rho_\mathrm{He} \approx 0.1 m_{He}$ cm^{-3}, and T and T_i is the kinetic energy per nucleon of the secondary and primary cosmic ray, respectively. In case

[2] In fact, there is a secondary (and tertiary, etc.) component in any cosmic ray species, but we will refer to the cosmic rays that are progenitors to purely secondary cosmic rays (and most dominantly produced in SNR) as 'primary'.

of production of a lepton, T is simply the total kinetic energy. Expression (1.1) simplifies when the production of heavy nuclei ($Z \gtrsim 4$) is considered. In the straight-ahead approximation, a nucleus simply strips off part of its nucleons, such that the differential cross section becomes a δ-distribution and the integration is trivial. The secondary flux is reduced by further spallation processes. For nuclei, this effect is relevant and the larger the number of nucleons, the larger the fragmentation cross sections. For leptons, it is negligible.

The Propagation of Cosmic Rays

Once cosmic rays are produced, they move through space. To model this process is highly non-trivial due to a large number of unknowns. First of all, the galaxy has a magnetic field in which the charged particles are deflected, their scattering can most likely be best understood as a random walk. There is assumed to be a regular and a random component of the galactic magnetic field, but the precise field values and distributions are unknown. Its average magnitude is estimated to be a few μG.

Secondly, the size of the propagation zone is unknown. It is usually assumed that cosmic rays move around within a certain region, in which they can reach any place. At some point, they escape from this area – the propagation zone – into outer space and do not return. Its size determines whether the observed cosmic rays are of local origin or, in contrast, traveled long distances through the galaxy and its halo. In particular, constraints on dark matter annihilation or decay strongly depend on the size of the propagation zone.

Thirdly, the timescales of propagation play a crucial role. Leptons suffer from energy losses due to interactions with the magnetic field and the photons, depending on their energy. Their cooling time depends mainly on the magnetic field strength. The other relevant timescale is the 'escape time' that determines how long the cosmic rays reside within the propagation zone. This timescale can be measured by determining isotope ratios of radioactive nuclei and is found to be roughly[3] 10 Myr at 10 GeV [14]. At higher energies it is unknown. For leptons, the relation between these two timescales determines if energy losses are relevant or not. As we will see in Chap. 3, this is an important issue for the interpretation of the cosmic positron data.

Finally, there may be other effects like convection blowing particles away from the galaxy, or reacceleration altering the cosmic ray spectrum. Due to the lack of measurements quantifying these effects, they are usually modeled with some parameters that are determined by fits to the cosmic ray data.

The near isotropy that is measured in cosmic ray data led to the conclusion that cosmic ray transport is driven by diffusion. Scattering off the magnetic field, the cosmic rays may go on a random walk and thus isotropize. One well established propagation model is the 'two zone diffusion model' that will be discussed in Chap. 2.

Alternatively, there is a simpler model that is called the 'leaky box model'. It assumes that the cosmic rays and their sources reside within some volume from which they escape after a specific time – the escape time. No assumptions about the details of particle motion in the propagation zone are made. We will take a more detailed look at this model in Chap. 3.

The free parameters of these models are usually determined from fits to secondary to primary ratios. The idea is that from the source term of the secondary cosmic rays and their measured flux, one can infer information about the propagation process. Systematic errors can be reduced by dividing by the primary component. In practice, not many of these ratios have been measured, but a very suitable

[3] A Myr (Megayear) equals 10^6 years.

candidate for the secondary species is boron, as no primary contamination is expected. It is mainly produced from carbon nuclei scattering off the ISM, so the secondary to primary ratio to look at is B/C. Another candidate is the antiproton to proton ratio, $\bar{p}/p$, which offers a consistency check but does not probe as large energies due to the lack of data.

As stated above, often the secondary to primary ratios are used to determine the parameters of the propagation model. However, the physical quantity that is actually probed is the cosmic ray grammage [8]

$$X_{\mathrm{esc}}(\mathcal{R}) = \frac{n(\mathcal{R})}{Q(\mathcal{R})} \,, \tag{1.2}$$

which is the ratio of two important quantities: the cosmic ray net source term Q, i.e. the total production rate (corrected for spallation losses) of particles per time, volume and energy; and the corresponding cosmic ray distribution in the galaxy n, i.e. the number of particles per time, area and energy. The latter is connected to the cosmic ray flux, Φ, with $\beta = v/c$, by $\Phi = \frac{\beta}{4\pi} n$, which takes the distribution in the solid angle into account. In general, all these quantities depend on the rigidity $\mathcal{R} = p/Z$, which is the momentum to charge ratio and a useful quantity for cosmic rays as different particle types with the same rigidity behave the same in a magnetic field. Furthermore, n, Φ and Q depend on the spatial coordinate, which we will most of the time not state explicitly. The grammage is the spallation-weighted average column density of ISM that is seen by a cosmic ray traveling from its source to Earth. Making use of measured secondary to primary ratios, e.g. B/C, and the boron production and spallation cross sections, the grammage can be deduced directly from data [15]:

$$X_{\mathrm{esc}} = \frac{(B/C)}{\sum_{P=C,N,O,\ldots} (P/C) \frac{\sigma_{P\to B}}{m_{\mathrm{ISM}}} - (B/C) \frac{\sigma_B}{m_{\mathrm{ISM}}}} \,. \tag{1.3}$$

The ISM consists of roughly 90% hydrogen and 10% helium, such that the average mass is $m_{\mathrm{ISM}} = 1.3 m_p$. Again, $\sigma_{P\to B}$ and σ_B are the secondary production and spallation cross sections, respectively, and the sum runs over all relevant primary cosmic ray species P.

These considerations suggest an approach that is much simpler than any explicit propagation model, namely to use the rigidity dependent scaling law $n = X_{\mathrm{esc}} Q$ (cf. Eq. (1.2)). If the grammage is derived from data like in Eq. (1.3), it can be used to predict the cosmic ray flux of any other particle species once its source term is known. Of course, this approach does not account for additional effects that may be important, of which one is the energy losses for leptons. Still, it can be used to get a rough estimate of the expected flux and, in case of leptons, an upper bound, which turns out to be remarkably close to the measured data. We will address this point in Chap. 3.

1.1.3 γ-rays

Typically the expression 'cosmic rays' focuses on charged particles, but, of course, most signals from outer space are photons. The study of astrophysical light signals is complicated since there are many sources that are not well understood, e.g. Radio Loop 1 [16], or the various processes going on in the galactic center [17]. On the other hand, the spatial resolution is much better as the light rays are not affected by magnetic fields and travel on straight lines (or geodesics, to be precise).

In astrophysics, the electromagnetic spectrum is divided into different parts, see e.g. Ref. [18]. Photons with energies above 100 keV, i.e. wavelengths below roughly 0.01 nm, are called γ-rays. Due to their large energy, they can only be produced in nuclear reactions or decay, or in high energy

particle collisions. The latter occur when cosmic rays interact with the ISM, and so γ-ray astronomy can be very helpful in tracing the cosmic ray and the ISM distribution. More about this will be discussed in Chap. 3. Below this energy down to wavelengths of 20 nm, one speaks of X-rays. They are radiated off by gas in galaxy clusters, the solar corona or supernova remnants. The latter also cause ultraviolet (UV) radiation, which has wavelengths up to 400 nm. Another big contribution to UV radiation comes from stars. They have a broad, nearly black body spectrum with a maximum luminosity at a frequency that depends on the temperature. Very massive, and accordingly hot, stars radiate mostly in the UV range, while the lighter ones have their maximum in the visible range 400-700 nm. Colder objects like planets or clouds of dust and gas emit infrared radiation with wavelengths up to a millimeter. Microwave radiation is available from the cosmic microwave background (CMB) and also produced by pulsars and active galaxies. Photons with very low energy and wavelengths above 1 meter are in the radio range and originate from old supernova remnants and cold gas.

In the visible range and for large wavelengths in the radio range, the atmosphere is transparent and the radiation can be detected in ground based experiments. For other energies, the atmosphere is more absorptive, and so they are better analyzed through experiments that are hosted by satellites.

1.2 Dark Matter

In this section we review the basic knowledge about dark matter[4]. We start with the main observations that support the existence of a dark matter component and follow by briefly presenting the various types of models that are discussed in the literature. Then we describe the classical detection techniques and explain the arguments about stellar cooling that additionally constrain the parameters of some dark matter models.

1.2.1 Evidence

The first hints for a dark component of matter were found by astronomers of the late 19th and early 20th century [21]. The study of stellar motions and galactic rotation curves revealed that their kinematics are not consistent with Newton's gravitational law[5] and the amount of visible matter. The latter can be estimated by counting stars and using the relations between their mass, luminosity and spectral properties. Clouds of gas and dust are also identified from typical spectral properties, e.g. the 21 cm line of the hyperfine structure transition in neutral hydrogen.

In the Newtonian theory of gravity, a stable orbit exists if the kinetic energy of the surrounding object is smaller than its energy in the gravitational potential. In case of a circular orbit, the rotational velocity is found to be $v = \sqrt{GM/R}$, depending on Newton's constant G, the central mass M and the radial distance to the center of mass R. Ignoring possible modifications due to an inhomogeneous mass distribution, one can make a simple prediction: (far) outside a galactic center, the rotational velocity of stars should decrease with radial distance. Investigations of single stars located far away from the galaxy, and H-I clouds that can also be found at large distances (tens of kpc), revealed that this is not the case [22–24]. Instead, the rotation velocity is constant over large scales.

Apart from galactic rotation curves, missing mass was also found in galaxy clusters by Fritz Zwicky [25]. The kinematic motions of the galaxies surrounding each other suggested a dark mass

[4] For more detailed reviews, see e.g. [19, 20].

[5] Note that the corrections from general relativity are comparatively small in this context and do not resolve the problem.

in the cluster that exceeds the luminous mass by a factor of a few hundred. Later, gravitational lensing was understood in detail, which allows very precise measurements of the mass of the lensing object [26, 27]. This technique confirmed the previous observations and gave rise to many more measurements that showed a discrepancy between visible and total mass in galaxies and galaxy clusters [28].

One particularly interesting observation was made in the Bullet cluster, which is formed by two colliding galaxy clusters. Gravitational lensing allowed reconstruction of the overall mass distribution which deviates significantly from the distribution of the baryonic mass, which radiates visible light [29].

Additional hints for the existence of dark matter come from cosmological observables like the cosmic microwave background (CMB) and simulations of structure formation. The power spectrum of the CMB fluctuations shows several acoustic peaks. The third peak is sensitive to the density of atoms and the total density of matter at photon decoupling and is not consistent with baryonic matter only [30]. This means that there is evidence for an attracting force that smoothed the fluctuations, for example through a dark matter component that bound matter gravitationally without experiencing disruptions due to electromagnetic interactions.

Later in the history of the Universe, structures formed. If there were only ordinary matter, its interaction with radiation would have smoothed out density perturbations, and the formation of stars, galaxies and clusters would have taken much longer. Simulations show that this problem is resolved if there is a cold dark matter component, that formed clumps first and attracted the baryonic matter to join in the structures [31].

All these observations, in particular the unexpected shape of rotation curves, led to two possible conclusions. Either there may be an unknown matter component that does not interact through the electromagnetic force (or if it does, only very weakly) and is thus called ‘dark matter’. To account for the observed kinematic anomalies it must form a big halo around galaxies that exceeds the dimensions of the visible component. There must also be a large component of dark matter in galaxy clusters and its average density must exceed the baryonic matter by roughly a factor of six.

Alternatively, the gravitational law may have to be modified on large scales. Some of these empirical theories of modified gravity are summarized under the name MOND (Modified Newtonian Dynamics) [32]. They have successfully explained some of the phenomena observed in galaxies that are not as easily explained with dark matter. One example is the Tully-Fisher-relation [33, 34], that reports a strong correlation between the total baryonic mass of a galaxy and its asymptotic rotation velocity. More recently, this relation has been refined to match at various distances from the galactic center [35, 36]. If there is dark matter, these relations suggest that it follows the distribution of ordinary matter, which is far from trivial. However, the theories of modified gravity fail to explain the kinematics of galaxy clusters. Furthermore, no cosmological model has been developed that explains the power spectrum of the CMB or structure formation.

To the contrary, the theory of dark matter is remarkably successful in explaining measurements on cosmological as well as on (inter)galactic scales – without making big assumptions about its concrete nature. It is for this reason that many models have been worked out and a huge experimental effort has been made to search for the mysterious unseen massive particles. In the next section we give a brief overview about some of the dark matter candidates.

1.2.2 The Model Landscape

Properties

The variety of dark matter candidates is huge, since only few properties are actually known. First of all, its electric charge must be very small or zero, otherwise it would not be dark. Secondly, it cannot interact too much through the strong force. With a color charge, the dark matter would couple to nuclei, but no isotopes with varying mass have been observed. Thus, the only unconstrained Standard Model interaction the dark matter could couple with is the weak force. In addition, there may be dark forces that couple the dark matter to the Standard Model sector and/or give rise to a self-interaction. The latter is constrained from the Bullet cluster, $\sigma_{\mathrm{SI}}/m_{\mathrm{DM}} < 2\ \mathrm{cm}^2/\mathrm{g}$ [37]. Still, constraints on the couplings are hard to translate into macroscopic properties. There are only few constraints on the clump size of dark matter, and it may also be smoothly distributed. If dark matter is made of fermions of just one type, the Pauli principle constrains it to be heavier than ~ 1 keV to account for all of the dark matter in dwarf galaxies [38, 39].

From the anisotropies in the CMB one can conclude that dark matter must be 'cold', i.e. non-relativistic at photon decoupling. Otherwise the structures would have been washed out by the high energy particles. Large scale structures would have formed first and then collapsed into smaller structures, but observations support the opposite [40, 41].

Furthermore, there are constraints on the effective number of relativistic degrees of freedom in the early universe [42, 43]. Relativistic particle species in the thermal bath affect the expansion of the Universe like radiation. If apart from the neutrinos there are other relativistic particles present, the Universe's expansion is accelerated. As a consequence, the predictions of Big Bang Nucleosynthesis (BBN) are modified, but the Standard Model predictions are in good agreement with measurements. Thus, the number of extra relativistic degrees of freedom is constrained to be much smaller than 1 [44], and depends not only on the number of relativistic particle species but also on their couplings that determine the time of thermal freeze-out. Particles of masses above a few MeV, with the precise number depending on the species, avoid this constraint as they are sufficiently cold and do not anymore contribute to the relativistic degrees of freedom during BBN.

Candidates

In principle, dark matter does not necessarily have to be a new kind of elementary particle. One possibility is that it consists of dark objects made of baryonic matter, like neutron stars or black holes, which are summarized under the name MACHOs (MAssive Compact Halo Objects). These big objects have been searched for through weak gravitational lensing, but no abnormal number of dark compact objects has been found. Hence, MACHOs ranging from 10^{-8} to 10^{2} solar masses have been ruled out to contribute to the dark matter at a significant level. Further constraints come from BBN and the CMB, that exclude such a large amount of baryonic matter in the early universe. To date, the microlensing surveys offer the most stringent bounds on the size of dark matter clumps.

An alternative is provided by primordial black holes, which are black holes that formed due to density fluctuations in the very early universe. As they are cold and do not interact with the thermal bath, they behave like non-relativistic, non-baryonic matter. The possible mass range covers roughly 40 orders of magnitude, whereof most of the parameter space is excluded by the MACHO searches [45]. In addition, primordial black holes with a mass lighter than 10^{11} kg would not have survived until today but evaporated emitting Hawking radiation, although this effect is yet to be experimentally confirmed.

For a long time there seemed to be an allowed window for primordial black holes with masses below the MACHO limit, but it is now in tension with recent microlensing searches [46].

In contrast to the baryonic dark matter theories, models where the dark matter may be made of one (or more) unknown elementary particle(s) also exist. With the few conditions described above, the model landscape is enormous and miscellaneous ideas have been pursued. Here, we briefly review the most prominent examples.

One of the more simple ideas is that dark matter are particles that interact through the weak force, just like neutrinos. Neutrinos themselves are not a viable candidate since they are not 'cold' and are fermions of sub-eV mass, so it turns out that their contribution to the dark matter is only about 1% [47]. However, what is often predicted in approaches to explain the neutrino masses are heavy neutrinos. They are singlets under the Standard Model gauge group and are thus called sterile neutrinos and could be the dark matter [48].

But there could also be other Weakly Interacting Massive Particles, the so-called WIMPs, that are coupled to the Standard Model, either through *the* weak force or through *a* weak force. These possible interactions open various detection channels that shall be discussed in the next section. The motivation for this class of particles is further supported by what is called the 'WIMP miracle': if the dark matter was thermally produced in the early universe, the cross section giving the right relic abundance is just of the order of the weak force, provided its mass is in the GeV to TeV range. A long standing WIMP dark matter candidate is the neutralino, that arises in supersymmetric extensions of the standard model [49]. In these models the neutralino is typically the lightest supersymmetric particle and protected from decay into Standard Model particles through a symmetry, R-parity.

Another idea that receives a lot of attention are axions or axion like particles (ALPs) [50]. The classical axions arise in one possible solution to the strong CP problem and are light ($m \sim 10^{-5} - 10^{-3}$ eV), scalar particles [51–53]. Due to very weak couplings, in the early universe they do not thermalize with the Standard Model sector but have to be produced non-thermally, e.g. via the misalignment mechanism [54]. The weak couplings to photons allow for different kinds of experimental searches, but so far no signal has been found.

One may consider scalar particles with even smaller masses, down to 10^{-21} eV, where the wavelength of the particles is of the same size as dwarf galaxies [55, 56]. This so-called ultralight dark matter, forms a Bose-Einstein condensate and has thus somewhat peculiar properties. In particular, it helps to resolve the core-cusp problem, which is a discrepancy between the simulations and the observations of the shape of galactic cores [57].

The last class of dark matter models we want to discuss here are the ones with a dark photon [58, 59] or Higgs portal [60]. In the first case, there may be an additional U(1) gauge group whose gauge boson is called the dark photon and is in some way coupled to the Standard Model photon, e.g. through kinetic mixing. In the second case, the dark matter has a direct coupling to the Higgs field. In both cases, the couplings to the Standard Model open diverse production and detection channels.

Various other more or less exotic ideas about the nature of dark matter have been proposed, for detailed reviews, see e.g. [20, 61].

1.2.3 Detection Techniques

If there is any kind of (sufficiently large) coupling between the dark matter and the Standard Model, typically three detection techniques are possible.

First, dark matter may be produced at a collider and escape from the detector as an invisible state.

Consequently, it can only be detected if an additional particle, e.g. initial or final state radiation, is produced in the same process. From the missing momentum one can then deduce that dark matter was part of the interaction[6]. So far, at the Large Hadron Collider (LHC) or earlier colliders, no signal over the Standard Model background has been observed.

Secondly, there may be annihilations or decay of dark matter particles into the Standard Model particles in the galaxy. Depending on the model, such processes result in γ-rays and/or cosmic rays, that could be observed over the astrophysical backgrounds. However, a precise understanding of these rays is difficult. For γ-rays, there is an ongoing debate about the astrophysical background sources around the galactic center [62, 63]. For charged cosmic rays, there is no spatial resolution due to scattering off the turbulent magnetic field. We will investigate the astrophysical cosmic rays in Chap. 2 and 3. In the first of these, we restrict ourselves to a well-established diffusion model, discuss its systematic uncertainties and derive limits on the dark matter annihilation cross section. We also address a claimed excess in the antiproton spectrum [1]. In Chap. 3, we question the general setup of this diffusion model, discuss various aspects of the propagation of charged cosmic rays and propose two alternative models.

Thirdly, the dark matter could scatter off Standard Model particles (nuclei or electrons) in a direct detection experiment in a laboratory on Earth, for example. The recoil energy transferred to a nucleus or an electron may be measured by a very sensitive detector, well shielded from background signals. Dark matter particles are expected to move with the local rotation velocity which is about $v = 10^{-3}c$. Thus, the expected recoil energies are very small. Direct detection experiments have ruled out a large part of the parameter space that was favored for WIMP dark matter. We will discuss the potential reach of future direct detection techniques for light dark matter with a small coupling to light in Chap. 4.

Apart from these classical search strategies, a big experimental effort has been made to search for more specific dark matter candidates, e.g. axions [64] or dark photons [65]. Another search area includes the study of astrophysical objects, for example the timescales of stellar cooling [66]. It has been worked out that energy loss mechanisms that occur in addition to the ones from the standard stellar models can be constrained. Thus, models in which dark matter can be produced in the stellar plasma and carry away energy from the star, receive strong limits on the couplings to the Standard Model. We review these arguments in Chap. 4 and derive the resulting limits for the dark matter models under consideration.

[6] Of course, missing momentum is also observed in processes involving neutrinos. This contribution is estimated through Monte-Carlo simulations and accounted for in the analyses.

CHAPTER 2

A Precision Search for WIMPs with Charged Cosmic Rays

This chapter is based on Ref. [67], published together with Martin Winkler.

2.1 Introduction

The last decade has seen dramatic progress in the measurement of charged cosmic ray fluxes. As the experiments entered new territory in energy and precision, a number of surprises came along. Most strikingly, the positron flux failed to show the strong decrease with energy which would have established it as a secondary, i.e. one that is produced by scattering of protons or nuclear cosmic rays on the interstellar matter. When the rise of the positron fraction was unambiguously proven by PAMELA [68], it seemed that dark matter discovery was within reach. The wave of excitement prevailed until gamma ray [69, 70] and CMB data [71–73] put increasingly strong pressure on this interpretation which required annihilation rates far beyond those of Weakly Interacting Massive Particles (WIMPs). Skepticism was later also raised on whether dark matter annihilations can account for the positron spectrum at the precision level (see e.g. [74]). In this light, an astrophysical origin of the positron excess appears to be preferred.

The story of cosmic ray antiprotons shares a parallel with positrons: at the first data release by AMS-02, the antiproton spectrum came out significantly harder than expected from secondary production [75]. But since then, the secondary background passed through a major revision. Cosmic ray propagation has been recalibrated to the AMS-02 boron to carbon (B/C) data [76] (see also [77, 78]). In addition, the experimentally established increase of the antiproton production cross section with energy has been incorporated [79, 80]. The updated background features significantly more high energy antiprotons. It is consistent with the hard high energy spectrum observed by AMS-02 [80, 81].

Supposing that dark matter signals dominate neither of the two antimatter fluxes at any energy it may seem that this is the time for despair. But quite the contrary: AMS-02 has reduced experimental errors in the fluxes to the few percent level over a wide energy range [82–84]. By this, it has gained sensitivity to subdominant signals which can be identified in a spectral analysis. Even if the high energy positron spectrum is dominated by an astrophysical source, the low energy part is still very useful in constraining dark matter models as well as cosmic ray propagation. In the antiproton channel AMS-02 can even realistically probe canonical thermal WIMPs – the target of indirect dark matter searches for decades. Indeed, an antiproton excess consistent with a thermal WIMP of mass $m_{\rm DM} \sim 80\,\text{GeV}$ has already been reported in the AMS-02 data [1, 85]. But the robustness of this signal needs to be investigated further.

In this work, we will attempt to systematically quantify and incorporate the dominant uncertainties in the antiproton flux. These are related to hadronic production cross sections as well as to the propagation of charged cosmic rays through the galaxy and the heliosphere. Our approach employs the combination of antiproton, positron and B/C data of AMS-02. Cosmic rays are propagated within the two-zone diffusion model [86–88]. Positrons are consistently treated within the same framework through the pinching method [74]. The propagation parameters which control diffusion, convection and reacceleration are obtained by simultaneously fitting the B/C ratio [83] and the antiproton spectrum [84] of AMS-02. The size of the diffusion halo, posing a notorious difficulty for indirect dark matter detection, is efficiently constrained from the low-energy positron spectrum. Our treatment of solar modulation includes charge-sign dependent effects which are determined from the time-dependence of the antiproton flux as extracted from the PAMELA [89] and AMS-02 [84] data. The antiproton cross sections relevant for secondary production in cosmic ray scattering are taken from the recent comprehensive analysis [80]. Nuclear fragmentation cross sections which enter the boron source term are modeled from a wide collection of accelerator data. For both, antiprotons and boron, we map the cross section uncertainties into the predicted fluxes and include them into the fit in the form of covariance matrices.

We observe an overall good agreement of the antiproton and B/C data with the background prediction. By performing a spectral analysis we derive strong constraints on hadronic dark matter annihilation. While we confirm the slight excess [1, 85] at $m_{\mathrm{DM}} \sim 80$ GeV in the $b\bar{b}$-channel, we show that it becomes insignificant once all relevant uncertainties and the look-elsewhere effect are considered. We finally comment on possibilities to reduce uncertainties in the cosmic ray fluxes in order to further increase the sensitivity of AMS-02 to dark matter annihilations.

2.2 Cosmic Ray Propagation

As discussed in Sec. 1.1.2, protons and most of the nuclei in cosmic rays are referred to as primaries. They correspond to galactic matter which has been energized by supernova shock acceleration also known as (first order) Fermi acceleration. When a primary species propagates through the galaxy it can scatter on the interstellar gas and create a so-called secondary cosmic ray. This production mode is very important for certain nuclei like lithium, beryllium and boron. In addition, a large fraction of the antimatter in cosmic rays is believed to be of secondary origin. Independent of their production, cosmic rays follow complicated trajectories which are controlled by the magnetic fields in the galactic halo. We shall now briefly summarize our conventions for cosmic ray propagation before turning to the solar modulation of charged particles in the heliosphere.

2.2.1 Diffusion Model

On their passage through the galaxy cosmic rays scatter on magnetic field inhomogeneities. This induces a random walk which is equivalently described as spatial diffusion. Convective winds, if they exist, blow charged particles away from the galactic disc. In addition, interaction of cosmic rays with matter, light and magnetic fields leads to energy losses and annihilation, while magnetic shock waves may induce reacceleration. All relevant processes are encoded in the diffusion equation. While cosmic ray propagation codes like GALPROP [90–92] and DRAGON [93, 94] aim at a fully numerical solution, the spatial part of the diffusion equation can also be solved analytically under slightly simplifying assumptions. In the two-zone diffusion model [86–88], which we employ here,

diffusion is taken to occur homogeneously and isotropically in a cylinder of radius R and half-height L around the galactic disc. The disc of thickness $2h = 0.2$ kpc is taken to contain a constant number density of hydrogen and helium ($n_{\rm H} = 0.9\ {\rm cm}^{-3}$, $n_{\rm He} = 0.1\ {\rm cm}^{-3}$). Assuming steady state, the space-energy density N_i of a stable species i is related to its differential production rate (source term) q_i as

$$\begin{aligned} &- K\Delta N_i + {\rm sgn}(z) V_c\, \partial_z N_i + \partial_E(b_{\rm halo} N_i) + 2h\delta(z)[\partial_E(b_{\rm disc} N_i - K_{EE}\, \partial_E N_i) + \Gamma_{\rm ann}\, N_i] \\ &= 2h\delta(z) q_i^{\rm disc} + q_i^{\rm halo}\,, \end{aligned} \tag{2.1}$$

where E denotes the total energy of i. The extension of the galactic disc in axial (z-) direction has been neglected and processes confined to the disc were multiplied by $2h\delta(z)$ in order to keep proper normalization. We have split the source term into a disc component $q_i^{\rm disc}$ and a halo component $q_i^{\rm halo}$. The first term on the left-hand side accounts for spatial diffusion. Magnetohydrodynamics considerations suggest [95]

$$K = K_0 \beta \left(\frac{\mathcal{R}}{\rm GV}\right)^{\delta}\,, \tag{2.2}$$

where K_0 is a normalization constant, δ the power law index, β and $\mathcal{R}$ the velocity and rigidity of the cosmic ray particle. We will later also consider a modification of the diffusion term which is motivated from observed primary cosmic ray spectra (see Sec. 2.5.1). The second term in (2.1) accounts for convection. The convective wind velocity V_c controls its strength. Reacceleration by magnetic shock waves is modeled as a diffusion in momentum space which is encoded in the term [88]

$$K_{EE} = \frac{4}{3}\frac{V_a^2}{K}\frac{p^2}{\delta(4-\delta)(4-\delta^2)}\,. \tag{2.3}$$

The Alfvèn speed V_a occurs quadratically as reacceleration corresponds to second order Fermi acceleration.[1] The term

$$b_{\rm disc} = b_{\rm coul} + b_{\rm ion} + b_{\rm brems} + b_{\rm adiab} + b_{\rm reac} \tag{2.4}$$

includes energy losses in the galactic disc by Coulomb interactions, ionization and brems-strahlung, adiabatic energy losses caused by the flip of the convective wind vector at the disc as well as energy gains by reacceleration drift. We take $b_{\rm coul}$, $b_{\rm ion}$, $b_{\rm brems}$ from [91] and $b_{\rm adiab}$, $b_{\rm reac}$ from [88]. Leptonic cosmic rays in addition lose energy in the halo due to inverse Compton scattering and synchrotron emission,

$$b_{\rm halo} = b_{\rm ic} + b_{\rm synch} = -(E^2/\tau_E)\ {\rm GeV}^{-2}\,. \tag{2.5}$$

As we shall only consider low energy lepton fluxes in this work, we can employ the Thomson limit and use a constant $\tau_E = 10^{16}$ s (see e.g. [96]). Annihilation in the galactic disc on the other hand is mainly relevant for hadronic cosmic rays. The annihilation cross sections for nuclei are taken from [97, 98] and for antiprotons from [99, 100].[2] In the case of antiprotons we also have to consider inelastic (non-annihilating) scattering with the interstellar matter. This effect is taken into account through a tertiary source term as described in [87].

We now turn to the solution of the diffusion equation for secondary cosmic rays. We will approx-

[1] For practical purposes, the height of the reacceleration zone is taken to coincide with the disc height h. A difference between the two can be absorbed into a redefinition of V_a which is anyway a free parameter [86].

[2] The antiproton annihilation cross section was interpolated between the two parameterizations as in [101].

imate secondary source terms $q_i^{\rm sec}$ as spatially constant in the galactic disc. This amounts to assuming radially constant fluxes of the primary cosmic ray progenitors as well as constant density of the interstellar medium. While this situation is not expected to hold in reality, deviations can usually be absorbed into the propagation parameters. Local secondary fluxes are expected to be nearly unaffected as long as all species are treated within one universal framework. We will, furthermore, work in the limit $R \to \infty$ which yields identical results to a radially finite diffusion halo as long as $L \ll R$ (see e.g. [102]).[3] For secondary nuclei including antiprotons, energy losses in the halo are negligible and the spatial part of the diffusion equation can be solved analytically. The space energy density at $z = 0$ is determined by the differential equation in energy [86, 87]

$$\left(2h\Gamma_{\rm ann} + V_c + V_c \coth\left[\frac{V_c L}{2K}\right]\right) N_i + 2h\partial_E(b_{\rm disc}\, N_i - K_{EE}\, \partial_E N_i) = 2h(q_i^{\rm sec} + q_i^{\rm ter})\,, \tag{2.6}$$

where the tertiary source term $q_i^{\rm ter}$ is only relevant for antiprotons. This equation has to be solved numerically. The interstellar flux is related to the space-energy density via $\Phi_i^{\rm IS}(E) = \beta N_i/(4\pi)$. It is more common to specify fluxes in terms of the rigidity $\Phi_i^{\rm IS}(\mathcal{R}) = \Phi_i^{\rm IS}(E) dE/d\mathcal{R}$ or the kinetic energy per nucleon T.

In the case of positrons, the solution requires an additional step as energy losses occur in the disc and in the halo. We follow the "pinching method" [74] and first solve the diffusion equation for secondary positrons in the high energy limit, where we include only diffusion and halo energy losses. At $z = 0$ this leads to the integral equation $N_{e^+}^{\rm HE} = \int_E^\infty dE'\, q_{e^+}^{\rm sec}(E')\, \eta(\lambda_D)/|b_{\rm halo}(E)|$, where η in terms of the diffusion length λ_D can be taken from [96]. In the next step we want to include convection, reacceleration and energy losses in the disc. In order to follow the procedure for hadrons, the halo energy losses must be "pinched" into the disc. We substitute $b_{\rm halo} \to 2h\delta(z)\, b_{\rm pinched}$ and solve the high-energy diffusion equation once again. Requiring that the solution remains unchanged by this replacement, we can fix

$$b_{\rm pinched} = \frac{1}{N_{e^+}^{\rm HE}} \int_E^\infty dE_0 \left(\frac{K(E_0)\, N_{e^+}^{\rm HE}(E_0)}{hL} - q_{e^+}^{\rm sec}(E_0)\right). \tag{2.7}$$

with $N_{e^+}^{\rm HE}$ from above. The term $b_{\rm pinched}$ is the "translation" of the halo loss term $b_{\rm halo}$ into a disc loss term. After replacing $b_{\rm halo}$ with $2h\delta(z)\, b_{\rm pinched}$ in the full diffusion equation (2.1), the solution for positrons proceeds completely analogous as for antiprotons and boron.

If a primary antiproton (or positron) source term is induced by dark matter annihilation, it carries a spatial dependence which is determined by the dark matter profile (see Sec. 2.4). The solution of the diffusion equation then requires a Bessel expansion in the radial coordinate. The procedure has been described in detail in [103, 104] and shall not be repeated here.[4]

[3] Even if $L \ll R$ was not fulfilled, the difference in predicted secondary fluxes can again be compensated by a change of propagation parameters.

[4] There arises a small technical difficulty as the Bessel expansion does not converge if we set $R \to \infty$. However, we verified that primary fluxes rapidly converge if we increase R beyond L. Therefore, the practical solution is to set R to a large but finite value for which we choose $R = 5\, L$.

2.2.2 Solar Modulation

The solar system is surrounded by the heliosphere, a region of space which is permeated by the solar wind. The latter shapes the solar magnetic field whose main component is a dipole which inverts its polarity every 11 years. The two magnetic domains with inward and outward pointing field are separated by the heliospheric current sheet. Due to the solar wind outflow caused by the Sun's rotation, the magnetic field lines are distended near the equator. Since the Sun's rotational axis is misaligned with the direction of the dipole, the solar magnetic field gets twisted and a wavy pattern of the current sheet emerges.

On their passage through the heliosphere, cosmic rays are affected by the solar magnetic field. The dominant effects are diffusion, drifts, convection, and adiabatic energy losses. In the widely used force field approximation [105], solar modulation is described by a single parameter, the Fisk potential ϕ which only depends on time. Cosmic ray fluxes at the top of the Earth's atmosphere (TOA) are related to interstellar fluxes as

$$\Phi^{\mathrm{TOA}}(T) = \frac{2mT + T^2}{2m\,(T + \frac{Z}{A}\phi) + (T + \frac{Z}{A}\phi)^2}\,\Phi^{\mathrm{IS}}(T + \tfrac{Z}{A}\phi)\,. \tag{2.8}$$

This simple analytic solution is found if a constant radial solar wind and isotropic diffusion in the heliosphere are assumed. Unfortunately, the force field approximation cannot account for charge-sign dependent effects which have been established in cosmic ray spectra. It was argued in [106, 107] that the dominant charge-breaking effect in solar modulation is connected to the heliospheric current sheet. During a negative polarity phase, negatively charged particles access the heliosphere on rather direct trajectories along the poles. Positively charged particles enter by inward drift along the current sheet. In particular, in the case of a very wavy current sheet, they spend significantly more time in the heliosphere and lose more energy. The solar magnetic field has last flipped its polarity from negative to positive between November 2012 and March 2014 [108]. After the flip, the situation reverses and negatively charged particles are more affected by solar modulation. This is evident e.g. in the time-dependent e^+/e^- ratio measured by PAMELA between 2006 and 2015 [109]. The polarity flip is followed by a strong rise of e^+/e^- at low energy.

In [110] a simple modification of the force field approximation was proposed where (2.8) is still valid but particles are treated depending on their charge. The Fisk potential for positive (+) and negative (−) charges reads

$$\phi^{\pm}(t,\mathcal{R}) = \phi_0(t) + \phi_1^{\pm}(t)\,\mathcal{F}\Big(\frac{\mathcal{R}}{\mathcal{R}_0}\Big)\,. \tag{2.9}$$

The second term on the right-hand side incorporates the increased energy loss along the current sheet faced by particles whose charge sign does not match the polarity. In a positive (negative) polarity phase $\phi_1^+ = 0$ ($\phi_1^- = 0$). We will take ϕ_0, $\phi_1^{\pm}$ to be the parameters averaged over the time scale of the experiment. At rigidity $\mathcal{R} \gg \mathcal{R}_0$ the particle's Larmor radius is larger than the scale of magnetic field irregularities and its motion is controlled by the average field. Here $\mathcal{R}$ stands for the rigidity before entering the heliosphere (interstellar rigidity). Down to $\mathcal{R} \sim 2$ GV we can approximate $\mathcal{F}$ from [110] by

$$\mathcal{F} = \frac{\mathcal{R}_0}{\mathcal{R}} \tag{2.10}$$

up to a normalization constant which can be absorbed into $\phi_1^{\pm}$. We set $\mathcal{R}_0 = 1$ GV in the following without loss of generality. In [110] $\phi_0, \phi_1^{\pm}$ were related to the strength of the solar magnetic field and the waviness of the heliospheric current sheet (tilt angle). However, the AMS-02 data were partly

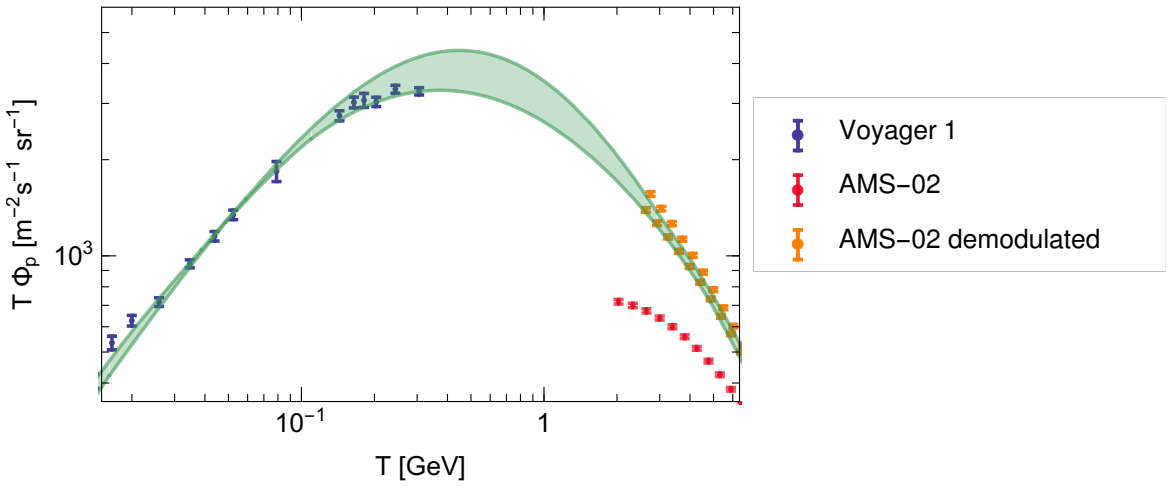

Figure 2.1: Low energy proton flux measured by Voyager and AMS-02. Also shown are AMS-02 data demodulated by a Fisk potential of 0.72 GV (upper orange error bars) and 0.6 GV (lower orange error bars). The green band is the envelope of interstellar proton fluxes determined in [111–113].

taken during a phase of polarity reversal. While the functional form (2.9) may still approximately hold in this period[5] the connection to solar observables becomes less transparent due to the rapidly changing magnetic field configuration. Therefore, we follow a different strategy and extract $\phi_0, \phi_1^{\pm}$ from cosmic ray data.

Data from the Voyager spacecraft [114] play an important role in pinning down the solar modulation of cosmic rays. Voyager 1 crossed the heliopause in 2012 and provided the first measurement of the interstellar proton flux. This has triggered several recent determinations of the Fisk potential for AMS-02 under the assumption of the force field approximation [111–113].[6] These rely on different parameterizations of the interstellar flux which were fit to the AMS-02 [115] and Voyager data simultaneously. The obtained values are in the range $\phi^+_{\text{AMS-02}} = 0.60 - 0.72$ GV. In Fig. 2.1 the envelope of the interstellar fluxes [111–113] is shown with the Voyager and AMS-02 data. To guide the eye we also depict the AMS-02 data demodulated with Fisk potentials of $\phi^+_{\text{AMS-02}} = 0.60, 0.72$ GV which captures the range of uncertainties related to the choice of parameterization. Larger or smaller Fisk potentials appear to require unphysical inflections in the shape of the interstellar flux in order to connect the two data sets.

The AMS-02 proton data were taken in the time interval 2011/05-2013/11, i.e. before and during the solar polarity flip. Nevertheless, there is indication that deviations from the force field approximation are small for positive charges. The dedicated solar modulation code HelMOD [116] yields virtually identical results for protons as the force field approximation with $\phi^+_{\text{AMS-02}} = 0.6$ GV. In [113] it was argued that a slight evolution of the Fisk potential from $\phi^+_{\text{AMS-02}} = 0.49$ GV at $T = 5$ GeV to $\phi^+_{\text{AMS-02}} = 0.59$ GV at $T = 0.1$ GeV would somewhat improve the fit to Voyager and AMS-02. Even in

[5] The parameter $\phi_1^{\pm}$ induces a slightly stronger energy loss of negatively compared to positively charged particles or vice versa. This is a plausible ansatz for a charge-breaking effect beyond the physical motivation given above.

[6] In [111] the Fisk potential $\phi^+_{\text{AMS-02}} = 0.64$ GV for AMS-02 is not explicitly given, but can easily be obtained from the provided interstellar flux.

this case, the value obtained within the force field approximation is still valid as an upper limit over the full energy range. We will therefore set $\phi^+_{\text{AMS-02}} = \phi_{0,\text{AMS-02}} = 0.60 - 0.72$ GV, $\phi^+_{1,\text{AMS-02}} = 0$ in the following. While the upper limit on $\phi^+_{\text{AMS-02}}$ appears sufficiently robust, the lower limit will not play a role in the subsequent analysis. Compared to protons and positrons the B/C data were taken over a longer time period over which modulation may have changed. We can safely neglect this as B/C is anyway rather insensitive to the choice of the Fisk potential.[7]

Finally, we have to account for negative charges, i.e. antiprotons. The corresponding AMS-02 data were taken between 2011/05 and 2015/05, i.e. before, during and after the solar polarity reversal. The strong increase of e^+/e^-, which set in in 2014 [109], hints at a significant charge-dependence in the modulation which may be traced back to a non-vanishing ϕ^-_1. In order to pin down this effect, we compare the AMS-02 antiproton data [84] with those of PAMELA [89]. Specifically, we consider the ratio of antiproton fluxes $\bar{p}_{\text{AMS-02}}/\bar{p}_{\text{PAMELA}}$ observed at the two experiments as shown in Fig. 2.9.[8] Within reason this ratio is insensitive to the assumed interstellar antiproton flux and, rather, depends on the difference in solar modulation between the two experiments $\Delta\phi^- = 0.2\,\text{GV} + \phi^-_{1,\text{AMS-02}}\,\mathcal{F}(\frac{\mathcal{R}}{\mathcal{R}_0})$. Here we took into account that PAMELA was operating in a negative polarity period (2006-2009) and determined the difference in ϕ_0 from the proton data [115, 117].[9] For $\mathcal{F}$ we use (2.10) as interstellar rigidities fulfill $\mathcal{R} \gtrsim 2$ GV. The remaining free parameter can be obtained by fitting to $\bar{p}_{\text{AMS-02}}/\bar{p}_{\text{PAMELA}}$. As can be seen in Fig. 2.9 the decrease of the AMS-02 antiproton flux compared to PAMELA towards low rigidity indeed favors a non-vanishing $\phi^-_{1,\text{AMS-02}} \simeq 0.7$ GV (see Sec. 2.5.2). In order to briefly summarize our treatment of solar modulation, we employ the Fisk potential for positively and negatively charged particles

$$\phi^+_{\text{AMS-02}} = \phi_{0,\text{AMS-02}}\,, \qquad \phi^-_{\text{AMS-02}} = \phi_{0,\text{AMS-02}} + \phi^-_{1,\text{AMS-02}}\,\frac{\mathcal{R}_0}{\mathcal{R}}\,. \tag{2.11}$$

and allow $\phi_{0,\text{AMS-02}}$ to float in the interval $\phi_{0,\text{AMS-02}} = 0.6{-}0.72$GV. $\phi^-_{1,\text{AMS-02}}$ is treated as a free parameter which will efficiently be constrained by including $\bar{p}_{\text{AMS-02}}/\bar{p}_{\text{PAMELA}}$ into our fits.

2.3 Secondary Production of Charged Cosmic Rays

Secondary cosmic rays descend from scattering of primary cosmic rays in the interstellar gas. A strategy to determine secondary fluxes often pursued in the literature is to start with a parameterization of primary sources and then to calculate the fluxes of all primary and secondary species simultaneously from the network of scattering and spallation reactions in the galactic disc. While this global approach certainly has its merits, it requires a huge number of inputs, e.g. about 2000-3000 nuclear fragmentation cross sections [118]. In our case, where we are mainly interested in a limited number

[7] An increase of $\phi^+_{\text{AMS-02}}$ would result in a stronger modulation and hence a decrease of the boron flux. At the same time, a larger Fisk potential enhances the interstellar fluxes of the boron progenitors (e.g. carbon) compared to the TOA fluxes measured at AMS-02. The corresponding increase of the boron source term would efficiently cancel the modulation-caused decrease of the boron flux.

[8] For the direct comparison we had to rebin the AMS-02 data in order to match the PAMELA bins. This was achieved by fitting a smooth function $\Phi^{\text{smooth}}_{\bar{p}}$ through the AMS-02 data. For rigidity bins $\{\mathcal{R}_1,\mathcal{R}_2\}$ which had to be split at $\mathcal{R}'$, we distributed the detected events below and above $\mathcal{R}'$ according to the ratio $\int_{\mathcal{R}_1}^{\mathcal{R}'} d\mathcal{R}\,\Phi^{\text{smooth}}_{\bar{p}} / \int_{\mathcal{R}'}^{\mathcal{R}_2} d\mathcal{R}\,\Phi^{\text{smooth}}_{\bar{p}}$. The rebinning only affects a limited number of bins and is not expected to introduce significant systematic errors.

[9] We used PAMELA proton data above $T = 2$ GeV for which $\phi^+_{1,\text{PAMELA}}$ is negligible.

of secondary species (boron, antiprotons and positrons), it is wise to choose a more economical path. Rather than dealing with the full network, we will determine the fluxes of the direct progenitors of boron, antiprotons and positrons from the available experimental data. This reduces the number of relevant production cross sections to a more manageable number of 24 (48 if we include production on helium) and the relevant primary fluxes to 8. These will be parameterized in the following.

2.3.1 Boron Production Cross Section

The element boron (B) plays a significant role in cosmic ray physics. Its importance relates to the fact that boron is presumably a pure secondary which makes it an ideal target to study cosmic ray propagation effects. The two stable boron isotopes, ^{11}B and ^{10}B, mainly descend from the spallation of carbon (C), oxygen (O) and nitrogen (N), but also neon (Ne), magnesium (Mg), and silicon (Si) yield non-negligible contributions. In the spallation processes, the kinetic energy per nucleon is approximately preserved, i.e.

$$\left(\frac{d\sigma_{ij\to a}}{dT}\right) = \sigma_{ij\to a}\delta(T' - T)\,, \tag{2.12}$$

where T' and T stand for the kinetic energy per nucleon of the incoming primary and outgoing secondary particle. This equation is also referred to as "straight-ahead approximation". There exist several parameterizations of fragmentation cross sections in the literature [118–121], of which the one by Webber et al. [118] and the one implemented in GALPROP [121] are most commonly used. Unfortunately, the corresponding uncertainties have not been estimated in a systematic way. This is problematic as we later want to perform spectral fits to the B/C ratio in cosmic rays. Due to the small experimental errors in the flux, spallation cross sections are a comparable if not the dominant source of uncertainty. Therefore, we decided to redetermine the fragmentation cross sections for C, N, O, Ne, Mg, Si, B to B on hydrogen and helium. We shall derive the cross sections and the related uncertainties from a wide collection of experimental data. An additional motivation for this exercise are deviations from the Webber parameterization which are observed in some recent data sets.

We will follow the convention to include reactions proceeding through short-lived radioactive nuclei (e.g. $^{12}\mathrm{C} + p \to {}^{11}\mathrm{C} \xrightarrow{\beta^+} {}^{11}\mathrm{B}$), referred to as ghosts, as part of the spallation cross section. The term "short-lived" is to be understood on astrophysical scales and stands for lifetimes $\tau <$ kyr. The very long-lived isotope ^{10}Be which decays into ^{10}B is treated as a separate final state which will be considered in addition to ^{11}B and ^{10}B. We parameterize the fragmentation cross section of the nucleus i to boron on a hydrogen target as

$$\sigma_{i+p\to\mathrm{B}} = \sigma_{0,i}\,\frac{\Gamma_i^2\,(T - E_{\mathrm{th},i})^2}{(T^2 - M_i^2)^2 + \Gamma_i^2 M_i^2} + \sigma_{1,i}\left(1 - \frac{E_{\mathrm{th},i}}{T}\right)^{\xi_i}\left(1 + \frac{\Delta_i}{1 + (T_\mathrm{h}/T)^2}\right). \tag{2.13}$$

Above energy threshold, $E_{\mathrm{th},i}$, cross sections show a resonance peak whose normalization, position and width is set by the parameters $\sigma_{0,i}$, M_i and Γ_i. If one subtracts the peak, there appears a steady rise which continues up to $T \sim$ GeV with its smoothness controlled by ξ_i. While in the older literature (e.g. [122]) spallation cross sections were taken to be constant above this energy, a non-trivial behavior at $T = 1 - 5$ GeV was motivated by Webber et al. [118] on observational grounds. As we find that fits to the experimental data indeed improve significantly when allowing for a slow change of the cross section around $T_\mathrm{h} = 2$ GeV, we have added the term in the last brackets. In this way a very similar functional behavior as in the Webber parameterization can be achieved if preferred by the data. At

energies $T > 5\,\mathrm{GeV}$, where nuclear binding energies are irrelevant, spallation cross sections approach the asymptotic value $\sigma_{i+p\to \mathrm{B}} = \sigma_{1,i}\,(1 + \Delta_i)$. The existence of a plateau is commonly assumed in the literature but awaits experimental proof. As total inelastic cross sections are known to increase slowly with energy beyond $T = 10\,\mathrm{GeV}$, one may also speculate about a proportional rise in the individual spallation cross sections [123]. A full correlation between the cross sections is, however, ambiguous as the final state particle spectrum in inelastic collision also changes with increasing energy, where multiparticle production gains significance. Given the sparseness of high energy data we decided to follow the standard assumption of a plateau in the spallation cross sections.

Sufficient experimental data to perform our fits only exist for the most abundant isotope of the respective element (e.g. ^{12}C in the case of carbon). This leaves us with 20 considered isotopic fragmentation cross sections for which the collected data are shown in Fig. 2.2. A number of comments are in order: in some references [144, 148–150] only the charge-changing cross sections have been measured. These were translated into isotopic cross sections by using the hydrogen mass fractions given in [145]. If the latter were not specified (i.e. for Si, Mg and Ne) we used the Webber code as extracted from DRAGON in order to predict how the cross section is divided among the isotopes. In the case of silicon, a previous step was required as the charge-changing cross section was only measured down to Z=6 (carbon). Luckily, data down to Z=4,5 exist for a polyethylene target [151]. We determined the charge changing cross section to Z=4,5 on hydrogen by assuming that the ratio of cross section to Z=6 compared to Z=4,5 is the same for hydrogen and polyethylene.[10] The isotopic cross sections were then obtained as described above. We refrained from assigning a systematic error to this procedure as silicon only contributes to the boron production at the few percent level. Turning to the low energy part of the fragmentation cross sections, sufficient data to fit the resonance peak above threshold do not exist for Ne, Mg and Si. This is acceptable for our purposes as we will later deal with cosmic ray boron at $T > 0.4\,\mathrm{GeV}$ which is practically unaffected by the threshold behavior of the cross sections. Nevertheless, as a tiny effect may still arise due to the reacceleration of very low energy cosmic rays, we attempt to capture at least roughly the threshold behavior for the dominant boron progenitors C, N and O. In the case of nitrogen a very complicated structure with various peaks emerges which we slightly smooth out by combining energy bins in sets of two [124].[11] The low-energy data on the cross section for $^{12}\mathrm{C} \to {}^{10}\mathrm{B}$ were obtained from the isobaric cross section to A=10 [127, 142] by subtracting the (tiny) beryllium contribution [125].

We determined the best fit parameters for each individual cross section. The parameters $\sigma_{0,i}$, M_i, Γ_i (considered only for C, N, O) were kept fixed at their best fit values as variations hardly affect the boron flux in the relevant energy range (see above). The probability distribution of $\sigma_{1,i}$, ξ_i, Δ_i was determined from a $\Delta\chi^2$-metric with three degrees of freedom (d.o.f.).[12] Parameter values and uncertainties (for $\sigma_{1,i}$, ξ_i, Δ_i) are given in Tab. 2.1. In Fig. 2.2 we show the median cross sections and the uncertainty bands ($\pm 1\sigma$) following from the derived probability distribution on the cross section parameters. Correlations between uncertainties at different energies cannot be made visible in the figure, but are taken into account in the following.

In Tab. 2.2, we compare the fragmentation cross sections (summed over the two boron isotopes) from our fits with those from the Webber parameterization at two different energies. It can be seen

[10] This is justified as a very similar behavior of the charge changing cross sections down to Z=6 is observed for hydrogen and polyethylene.

[11] We conservatively assume 20% errors as no uncertainties were given in this reference.

[12] For some cross sections the parameter Δ_i is not well constrained due to the lack of high energy data. In order to avoid unphysical values of Δ_i we imposed the (conservative) constraint $|\Delta_i| < 0.5$.

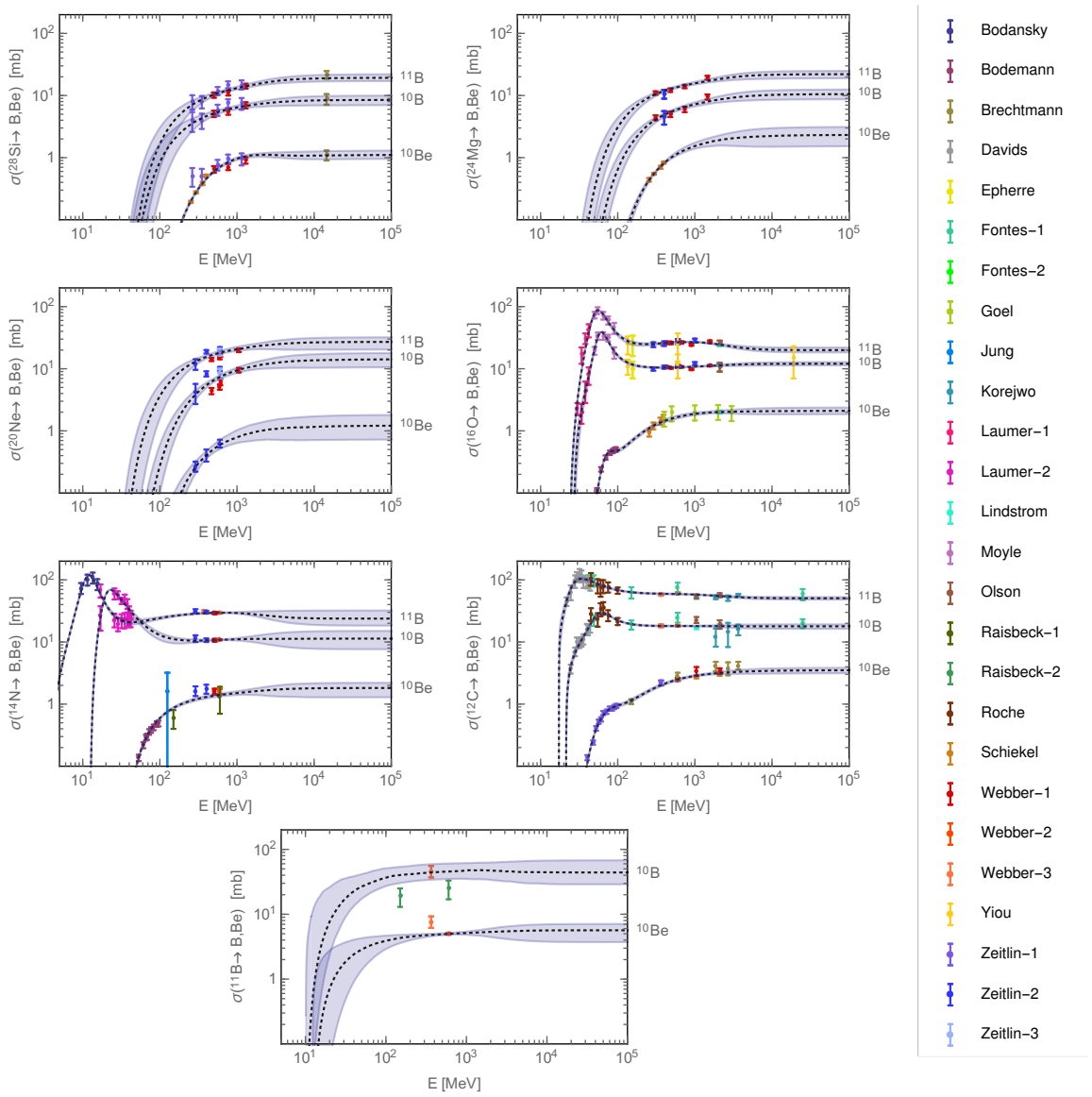

Figure 2.2: Isotopic cross sections for the fragmentation of ^{28}Si, ^{24}Mg, ^{20}Ne, ^{16}O, ^{14}N, ^{12}C, ^{11}B to ^{10,11}B and ^{10}Be. Also shown are our fits and the corresponding uncertainty bands. Experimental data are taken from Bodansky [124], Bodemann [125], Brechtmann [126], Davids [127], Epherre [128], Fontes-1 [129], Fontes-2 [130], Goel [131], Jung [132], Korejwo [133, 134], Laumer-1 [135], Laumer-2 [136], Lindstrom [137], Moyle [138], Olson [139], Raisbeck-1 [140], Raisbeck-2 [141], Roche [142], Schiekel [143], Webber-1 [144], Webber-2 [145], Webber-3 [146], Yiou [147], Zeitlin-1 [148], Zeitlin-2 [149], Zeitlin-3 [150]. In some cases the original data were processed in order to arrive at isotopic cross sections (see text).

Channel	$E_{\mathrm{th},i}$ [MeV]	$\sigma_{0,i}$ [mb]	M_i [MeV]	Γ_i [MeV]	$\sigma_{1,i}$ [mb]	ξ_i	Δ_i
$^{28}\mathrm{Si} \to {}^{11}\mathrm{B}$	26.7				$15.1^{+2.4}_{-1.6}$	$7.1^{+3.4}_{-2.2}$	$0.30^{+0.14}_{-0.21}$
$^{28}\mathrm{Si} \to {}^{10}\mathrm{B}$	29.0				$7.5^{+1.7}_{-0.9}$	$6.4^{+4.2}_{-2.3}$	$0.12^{+0.26}_{-0.29}$
$^{28}\mathrm{Si} \to {}^{10}\mathrm{Be}$	40.9				$1.71^{+0.15}_{-0.12}$	$12.1^{+0.6}_{-0.5}$	$-0.36^{+0.14}_{-0.10}$
$^{24}\mathrm{Mg} \to {}^{11}\mathrm{B}$	21.0				$17.6^{+2.0}_{-1.8}$	$7.4^{+2.1}_{-1.9}$	$0.29^{+0.15}_{-0.25}$
$^{24}\mathrm{Mg} \to {}^{10}\mathrm{B}$	22.5				$8.7^{+1.3}_{-1.1}$	$10.4^{+2.7}_{-2.5}$	$0.24^{+0.18}_{-0.29}$
$^{24}\mathrm{Mg} \to {}^{10}\mathrm{Be}$	36.0				$2.27^{+0.45}_{-0.23}$	$10.9^{+1.5}_{-0.9}$	$0.01^{+0.33}_{-0.34}$
$^{20}\mathrm{Ne} \to {}^{11}\mathrm{B}$	23.6				$23.3^{+5.3}_{-2.0}$	$6.7^{+3.8}_{-1.9}$	$0.17^{+0.22}_{-0.37}$
$^{20}\mathrm{Ne} \to {}^{10}\mathrm{B}$	23.6				$13.1^{+3.0}_{-2.0}$	$14.3^{+4.5}_{-3.4}$	$0.13^{+0.25}_{-0.36}$
$^{20}\mathrm{Ne} \to {}^{10}\mathrm{Be}$	37.2				$1.19^{+0.63}_{-0.30}$	$11.0^{+4.3}_{-3.0}$	$0.0^{+0.32}_{-0.34}$
$^{16}\mathrm{O} \to {}^{11}\mathrm{B}$	23.6	240	45.9	34.2	$31.4^{+1.7}_{-1.1}$	$4.0^{+1.1}_{-0.6}$	$-0.36^{+0.08}_{-0.07}$
$^{16}\mathrm{O} \to {}^{10}\mathrm{B}$	26.9	104	55.0	29.0	$10.9^{+0.3}_{-0.2}$	$1.3^{+0.4}_{-0.2}$	0.10 ± 0.08
$^{16}\mathrm{O} \to {}^{10}\mathrm{Be}$	36.6	1.3	62.3	45.2	$2.28^{+0.17}_{-0.16}$	4.9 ± 0.3	$-0.07^{+0.17}_{-0.15}$
$^{14}\mathrm{N} \to {}^{11}\mathrm{B}$	3.1	193	10.6	7.3	31.6 ± 0.8	$9.6^{+1.8}_{-1.6}$	$-0.24^{+0.28}_{-0.19}$
$^{14}\mathrm{N} \to {}^{10}\mathrm{B}$	12.5	360	16.9	14.1	$11.6^{+0.8}_{-0.5}$	$3.7^{+3.3}_{-1.5}$	$-0.02^{+0.36}_{-0.34}$
$^{14}\mathrm{N} \to {}^{10}\mathrm{Be}$	34.3				1.6 ± 0.09	$2.36^{+0.09}_{-0.08}$	$0.15^{+0.24}_{-0.34}$
$^{12}\mathrm{C} \to {}^{11}\mathrm{B}$	17.3	330	18.9	23.5	$60.2^{+1.1}_{-0.9}$	$0.47^{+0.15}_{-0.11}$	$-0.16^{+0.04}_{-0.05}$
$^{12}\mathrm{C} \to {}^{10}\mathrm{B}$	21.4	34.1	46.9	46.9	$18.4^{+0.4}_{-0.3}$	$0.75^{+0.07}_{-0.06}$	$-0.03^{+0.08}_{-0.10}$
$^{12}\mathrm{C} \to {}^{10}\mathrm{Be}$	29.5	0.24	14.9	242	3.5 ± 0.2	$7.0^{+0.5}_{-0.4}$	0.0 ± 0.13
$^{11}\mathrm{B} \to {}^{10}\mathrm{B}$	10.1				$49.0^{+14.4}_{-12.7}$	$2.7^{+1.6}_{-1.9}$	$-0.04^{+0.36}_{-0.32}$
$^{11}\mathrm{B} \to {}^{10}\mathrm{Be}$	12.3				$5.2^{+0.4}_{-0.2}$	$2.1^{+2.8}_{-1.5}$	$0.08^{+0.28}_{-0.39}$

Table 2.1: Fit parameters entering the fragmentation cross section parameterization (2.13).

Channel	σ(1 GeV)	σ_{Webber}(1 GeV)	σ(10 GeV)	σ_{Webber}(10 GeV)
$^{28}\text{Si} \rightarrow \text{B}$	$19.7^{+0.8}_{-0.9}$	13.2	$27.2^{+2.6}_{-2.7}$	14.2
$^{24}\text{Mg} \rightarrow \text{B}$	$23.0^{+0.9}_{-1.2}$	20.4	$31.8^{+3.3}_{-3.4}$	20.4
$^{20}\text{Ne} \rightarrow \text{B}$	$30.2^{+2.1}_{-1.7}$	21.9	$40.4^{+5.9}_{-6.6}$	21.1
$^{16}\text{O} \rightarrow \text{B}$	$37.6^{+0.5}_{-0.4}$	36.9	$32.3^{+1.9}_{-1.8}$	34.7
$^{14}\text{N} \rightarrow \text{B}$	$40.4^{+1.2}_{-1.1}$	41.2	$35.6^{+8.6}_{-6.1}$	37.1
$^{12}\text{C} \rightarrow \text{B}$	$76.0^{+0.8}_{-0.9}$	75.4	$68.6^{+2.5}_{-2.6}$	61.0
$^{11}\text{B} \rightarrow {}^{10}\text{B}$	$47.3^{+14.3}_{-12.2}$	40.5	$44.4^{+22.8}_{-15.1}$	39.0

Table 2.2: Comparison of the fragmentation cross sections into boron (^{11}B + ^{10}B) determined in this work with the parameterization by Webber.

that substantial differences exist for Si, Mg, Ne, for which we obtain systematically higher cross sections than Webber. For these three elements we employed recent data sets which did not enter in [118]. The effect on cosmic ray boron production, to which Si, Mg, Ne contribute about 10%, is not huge but may amount to a few percent. For C, N, O, our cross sections are in overall good agreement with those by Webber. Only for carbon, there appears a $\sim$ 10% discrepancy at high energy. The Webber parameterization shows a strong decrease of the carbon spallation cross section between $T = 1$ GeV and $T = 10$ GeV which is not preferred by our fit. In [118] it is argued that this decrease is backed up by the data of Korejwo et al. [133, 134]. Given that Korjewo et al. measured $\sigma(^{12}C \rightarrow B) = 65, 65.3, 72.8$ mb at $T = 1.87, 2.69, 3.66$ GeV this argument is not plausible at all. The only data point [129] at higher energy ($T = 25$ GeV) also speaks against the strong decrease albeit with large uncertainty. Unfortunately, existing data are insufficient to fully settle this issue and upcoming experimental efforts are eagerly awaited.

Besides the spallation of nuclei on hydrogen, also the spallation on helium contributes significantly to the boron flux. In [152] it was suggested to account for scattering on helium by multiplying the protonic fragmentation cross sections by an energy-dependent enhancement factor of the form

$$e^{\mu|(Z_i - Z_f) - f_i\delta|^\nu}\,, \tag{2.14}$$

where Z_i and Z_f denote the atomic number of the initial and final state nucleus respectively. The exponent ν as well as the functions δ, μ are extracted from iron fragmentation on a helium target at three different beam energies [152]. The coefficients f_i depend on the initial nucleus and are determined by interpolating between carbon, oxygen and iron fragmentation on helium.

While we employ the functional form (2.14), we refrain from using the parameters given in [152]. This is because the exponent $\nu = 1.43$ [152] leads to a very steep increase of cross sections with Z_i which is inconsistent with data on aluminum spallation by helium [144]. Furthermore, μ and δ determined in [152] lead to unphysical results for silicon and magnesium fragmentation at low energies. This can be seen from silicon carbon scattering [148] which is expected to show a similar low-energy behavior as silicon helium scattering. Our approach is, therefore, to refit the enhancement

factor using carbon, nitrogen, oxygen and aluminum instead of iron data. We find

$$\mu = 0.29 - \frac{0.056\,T}{\mathrm{GeV}}\,, \qquad \delta = 1.93 - \frac{0.45\,T}{\mathrm{GeV}}\,, \qquad \nu = 0.57\,, \tag{2.15}$$

where we assumed μ and δ to be linear functions of energy for $T < 1.6\,\mathrm{GeV}$ as in [152]. Above this energy μ and δ are taken to be constant.[13] The parameters $f_{\mathrm{C,N,O}}$ are fitted to the data sets [144, 152], while $f_{\mathrm{Ne,Mg,Si}}$ are obtained by linear interpolation between the values for oxygen and aluminum

$$\begin{aligned} f_{\mathrm{C}} &= -0.35 \pm 0.45\,, \quad f_{\mathrm{N}} = -0.8 \pm 0.64\,, \quad f_{\mathrm{O}} = 0.04 \pm 0.35\,, \\ f_{\mathrm{Ne}} &= 0.24 \pm 0.37\,, \quad f_{\mathrm{Mg}} = 0.45 \pm 0.38\,, \quad f_{\mathrm{Si}} = 0.65 \pm 0.4\,. \end{aligned} \tag{2.16}$$

Before we finish the discussion on spallation cross sections, we should emphasize that new precision data are urgently required. They are needed to eliminate systematic errors in the parameterizations of all relevant spallation cross sections (on hydrogen and helium) and to establish the high energy behavior. The data we employed in this work were taken over a period of more than four decades in time, using hugely varying experimental techniques. In some cases claimed uncertainties appear suspiciously small. We believe that our analysis contributes in identifying some of the most urgent measurements to be performed (e.g. carbon spallation at energies above a few GeV), but further work is certainly needed.

2.3.2 Antiproton Production Cross Section

Secondary antiprotons in cosmic rays mainly originate from proton proton collisions, but also processes involving helium yield a seizable contribution. Since antiprotons are generated with a smooth phase space distribution, the full differential cross section must be modeled at all relevant energies. Experimental data again play a crucial role in this as the cross section is dominated by soft QCD processes and cannot be calculated from first principles. A complication arises from the fact that about half of the antiprotons in cosmic rays stem from the decay of antineutrons which escape detection in laboratory experiments. This contribution must be modeled on the basis of symmetry arguments. In addition, antiprotons partly stem from the decay of strange hyperons which are metastable on detector scales. As in most experiments this contribution is rejected through cuts, it must be determined from the phase space distribution of the parent hyperons. A careful analysis of all relevant processes has been performed in [80, 153] which we will briefly review for completeness.

The (Lorentz) invariant differential cross section $f_{pp\to\bar{p}} \equiv f_{\bar{p}}$ can be expressed as

$$f_{\bar{p}} \equiv E\frac{d^3\sigma_{\bar{p}}}{dp^3} = f^0_{\bar{p}}\,(2 + \Delta_{\mathrm{IS}} + 2\,\Delta_{\Lambda})\,, \tag{2.17}$$

where the energy and three-momentum of the final state antiproton are denoted by E and p respectively. The index 0 indicates the prompt part of the antiproton production, while Δ_{Λ} stands for the hyperon induced contribution. Both are multiplied by the factor of two in order to account for antineutrons. A possible asymmetry between antineutron and antiproton production due to isospin effects

[13] There are no data above $T = 1.6\,\mathrm{GeV}$, but the enhancement factor should become constant around this energy [152].

is included through $\Delta_{\rm IS}$. The prompt cross section

$$f^0_{\bar{p}} = R\,\sigma_{pp\,\rm in}\,c_5\,(1-x_R)^{c_6}\left[1+X(m_{\rm T}-m_p)\right]^{-\frac{1}{X c_7}}\,, \tag{2.18}$$

is modeled in terms of the transverse momentum $p_{\rm T}$ and the radial scaling variable $x_R = E^*/E^*_{\rm max}$ with E^* denoting the antiproton energy in the center-of-mass frame and $E^*_{\rm max} = (s-8m_p^2)/(2\sqrt{s})$ the maximal energy. The function R accounts for near threshold production of antiprotons. It is taken to be unity at $T > 10$ GeV and

$$R = \left[1+c_9\left(10-\tfrac{\sqrt{s}}{\rm GeV}\right)^5\right]\exp\left[c_{10}\left(10-\tfrac{\sqrt{s}}{\rm GeV}\right)^2(x_R-x_{R,\rm min})^2\right] \quad \text{for } T \le 10\,\text{GeV}\,. \tag{2.19}$$

There occur two additional terms in $f^0_{\bar{p}}$ which violate radial scaling through their explicit energy-dependence: the inelastic cross section

$$\sigma_{pp,\rm in} = c_{11} + c_{12}\,\log\sqrt{s} + c_{13}\,\log^2\sqrt{s}\,, \tag{2.20}$$

grows slowly with $\sqrt{s}$. In addition, the term

$$X = c_8\,\log^2\left[\frac{\sqrt{s}}{4\,m_p}\right], \tag{2.21}$$

induces a flattening in the $p_{\rm T}$-distributions at large energy. It originates from multiple scattering of protons which goes along with the production of hard $p_{\rm T}$-jets. Coming back to (2.17), the hyperon contribution can be expressed as $\Delta_\Lambda = (0.81\pm0.04)\,(\bar{\Lambda}/\bar{p})$ with

$$\bar{\Lambda}/\bar{p} = c_1 + \frac{c_2}{1+(c_3/s)^{c_4}}\,, \tag{2.22}$$

where the second term on the right-hand side accounts for the increased strange hadron production which sets in at $\sqrt{s}\sim 100$ GeV. Finally, the asymmetry between antineutron and antiproton production is written as

$$\Delta_{\rm IS} = \frac{c_{14}}{1+(s/c_{15})^{c_{16}}}\,. \tag{2.23}$$

A non-vanishing $\Delta_{\rm IS}$ may be present at low energy, but the experimental data are not fully conclusive. In any case, the asymmetry disappears at high energy. The parameterization contains in total 16 parameters $c_1\ldots c_{16}$ which were fitted to a large set of experimental data in [80]. In Tab. 2.3 we provide median values and uncertainties for the c_i.[14]

In Fig. 2.3, we compare the integrated antiproton production cross section derived from (2.17) with the cross section obtained from the parameterizations of Tan et al. [154] and di Mauro et al. [155]. As can be seen, the cross section predicted by Tan et al. falls short at high energy as it does not account for the violation of radial scaling. Di Mauro et al. provide two parameterizations (in equations (12) and (13) of [155]) which were fit to data at $\sqrt{s}\le 200$ GeV. They differ substantially in the high energy regime due to different extrapolations.

The cross sections involving helium were predicted in [80] from an empirical model which was introduced in [162] for proton carbon scattering and first applied to helium in [153]. The invariant

[14] In some cases, the median values differ marginally from the best fit values provided in [80].

c_1	c_2	c_3	c_4
0.31 ± 0.04	0.30 ± 0.06	$(153^{+65}_{-57})^2$ GeV^2	1.0 ± 0.3
c_5	c_6	c_7	c_8
0.0467 ± 0.0038	7.77 ± 0.10	(0.168 ± 0.001) GeV	(0.0380 ± 0.0006) GeV^{-1}
c_9	c_{10}	c_{11}	c_{12}
0.0010 ± 0.0004	0.7 ± 0.04	(30.9 ± 0.4) mb	(-1.74 ± 0.17) mb
c_{13}	c_{14}	c_{15}	c_{16}
(0.71 ± 0.02) mb	$0.20^{+0.30}_{-0.18}$	$(31^{+47}_{-25})^2$ GeV^2	1.0 ± 0.3

Table 2.3: Parameters entering the antiproton production cross section (2.17) and related uncertainties.

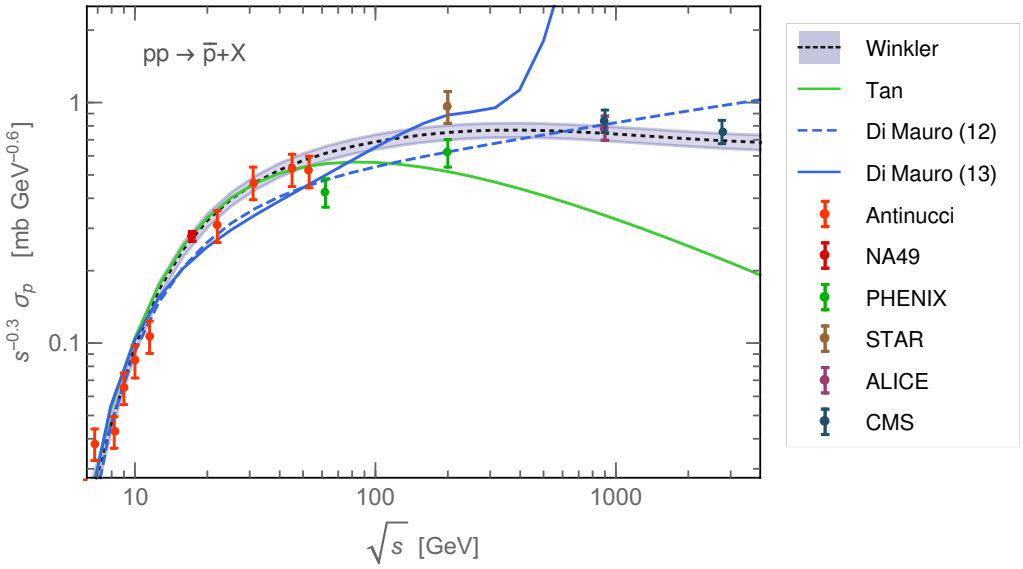

Figure 2.3: Antiproton production cross section employed in this work [80] compared to the cross section derived from the parameterizations of Tan et al. [154] and di Mauro et al. [155]. The contribution from antineutron decay is not included in this figure. Experimental data were taken from [156–161] and processed as described in [80].

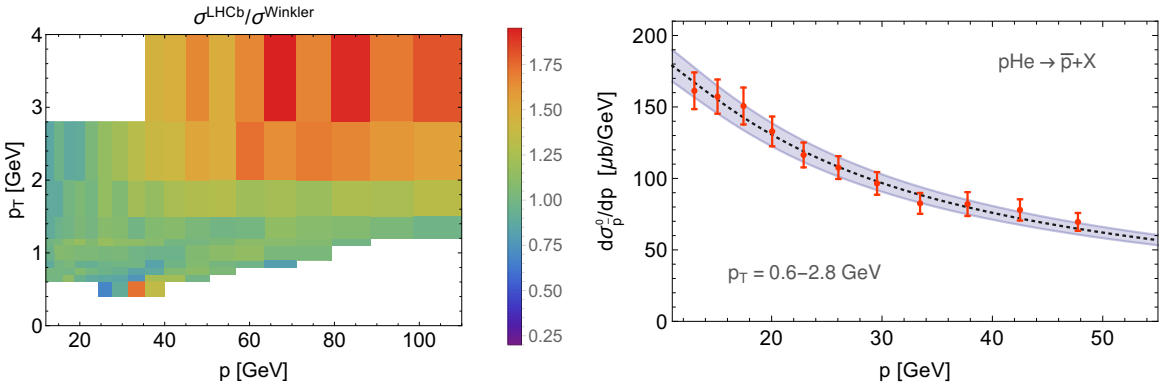

Figure 2.4: Prompt antiproton production cross section in proton helium scattering. In the left panel the full differential cross section predicted in [80] is compared to the LHCb data. The right panel refers to the cross section integrated over $p_T = 0.6 - 2.8$ GeV. Uncertainties on the prediction (blue band) are derived from the uncertainties in the parameters $c_1 - c_{16}$ [80].

antiproton production cross section is expressed in terms of $f_{\bar{p}}$ as

$$f_{ij\to\bar{p}} = \frac{\sigma_{ij,\mathrm{in}}}{\sigma_{pp,\mathrm{in}}} \left(\langle \nu_i \rangle F_{\mathrm{pro}}(x_f) + \langle \nu_j \rangle F_{\mathrm{tar}}(x_f) \right) f_{\bar{p}} \,, \tag{2.24}$$

where $i = p$,He and $j = p$,He stand for the projectile and the target particle respectively. The ratios of inelastic cross sections are taken to be $\sigma_{pp,\mathrm{in}} : \sigma_{p\mathrm{He},\mathrm{in}} : \sigma_{\mathrm{HeHe},\mathrm{in}} = 1 : 3.2 : 7.7$ [153]. The projectile and target overlap functions are defined in terms of the Feynman scaling variable $x_f = p^*_{\mathrm{L}}/(2\sqrt{s})$ [162], where p^*_{L} denotes the longitudinal antiproton momentum in the center-of-mass frame. The average number of interacting nucleons in the projectile and target $\langle \nu_{i,j} \rangle$ can be expressed in terms of the inelastic cross sections $\langle \nu_i \rangle = A_i \, \sigma_{pp,\mathrm{in}}/\sigma_{ip,\mathrm{in}}$, where A_i denotes the mass number of the nucleus i.

The antiproton production in proton helium scattering has recently been measured for the first time with the LHCb-SMOG detector [163] which provides an important test for the parameterization [80]. Incoming protons with energy 6.5 TeV were scattered on a helium gas target at rest. The data refer to the prompt antiproton production which can be obtained by replacing $f_{\bar{p}}$ with $f^0_{\bar{p}}$ in (2.24). In addition, the target component (the term including F_{tar}) has to be multiplied by $(1 + 0.5\,\Delta_{\mathrm{IS}})$ to account for the difference between a proton and a mixed proton-neutron target.[15] This factor is, however, almost negligible at the considered energy. A detailed comparison of the prediction [80] with the LHCb data is provided in Fig. 2.4. It can be seen that very good agreement is obtained for $p_T \leq 2\,\mathrm{GeV}$. At higher p_T the measured cross section somewhat exceeds the prediction. But as $p_T > 2\,\mathrm{GeV}$ contributes $\lesssim 1\%$ to the total cross section, this difference has negligible impact on the cosmic ray antiproton flux. Since the p_T-integrated cross section is in remarkably good agreement with the data (see Fig. 2.4) we will employ the parameterization (2.24) without modification.

[15] Note that the factor Δ_{IS} does not appear in (2.24). While the relative number of produced antiprotons to antineutrons differs between a proton and neutron target if $\Delta_{\mathrm{IS}} \neq 0$, the total number of antinucleons does not.

2.3.3 Positron Production Cross Section

Secondary positrons, similar to antiprotons, mainly stem from proton proton scattering as well as from processes involving helium. In most cases, positrons descend as final states from the decay chains of pions and kaons. There exist several parameterizations of the inclusive cross section for positron production in the literature. These rely either on analytic fits to experimentally measured meson spectra [164–166] or on Monte Carlo simulation [167]. In our analysis, we will not attempt to fit the positron flux over the full energy range. Rather we will use the minimal secondary positron flux to constrain the size of the diffusion halo L. Different from the case of boron and antiprotons, we do not require an uncertainty band for positron production, but merely a robust lower limit. Therefore, we do not attempt to evaluate the production cross section ourselves and, instead, employ the parameterization of Kamae et al. [167].[16] It was pointed out in [96] that this parameterization yields positron fluxes up to a factor of two smaller compared to [164, 165] which will result in a conservative bound on L.

2.3.4 Progenitors of Secondary Cosmic Rays

A robust parameterization of primary fluxes[17] is another important ingredient in predicting the source terms of secondary cosmic rays. While antiprotons and positrons mainly stem from collisions involving proton and helium, the production of boron results from spallation of carbon, oxygen, nitrogen and subdominantly silicon, magnesium and neon. We model the interstellar fluxes as a function of rigidity $\mathcal{R}$ as

$$\Phi_i^{\rm IS}(\mathcal{R}) = \frac{\mathcal{R}}{\sqrt{\mathcal{R}^2 + \mathcal{R}_{l,i}^2}}\, \alpha_i \left(\frac{\mathcal{R}}{\rm GV}\right)^{-\gamma_i} \left(1 + \left(\frac{\mathcal{R}}{\mathcal{R}_b}\right)^{\Delta\gamma/s}\right)^s . \tag{2.25}$$

The first factor on the right-hand side allows to fit the low energy part of the spectra, while α_i and γ_i set the normalization and the power law index of the flux. The last term accounts for the observed spectral hardening at rigidity $\mathcal{R}_b$. As there is indication that primary cosmic rays share the position and form of the spectral break [123, 168], we choose the parameters $\mathcal{R}_b$, $\Delta\gamma$ and s to be universal among the considered species. The origin of the spectral break will be discussed in Sec. 2.5.1. The isotopic composition of fluxes, which is assumed to be rigidity-independent, is estimated from the cosmic ray data base. We neglect a deuteron contamination of the proton flux and set ^{3}He : ^{4}He = 0.15 : 0.85, ^{12}C : ^{13}C = 0.93 : 0.07, ^{14}N : ^{15}N = 0.55 : 0.45, ^{16}O : ^{17}O : ^{18}O = 0.96 : 0.02 : 0.02. The Ne, Mg, Si fluxes, which contribute only subdominantly to boron production, are identified with the leading isotopes ^{20}Ne, ^{24}Mg and ^{28}Si for simplicity.

The parameterization (2.25) was fit to the published (H, He) or preliminary (C, N, O) data of AMS-02 [115, 169, 170], see Fig. 2.5 and 2.6. In the case of C, N, O, fluxes are given in terms of the kinetic energy per nucleon and the parameterization was translated accounting for the isotopic composition. Uncertainty bands were determined in a slightly simplified two step procedure: first, we derived the probability distribution of the break parameters. Then we kept the break parameters fixed at their best fit values and determined the probability distributions for the individual α_i, γ_i, $\mathcal{R}_{l,i}$, employing

[16] A number of typos have been corrected with the kind help of the authors.

[17] We use a loose terminology here and call the progenitors of boron, antiprotons and positrons primaries. Strictly speaking the progenitor fluxes contain a secondary admixture themselves.

species	α_i [$m^{-2}sr^{-1}s^{-1}GV^{-1}$]	$\mathcal{R}_{l,i}$ [GV]	γ_i
p	$(2.79 \pm 0.01) \cdot 10^4$	2.74 ± 0.04	2.889 ± 0.001
He	$(4.01 \pm 0.02) \cdot 10^3$	2.97 ± 0.05	2.795 ± 0.001
C	123 ± 1	3.91 ± 0.09	2.765 ± 0.002
O	119 ± 1	4.19 ± 0.11	$2.743^{+0.002}_{-0.003}$
N	57 ± 1	5.68 ± 0.16	$2.968^{+0.004}_{-0.003}$
ratio	λ_i	ζ_i	
Ne/O	0.158 ± 0.002	-0.01 ± 0.01	
Mg/O	0.205 ± 0.004	-0.02 ± 0.01	
Si/O	0.153 ± 0.003	0.03 ± 0.01	

Table 2.4: Parameters entering the boron progenitor fluxes (2.25) (upper part) and parameters determining the ratios Ne/O, Mg/O, Si/O (lower part).

a $\Delta\chi^2$-metric with 3 d.o.f. for each species. In Tab. 2.4 we present the resulting median parameters and uncertainties. The large power-law index γ_N is explained as the nitrogen flux carries a strong secondary component. For the parameters characterizing the spectral break, we obtain $\mathcal{R}_b = 275^{+23}_{-22}$ GeV, $\Delta\gamma = 0.157^{+0.020}_{-0.012}$ and $s = 0.074^{+0.008}_{-0.007}$. As the AMS-02 data refer to TOA fluxes, the interstellar fluxes depend on assumptions regarding solar modulation. In order to derive the values in Tab. 2.4, we assumed the Fisk potential $\phi^+_{2,\text{AMS-02}} = 0.72$ GV. Interstellar fluxes assuming any other Fisk potential for AMS-02 can still be parameterized using the values of Tab. 2.4. One simply has to modulate the so-obtained fluxes with the difference between 0.72 GV and the true Fisk potential of AMS-02.

For Ne, Mg, Si, AMS-02 data are not yet available. As ratio data are less affected by systematic errors if one compares different experiments, we fit Ne/O, Mg/O, Si/O as extracted from HEAO [171] with the function $\lambda_i(T/\text{GeV})^{\zeta_i}$. Fits are visualized in Fig. 2.6, parameter values and uncertainties are given in Tab. 2.4. The absolute Ne, Mg and Si fluxes are then obtained by multiplying the ratios with the oxygen flux derived from AMS-02.

2.3.5 Secondary Source Terms

We can now use the derived cross sections and progenitor cosmic ray fluxes to determine the secondary source terms of boron, antiprotons and positrons, following Eq. (1.1). The incoming fluxes Φ_i and the differential cross sections ($d\sigma_{ij\to a}/dT$) are taken from the previous sections. For the case of antiprotons one may equivalently use the cross section tables published in [80]. In the case of boron, we determine the source terms of the two isotopes ^{11}B and ^{10}B separately, assuming the isotopic composition of primaries specified in the previous section. In the first step, we used the cross sections derived in Sec. 2.3.1 for all isotopes of the same element (e.g. we assumed that the fragmentation cross section of ^{13}C is identical to the one of ^{12}C). In order to account for errors, we then applied a

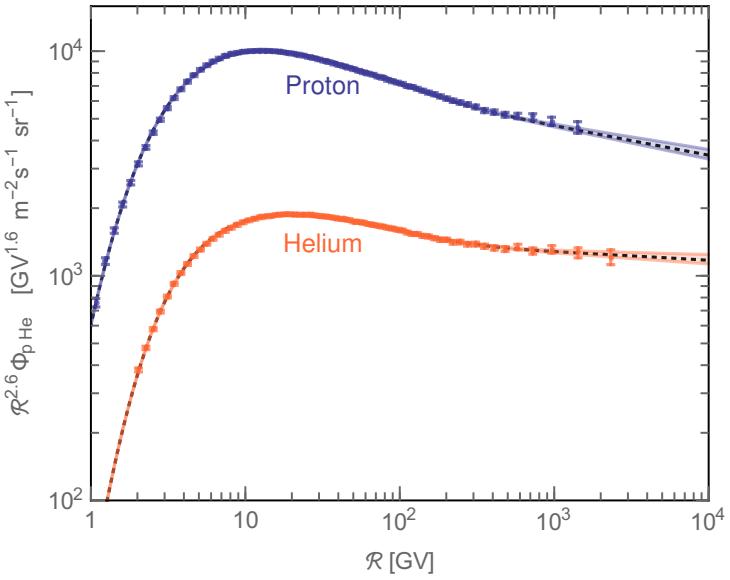

Figure 2.5: Proton and helium fluxes measured by AMS-02 and our fits with the corresponding uncertainty bands.

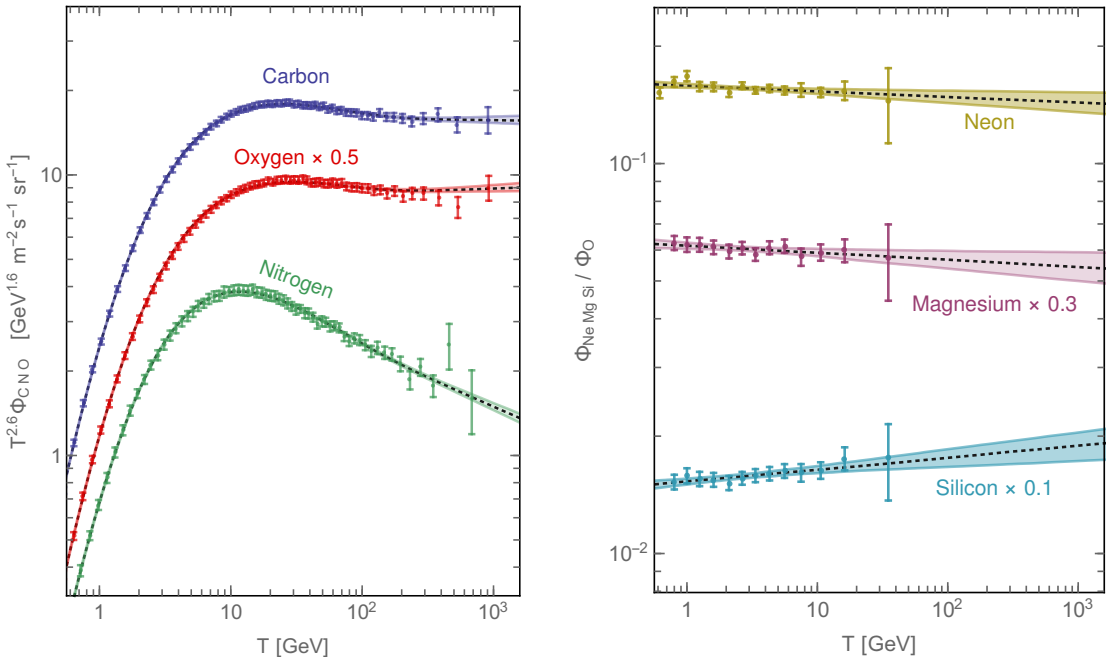

Figure 2.6: Fluxes of C, N, O measured by AMS-02 (left panel) and Ne/O, Mg/O, Si/O measured by HEAO (right panel). Our fits and the corresponding uncertainty bands are also shown.

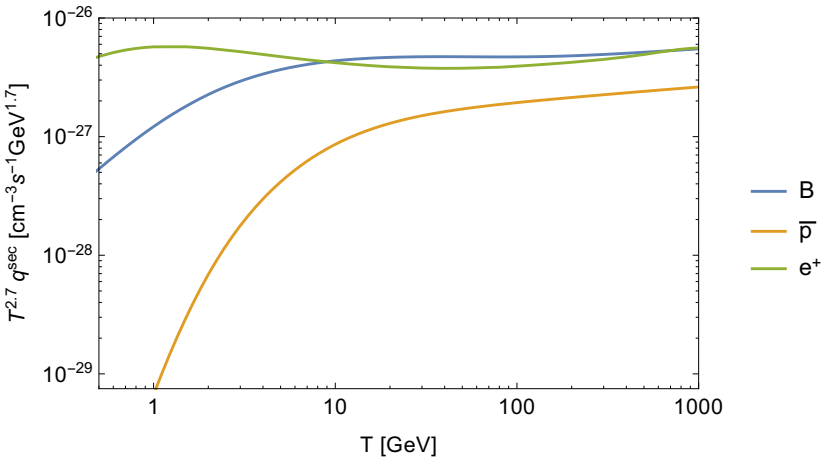

Figure 2.7: Secondary source terms of boron, antiprotons and positrons.

correction factor which was estimated from the Webber parameterization [118].[18] We note, however, that the correction only amounts to $\sim 1\%$ and can as well be neglected. Finally, we have to include boron production through the radioactive decay of ^{10}Be. For this purpose we simply add the source term of ^{10}Be to the source term of ^{10}B. This amounts to neglecting propagation effects on the abundance of ^{10}Be which would result from its long lifetime. The corresponding error on the total boron flux can be estimated to be $\lesssim 2\%$ [88]. We account for this by including an additional 2% normalization uncertainty in the boron flux on top of the uncertainties related to cross sections and primary fluxes.

In Fig. 2.7 we depict the secondary source terms of boron[19], antiprotons and positrons. It can be seen that $q^{\rm sec}_{\bar{p}}$ decreases more rapidly towards low energies compared to $q^{\rm sec}_{\rm B}$ and $q^{\rm sec}_{e^+}$ due to the higher threshold for antiproton production. At high energy, all source terms show an approximate power law behavior which is set by the progenitor fluxes. However, a slight increase of $q^{\rm sec}_{\bar{p}}$ and $q^{\rm sec}_{e^+}$ relative to $q^{\rm sec}_{\rm B}$ appears due to the violation of scaling which affects the antiproton and positron production cross sections (see Sec. 2.3.2).

2.4 Primary Antiprotons from Dark Matter Annihilation

While the secondary production of antimatter is well-established, one may also speculate about a primary component due to dark matter annihilation in the galactic halo. In the case of positrons, astrophysical contributions beyond secondary production (e.g. from pulsars) may well add to the flux. This complicates the dark matter analysis as one would have to deal with two unknown components simultaneously. Therefore, we decided to focus on the antiproton signal from dark matter annihilation in this work. We will later employ positrons to constrain cosmic ray propagation parameters, but this will only require knowledge of the secondary positron flux.

[18] We employed [118] and calculated $q^{\rm sec}_{\rm B}$ one time with isotope-dependent and one time with isotope-independent cross sections (using the cross sections of the leading isotopes). The correction factor corresponds to the ratio of the two.

[19] The ^{10}B source term contains a contribution from nucleon stripping of ^{11}B. The latter can be calculated once the propagation parameters are fixed and the ^{11}B-flux is known. In Fig. 2.7 we used the best fit configuration of Sec. 2.5.1.

The primary antiproton source term induced by dark matter annihilation reads

$$q_{\bar{p}}^{\text{prim}} = \frac{\rho_{\text{DM}}^2}{m_{\text{DM}}^2} \frac{\langle \sigma v \rangle}{2} \frac{dN}{dT} , \tag{2.26}$$

where dN/dT denotes the antiproton energy spectrum per annihilation process. We will consider $b\bar{b}$ and WW as final states and extract dN/dT for the two channels from [172]. While this choice may seem selective, we note that antiproton spectra in hadronic channels exhibit a similar shape. If a dark matter signal was present in the experimental data, we would typically observe an excess in $\bar{b}b$ or WW even if the true annihilation channel is not captured. The annihilation cross section $\langle \sigma v \rangle$ (averaged over the velocity distribution) determines the normalization of the primary signal. If dark matter is identified with a thermal WIMP, $\langle \sigma v \rangle$ is directly related to the dark matter density in the universe. For the canonical case of a velocity-independent σv, the observed density corresponds to [173]

$$\langle \sigma v \rangle \simeq 10^{-26}\ \text{cm}^3\ \text{s}^{-1} \times \frac{1}{\sqrt{g_*(T_F)}} \frac{m_{\text{DM}}}{T_F} , \tag{2.27}$$

where $T_F \simeq m_{\text{DM}}/20$ denotes the freeze-out temperature and g_* the effective number of degrees of freedom which can be taken from [174].

The dark matter density profile ρ_{DM} determines the normalization of the primary source term. While N-body simulations of cold dark matter suggest a Navarro-Frenk-White (NFW) profile [40], the backreaction of baryons on the dark matter halo is a field of active research. The local dark matter density ρ_0 constitutes another source of uncertainty. As the propagation of antiprotons washes out local features in the dark matter profile, the relevant quantity is the dark matter density averaged over a larger (∼kpc) scale. The latter is best assessed by global measurements which are converging at $\rho_0 \sim 0.4\ \text{GeV cm}^{-3}$ albeit with sizable uncertainties [175–178].

In order to capture the uncertainties in ρ_{DM}, we consider three representative dark matter halos which follow a generalized NFW (gNFW) profile

$$\rho_{\text{DM}} = \rho_0 \left(\frac{R_0}{r}\right)^{\gamma} \left(\frac{R_0 + r_s}{r + r_s}\right)^{3-\gamma} , \tag{2.28}$$

where r denotes the distance from the galactic center, R_0 the distance between galactic center and Sun and r_s the scale radius. The parameter γ determines the contraction of the profile. If not specified explicitly, we assume a standard NFW profile ($\gamma = 1$) and $\rho_0 = 0.38\,\text{GeV cm}^{-3}$ [178]. We will, however, also present results for a more conservative cored profile ($\gamma = 0$) with lower $\rho_0 = 0.3\ \text{GeV cm}^{-3}$ as well as a more aggressive cuspy profile ($\gamma = 1.3$) with $\rho_0 = 0.45\ \text{GeV cm}^{-3}$. In order to arrive at self-consistent halo models we took $R_0 = 8.2$ kpc and r_s for the NFW profile from [178] and determined the scale radii for the other two cases by keeping the amount of dark matter fixed within the radius $r = 50$ kpc. The parameters for the three profiles are summarized in Tab. 2.5.

We comment that a number of hydrodynamic simulations of Milky Way type galaxies which include baryonic effects have been performed. Most of them hint at a dark matter profile with slope $\gamma \sim 1$ or slightly larger down to the innermost part ($r \lesssim 1$ kpc), where a flattening may occur [179–182] (see however [183]). For the diffusion halos considered here, this suggests primary antiproton fluxes similar or larger than for the standard NFW profile. The cored profile with $\gamma = 0$ is somewhat disfavored, but shall, nevertheless, be included for the sake of a conservative approach.

Profile	ρ_0 [GeV cm^{-3}]	r_s [kpc]	R_0 [kpc]	γ
NFW	0.38	18.6	8.2	1
gNFW$_{\gamma=0}$	0.30	12.3	8.2	0
gNFW$_{\gamma=1.3}$	0.45	17.2	8.2	1.3

Table 2.5: Dark matter profiles considered in this work.

2.5 Combined Analysis of Charged Cosmic Ray Data

The AMS-02 experiment has provided high precision data on the antiproton flux and the B/C ratio. In this section we aim at investigating the consistency of the AMS-02 data with a secondary origin of the two species and at determining the favored propagation configuration. Experimental errors have shrunk to a level where they no longer dominate over uncertainties in the predicted fluxes. Therefore, we will carefully include uncertainties in the production of boron and antiprotons in our analysis. Since the secondary fluxes of boron and antiprotons are insensitive to a particular combination of propagation parameters, we will employ positrons in the last step, to lift this degeneracy.

2.5.1 B/C and the Diffusion Break

The ratio of B/C in cosmic rays plays an important role in pinning down the propagation parameters. In the first step, we use B/C to investigate the origin of the spectral hardening observed in primary cosmic ray fluxes at rigidity $\mathcal{R} \gtrsim 200$ GV (see Sec. 2.3.4).[20] A plausible possibility is that this feature is already imprinted onto the primary source terms. In this case it might be related to non-linear effects in diffusive shock acceleration [185] or to different types of sources contributing to the observed spectra [186]. Alternatively, one may attribute the hardening to a propagation effect. The rigidity scaling of the diffusion term is set by the power spectrum of turbulences in the magnetic plasma. A break in the diffusion coefficient could arise due to the transition from diffusion on cosmic ray self-generated turbulence at low rigidity to diffusion on external turbulence at high rigidity [187]. Similarly, an effective break results if the inner and outer part of the diffusion halo are dominated by turbulences of different type [188]. The following modification of the diffusion term has been suggested [123]

$$K = \frac{K_0 \beta \left(\frac{\mathcal{R}}{\mathrm{GV}}\right)^{\delta}}{\left(1 + \left(\frac{\mathcal{R}}{\mathcal{R}_b}\right)^{\Delta\delta/s}\right)^{s}} \,. \tag{2.29}$$

The origin of the spectral hardening affects the spectra of secondary cosmic rays. If it is attributed to primary sources, boron would simply inherit the break from its progenitors at virtually the same rigidity (as fragmentation preserves T). In the regime where diffusion dominates the propagation, B/C would thus resemble a flat power law. If, however, the hardening relates to diffusion, the boron flux would be affected twice: by the progenitor fluxes and by its own propagation. Hence, a spectral break would be observable in B/C. In [123] the high energy part of B/C was used to distinguish

[20] See [184] for a summary of possible physics scenarios behind the spectral hardening of primary fluxes.

between the two hypotheses within a simplified propagation model. We consider it worth repeating this analysis over the full energy, since we can also benefit from the fragmentation cross sections and primary fluxes derived in this work. Before we proceed, we should mention a caveat: the shape of primary spectra has also been explained in terms of nearby sources [189–192]. In this case local primary spectra would be markedly different from spatially averaged spectra in the galactic disc and our analysis would not hold. On the other hand, it has been argued in [193, 194] that a significant local fluctuation in the primary fluxes is unlikely within the established propagation models.

We determine the boron flux, as outlined in Sec. 2.2.1, for the standard diffusion term (2.2) and for the modified diffusion term (2.29). For the latter, we fix $\mathcal{R}_b = 275$ GV, $\Delta\delta = 0.157$ and $s = 0.074$ as required by the observed primary spectra. We checked that we can neglect uncertainties on these three parameters in our fits without changing results noticeably.[21] For both diffusion terms, the parameters controlling the interstellar boron flux are, thus, K_0, δ, L, V_c, V_a which must be determined by a fit to the AMS-02 data. Due to a degeneracy, there are indeed only four combinations of propagation parameters which enter, namely K_0/L, δ, V_c, $V_a/\sqrt{L}$. In order to arrive at B/C at the top of the atmosphere, we account for solar modulation as described in Sec. 2.2.2. B/C remains virtually invariant within the considered range of Fisk potentials $\phi_{0,\text{AMS-02}} = 0.6 - 0.72$ GV (see footnote 7). For our fits to converge we fix $\phi_{0,\text{AMS-02}} = 0.72$ GV without affecting the results.

We include the uncertainties related to the boron source term in the form of a covariance matrix $\Sigma^{\text{B/C,source}}$ which we determine as follows: We randomly generate a large number of tuples $\{\sigma_{1,i}, \xi_i, \Delta_i, f_i, \mathcal{R}_{l,i}, \alpha_i, \gamma_i, R_b, \Delta\gamma, s\}$ from the probability distributions of the parameters. The probability distributions are derived from experimental data as described in Sec. 2.3. Since i runs over the 6 relevant boron progenitors, the tuples are sets of 45 parameters which fix boron production completely. For each tuple we determine the corresponding B/C ratio in the 67 rigidity bins of AMS-02. The covariance between the ith and the jth bin of AMS-02 is then obtained as

$$\Sigma_{ij}^{\text{B/C,source}} = \Big\langle (B/C)_i - \langle B/C\rangle_i \Big\rangle \Big\langle (B/C)_j - \langle B/C\rangle_j \Big\rangle , \tag{2.30}$$

where $(B/C)_i$ denotes the predicted B/C in the ith bin. The averaging is performed over the B/C ratios corresponding to the different parameter tuples. A slight complication occurs as the covariance matrix is sensitive to the choice of propagation parameters. Since we want to avoid evaluating (2.30) for each set of propagation parameters, we define the relative covariance matrix

$$\tilde{\Sigma}_{ij}^{\text{B/C,source}} = \frac{\Sigma_{ij}^{\text{B/C,source}}}{(B/C)_i (B/C)_j} . \tag{2.31}$$

The relative covariance matrix remains (nearly) constant under variations in the propagation. Therefore, in practice we just have to determine $\tilde{\Sigma}_{ij}^{\text{B/C,source}}$ for one set of propagation parameters[22] and then obtain $\Sigma_{ij}^{\text{B/C,source}}$ by scaling it with the predicted B/C according to (2.31).

On top of $\Sigma_{ij}^{\text{B/C,source}}$, the experimental errors of AMS-02 are added. The full covariance matrix reads $\Sigma_{ij}^{\text{B/C}} = \Sigma_{ij}^{\text{B/C,source}} + \left(\sigma_i^{\text{AMS}}\right)^2 \delta_{ij}$ with σ_i^{AMS} denoting the quadratic sum of statistical and systematic errors in the ith bin. In the absence of detailed information provided by the AMS-02 collaboration,

[21] We will, however, include uncertainties in the break parameters of primary fluxes.

[22] As the one set of propagation parameters we choose the configuration which minimizes $\chi^2_{\text{B/C}}$ in (2.32) if only experimental errors of AMS-02 are included.

we took systematic errors to be uncorrelated.[23] The χ^2 test statistic is defined as

$$\chi^2_{\mathrm{B/C}} = \sum_{i,j=1}^{67} \left((B/C)_i - (B/C)_i^{\mathrm{AMS}}\right) \left(\Sigma^{\mathrm{B/C}\,-1}\right)_{ij} \left((B/C)_j - (B/C)_j^{\mathrm{AMS}}\right), \tag{2.32}$$

where $(B/C)_i^{\mathrm{AMS}}$ denotes the measured ratio in bin i.

In Tab. 2.6 we provide the best fit propagation parameters separately for the diffusion terms (2.2) and (2.29). The corresponding B/C ratios compared to the AMS-02 data are shown in Fig. 2.8. The error bands indicate the diagonal part of the boron production uncertainties contained in $\Sigma_{ij}^{\mathrm{B/C,source}}$. We note, however, that $\Sigma_{ij}^{\mathrm{B/C,source}}$ carries a strong degree of correlation, in particular the high energy part.[24] Both fits yield an acceptable $\chi^2_{\mathrm{B/C}}$, but we observe that a substantially better fit is obtained with the modified diffusion term including the break ($\Delta\chi^2_{\mathrm{B/C}} = 16.2$). As the break in the modified diffusion term was fixed by primary fluxes, the improvement comes without the cost of additional free parameters. We now want to quantify the preference for a diffusion break within frequentist statistics. For this purpose we generated a large number of mock data sets under the hypothesis of standard diffusion.[25] For each mock data set we determined the minimal $\chi^2_{\mathrm{B/C}}$ for standard diffusion and for modified diffusion allowing K_0 and δ to float. The chance for an accidental improvement as large as $\Delta\chi^2_{\mathrm{B/C}} \geq 16.2$ with modified diffusion turns out to be 1/250000. Formally, this corresponds to a $4.5\,\sigma$ exclusion of standard diffusion against the alternative hypothesis of modified diffusion. Our results are in good agreement with [123] and indicate strong preference for a break in the diffusion coefficient. In the following, we will hence fix the diffusion term to the form of (2.29). Upcoming cosmic ray data on other secondary nuclei will provide important tests for this assumption. The strong spectral break observed in the lithium and beryllium flux [195] may already be seen as another hint for a diffusion break.

Turning to the other propagation parameters, we observe that B/C does not favor significant convection or reacceleration effects. Seizable reacceleration velocities $V_a \gtrsim 20$ km/s tend to produce a bump in B/C at rigidities of a few GV which is not observed in the AMS-02 data. As can be seen, there is a shape in the residuals (see Fig. 2.8) which is not unexpected in the presence of correlated errors. If anything, it indicates some difficulty in reproducing a sufficiently concave B/C spectrum at low rigidity. While convective winds lead to reduction of the flux at $\mathcal{R} \lesssim 100$ GV – seemingly going in the right direction – this decrease is too smooth over rigidity to improve the fit. It would be interesting to explore if convection can affect the boron flux more favorably in the presence of a non-vanishing spatial gradient in the convective wind. The slope of the diffusion coefficient was kept as a free parameter in our analysis. However, special mention should be made of the fit values $\delta = 0.507$ and $\delta + \Delta\delta = 0.35$ below and above the spectral break. These values are remarkably close to 0.5 and 0.33 corresponding to a Kraichnan [196] and Kolmogorov [197] spectrum of turbulence. If the break in the diffusion coefficient results indeed from the interplay between turbulences of two types [193], one may wonder if they can be related to the Kraichnan and Kolmogorov theories, respectively.

[23] Even if this approximation is oversimplistic, it is not expected to impact our fits dramatically as uncertainties contained in $\Sigma_{ij}^{\mathrm{source}}$ exceed systematic errors of AMS-02.

[24] When determining $\chi^2_{\mathrm{B/C}}$ we, of course, took into account the full covariance matrix.

[25] We performed a Cholesky decomposition of $\Sigma_{ij}^{\mathrm{B/C}}$ to generate mock data with correlated uncertainties.

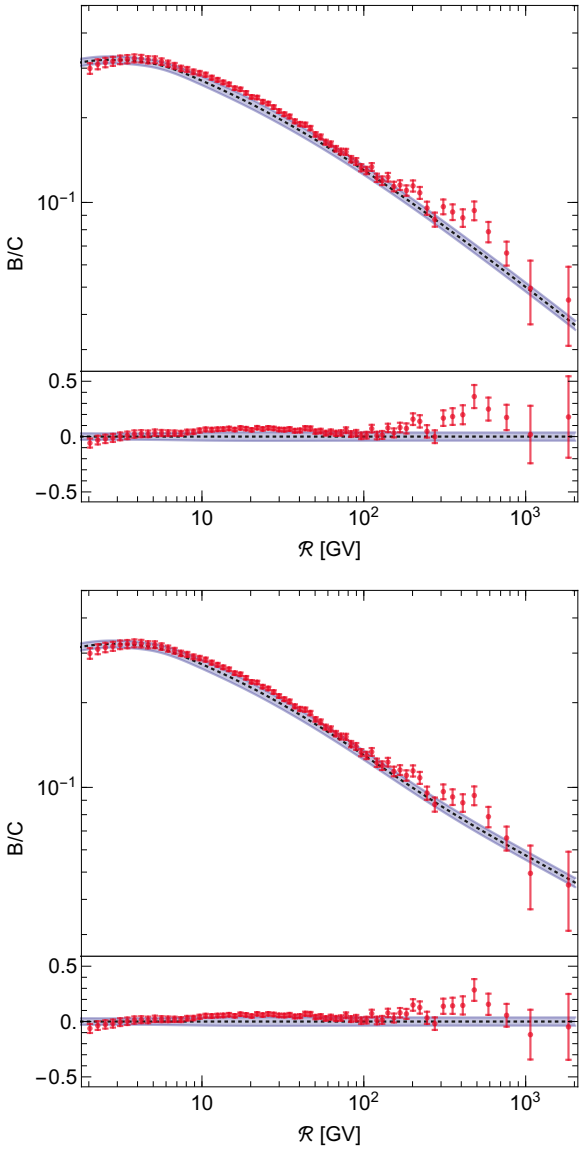

Figure 2.8: Fit to the AMS-02 B/C spectrum assuming standard diffusion (left panel) and assuming a spectral break in the diffusion coefficient (right panel). Residuals are shown in the lower subpanels.

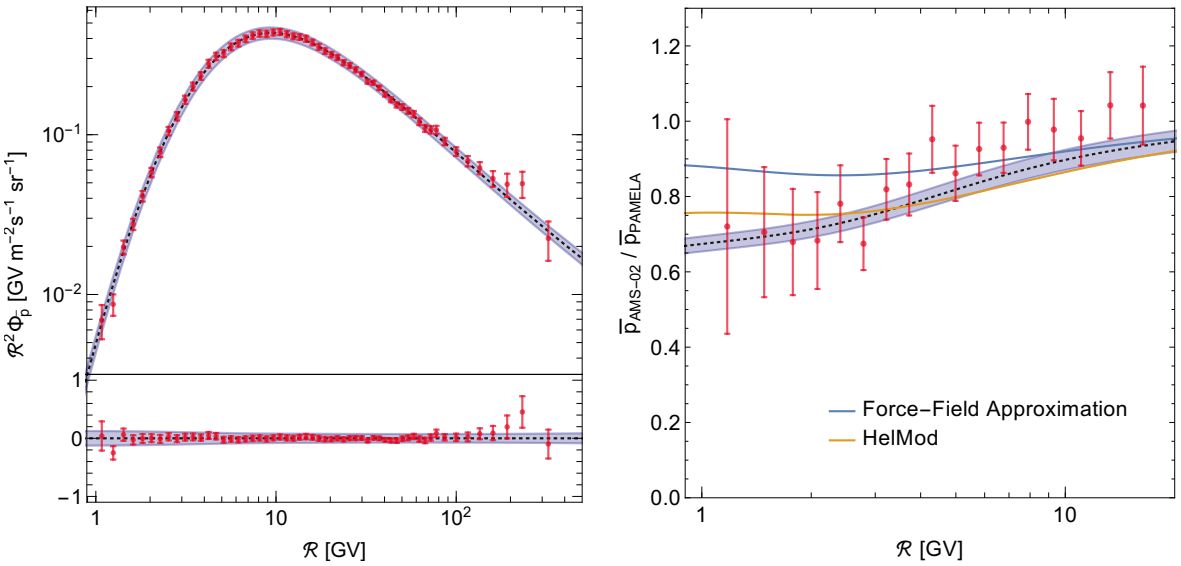

Figure 2.9: Fit to the AMS-02 antiproton spectrum (left panel) and the ratio of antiproton spectra observed at AMS-02 and PAMELA (right panel). The ratio depends on the assumptions of solar modulation and is also shown for the standard force field approximation and for the HelMod model.

2.5.2 Antiproton and B/C Fit

At the time when the first AMS-02 antiproton data were released [75], the spectrum was considered surprisingly hard. This triggered speculations about a possible primary component due to dark matter annihilations [198–200]. But subsequent analyses revealed that the secondary antiproton flux had been underestimated and might indeed account for the shape of the observed spectrum. An important role is played by the increase of antiproton production cross sections due to scaling violation [79, 80]. We now want to extend on [80] and investigate whether the AMS-02 antiproton spectrum is consistent with secondary production at the precision level. We rigorously include uncertainties in the antiproton source term in the form of the covariance matrix $\Sigma^{\bar{p},\text{source}}$. The latter is obtained in complete analogy to $\Sigma^{\text{B/C,source}}$ by mapping uncertainties in cross section and primary flux parameters into uncertainties in the antiproton flux (see previous section). The full covariance matrix $\Sigma^{\bar{p}}$ includes the experimental errors of AMS-02 and enters the χ^2-test as in (2.32). We account for solar modulation via the Fisk potential $\phi^-_{\text{AMS-02}}$ defined in (2.11). The two force field parameters $\phi_{0,\text{AMS-02}}$ and $\phi^-_{1,\text{AMS-02}}$ are allowed to float, but we impose $\phi_{0,\text{AMS-02}} = 0.6 - 0.72$ GV for consistency with Voyager. The propagation parameters and the solar modulation parameters are determined by a simultaneous fit to the AMS-02 antiproton data [84] and to the ratio of antiproton spectra observed at AMS-02 and PAMELA [89] (see Sec. 2.2.2).[26] We included an additional 2% correlated normalization uncertainty in our fit to $\bar{p}_{\text{AMS-02}}/\bar{p}_{\text{PAMELA}}$ which accounts for a small systematic offset observed between PAMELA and AMS-02 at high energy. The best fit parameters can be found in Tab. 2.6. The corresponding spectra and uncertainty bands are visualized in Fig. 2.9.

The quality of the fit to the antiproton spectrum is remarkably good, we obtain $\chi^2_{\bar{p}} = 21.3$ for

[26] As uncertainties in the ratio are strongly dominated by PAMELA, we can treat $\bar{p}_{\text{AMS-02}}/\bar{p}_{\text{PAMELA}}$ as independent.

57 rigidity bins.[27] Residuals have no particular shape and are controlled by statistical fluctuations. The shape of $\bar{p}_{\text{AMS-02}}/\bar{p}_{\text{PAMELA}}$ is also well reproduced up to a slight offset. The latter is likely caused by systematics between PAMELA and AMS-02. The charge asymmetric term $\phi^-_{1,\text{AMS-02}}$ in the Fisk potential is crucial in accounting for the observed decrease in the ratio towards low rigidity. This is in contrast to the standard force field approximation ($\phi^-_{1,\text{AMS-02}} = 0$), which predicts a nearly constant $\bar{p}_{\text{AMS-02}}/\bar{p}_{\text{PAMELA}}$. As a cross check for our treatment of solar modulation we also calculated the ratio of fluxes with the HelMod code and found reasonable agreement with our fit (see Fig. 2.9).

While one is tempted to interpret the good fit to be in favor of a secondary origin of antiprotons, the comparison with B/C is still to be made. Within our assumptions on cosmic ray propagation the antiproton flux and B/C should be explainable by an identical set of propagation parameters. If one compares the best fit propagation parameters of Tab. 2.6 it is striking that antiproton data – in contrast to B/C – favor a large reacceleration velocity. While such high V_a would have considerable impact on the antiproton spectrum, the effect on the boron flux would be more dramatic. Due to the lower threshold energy for boron compared to antiproton production, there is more low energy boron available which can be reshuffled to high energies through reacceleration (see Fig. 2.7). Large V_a leads to a bump in B/C – not seen in the AMS-02 data. In order to investigate the compatibility further, we perform a simultaneous fit to the B/C and antiproton spectra of AMS-02. Again we include $\bar{p}_{\text{AMS-02}}/\bar{p}_{\text{PAMELA}}$ to constrain solar modulation.

The favored parameters of the joined fit are shown in the last column of Tab. 2.6, the corresponding fluxes and uncertainties are depicted in Fig. 2.10. Remarkably, B/C and antiprotons can be fit simultaneously with $\chi^2/\text{d.o.f.} < 1$. This implies that both spectra are, indeed, consistent with pure secondary production. The fit is considerably better than one may conclude by eye due to correlations in the uncertainties in $\Sigma^{\text{source}}_{ij}$. Nevertheless, we observe a clear rise in $\chi^2_{\bar{p}}$ compared to the fit without B/C. In the high energy regime, there appears a slight offset between predicted antiproton flux and data which is, however, within the margin of cross section uncertainties. The increase in $\chi_{\bar{p}}$ is indeed mainly driven by the low energy spectrum. The combined fit picks a reacceleration velocity significantly lower than the fit with antiprotons alone. This manifests itself in the antiproton flux exceeding the data at $\mathcal{R} < 4$ GV and falling short above. The residuals exhibit a modest peak at rigidity $\mathcal{R} \sim 10$ GV. The 12 AMS-02 bins at $\mathcal{R} = 7 - 20$ GV increase $\chi^2_{\bar{p}}$ by ~ 10 compared to the pure antiproton fit. This increase is not larger since cross section uncertainties can partly explain a peak: proton proton scattering resides in a scaling regime at $\sqrt{s} \simeq 10 - 50$ GeV. However, at $\sqrt{s} < 10$ GeV near-threshold effects contained in the function R (2.19) play a role. Lowering of the parameter c_9 within uncertainties would manifest itself in a decrease of the antiproton spectrum at $R \lesssim 10$ GV. Simultaneously, the asymmetry between antineutron and antiproton production (cf. (2.23)) may increase the antiproton flux at $\mathcal{R} \lesssim 30$ GV compared to the median parameter choice. Among other possibilities, the interplay between these two effects could lead to a smooth bump in the residuals at $\mathcal{R} \sim 10$ GV. Despite the overall consistency of B/C and antiprotons with standard secondary production, there is still room for modifications. If an alternative hypothesis is able to capture the shape of residuals, it may still be statistically preferred at a significant level. In Sec. 2.6 we will explore whether a significant improvement of the fit arises in the presence of a primary antiproton component from dark matter annihilation.

[27] While this value of χ^2 may look suspiciously small, we remind the reader that the absolute $\chi^2_{\bar{p}}$ does not have a rigorous statistical interpretation until the systematic errors of AMS-02 have been taken into account.

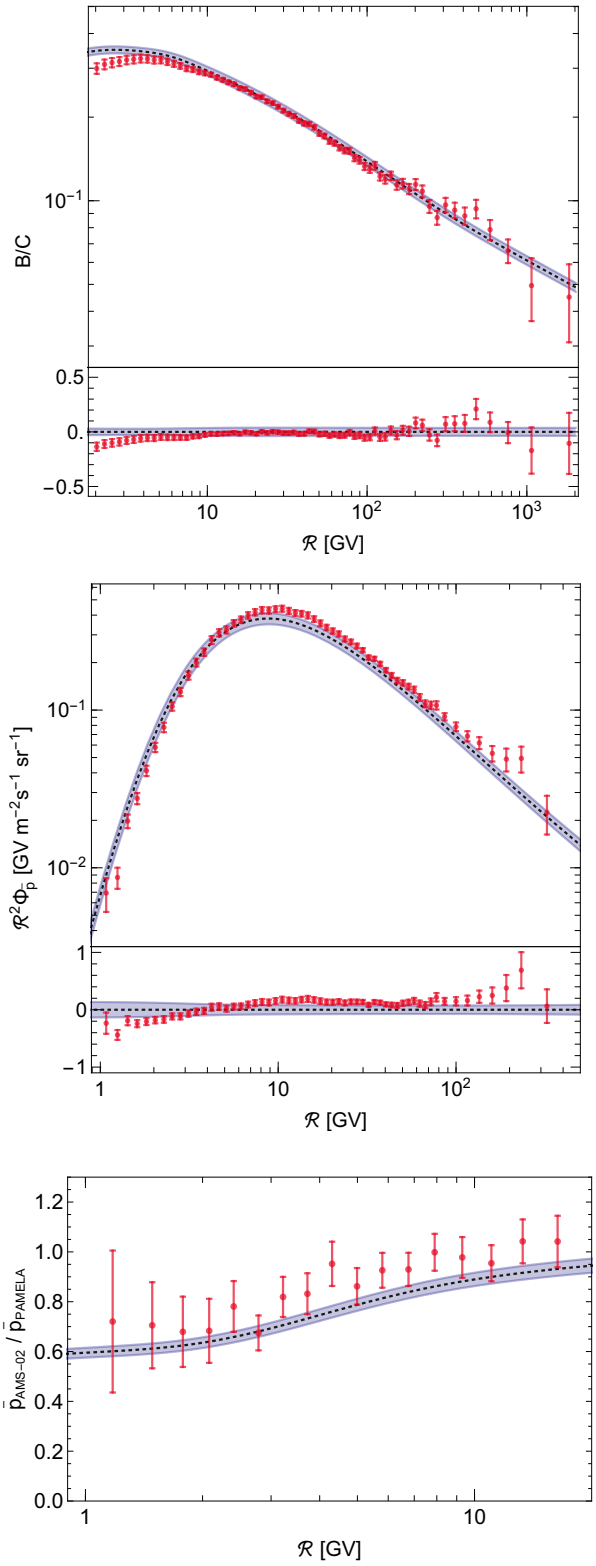

Figure 2.10: Best fit spectra of the combined B/C + $\bar{p}$ fit.

Best Fit	B/C (w/o break)	B/C (w/ break)	$\bar{\text{p}}$ (w/ break)	B/C + $\bar{\text{p}}$ (w/ break)
K_0 $[\frac{\text{kpc}^2}{\text{Gyr}}]$	$39.6 \cdot L_{4.1}$	$34.3 \cdot L_{4.1}$	$39.5 \cdot L_{4.1}$	$32.5 \cdot L_{4.1}$
δ	0.479	0.507	0.446	0.506
V_a $[\frac{\text{km}}{\text{s}}]$	0	0	$59.7 \cdot \sqrt{L_{4.1}}$	$15.6 \cdot \sqrt{L_{4.1}}$
V_c $[\frac{\text{km}}{\text{s}}]$	0	1.3	0	0
$\Delta\delta$	*no break*	0.157	0.157	0.157
$\mathcal{R}_b$ [GV]		275	275	275
s		0.074	0.074	0.074
ϕ_0 [GV]	0.72	0.72	0.72	0.72
ϕ_1 [GV]			0.66	0.84
$\chi^2_{\text{B/C}}$ (67 bins)	64.2	48.0		55.1
$\chi^2_{\bar{p}}$ (57 bins)			21.3	47.9
$\chi^2_{\text{AMS/PAM}}$ (17 bins)			10.9	12.6

Table 2.6: Best fit propagation and solar modulation parameters corresponding to the B/C, the $\bar{p}$ and the combined B/C + $\bar{p}$ fit. For the B/C fit the cases without and with diffusion break are considered. The goodness of fit is indicated by the χ^2-values. The acronym $L_{4.1}$ stands for $L/4.1$ kpc.

2.5.3 Positron Constraints on the Diffusion Halo

The cosmic ray positron flux experiences a spectral hardening at $\mathcal{R} \gtrsim 10$ GV which has been established by the PAMELA collaboration [68]. Within standard assumptions, this shape cannot be explained by secondary production. However, it was pointed out that the excess can be reconciled with secondary positrons if one employs a mechanism to avoid energy losses in the galactic halo [15, 201–203], as we will investigate in Chap. 3. Furthermore, there exist attempts to describe positrons as secondaries within modified diffusion models [204, 205] or through invoking acceleration of secondaries in supernova remnants [206–208]. Alternatively, a primary contribution to the flux may resolve the positron puzzle. While a dark matter interpretation is difficult to reconcile with complementary indirect detection probes [69–73], pulsars might account for the excess without conflicting other observations [209, 210] (see however [12]). In this section we will assume standard propagation of positrons but will otherwise stay agnostic about the origin of the positron anomaly. Independent of which contributions are added to the positron flux, the secondary background alone must not overshoot the data of AMS-02.

Although our focus is on the antiproton flux from dark matter annihilation, positrons will still play an important role in the dark matter analysis. The primary antiproton flux strongly depends on the size of the diffusion zone L. This is easily understood as primary antiprotons originate from everywhere in the dark matter halo, but only those inside L may ever reach the Earth. The secondary spectra

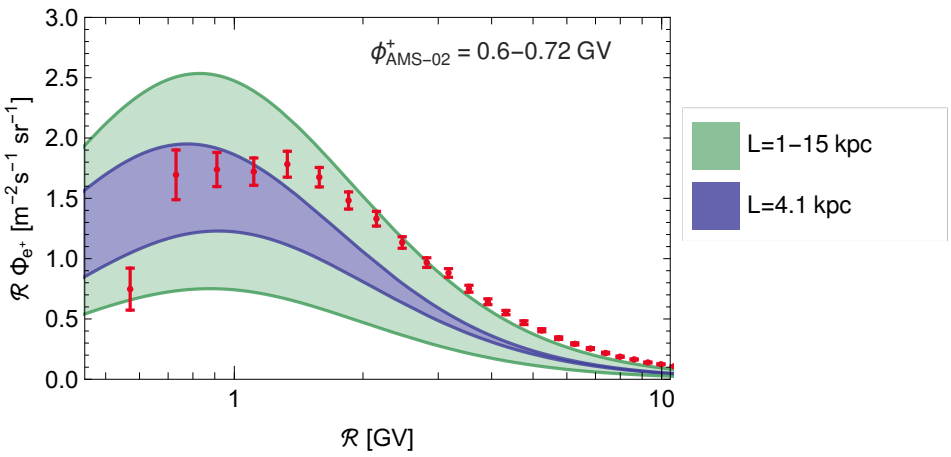

Figure 2.11: Positron flux for the propagation parameters from the B/C + $\bar{p}$ fit (see Tab. 2.6). The size of the diffusion halo has been set to the values stated in the plot legend. The width of the bands includes the uncertainty in solar modulation corresponding to $\phi^+_{\text{AMS-02}} = 0.6 - 0.72$ GV.

of antiprotons and B/C only constrain the combination L/K_0, not the absolute size L. Positrons can lift this degeneracy. Different from hadronic cosmic rays, positrons experience energy losses in the diffusion halo which limits the distance from which positrons reach the Earth. As a consequence, they are not very sensitive to the boundaries of the diffusion halo, but rather to the diffusion coefficient K_0. The fact that hadronic and positron secondary fluxes depend on different combinations of K_0 and L, can be used to efficiently constrain L [74, 211].

We now wish to determine the minimal allowed L for the propagation configuration which best fits the antiproton and B/C data. For this purpose we fix K_0/L, δ, V_c and $V_a/\sqrt{L}$ to the values shown in the last column of Tab. 2.6 and calculate the corresponding positron spectra as described in Sec. 2.2.1. The positron flux modulated with $\phi^+_{\text{AMS-02}} = 0.6-0.72$GV is shown in Fig. 2.11. Our limit is derived for $\phi^+_{\text{AMS-02}} = 0.72$ GV which yields the smallest (most conservative) positron flux within the considered range. We decrease L until the secondary positron flux exceeds the 95% CL upper limit in one of the bins. As it is always the first bin which sets the strongest constraint, we do not need to assign a statistical penalty for the choice of bin. The lower limit we obtain is $L = 4.1$ kpc. Our constraint is significantly weaker than $L > 8.5$ kpc derived in [74]. The difference finds its explanation in the propagation configurations considered in [74]. These stem from an older B/C analysis [86] and feature large V_A. Strong reacceleration increases the low energy positron flux and tightens the constraint on L. For the reacceleration velocity favored by our B/C + $\bar{p}$ fit, the weaker constraint applies. In the next section we will use the lower limit $L = 4.1$ kpc to derive constraints on dark matter annihilation. As the best fit propagation parameters are hardly affected by including primary antiprotons in the fit, it is justified to keep the lower limit on L fixed in the following.

Caveats in our constraint on L exist if halo energy losses for positrons are substantially stronger than considered in Sec. 2.2.1 or if solar modulation deviates strongly from the force field approximation. On the other hand such deviations are hardly observed in the AMS-02 proton spectrum (see Sec. 2.2.2). In addition, we remind the reader that the positron source term was derived with the cross section parameterization of Kamae et al. [167] which yields the lowest (most conservative) positron

flux among the alternatives. In this light, we consider $L > 4.1$ kpc as a sufficiently robust lower limit. Further indications against a diffusion halo $L \lesssim 4$ kpc arise from the diffuse gamma ray background [212] and from radio data [213–215], but different interpretations are possible and we will get back to this discussion in Sec. 3.2.3.

2.6 Dark Matter Search

We confirmed in Sec. 2.5.2 that the observed antiproton and B/C spectra are consistent with secondary production. However, at the precision level, some structures appeared in the residuals of the fit. A modest peak at $\mathcal{R} \sim 10$ GV matches with the excess pointed out in [1, 85]. There, it was tentatively interpreted as a matter signal. We now want to investigate the robustness of the signal with respect to uncertainties in the secondary backgrounds. We consider $b\bar{b}$ and WW as exemplary dark matter annihilation channels. The corresponding primary antiproton fluxes are derived from the source terms (2.26). We choose the standard NFW profile (see Tab. 2.5) and consider the dark matter mass ranges $m_{\rm DM} = 7 - 3000$ GeV and $82 - 3000$ GeV for $b\bar{b}$ and WW respectively. The annihilation cross section is taken to be a free parameter, we only require $\langle\sigma v\rangle > 0$. The size of the diffusion halo, which controls the normalization of the primary flux, is set to the minimum $L = 4.1$ kpc derived in Sec. 2.5.3. A combined fit to the antiproton and B/C spectra is performed – this time including the primary antiprotons. The primary flux component must be strongly subdominant not to spoil the combined fit. Therefore, it is justified to neglect uncertainties in the primary flux related to annihilation spectra. Uncertainties in the secondary fluxes are, however, fully taken into account.

Dark matter annihilations lead to a slight improvement of the fit which is more pronounced in the $b\bar{b}$ channel. The best fit parameters can be found in Tab. 2.7. Propagation parameters do not change considerably compared to the fit without dark matter. A slightly stronger solar modulation of antiprotons is preferred to mitigate the increase of the low energy flux caused by the primary component. The favored dark matter mass resides at $m_{\rm DM} \sim 80\,$GeV for both channels (slightly above threshold for WW). As can be seen in Fig. 2.12, the corresponding primary flux (scaled by $\mathcal{R}^2$) peaks at $\mathcal{R} \sim 10$ GV and (partly) absorbs the residuals at this rigidity. The preferred annihilation cross section $\langle\sigma v\rangle \sim 10^{-26}\,\mathrm{cm}^3/\mathrm{s}$ matches the expectation of a thermal WIMP up to a factor of two. The normalization is sensitive to the considered dark matter profile. It may, furthermore, be augmented by leptonic channels which leave the antiproton flux unaffected. The observed best fit properties are, hence, consistent with a thermal WIMP interpretation.

In the next step, we determine the significance of the excess corresponding to the observed $\Delta\chi^2$. At fixed $m_{\rm DM}$, $\Delta\chi^2$ under the background hypothesis is expected to follow a $0.5\chi^2_{0\,\mathrm{d.o.f}} + 0.5\chi^2_{1\,\mathrm{d.o.f}}$ distribution as the alternative (background + signal) has one additional positive parameter, $\langle\sigma v\rangle$. The local significance is hence $2.2\,\sigma$ for $b\bar{b}$ and $1.6\,\sigma$ for WW. The global significance is affected by the look-elsewhere effect: if the excess is a statistical fluctuation it may have occurred at any mass. Therefore, we generated a large sample of mock experimental data under the background hypothesis and determined the largest excess due to fluctuations in the considered range of $m_{\rm DM}$.[28] In 14% (25%) of the mock data we find an excess at least as large as the one observed in the $b\bar{b}$ (WW) channel. Formally, this corresponds to a global significance of $1.1\,\sigma$ ($0.7\,\sigma$) for $b\bar{b}$ (WW). Clearly, the case for dark matter in the AMS-02 data is not very strong.

[28] Naively, one may think that global probability distribution of $\Delta\chi^2$ is simply a χ^2-distribution with two degrees of freedom. This assumption is wrong as Wilks' theorem does not apply to cases, where a parameter (in this case $m_{\rm DM}$) is only defined under the alternative hypothesis [216, 217]. Therefore, Monte Carlo simulation cannot be avoided.

Channel	$\bar{b}b$	WW
m_{DM}	78.7 GeV	85.2 GeV
$\langle\sigma v\rangle$ $[\frac{\mathrm{cm}^3}{\mathrm{s}}]$	$0.91 \cdot 10^{-26}$	$1.0 \cdot 10^{-26}$
K_0 $[\frac{\mathrm{kpc}^2}{\mathrm{Gyr}}]$	34.0	33.7
L [kpc]	4.1	4.1
δ	0.499	0.500
V_a $[\frac{\mathrm{km}}{\mathrm{s}}]$	15.0	15.1
V_c $[\frac{\mathrm{km}}{\mathrm{s}}]$	0	0
$\Delta\delta$	0.157	0.157
$\mathcal{R}_b$ [GV]	275	275
s	0.074	0.074
ϕ_0 [GV]	0.72	0.72
ϕ_1 [GV]	0.95	0.96
$\chi^2_{\mathrm{B/C}}$	53.2	53.6
$\chi^2_{\bar{p}}$	43.2	45.0
$\chi^2_{\mathrm{AMS/PAM}}$	14.5	14.6
$\Delta\chi^2$	4.7	2.4
p_{local}	0.015 ($2.2\,\sigma$)	0.061 ($1.6\,\sigma$)
p_{global}	0.14 ($1.1\,\sigma$)	0.25 ($0.7\,\sigma$)

Table 2.7: Propagation, solar modulation and dark matter parameters yielding the best fit to the B/C and antiproton data. Dark matter annihilations into $b\bar{b}$ and WW are considered. Also shown is the goodness of the fit and the significance at which the pure secondary hypothesis is "excluded" against a dark matter interpretation.

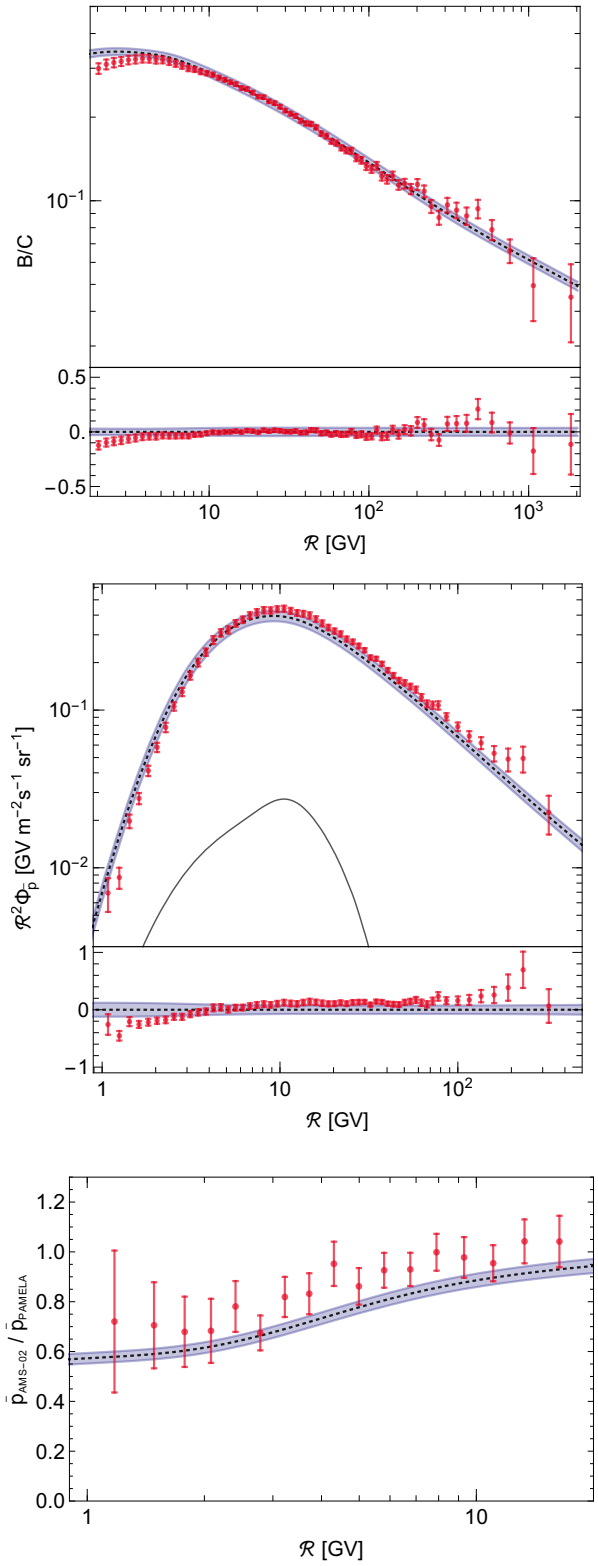

Figure 2.12: Best fit spectra of the combined B/C + $\bar{p}$ fit including a primary antiproton component from dark matter annihilation into $b\bar{b}$. The best fit primary antiproton flux is indicated in the upper right panel (solid black line).

We can directly compare our results to the previous analyses. While we have confirmed the presence of a modest antiproton excess at the same rigidity as in [1, 85], the significance of the excess is substantially lower in our analysis. The decrease in significance is likely driven by the inclusion of cross section uncertainties. We outlined in Sec. 2.5.2 how variations in cross section parameters can lead to a "bumpier" secondary spectrum around $\mathcal{R} \simeq 10$ GV. This possibility effectively enters our fit via the covariance matrix $\Sigma^{\bar{p},\text{source}}$. An additional reduction in significance occurs as – different from [1] – we included the low energy spectrum which tends to exceed the data. But differences compared to [1, 85] also exist in the considered species and in the underlying propagation model.

In order to either eliminate or establish the excess, a further decrease of uncertainties is desirable. New measurements of antiproton and boron production cross sections at low energy would be very helpful in this regard. Even annihilation cross sections on the interstellar matter will have to be revisited in order to reach percent level accuracy. Even if the excess persisted after raising the precision, alternative explanations to dark matter would have to be explored – unless one would find complementary evidence in cleaner channels like antideuterium or antihelium [218]. An increase of the reacceleration velocity could, for example, completely flatten out the residuals in the antiproton spectrum at $\sqrt{s} \sim 10$ GeV. While this possibility was disfavored by B/C, it could be revived through a modification of the diffusion model at very low energy. For example in [219, 220], an enhancement of the diffusion term at $\mathcal{R} \lesssim$ few GeV has been motivated which would reduce the low energy fluxes of antiprotons and boron. Given the present (in)significance of the excess, we shall for now refrain from investigating this further.

Rather, we will now derive limits on the dark matter annihilation cross section. We again consider $b\bar{b}$ and WW final states and assume the NFW dark matter profile. The diffusion halo size is set to the lower limit $L = 4.1$ kpc. This is the most conservative choice, as any larger halo would result in stronger constraints on dark matter. For each m_{DM} we allow the propagation parameters to float and determine the best fit annihilation cross section and corresponding $\chi^2_{\text{best}}(m_{\text{DM}})$ imposing $\langle\sigma v\rangle > 0$. The 95% CL upper limit on $\langle\sigma v\rangle$ is then obtained by requiring $\chi^2(m_{\text{DM}},\langle\sigma v\rangle) - \chi^2_{\text{best}}(m_{\text{DM}}) = 2.71$.[29] In addition to the actual limit, we derive the expected limit under the background hypothesis. The latter is extracted from a large sample of generated mock data by taking the median limit within the sample.[30] Observed and expected 95% CL upper limits on the annihilation cross section are shown in Fig. 2.13 together with the 1 and 2 σ uncertainty bands on the expected limit.

The discussed excess at $m_{\text{DM}} \sim 80$ GeV is clearly visible by the weakening of limits around this energy. However, the downward fluctuation in the $b\bar{b}$-constraint around $m_{\text{DM}} \sim 10$ GeV is actually even more pronounced. At high mass $m_{\text{DM}} \gtrsim$ TeV observed and expected limits are very close. Dark matter explanations which had been introduced to account for a hardening of the high energy antiproton spectrum are not required. The parameter space of thermal WIMPs is severely constrained. For the considered NFW profile, thermal WIMPs with mass $m_{\text{DM}} < 570$ GeV are excluded if they annihilate into bottom quarks.[31] Limits in the WW channel are only slightly weaker. Similar exclusions are also expected for other hadronic dark matter annihilation channels, while leptonic channels provide a loophole to the antiproton constraints. In Fig. 2.14 we illustrate the dependence of limits on the properties of the dark matter halo. For the cored profile with $\rho_0 = 0.3$ GeV cm^{-3}, exclusion still holds for $m_{\text{DM}} < 45$ GeV and $m_{\text{DM}} = 185 - 320$ GeV in the $b\bar{b}$ channel. Constraints on WW shift

[29] In principle, the propagation parameters should be refitted for every combination of $m_{\text{DM}}, \langle\sigma v\rangle$. We checked for a few examples that the refitting has negligible impact on the constraints. Therefore, we avoided this time-consuming procedure.

[30] Variations in the propagation parameters were neglected when deriving the expected limit.

[31] The exclusion holds for a velocity-independent annihilation cross section.

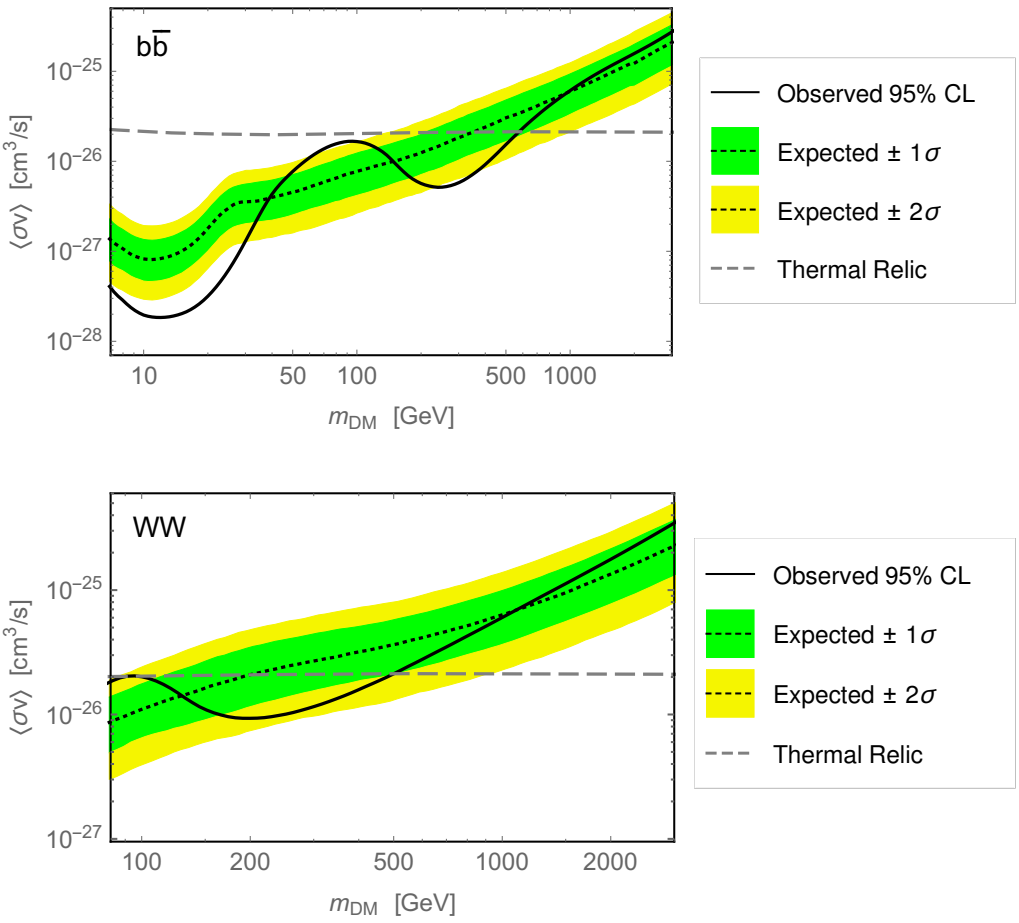

Figure 2.13: Constraints on dark matter annihilation into $b\bar{b}$ and WW derived from the antiproton and B/C data of AMS-02. Expected limits are also shown.

slightly above the thermal cross section in the whole mass range. This choice of profile might be a bit too conservative, but already for small deviation from the canonical NFW profile, WIMP masses $m_{\mathrm{DM}} \sim 80$ GeV become allowed. In the case of the contracted profile of Tab. 2.5, thermal WIMPs with hadronic annihilations can be excluded for masses up to TeV.

We can compare our constraints to [1, 85] and find them to be in reasonable agreement despite very complementary approaches. Uncertainties present in [1, 85] related to the size of the diffusion halo where avoided in our analysis as we used positrons to limit L. We also note that inclusion of cross section uncertainties in the secondary flux did not considerably weaken the limits. While cross section mismodeling can lead to features in the residuals, these are typically smoother than those induced by primary signals.

It is also interesting to put our results into comparison with gamma ray searches for dark matter. An excess in the gamma ray flux from the galactic center was pointed out in [221]. In Fig. 2.14, we depict the corresponding $2\,\sigma$ confidence regions for the case that it is interpreted in terms of dark matter. The preferred regions were derived using the spectrum [222] which is, however, subject to

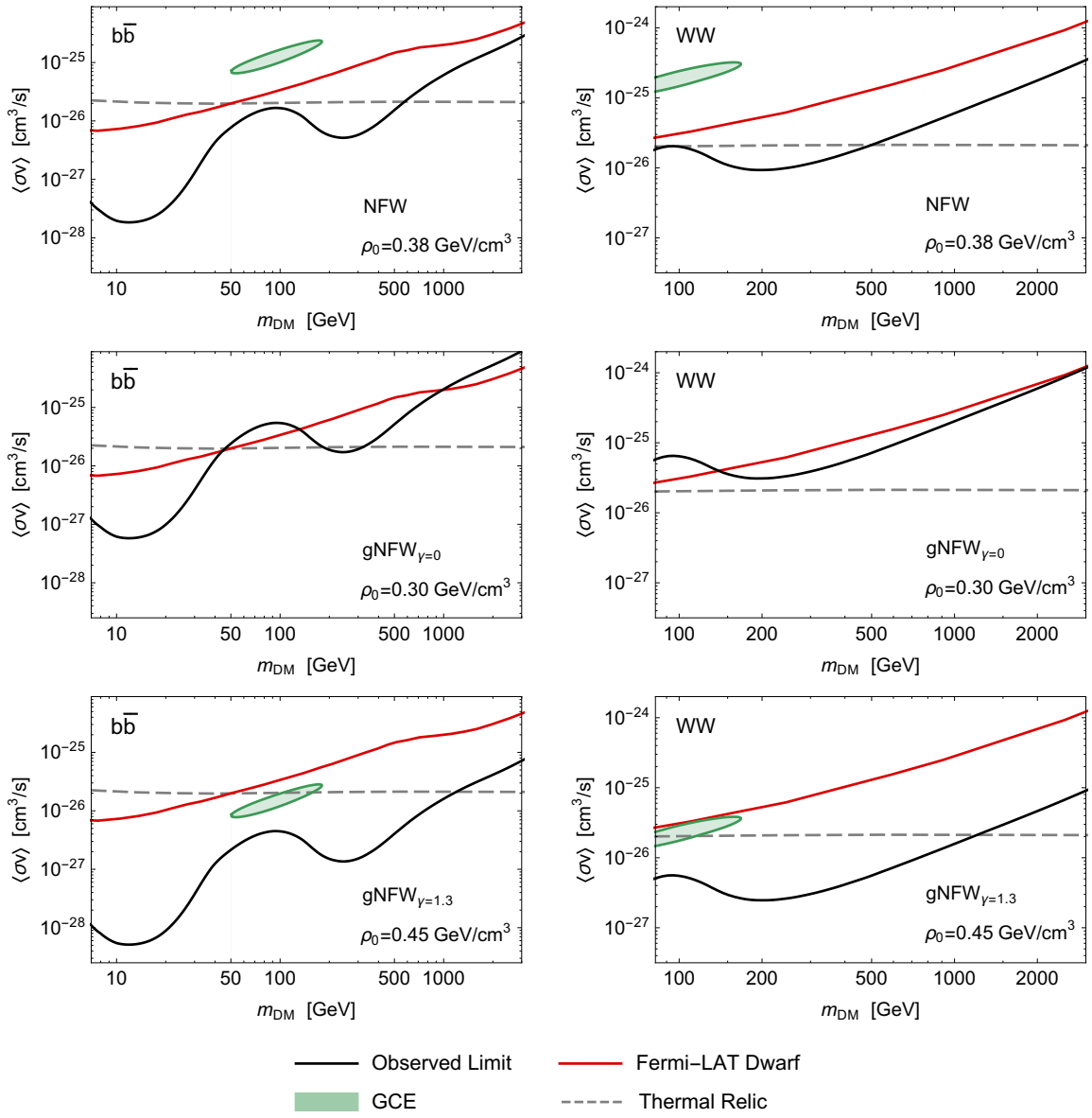

Figure 2.14: Limits on dark matter annihilation as in Fig. 2.13 for the canonical NFW profile, a cored, and a contracted gNFW profile (see Tab. 2.5). Also shown are the gamma ray constraints from dwarf galaxies as well as the confidence regions for the dark matter interpretation of the galactic center excess (see text).

seizable uncertainties [17]. It may seem intriguing that the gamma ray excess hints at a dark matter candidate with similar mass as the antiproton excess discussed earlier [223]. On the other hand, a consistent picture in terms of hadronic dark matter annihilations does not really emerge as cross sections required for the gamma ray excess are excluded by antiprotons. We also note that strong arguments for an astrophysical interpretation of the gamma ray excess in terms of point sources have been presented [224–226]. The strongest gamma ray constraints are set by the emission of dwarf galaxies [227, 228]. As shown in Fig. 2.14, antiproton limits in the considered channels are stronger by a factor 1.5-50 for the canonical NFW profile. Even for the very conservative cored profile, antiproton constraints dominate over a wide mass range.

2.7 Conclusion

In this work we performed a systematic search for dark matter signals in the AMS-02 antiproton data. We included B/C and positron data in our analysis in order to narrow down uncertainties in the propagation of charged cosmic rays. A careful treatment of solar modulation including charge-sign dependent effects allowed us to reliably interpret spectra down to the lowest energies. Uncertainties in the secondary source terms of antiprotons and boron were rigorously modeled from the available accelerator data and embedded into a powerful spectral analysis. In particular, we investigated a reported antiproton excess at $\mathcal{R} \sim 10$ GV. The latter had been interpreted in terms of a WIMP with mass $m_{\rm DM} \sim 80$ GeV and hadronic annihilations. Dark matter with similar properties had previously been considered as the explanation of the bright GeV gamma ray spectrum in the galactic center. We find that the boron and antiproton fluxes are consistent with pure secondary production. A mild antiproton excess corresponding to $m_{\rm DM} \sim 80$ GeV is confirmed. But its significance hardly exceeds $1\,\sigma$, once all relevant uncertainties and the look-elsewhere effect are taken into account. Even if this tiny excess is taken serious, the required dark matter annihilation cross section does not fit to the galactic center excess. A consistent common explanation does not emerge, unless one assigns a fraction of the gamma ray excess to other sources.

In the absence of a conclusive signal, we provided strong limits on dark matter annihilations into $b\bar{b}$ and WW (see Fig. 2.13 and 2.14). For a standard NFW dark matter profile these exclude thermal WIMPs with masses up to 570 GeV (100 − 500 GeV) in the $b\bar{b}$-channel (WW-channel). The mass window at $m_{\rm DM} \sim 80$ GeV, however, opens up for slightly more conservative choices of the dark matter halo. Antiproton limits are significantly stronger than gamma ray limits from dwarf spheroidal galaxies over wide mass ranges, even for cored dark matter profiles.

Although antiprotons are already a very powerful channel, strong improvements in sensitivity are within reach. Due to the high precision of the data, uncertainties in the secondary spectra are currently still the most limiting element. In our analysis we were already facing some limitations in fully resolving the antiproton excess at $\mathcal{R} \sim 10$ GV. The astrophysical antiproton background at this energy is affected by the transition from near-threshold to scaling behavior in the secondary production at $\sqrt{s} \sim 10$ GeV. The modeling of this energy regime still relies on accelerator data from the early 1970s with seizable uncertainties. Interpretation of the B/C spectrum faces similar challenges: even the most important reaction for boron production, the nucleon stripping of carbon, has only been measured with reasonable precision up to $T \simeq 4$ GeV. At the present stage, small residuals we observed in our fits to the antiproton and B/C data are consistent with uncertainties. However, they could turn into real features once the next level of precision is reached. It is encouraging that the variety of upcoming cosmic ray data will soon allow for new insights. In order to fully exploit the potential of cosmic ray

observations, new measurements of particle physics cross sections are urgently needed. Not only is this important to further explore the parameter space of thermal WIMPs, but also to search for other cosmic ray sources and to develop the global picture of cosmic ray propagation.

After all, the choice of the propagation model remains one of the biggest systematic uncertainties of cosmic ray and dark matter analyses. In the next chapter, we want to turn towards the interpretation of cosmic ray electron and positron spectra, and motivate a critical view on homogeneous diffusion models.

CHAPTER 3

Cosmic Ray $e^{\pm}$ at High Energy: a Local and Recent Origin for TeV Cosmic Rays?

The work presented in this chapter was done in collaboration with Kfir Blum and some of the results are published in Ref. [229].

3.1 Introduction

Measurements of galactic cosmic rays (CR) in the energy range from 1 GeV to 10^4 GeV have improved significantly in the last decade. In particular, for $e^{\pm}$ the individual fluxes of e^+ and e^- up to ~ 1 TeV and the total $e^+ + e^-$ (in the following denoted by $e^{\pm}$) flux up to ~ 10 TeV became available thanks to the PAMELA [68], AMS02 [230], DAMPE [231], CALET [232, 233], Fermi-LAT [234], HESS [235, 236], VERITAS [237], and MAGIC [238] experiments. Some of the key measurements are summarised in Fig. 3.1. The e^+ flux in Fig. 3.1 is shown multiplied by a factor of 2: we will explain the reason for this presentation shortly.

It is obvious from Fig. 3.1, that e^- and e^+ below ~ 1 TeV come from different sources: the e^- flux is larger than the e^+ flux by a factor of $O(10)$. Most of the e^- flux in this energy range is thought to be primary, namely, arising from Fermi acceleration of ambient e^- at astrophysical shocks. The origin of e^+ is not known. There are suggestions that e^+ are produced by exotic primary sources like dark matter annihilation (see, e.g. [239–242]) or pulsars (see, e.g. [210, 243–245]). Alternatively, e^+ may come from secondary production by CR nuclei collisions with Interstellar Matter [201].

There is an important hint in the data, that supports a secondary origin for e^+. This point was noted in [201, 202] and we briefly review it here. In Fig. 3.1 we supplement the experimental data with a theory calculation, shown by the shaded bands. The calculation shows the secondary flux of e^+ that would occur if radiative energy losses of e^+ are not important. Typically, $e^{\pm}$ are assumed to experience energy losses during the propagation from their production point to the Earth. However, if we "turn off" radiative losses, then the propagation problem for secondary e^+ becomes equivalent to that for secondary CR nuclei, like B and $\bar{p}$. To compute the shaded bands in Fig. 3.1, we use the measured fluxes of B or $\bar{p}$ to calibrate out the effect of propagation and obtain the (no-loss) flux of secondary e^+.

The answer that we get by "turning off" energy losses, is an upper bound to the flux of secondary e^+ [201]. In Fig. 3.1, the gray shaded band shows the upper bound that we obtain when using B/C data from AMS02 to calibrate out the propagation. The orange band shows the result of the same exercise, but this time using B/C data from CREAM that extends to higher rigidity. The purple band shows the result of a similar exercise, using $\bar{p}$ data from AMS02.

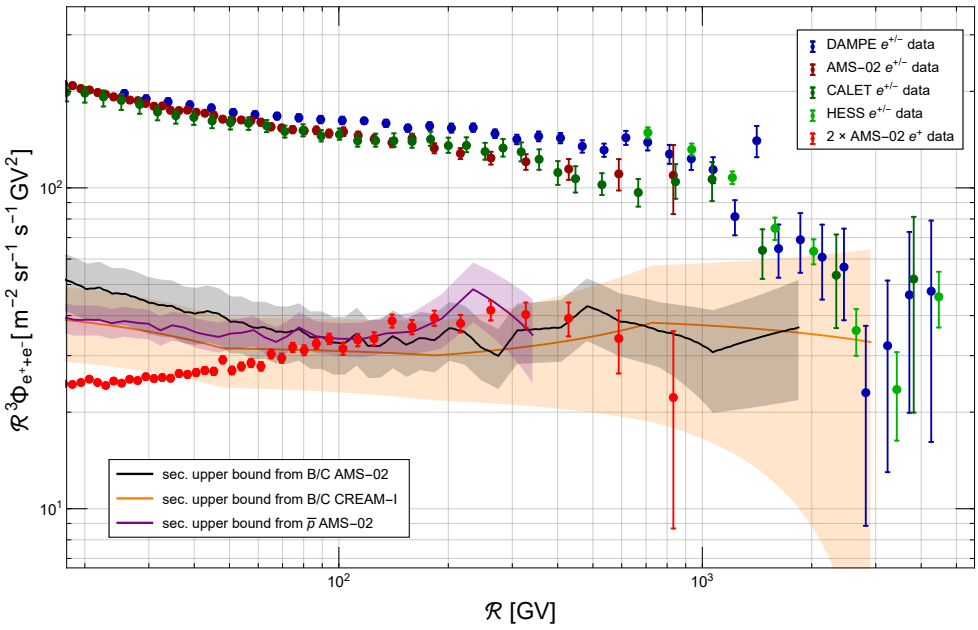

Figure 3.1: $e^{\pm}$ flux from DAMPE (blue), HESS (light green), CALET (dark green), and AMS02 (dark red), and (**2**×) e^{+} flux from AMS02 (light red), compared with the secondary $e^{\pm}$ upper bound derived from AMS02 B/C (black), CREAM-I B/C (orange), and AMS02 $\bar{p}$ (purple). See text for references.

The measured e^{+} flux saturates the secondary e^{+} flux upper bound [202]. We think that this saturation of the secondary bound motivates the hypothesis that e^{+} are secondary. The theoretical challenge that follows, is to explain what CR propagation scenario, if any, could result with ineffective radiative energy losses for secondary e^{+}. The scope of this work is to investigate these scenarios and check consistency with astrophysical data and implications.

In the next section we consider the $e^{\pm}$ data at $E > 1$ TeV. We show that both the hint for a secondary source for e^{+}, and the theoretical challenge accompanying this interpretation, are reinforced by this data. In Sec. 3.3, we report another coincident trend in CR e^{+} and nuclei. In Sec. 3.4 we present two new propagation models that can describe the (high energy) $e^{\pm}$ from purely secondary origin, together with the cosmic nuclei data. Details of the calculation are given in App. 3.A. The overall results are summarized and discussed in Sec. 3.5.

3.2 $e^{\pm}$ at High Energy

This section consists of three parts. First, we discuss the high energy $e^{\pm}$ data. Second, we discuss the implications of our interpretation, which are thirdly compared to various kinds of astrophysical measurements.

3.2.1 $e^{\pm}$ at $E \gtrsim 3$ TeV match the secondary upper bound

Consider the high-energy $e^{\pm}$ data in Fig. 3.1, extending to $E \sim 5$ TeV. As discussed above, e^{-} at $E < 1$ TeV are mostly primary. At $E \gtrsim 1$ TeV, however, the $e^{\pm}$ flux falls off, in what may be a

radiative cooling cut-off (of the primary e^- component, possibly occurring at the e^- acceleration site). The point we wish to highlight here is that at yet higher energy, $E \gtrsim 3$ TeV, the flux fall-off appears to slow down. Interestingly, the flux at $E \gtrsim 3$ TeV is consistent with the secondary upper bound and does not drop below it. It is for this reason – to compare the secondary upper bound prediction with the total $e^{\pm}$ measured flux – that we have shown the e^+ flux multiplied by a factor of 2: High-energy secondary production of e^+ comes along with an almost equal production of e^- [166], so the lines we show account for the secondary upper bound for $e^+ + e^-$ together.

The $E \gtrsim 3$ TeV saturation of the measured $e^{\pm}$ flux with the secondary bound is a new hint in favour of the secondary source hypothesis for e^+ (and, at these energies, e^-). This interpretation reinforces the challenge of explaining why radiative energy losses do not affect the flux of secondary $e^{\pm}$. The only way to achieve this, is by a short propagation time for TeV secondary CR: shorter than the radiative cooling time of TeV $e^{\pm}$. In the next section we discuss this possibility.

A more direct check of multi-TeV secondary $e^{\pm}$ would be achieved by measuring the $e^+/e^{\pm}$ ratio at these energies. If our interpretation is correct, the $e^+/e^{\pm}$ ratio should asymptotically approach the value $1/2$. Furthermore, the e^+ flux, shown in Fig. 3.1 up to $E \sim 800$ GeV, should extend smoothly up to $E \gtrsim 3$ TeV, without intermediate cut-off.

3.2.2 Secondary $e^{\pm}$ at $E \gtrsim 3$ TeV require short propagation time

How could CR $e^{\pm}$, at $E \gtrsim 3$ TeV, not be significantly affected by radiative energy losses during the propagation? Commonly adopted steady-state diffusion models of CR propagation [246] predict, to the contrary, that energy losses should completely dominate the behaviour of the secondary $e^{\pm}$ flux at these energies.

Radiative losses become ineffective if the CR propagation time-scale, $t_{\rm esc}$, is shorter than the $e^{\pm}$ radiative loss time-scale, $t_{\rm cool}$ [201]. It is important to note, that the widely used diffusion models for CR propagation have been calibrated along the years to fit observations of mostly stable nuclei, from primary p, He, C, O, Fe to secondary B, Li, sub-Fe[1], and recently $\bar{p}$. Stable CR nuclei test the amount of nuclear transformation undergone by CR during propagation. This constrains the column density of target material traversed along the CR path. Stable nuclei data are not, however, sensitive to the *time* it takes the CR to traverse that column density. Traditionally, CR models attempted to overcome this ambiguity about propagation time by fitting low-energy secondary radioactive isotopes (notably ^{10}Be), and some scarce radioactive-sensitive elemental data (notably the Be/B ratio) [14, 201, 247]. Measurements of ^{10}Be do not help much: the data only extends to $\mathcal{R} \lesssim 1$ GV, while the riddle we face with the $e^{\pm}$ appears at $\mathcal{R} \gtrsim 100$ GV. The measurements of Be/B [195] provide useful constraints up to $\mathcal{R} \sim 20$ GV, however (i) the interpretation is impeded by systematic uncertainties of fragmentation cross sections, and (ii) there is little information at $\mathcal{R} \gtrsim 30$ GV, because the Lorentz-dilated observer frame lifetime of ^{10}Be, $t_{\rm d} \approx 20\,(\mathcal{R}/20\ {\rm GV})$ Myr, becomes longer than the CR propagation time so that Be becomes just another effectively-stable secondary, like B. In short, the e^+ and $e^{\pm}$ data itself is, to date, the only probe of the CR propagation time available at high energies, $\mathcal{R} \gtrsim 30$ GV.

If we take it from Fig. 3.1 that at $\mathcal{R} \gtrsim 3$ TV, $e^{\pm}$ are secondary, then given an estimate of the effective $e^{\pm}$ cooling time at these energies, $t_{\rm cool}$, we can deduce an upper bound $t_{\rm esc} < t_{\rm cool}$. The cooling time can be calculated given an estimate of the interstellar radiation field (ISRF) and magnetic fields in the propagation region [248]. In the left panel of Fig. 3.2 we show three ISRF models, taken from recent literature [249, 250]. In addition to the ISRF, we consider two possibilities for the characteristic

[1] Sc-Ti-V-Cr.

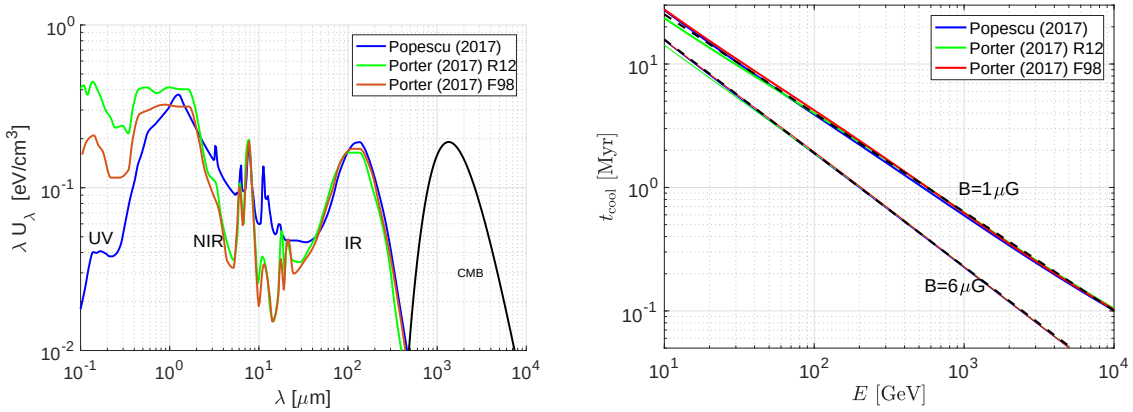

Figure 3.2: **Left:** ISRF models. **Right:** $e^{\pm}$ cooling time vs. energy, for three ISRF models [249, 250]. Upper dashed line (relevant for $B = 1$ μG) shows $4\,(\mathcal{R}/100\ \mathrm{GV})^{-0.8}$, lower dashed line (relevant for $B = 6$ μG) shows $1.9\,(\mathcal{R}/100\ \mathrm{GV})^{-0.92}$.

magnetic field in the propagation region: $B = 1$ μG (upper set of lines) and 6 μG (lower lines). This range of B roughly spans the expectations for the real situation in an average region in the Galaxy. In the right panel we show the radiative cooling time, $t_{\rm cool}$, computed using these ISRF and magnetic field models. The different lines at given B are difficult to resolve by eye, meaning that the different ISRF models do not lead to significant spread in the predicted $t_{\rm cool}$.

The upper dashed line in the right panel of Fig. 3.2 shows the function $4\,(\mathcal{R}/100\ \mathrm{GV})^{-0.8}$. The lower dashed line shows $1.9\,(\mathcal{R}/100\ \mathrm{GV})^{-0.92}$. We show these power-law fits of $t_{\rm cool}$ in order to demonstrate two points. The first point is that with the ISRF models of [249, 250], we do not find room for pronounced Klein-Nishina steps [251][2]. The second point is that a power-law approximation of $t_{\rm cool}$ deviates from the naive expectation in the Thomson limit, $t_{\rm cool} \propto \mathcal{R}^{-1}$. The Klein-Nishina effect causes $t_{\rm cool} \sim \mathcal{R}^{-\gamma}$ with $\gamma < 1$.

From Fig. 3.2 we have $t_{\rm cool}(3\ \mathrm{TV}) \sim (0.08 - 0.25)$ Myr. We read from this, in conjunction with Fig. 3.1, an approximate upper limit for the CR propagation time,

$$t_{\rm esc}(\mathcal{R} = 3\ \mathrm{TV}) \lesssim 0.1\ \mathrm{Myr}. \tag{3.1}$$

How far off is Eq. (3.1), compared to the expectations from homogeneous steady-state diffusion models? With commonly adopted values for the parameters of these models, a diffusion coefficient of $K \approx 4 \times 10^{28}\,(\mathcal{R}/1\ \mathrm{GV})^{0.33}$ cm^2/s, and a CR halo scale height of $L \approx 5$ kpc, the escape time in the diffusion model, $t_{\rm esc}^{\rm diff} = L^2/(2K)$, is expected to be $t_{\rm esc}^{\rm diff}(\mathcal{R} = 3\ \mathrm{TV}) \sim 10$ Myr, a factor of ~ 100 longer than is permitted by Eq. (3.1). Either the diffusion model is wrong, or else the $e^{\pm}$ are not secondary. The contradiction remains even if we consider only the lower energy e^+, at $\mathcal{R} \sim 300$ GV, to be secondary. Here the discrepancy between the upper bound on $t_{\rm esc}$ and the value expected in the

[2] The free $e^{\pm}$ scatter elastically with electromagnetic radiation, e.g. from starlight of different stellar types or from the CMB. Depending on the temperature T of the photon graybody distribution, the inverse Compton process can be approximated by the Thomson cross section for leptons below the Klein-Nishina energy $E_K = 0.27 m_e^2 c^2/(k_B T)$. Above this critical energy, the full Klein-Nishina cross section has to be applied and the energy losses reduce (slightly). In the measured spectrum, this could be observed as a small spectral hardening, a so called called Klein-Nishina step. For more details, see also [248].

diffusion model is about a factor of 10.

3.2.3 Consistency of short propagation time with astrophysical observations

We want to check if the short propagation time is consistent with astrophysical observations that give hints about cosmic ray propagation. In the following list, the first two points summarize the conditions implied by secondary $e^{\pm}$ at high energy, followed by a list of available observations and measurement. Their relations will be discussed right afterwards.

1. As pointed out above, secondary $e^{\pm}$ beyond 3 TeV require **short escape time $t_{\rm esc} \lesssim 0.1$ Myr** at this energy.

2. **ISM in the propagation region**: The CR grammage, deduced at $\mathcal{R} = 1$ TV from B/C and other nuclei data, is $X_{\rm esc}(\mathcal{R} = 1\ {\rm TV}) \approx (1 \pm 0.5)\ {\rm g/cm^2}$ [15]. An extrapolation to $\mathcal{R} = 3$ TV, assuming ${\rm B/C} \sim \mathcal{R}^{-0.33}$ (observed to be approximately valid for $\mathcal{R} \lesssim 1$ TV), gives $X_{\rm esc}(\mathcal{R} = 3\ {\rm TV}) \approx (0.7 \pm 0.3)\ {\rm g/cm^2}$. Regardless of the details of the source of CR, an 0.1 Myr propagation time requires an average number density for H in the propagation region[3] [15, 202],

$$\langle n_{\rm ISM} \rangle = \frac{X_{\rm esc}}{1.3\, m_p\, c\, t_{\rm esc}} \approx (3.5 \pm 1.5)\ {\rm cm^{-3}} \qquad \text{at } \mathcal{R} = 3\ {\rm TV}. \tag{3.2}$$

   Eq. (3.2) signifies an important constraint: secondary $e^{\pm}$ at TeV energies require an ISM environment that is rather dense. It is interesting to compare this requirement to the observed properties of the local ISM.

3. The **Local Bubble** (LB) is a very low density region ($n_{\rm ISM} < 0.01\ {\rm cm^{-3}}$) of irregular shape, that occupies the near ~ 100 pc around the Sun [4–6]. The LB contains interstellar clouds of densities $n_{\rm ISM} \sim 0.1\ {\rm cm^{-3}}$ [252], but the volume filling factor of these clouds is at the level of 10%. Starlight extinction maps [5] reveal that the LB is bordered by denser ISM with $n_{\rm ISM}$ of at least $O(1)$ H particles per ${\rm cm^3}$.

4. **Estimates for the diffusion coefficient from pulsar wind nebulae (PWN)**: Pulsars have strong electromagnetic fields in which high energy electron-positron pairs are produced, which then diffuse away from the source and up-scatter CMB photons through inverse Compton scattering (ICS). The radiation can be used to trace the $e^{\pm}$ distribution that contains information about the CR transportation properties. HAWC measurements of extended multi-TeV γ-ray emission, seen around the pulsars Geminga and PSR B0656+14 [12], support a diffusion coefficient $K_{\rm HAWC} = (4.5 \pm 1.2) \times 10^{27}\ {\rm cm^2/s}$ at 100 TeV, a factor of 400 lower than that extracted from homogeneous diffusion models. Geminga and PSR B0656+14 are relatively contemporary and local to us: their ages and distances are ~ 0.3 Myr, 0.1 Myr and 250^{+120}_{-62} pc, 288^{+33}_{-27} pc, respectively [253]. The extension of their γ-ray halos reaches up to 50 pc. The HAWC measurements may therefore provide us with a reasonable estimate of the CR transport velocity in our galactic neighborhood.

   Another estimate was performed by the High Energy Spectroscopic System (HESS) collaboration [254]. They infer the properties of particle transportation from the γ-ray spectrum of the PWN HESS J1825-137. Assuming a distance of 4 kpc, the angular diameter of the confinement

[3] The factor of 1.3 in the denominator of Eq. (3.2) accounts for He in the ISM.

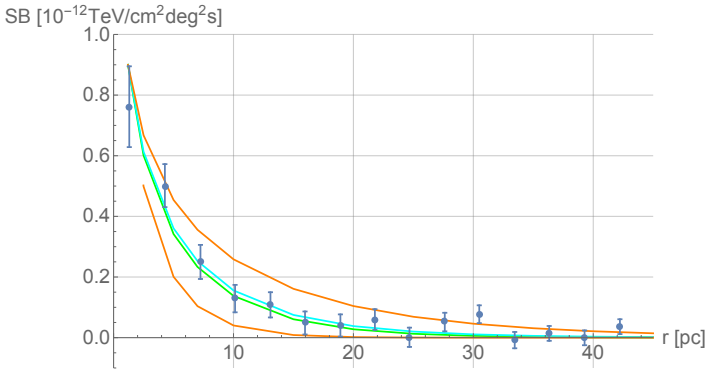

Figure 3.3: HAWC γ-ray surface brightness (SB) profile of Geminga. Data are from [12]. Green line shows the result of the diffusion model fit adopted by HAWC [12], using $K = K_0\,(\mathcal{R}/100\text{ TV})^{\delta}$ with $\delta = 0.33$ and $K_0 = 3.2\times10^{27}$ cm^2/s. Cyan (partially overlapping with the green) shows the result using $K_0 = 3.2\times10^{27}$ cm^2/s and $\delta = 0$. The upper and lower orange lines show the results for $K_0 = 0.25 \times 3.2 \times 10^{27}$ cm^2/s and $K_0 = 4 \times 3.2 \times 10^{27}$ cm^2/s, respectively, with $\delta = 0.33$. The pulsar injection rate is adjusted so that all models give the same SB of 0.9×10^{-12} TeV/cm^{2}deg^{2}s at $r = 1.2$ pc.

region is $\sim$ 100 pc. The estimated lifetime of the pulsar is 21 kyrs, s.t. this implies a diffusion coefficient of[4] $K_{\rm HESS} \approx 1 \times 10^{28}$ cm^2/s at $\sim$ 700 GeV, which is the energy where the spatial extension is maximal. Comparing the two measurements, we find that interestingly they are very close to each other, $K_{\rm HESS}$ (at 700 GeV) is only about twice as big as $K_{\rm HAWC}$ (at 100 TeV).

Note however, that in general these values have to be interpreted with care: at the boundary of the PWNs, escape effects could play a role. If this is the case, the real diffusion coefficients are larger than these estimates.

5. **No evidence for energy-dependent diffusion**: The values for the diffusion coefficient discussed above show no indication for energy-dependent diffusion. Neither is the analysis [12] by the HAWC collaboration affected by the assumption about the spectral index of the diffusion coefficient: In Fig. 3.3 we show their data on the surface brightness (SB) of Geminga as a function of the radial distance. We reanalyze the data assuming a spectral index $\delta = 0.33$ (green) and $\delta = 0$ (cyan), which hardly makes a difference (see Fig. 3.3).

   Also the HESS collaboration investigates the radial extend of the PWN HESS J1825-137 with energy [254]. Here, $\delta = 0$ is favored over non-zero values, and additionally they include advection (a bulk particle flow) to find a better description of the data.

6. **Simulated diffusion in artificial random magnetic field realizations**: Ref. [255] discusses the propagation of CR in regular and turbulent Gaussian random fields. The analysis reveals that a dominant isotropic turbulent component is disfavored. Instead, it supports a strongly anisotropic scenario, otherwise the CR spend too much time in the galaxy and accumulate too much grammage, contradicting observations. As a consequence, the number of CR sources contributing to the flux measured in the solar neighborhood is reduced to order one. Thus, the

[4] In the reference, the given value is 1.4×10^{29} cm^2/s at $\sim$ 700 GeV. It relates to the value derived above in the following way: since the pulsar sits roughly in the middle of the PWN, the distance traveled by the CR is only $\sim$ 50 pc. Furthermore, the definition of the diffusion radius applied by HAWC ($r = 2\sqrt{Kt}$) and HESS ($r = \sqrt{2Kt}$) imply a relative factor of two between the measured diffusion coefficients. For the sake of comparison, we apply the definition used by HAWC.

steady-state picture could be valid only at low energies ($\lesssim$ 10 GeV), whereas at large energies the contribution of single sources dominates the flux.

The diffusion coefficient derived from the simulations around 10^3 TeV (s.t. the gyro-radius is within the turbulence) supports slow diffusion for μG magnetic field strength.

7. **One (!) potential cooling break in the $e^{\pm}$ spectrum**: DAMPE and HESS report a spectral hardening around $\sim$ 1 TeV in the $e^{\pm}$ spectrum[5]. If it is true that there is exactly one spectral break in the $e^{\pm}$ spectrum, it implies that the primary CR that reach us stem from a few (or possibly one dominant) sources of similar age. If in contrast, CR traveled more than a few 100 pc in less than the cooling time of the high energy particles, $\sim$ 0.1 Myr, the cooling breaks of different sources with individual characteristic age should be visible.

8. **On average 2 supernovae per Myr in an area of 100 pc radius**: In the galactic disc, within an area of radius 100 pc, the supernova rate is roughly 2 per Myr. Observations in the local ISM [6] suggest that about 10-20 supernovae (SN) occurred in the Gould's Belt region, within $\sim$ 400 pc from the Sun, in the last $\lesssim$ 10 Myr[6].

9. **A 'sea' of cosmic rays**: γ-ray observations indicate evidence for what they call a 'cosmic ray sea' [13]: the CR density does not fluctuate by more than $O(1)$ across different regions in the galactic disc. Further, the CR seem to permeate molecular clouds basically undisturbed.

   Measurements of the γ-ray flux produced by CR-ISM interactions can probe the CR distribution, given reliable estimates of the target ISM mass and mass distribution in the line of sight. Applied to the local Solar system neighbourhood, $r \lesssim 1$ kpc, these measurements point to a CR density that is approximately uniform to about $\sim$ 20%, up to scale heights of at least $\sim$ 100 pc above the galactic plane and up to energies of some hundred GeV. A comprehensive, large-scale analysis was done in Ref. [13].

   Ref. [257] analyzed γ-ray emission from CR interactions in near-by molecular clouds, located at distances ranging between $\sim$ 100−270 pc. The reported γ-ray emissivities in the energy range $E_\gamma = (0.25 - 10)$ GeV (corresponding to primary proton energy $E_{\rm CR} \lesssim 100$ GeV) fluctuate by about 20% around a mean that is consistent with the locally measured CR flux. A similar result was found by [258], considering clouds at distances of $\sim 100 - 400$ pc, and γ-ray energies up to 100 GeV (corresponding to TeV primary protons).

   Ref. [259] converted dust opacity maps into H column density, and studied the correlation with γ-ray flux at $E_\gamma > 2$ GeV for the Orion A and Taurus giant molecular clouds (GMCs), located at distances of $\sim$ 500 and $\sim$ 140 pc, respectively. The reported γ-ray emissivity is consistent with the one that would result from the locally measured CR flux. Furthermore, the high degree of correlation between dust opacity and γ-ray emissivity implies that CR at $E_{\rm CR} \gtrsim 20$ GeV permeate the GMCs uniformly.

   Ref. [258] studies γ-ray emission from the Chamaeleon complex, a collection of molecular clouds at a distance of roughly 150 pc and a spatial extension of $30 - 40$ pc. They find that there is no concentration or exclusion of CR in the very dense regions of the cloud. In contrast,

[5] Note that so far, the data detected by CALET and AMS-02 do not confirm this break.

[6] This local picture is roughly consistent with the global SNe rate in the Milky Way, of about 1 SN per 30 years [256], assuming that this total SNe rate is uniformly distributed in a disk of radius $R_{disk} \sim 15$ kpc.

the CR distribution is uniform and exceeds the flux measured in the solar neighborhood by only up to 20%.

To the contrary, there are analyses indicating a decreasing amplitude and a softening of the CR proton spectrum with galactocentric distance [260]. The discrepancy reaches more than an order of magnitude around 1 TeV, whereas in the anti-center direction the flux of multi-GeV protons seems to be similar to our local measurements [261]. Deviations of order one are also found in Ref. [13], the inferred cosmic ray flux in MCs differs stronger from the local one, the closer the clouds are to the galactic center.

10. **Dynamics of the ISM/MCs**: The local ISM, on distance scales below $\sim$ 1 kpc, is far from steady-state. Molecular clouds condense and form stars over a few- to a few ten-Myr time scales. Stellar winds and supernovae explosions drive shocks through the ISM, sweeping-up the gas and forming filaments and bubbles, colliding and dispersing on sub-Myr time scales [262] (for a recent review, see [6]).

    Recent dynamics [16] suggests a model in which the shock front of Loop I (L1) has hit the LB cavity about 10 kyr ago. In this model, L1 is a bubble formed about $\sim$ 8 Myr ago by a few Supernovae, while the LB is a more recent cavity that formed $\sim 1-2$ Myr ago.

11. **γ-ray and radio halo**: Ref. [263] investigates γ-rays below 10 GeV coming from clouds above the galactic plane, up to a galactic height z of 7 kpc. They confirm a decrease in flux with distance from the disc and report a 50% decline at 2 kpc height. Their fits support a small halo ($\sim 2 \pm 2$ kpc) and a fast decrease of the γ-rays as z increases.

    Similar observations are made by radio-astronomy[7]: galaxies have synchrotron halos at the scale of several kpc, coming from electrons of energy $\lesssim$ 10 GeV. The extension of the radio halo reaches several kpc, decreasing in size with increasing frequency. Roughly 10% of the radiation in the radio range originates from the galactic disc. As the observed radio halo is roughly a factor of $\sim$ 100 bigger than the disc, the emissivity of the halo is about an order of magnitude less than in the disc, falling off rapidly between 0.1 and 1 kpc.

What do we conclude from the observations discussed above? Let us consider $e^{\pm}$ of energy $\geq$ 1 TeV. According to point 1, we want to check if the short propagation time, $t_{\rm esc} \sim 0.1$ Myr, is consistent with all statements.

- First of all, the diffusion coefficient measured by HAWC and HESS, see point 4, contribute to an upper limit on the efficiency of diffusion. Another hint into the same direction is found from the spectral properties of the $e^{\pm}$ spectrum, see 7. Both observations indicate that within 0.1 Myr, (TeV) CR travel a distance of maximal some hundreds of parsecs.

  A lower limit on the efficiency of CR propagation is supported by the observation of a homogeneous cosmic ray sea, see 9. More concretely, it implies a transport rate sufficiently fast to smooth out variations of the ISM and the cosmic ray sources, see 10. The γ-ray data indicate a homogeneous CR distribution up to some hundreds of GeV. At these energies, the constraints on the propagation time are relaxed by a factor $\sim$10, so the CR can easily form a homogeneous flux.

[7] For a detailed review see Ref. [8]

It has further been pointed out that the diffusion coefficient measured by HAWC and HESS in the vicinity of pulsars may not be representative for the entire galaxy. Instead, CR transport may be more efficient far away from those objects, and then the propagation could be even more efficient [204, 264]. However, there is no observational evidence for this hypothesis yet.

- With the diffusion coefficient extracted from the γ-ray observations, within 0.1 Myr, CR (possibly independent of energy) can travel a distance of $\sim$ 100 pc. This is roughly the size of the Local Bubble. As emphasized in point 2, the average density seen by the cosmic rays indicates that they must have resided in an overdense region before leaking into the LB. This is the most critical point. However, if the LB formed through a supernova explosion in a (molecular) cloud, there may indeed be high density regions at its boundary. This scenario is discussed in the literature (see e.g. [6]) and can be probed through starlight- and dust-extinction maps.

- The points 6, 7 and 8 seem to indicate that time-dependent CR injection may be important, in contrast to the often assumed steady-state picture. Within an area of radius 100 pc, the SN rate is roughly 2 per Myr. If the supernova remnants accelerate and eject cosmic rays on a timescale of $0.1 - 1$ Myr, we might just see recent sources dominating the CR flux.

  In our case, this means that there could be a local source that dominates the CR flux in the vicinity of the sun at high energies, as suggested in [265]. There is some potential tension between this hypothesis and the observation of a similar CR spectrum allover the galaxy. However, the hypothetical local source seems to dominate the CR flux above $\sim$ 200 GeV, and the γ-ray observations support a homogeneous CR sea only up to some hundreds of GeV. Thus, at this stage, there is no evidence against a local source.

- A kpc CR halo, see 11, does not necessarily contradict the picture of local and recent cosmic rays. As the galactic magnetic field (GMF) decreases with distance from the galactic disc, it is possible that particles cannot easily return once they left the disc. They could scatter upwards, being trapped in the halo for a while before they escape into intergalactic space. However, this picture implies a magnetic field that is dominantly random or parallel to the galactic disc. If there is a strong magnetic field perpendicular to the disc it can offer fast transport of CR, potentially back into the disc. To illuminate the discussion, a more robust understanding of the GMF could help.

  The simulations discussed in point 6 indicate that anisotropic diffusion has to play an important role, which supports the idea of particles slowly moving upwards but not back.

  The radio data, see 11, suggest that the electron density (or/and the magnetic field) decreases significantly above galactic heights of $\sim$ 100 pc, which would also point towards anisotropic diffusion.

In summary, there is only one observation that is in a certain tension with the short propagation time required by secondary $e^{\pm}$ at high energy. That is the comparatively large average number density of the ISM, see 2, in contrast to the low density inside the LB, see 3. It is possible to have an average density of ~ 3 cm^{-3} in the propagation region, if the LB is surrounded by dense regions. The origin of the LB is under debate, and one popular explanation is that it formed through a supernova explosion that blew away the local ISM. In that case, overdense regions outside of the shock front are expected.

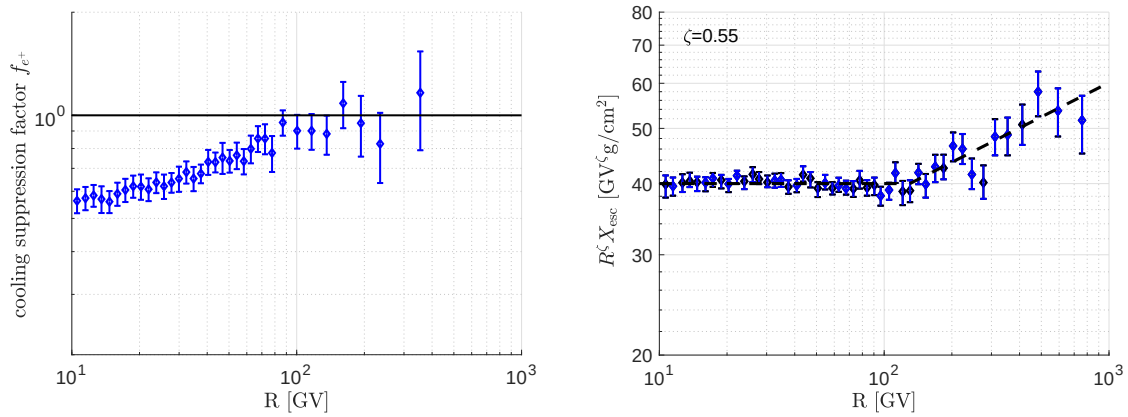

Figure 3.4: **Left:** e^+ cooling suppression factor, derived from e^+ and $\bar{p}$ data. **Right:** CR grammage, derived from nuclei data. The dashed line highlights the hardening break in $X_{\rm esc}$. It starts at $\mathcal{R} = 130$ GV with slope $\mathcal{R}^{0.2}$.

3.3 Coincident Trends in Nuclei and Positrons

It is interesting to inspect the behaviour of e^+ alongside the behaviour of secondary nuclei. In Fig. 3.4, in the left panel, we plot the measured e^+ flux divided by the theoretical secondary e^+ upper bound. We denote this ratio by $f_e^{\rm obs}$. Note that in this calculation, we use $\bar{p}$ data to extract f_e directly, without reference to B/C or any other nuclei data. Then, in the right panel, we plot the grammage $X_{\rm esc}$ calculated from nuclei data (scaled by a factor of $\mathcal{R}^\zeta$ with $\zeta = 0.55$, to highlight the spectral shape).

As noted before, the left panel of Fig. 3.4 shows the e^+ flux rise and saturation with the secondary upper bound, signified by $f_e^{\rm obs} = 1$. Comparing this to the right panel, we note that the saturation rigidity of $f_e^{\rm obs}$, $\mathcal{R} \sim 100$ GV, is close to a hardening break seen in $X_{\rm esc}$: at $\mathcal{R} \gtrsim 100$ GV, the spectral index of $X_{\rm esc}$ is hardened by $\Delta\zeta \approx 0.2$. This is highlighted by the dashed line. The spectral hardening, that we exhibit here in terms of the CR grammage $X_{\rm esc}$, is consistent with analyses by the AMS02 collaboration [195] (see also Sec. 2.5.1).

Again, the relation between these features observed in the loss suppression factor (inferred from CR e^+) and in the grammage (derived from CR nuclei) may be accidental, or alternatively, it points at a common origin.

3.4 Explicit Models of Propagation

Propagation models describing the positron data together with the nuclei data need to have an escape time that is steeply falling with increasing CR rigidity. Since the measured CR grammage $X_{\rm esc}$ shows only a relatively mild rigidity dependence, roughly $X_{\rm esc} \propto \mathcal{R}^{-0.5}$, this can only be achieved in models where the rigidity dependence of the escape time is not directly inherited from that of $X_{\rm esc}$. As an example for such a scenario, we will consider a scale height of the CR halo that decreases with increasing CR rigidity, as motivated in [201]. From a phenomenological perspective this idea is plausible: The GMF decreases with distance from the galactic disc. In this inhomogeneous magnetic field, it is expected that high energy cosmic rays escape faster from the magnetic halo, whereas CR of lower energies are more easily trapped. A particle's gyroradius increases with its rigidity,

and if the latter is larger than the scale of the perturbations, then, roughly speaking, the particle is not bound by the magnetic field. In terms of magneto-hydrodynamics, this means that a rigidity dependent propagation zone could arise if the ratio between the power in large-scale to that in small-scale magnetic field perturbations decreases with increasing distance from the galactic disc. In this section we want to explore this possibility within a diffusion model and a leaky box model.

3.4.1 Diffusion Model

In section 3.3 we introduced the loss-suppression factor $f_{e^+} \leq 1$ which is technically defined by

$$n_{e^+}(\mathcal{R}) = f_{e^+}(\mathcal{R})\, Q_{e^+}(\mathcal{R})\, X_{\rm esc}(\mathcal{R}) \tag{3.3}$$

$$= f_{e^+}(\mathcal{R})\, n_{e^+,\rm no\,loss}(\mathcal{R})\,. \tag{3.4}$$

n_{e^+} and Q_{e^+} are the positron distribution in the galaxy and source term, respectively, like introduced in Sec. 1.1.2. We generalise the two-zone model by allowing the boundary condition to depend on CR rigidity, $L = L(\mathcal{R}) = L_0\mathcal{R}^{-\delta_L}$ with $\delta_L \geq 0$. This model solves

$$-K\partial_z^2 n + 2h\delta(z)\Gamma n - \partial_{\mathcal{R}}\left(\frac{\mathcal{R}n}{t_c}\right) = 2h\delta(z)Q\,, \tag{3.5}$$

where the diffusion coefficient K and the cooling time t_c can be a generic function of the CR rigidity $\mathcal{R}$. The cosmic ray sources are located in the galactic disc at position $z = 0$. Notice we inserted a factor of $2h$ in front of the $\delta(z)$, with h the thin disc scale height. This defines Q as the mean production rate density inside the thin disc. For a secondary CR species s, Q is related to the production per unit column density Q_s of Eq. (3.3) via

$$Q = c\rho_{\rm ISM}Q_s = \frac{cX_{\rm disc}}{2h}Q_s, \tag{3.6}$$

where $X_{\rm disc} = 2h\rho_{\rm ISM}$.

We include losses in the ISM via the Γ term, localised in the thin disc, that can be written as $\Gamma = n_{ISM}\sigma c$. For e^+ this term approximates bremsstrahlung losses, with $\Gamma = -\frac{X_{\rm disc}c}{2hX_{\rm brem}}\left(1 + \left(\frac{\partial \log n}{\partial \log \mathcal{R}}\right)\right)$ and $X_{\rm brem} \approx 60$ g/cm^2. For $\left(\frac{\partial \log n}{\partial \log \mathcal{R}}\right) \approx -3$, this gives an effective bremsstrahlung time scale $\Gamma^{-1} \approx$ 15 Myr [15].

For CR nuclei we can neglect the energy losses in Eq. (3.5) and solve the model for the grammage

$$X_{\rm esc} = \frac{n_s(\mathcal{R},z=0)}{Q_s} = \frac{X_{\rm disc}Lc}{2K}\,, \tag{3.7}$$

and define the escape time

$$t_{\rm esc} = \frac{L^2}{2K} = \frac{X_{\rm esc}L}{X_{\rm disc}c}\,. \tag{3.8}$$

If the diffusion coefficient is constant, then from Eq. (3.7) it follows that the grammage is proportional to the rigidity dependent boundary, which fixes $\delta_L \approx 0.5$. The spectral break observed in primary cosmic rays as well as in the grammage could originate from a softening of this slope, e.g. when the gyro-radius of the particles becomes larger than the scale of the MHD turbulences.

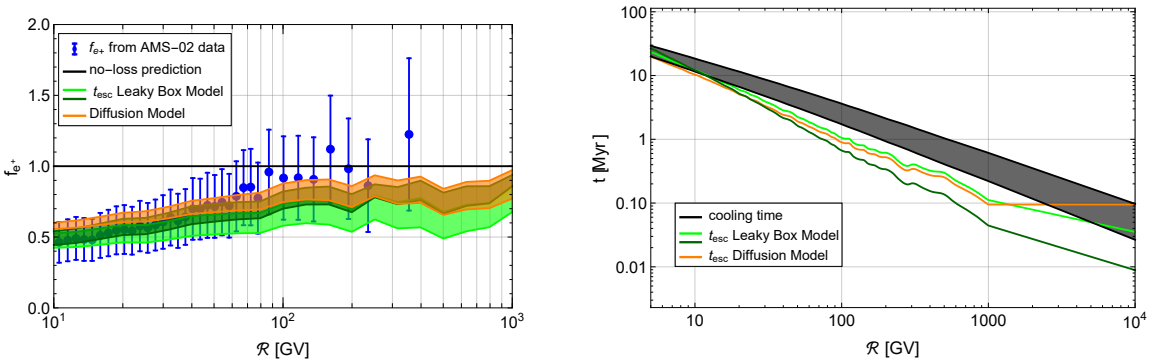

Figure 3.5: **Left:** e^+ cooling suppression factor, derived from e^+ and $\bar{p}$ data, together with f_{e^+} derived in the diffusion model (orange) and the leaky box model (green/dark green). **Right:** Relevant time scales for the models on the l.h.s.

The crucial point of this model is demonstrated in Eq. (3.8): If the halo size varies with the rigidity of the particle, the escape time is not just proportional to the grammage but could decrease more quickly. This is the relevant feature that allows to describe the positron data from a purely secondary origin.

We demonstrate this property in Fig. 3.5, showing the observed loss suppression factor (cf. section 3.3) together with the one derived in this model (orange). The computation can be found in App. 3.A. The width of the orange band accounts for the uncertainties in the cooling time from the GMF. The grammage in Eq. (3.8) is taken directly from the B/C data [166] and extrapolated towards higher rigidity by a constant[8]. The model parameters entering the computation are the halo size L and diffusion coefficient K. For the halo size, we use a broken power-law: $L = (\mathcal{R}/10\text{GV})^{-\delta_L}$ kpc with $\delta_L = 0.5$ at $\mathcal{R} \leq 1$ TV and $\delta_L = 0$ at $\mathcal{R} > 1$ TV. In this way, the model reproduces the measured (and extrapolated) grammage. We take a diffusion coefficient that is constant with rigidity: $K = 4.8 \times 10^{27} \text{cm}^2/\text{s}$. This value is close to the value deduced from the HAWC observation of the Geminga ICS halo[9] [12] ($K_{\text{HAWC}} = 4.2 \pm 1.2 \times 10^{27} \text{cm}^2/\text{s}$ at 100 TeV). The grammage of the galactic disk X_{disc} is fixed by setting $h = 100$ pc and $\rho_{\text{ISM}} = 3 \times 1.3 m_p$ cm^{-3}.

3.4.2 Leaky Box Model

The same exercise can be done in the leaky box model (LBM), which solves

$$\frac{n}{t_{\text{esc}}} - \partial_{\mathcal{R}} \left(\frac{\mathcal{R} n}{t_c} \right) = \frac{q}{V}, \tag{3.9}$$

where V is the volume of the CR confinement region and q is the total secondary CR production rate within that volume. Note that there is no need to assume that the CR production is distributed uniformly in the CR confinement volume. Instead, what is assumed here is that CR bounce and

[8] The results presented in the left panel of Fig. 3.5 barely depend on the shape of the grammage above the break, hence the form of extrapolation is not relevant.

[9] To be clear: we are *not* assuming here that the locally measured CR originate from Geminga. Indeed, if the adopted value of K is approximately correct, then Geminga's contribution to locally measured CR is negligible. We are simply suggesting that the CR diffusion coefficient, inferred from the observations of Geminga, could apply locally.

isotropise quickly within the volume V, so the steady-state distribution n is uniform[10] in V. The grammage in this model is given by

$$X_{\rm esc} = 1.3 m_p c N \frac{t_{\rm esc}}{V} \,, \tag{3.10}$$

with N the total number of ISM particles relevant for the production of the CR. As in the diffusion model, the important point is that $t_{\rm esc}$ is not proportional to $X_{\rm esc}$, as can be seen from Eq. (3.10).

The loss suppression factor in the LBM is given in App. 3.A and displayed as the green and dark green band in Fig. 3.5. Once again, the width of the bands encompasses the uncertainties of the cooling time. We choose the escape time to vary as $t_{\rm esc} = 1.1 X_{\rm esc}[{\rm g/cm^2}] \times (\mathcal{R}/10{\rm GV})^{-\delta_L}$ Myr with $\delta_L = 0.5$ (light green) and $\delta_L = 0.7$ (dark green). Again, the grammage is inferred from the data, s.t. our model is consistent with CR nuclei.

3.5 Summary and Discussion

We have presented some new evidence, supporting the possibility that CR e^+ are dominantly coming from secondary production:

1. As shown in Fig. 3.1, measurements of the $e^\pm$ flux at $E \sim 3$ TeV are consistent with the flux expected from secondary production, if radiative energy losses during secondary $e^\pm$ propagation are not important. This coincidence with the secondary flux adds to the earlier observation, that the e^+ flux in the range $E \sim 100 - 800$ TeV saturates the no-loss upper bound. We note that direct parametrisation of LHC data, necessary for the calculation of secondary $e^\pm$ production at multi-TeV energies, have now become available [166].

2. As shown in Fig. 3.4, the transition of the e^+ data, into saturating the secondary upper bound, occurs at $\mathcal{R} \sim 100$ GV and is correlated with another observed transition in the CR grammage $X_{\rm esc}$, derived from secondary nuclei B, and also confirmed for Li and Be [195].

Interpreting Fig. 3.1 to imply that e^+ are secondary in the entire measured energy range $E \sim (10 - 10^4)$ GeV, we would deduce that the propagation time of CR satisfies $t_{\rm esc}(\mathcal{R} = 10\ {\rm GV}) \gtrsim 10$ Myr (based on the hint for $O(1)$ suppression of the e^+ flux at this energy), and $t_{\rm esc}(\mathcal{R} = 3\ {\rm TV}) \lesssim 0.1$ Myr (based on the hint for negligible effect of loss). Thus, $t_{\rm esc}$ must decrease fast with $\mathcal{R}$. If the propagation time was a smooth power-law in rigidity, $t_{\rm esc} \propto \mathcal{R}^{-\alpha}$, then we must deduce $\alpha \gtrsim 0.8$. More precisely, the requirement is, roughly, $t_{\rm esc} \lesssim t_{\rm cool}$ for $\mathcal{R} \gtrsim 100$ GV. In the Thomson limit one has $t_{\rm cool} \propto \mathcal{R}^{-1}$. However, Klein-Nishina corrections due to the UV component in the ISRF lead to $t_{\rm cool} \sim \mathcal{R}^{-\alpha_c}$, with $\alpha_c \sim 0.8$ in the energy range of interest. This possibility was considered in [201], where it was also noted that to accommodate B/C data, which constrains the CR grammage to follow $X_{\rm esc} \propto \mathcal{R}^{-\delta}$ with $\delta \approx 0.4 - 0.5$, the characteristic scale height of the CR halo must be rigidity-dependent.

As a proof of concept, we implemented two models that provide these characteristics, i.e. a diffusion model and a leaky box model with rigidity-dependent propagation volume V. In these setups, the escape time is proportional to $t_{\rm esc} \propto X_{\rm esc} V$. Hence, $t_{\rm esc}$ is *not* proportional to the CR grammage

[10] As an illustrative example with a non-uniform source, consider a black-body cavity for photons, where we turn on a point-like light bulb inside a closed cavity and let the photons randomise inside, escaping through some little hole in the cavity. The steady state distribution of photons in the cavity will be spatially uniform and will satisfy the "LBM equation".

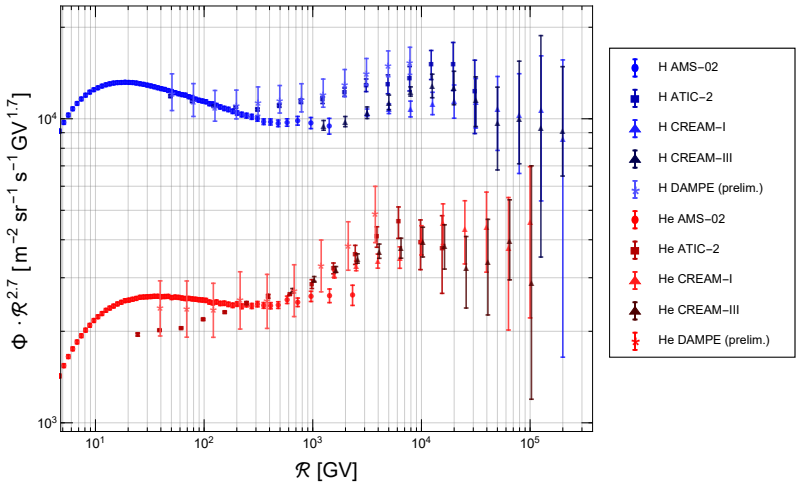

Figure 3.6: Experimental CR p and He data. The spectra do not follow a simple power-law distribution. Instead, we may be seeing the characteristics of a few single sources in our neighborhood.

(like in typical homogeneous diffusion models), but decreases faster with rigidity $\mathcal{R}$ (in fact, faster than the cooling time). Thus, energy losses for leptons are not relevant up to TeV energies. Accordingly, the positron data are fully consistent with secondary CR. The diffusion coefficient applied in the propagation models matches the values measured by HAWC and HESS. It is plausible to expect that the rigidity dependence of the propagation volume softens at some point, which could account for the observed spectral break in the CR grammage and the primary CR.

Certainly, a smooth power-law model for $t_{\rm esc}$ must give over to another behavior at yet higher rigidity, probably by $\mathcal{R} \sim 100$ TV. The reason is that accepting power-law $t_{\rm esc}$ all the way to very high rigidities, with $\alpha \gtrsim 0.8$, we would be led to $t_{\rm esc}(\mathcal{R} = 500\ {\rm TV}) \lesssim 2$ kyr. This is an unacceptably small value for $t_{\rm esc}$: if there were a CR source near Earth in the last 2 kyr, we would have noted it.

In the models discussed above, with a propagation time of the order of 0.1 Myr at rigidity 2 TV, high energy CR are recent and local. We check the consistency of this hypothesis with various astrophysical data. There is one critical point, namely that the measured grammage implies that the average ISM density seen by TV CR must be of the order of a few H particles per cm^3. This is only possible if there are overdense regions at the boundary of the Local Bubble. It can be tested e.g. by starlight-extinction maps [5] and other searches for astrophysical radiation.

Another possibility is that CR in the range between few GV to TV are not well described by some global, smooth power-law propagation history. Instead, it may be the case that we are seeing transitions between different populations of CR sources, with an older population of sources, characterised by $t_{\rm esc} \gtrsim 10$ Myr, dominating the CR below $\mathcal{R} \sim 10$ GV, and other sources, possibly a single source [265], characterised by $t_{\rm esc} \sim 0.1$ Myr, dominating the flux above $\mathcal{R} \sim 100$ GV.

Either way, with a short propagation time of ~ 0.1 Myr, we expect to see structure in the CR flux, reflecting a transition between different populations of sources or different mechanisms of CR propagation. Proton and helium measurements, extending from sub-TV up to several PV [266] (see [267] for a recent review of relevant measurements), do not seem inconsistent with such transitions, in the sense that the data do not appear to be well described by a simple power-law, but rather suggest a certain degree of structure (see Fig. 3.6). This observation supports our point, and will hopefully

receive further investigation to unveil the origin of the CR at the TV scale and beyond.

3.A Derivation of the Loss Suppression Factor

3.A.1 Diffusion Model

To find a solution of Eq. (3.5), it is useful to expand the CR density in a Fourier series,

$$n(\mathcal{R},z) \quad = \quad \sum_{m=0}^{\infty} n_m(\mathcal{R}) \cos\left[\frac{(2m+1)\pi z}{2L}\right], \tag{3.11}$$

where $\int_{-1}^{1} dz \cos\left[\frac{(2m+1)\pi z}{2L}\right] \cos\left[\frac{(2n+1)\pi z}{2L}\right] = L\delta_{mn}$. Eq. (3.5) then becomes

$$\begin{aligned} &\left[\frac{(2m+1)^2\pi^2}{8} - \left(\frac{\partial \log L}{\partial \log \mathcal{R}}\right)\frac{t_{\rm esc}}{4t_c}\right]\frac{n_m}{t_{\rm esc}} + \frac{cX_{\rm disc}\Gamma_s}{L}\sum_k n_k \quad + \\ &\left(\frac{\partial \log L}{\partial \log \mathcal{R}}\right)\sum_{k\neq m}\frac{(-1)^{k+m}(2m+1)(2k+1)}{4(k-m)(k+m+1)}\frac{n_k}{t_c} - \partial_{\mathcal{R}}\left(\frac{\mathcal{R}n_m}{t_c}\right) \quad = \quad \frac{cX_{\rm disc}}{L}Q_{e^+}. \end{aligned} \tag{3.12}$$

We can now write Eq. (3.12) in matrix form,

$$-\partial_{\mathcal{R}}\left(\frac{\mathcal{R}N}{t_c}\right) + \frac{1}{t_{\rm esc}}AN \quad = \quad q, \tag{3.13}$$

where N and q are column vectors and A a square matrix. In practice we can truncate N and keep only the first few entries, because the high-m entries have rapidly decreasing effective escape time. We can write the solution as

$$N(\mathcal{R}) \quad = \quad t_c(\mathcal{R})\int_1^{\infty} dx \exp\left[-\int_1^x \frac{dy}{y}\frac{t_c(y\mathcal{R})}{t_{\rm esc}(y\mathcal{R})}A(y\mathcal{R})\right]q(x\mathcal{R}). \tag{3.14}$$

At $z = 0$ we have

$$\begin{aligned} n(\mathcal{R},0) \quad &= \quad cX_{\rm disc}t_c\int_1^{\infty} dx\,\frac{Q_{e^+}(x\mathcal{R})}{L(x\mathcal{R})}\sum_{m,k=0}^{\infty}\exp\left[-\int_1^x \frac{dy}{y}\frac{t_c(y\mathcal{R})}{t_{\rm esc}(y\mathcal{R})}A(y\mathcal{R})\right]_{mk} \\ &= \quad X_{\rm esc}\frac{t_c}{t_{\rm esc}}\int_1^{\infty} dx\,\frac{Q_{e^+}(x\mathcal{R})L(\mathcal{R})}{L(x\mathcal{R})}\sum_{m,k=0}^{\infty}\exp\left[-\int_1^x \frac{dy}{y}\frac{t_c(y\mathcal{R})}{t_{\rm esc}(y\mathcal{R})}A(y\mathcal{R})\right]_{mk}. \end{aligned} \tag{3.15}$$

Finally, the loss suppression factor is:

$$f_{e^+} \quad = \quad \frac{t_c}{t_{\rm esc}}\int_1^{\infty} dx\frac{Q_{e^+}(x\mathcal{R})L(\mathcal{R})}{Q_{e^+}(\mathcal{R})L(x\mathcal{R})}\sum_{m,k=0}^{\infty}\exp\left[-\int_1^x \frac{dy}{y}\frac{t_c(y\mathcal{R})}{t_{\rm esc}(y\mathcal{R})}A(y\mathcal{R})\right]_{mk}, \tag{3.16}$$

$$\begin{aligned} A_{mk} \quad &= \quad X_{\rm esc}\Gamma_s + \frac{(2m+1)^2\pi^2}{8}\delta_{mk} \\ &\quad -\left(\frac{\partial \log L}{\partial \log \mathcal{R}}\right)\frac{t_{\rm esc}}{4t_c}\left[\delta_{mk} - (1-\delta_{mk})\frac{(-1)^{k+m}(2m+1)(2k+1)}{(k-m)(k+m+1)}\right]. \end{aligned} \tag{3.17}$$

3.A.2 Leaky Box Model

For the LBM with a rigidity-dependent CR halo, $V = V(\mathcal{R})$, the solution is

$$f = \frac{t_c}{t_{\rm esc}} \int_1^\infty dx \frac{q(x\mathcal{R})}{q(\mathcal{R})} \frac{V(\mathcal{R})}{V(x\mathcal{R})} e^{-\int_1^x \frac{dy}{y} \frac{t_c(y\mathcal{R})}{t_{\rm esc}(y\mathcal{R})}}. \tag{3.18}$$

Since $V \propto \frac{t_{\rm esc}}{X_{\rm esc}}$, and $X_{\rm esc}$ is well constrained observationally, it is useful to write the solution as

$$f = \frac{t_c}{t_{\rm esc}} \int_1^\infty dx \frac{q(x\mathcal{R})}{q(\mathcal{R})} \frac{t_{\rm esc}(\mathcal{R})}{t_{\rm esc}(x\mathcal{R})} \frac{X_{\rm esc}(x\mathcal{R})}{X_{\rm esc}(\mathcal{R})} e^{-\int_1^x \frac{dy}{y} \frac{t_c(y\mathcal{R})}{t_{\rm esc}(y\mathcal{R})}}. \tag{3.19}$$

In the LBM there is no distinction between spatial locations of bremsstrahlung vs. other radiative losses. We can therefore estimate the effect of bremsstrahlung by replacing $t_c \to t_c\,(1 + X_{\rm esc}\Gamma_s)^{-1}$.

CHAPTER 4

Light(ly)-coupled Dark Matter in the keV Range: Freeze-In and Constraints

This chapter is based on Ref. [268], published together with Jae Hyeok Chang and Rouven Essig.

4.1 Introduction

Dark matter (DM) with mass in the keV to GeV range has been receiving increased attention over the last few years. Numerous mechanisms exist for how such dark matter could have been produced in the early Universe. The mechanism of thermal freeze-out, which is perhaps the best studied mechanism, typically produces dark matter consistent with observations only between about ∼1 MeV to ∼100 TeV, being bounded below by bounds from Big Bang Nucleosynthesis (BBN) [269–271] and above by unitarity of the annihilation cross section [272]. However, besides producing dark matter below the GeV scale by traditional thermal freeze-out [273], various other related and non-thermal production mechanisms exist, see e.g. [274–296].

In this paper, we consider several models for dark matter down to keV masses for which the relic abundance can be produced from freeze-in [277, 278]. The couplings between the dark matter and Standard Model (SM) particles needed to obtain the observed relic abundance are typically very small, which naturally allows these models to avoid the BBN bound, since the dark matter particles will not be in chemical equilibrium with SM particles. We show that nevertheless, at least for sufficiently low masses, these models can be probed by constraints from the cooling of various stellar objects.

The models we consider are a dark matter particle coupled to a dark photon that mixes with the photon [58, 59, 297, 298], dark matter with an electric dipole moment (EDM), and dark matter with a magnetic dipole moment (MDM) [299–304]. These models can naturally have small interactions with electrically charged SM particles through a small kinetic mixing parameter (for the dark photon portal) or through a higher dimension operator (for the EDM/MDM models). In these models, if the couplings are sufficiently small, the dark matter particles are never in thermal equilibrium with the SM particles, but are produced gradually from the SM thermal bath over time to produce the correct relic abundance. This is called the freeze-in mechanism. Depending on the type of interaction, the production may be dominant at low temperatures (IR freeze-in) or also occur at high temperatures (UV freeze-in) [305]. The dark photon model has IR freeze-in, in which case the results do not depend on the reheating temperature, while the models with an electric or magnetic dipole moment have UV freeze-in, where the reheating temperature matters. We calculate the freeze-in parameters for these models, including the contributions from the plasmon decay [306–308].

The couplings needed for freeze-in are typically so small that these models cannot be constrained from laboratory experiments. However, constraints from stellar objects, such as red giant stars (RG),

horizontal branch stars (HB), and the Sun, can probe these small couplings [66, 307, 309–316]. In stellar objects, interactions of SM particles can produce the hypothetical dark sector particles. These dark sector particles can then carry away energy and change the evolution histories of the stellar objects. Since the observed stellar properties are consistent with predictions from the standard stellar models, we can constrain the couplings of the dark sector to the SM particles. Very roughly, since the temperature of the RG and HB stars reach about 10^8 K, dark sector particle masses up to about 10 keV can be probed efficiently, and masses up to 100 keV are also accessible.

The remainder of the paper is organized as follows. In Sec. 4.2, we describe the salient features of the models considered in this paper and some basic constraints on them. In Sec. 4.3, we describe the freeze-in production in some detail. Sec. 4.4 discusses the constraints from the RG stars, HB stars, and the Sun. Sec. 4.5 briefly describes the prospects for probing these models in the laboratory. We present our conclusions in Sec 4.6. Three appendices provide additional details for our calculations.

4.2 Light Dark Matter Models Interacting or Mixed with Photons

In this work we focus on dark matter interacting with photons, either via kinetic mixing through a heavy dark photon or directly due to an electric or magnetic dipole moment.

For the dark photon (A') portal, we will consider the dark matter candidate to be a fermion (χ) or a complex scalar (ϕ). The dark photon is the gauge boson of an additional broken U(1) gauge group, and it is kinetically mixed with the photon [58]. The Lagrangian is

$$\begin{aligned}\mathcal{L}_{A'} = &-\frac{1}{4}F'_{\mu\nu}F'^{\mu\nu} - \frac{\epsilon}{2\cos\theta_W}F'_{\mu\nu}B^{\mu\nu} - \frac{1}{2}m'^2A'_\mu A'^\mu \\ &+ \begin{cases}\bar{\chi}\left(i\gamma^\mu\partial_\mu + g_D\gamma^\mu A'_\mu - m_\chi\right)\chi, & \text{(Dirac fermion)}\\ \partial^\mu\phi\partial_\mu\phi^* - ig_DA'^\mu(\phi(\partial_\mu\phi^*) - (\partial_\mu\phi)\phi^*) + g_D^2A'^2_\mu|\phi|^2 - m_\phi^2|\phi|^2\,, & \text{(complex scalar)}\end{cases}\end{aligned} \tag{4.1}$$

where ϵ is the kinetic mixing parameter, θ_W the weak mixing angle, $g_D = \sqrt{4\pi\alpha_D}$ is the 'dark' gauge coupling, and $B_{\mu\nu}$ and $F'_{\mu\nu}$ are the field strength tensors of the hypercharge gauge boson and the dark photon, respectively. If the dark photon is massless, χ or ϕ is a millicharged particle, for which the stellar cooling constraints have already been discussed in the literature [311, 317]. Moreover, even if the dark photon is massive but ultralight $m' \ll m_\chi$, the constraints are similar to the millicharged case [318, 319]. We therefore focus here on the 'heavy' dark photon case, where $m' \sim O(m_\chi)$. We mainly focus on the case with $m' > 2m_\chi$ or $m' > 2m_\phi$, in which case the dark matter will consist of χ- or ϕ-particles, but we will also comment on the case with $m' < 2m_\chi$ or $m' < 2m_\phi$, in which case the dark matter can mostly consist of dark photons.

A model where the dark matter has an electric dipole moment (d_χ) or a magnetic dipole moment (μ_χ) is described by the following term in the Lagrangian

$$\mathcal{L}_{\text{EDM}} = -\frac{i}{2}d_\chi\bar{\chi}\sigma_{\mu\nu}\gamma^5\chi F^{\mu\nu}\,, \tag{4.2}$$

$$\mathcal{L}_{\text{MDM}} = -\frac{i}{2}\mu_\chi\bar{\chi}\sigma_{\mu\nu}\chi F^{\mu\nu}\,, \tag{4.3}$$

respectively. Writing these terms in a different way helps to read off the interaction vertices

$$\mathcal{L}_{\text{EDM}} = -id_\chi \bar{\chi}\left(\not{k}\gamma_\mu - k_\mu\right)\gamma^5 \chi A^\mu \,, \tag{4.4}$$

$$\mathcal{L}_{\text{MDM}} = -i\mu_\chi \bar{\chi}\left(\not{k}\gamma_\mu - k_\mu\right)\chi A^\mu \,, \tag{4.5}$$

where k is the momentum of the incoming photon. The d_χ and μ_χ have mass dimension -1. These effective operators must come from an underlying theory at a larger scale. As an example, the dipole moment can be induced by heavy charged particles (a fermion and a scalar) that couple the dark matter to the SM through a loop [303]. In such a scenario, for particles of positive/negative electron charge and mass M, the electric dipole moment would be given by

$$d_\chi \sim \frac{eg^2}{8\pi^2 M} \,, \tag{4.6}$$

where e is the electron charge and g is the coupling between the heavy charged particles and χ. A similar equation holds for μ_χ. The mass of the heavy charged particles M could be as light as ~100 GeV [320] (possibly even slightly smaller [321]) to avoid collider bounds, which can be combined with a limit of $g^2 < 4\pi$ requiring perturbativity to give an upper bound of $d_\chi \lesssim 0.5\ \text{TeV}^{-1}$. Note that this limit is stronger than the LEP limit on dark matter particles with electric or magnetic dipole moment directly, which is about $d_\chi \lesssim 4\ \text{TeV}^{-1}$ [322] for $m_\chi < 50$ GeV. However, in this simple model of an additional scalar and fermion generating the dipole moment, the dark matter mass also receives loop corrections of roughly [303]

$$\delta m_\chi \sim \frac{M^2}{2e} d_\chi \,. \tag{4.7}$$

Since the dark matter mass cannot (trivially) be smaller than its mass correction, we find an upper limit for the electric dipole moment of

$$d_\chi \lesssim 10^{-5} \frac{m_\chi[\text{MeV}]}{(M[\text{TeV}])^2}\ \text{TeV}^{-1} \,, \tag{4.8}$$

with a similar equation for the magnetic dipole moment. Of course, one could imagine different UV completions of the dark matter models with a dipole moment that do not have the same strong upper bound on the dipole moment.

General bounds on keV-to-GeV mass dark matter

Our main focus in this paper is on deriving the stellar constraints and freeze-in production of dark matter in the keV to GeV mass range. However, in the remainder of this section we briefly review other bounds on dark matter in or near this mass range.

If the dark matter is in chemical equilibrium with the SM bath in the early Universe, dark matter masses below ~9.4 MeV (for a Dirac fermion) or ~6.5 MeV (for a complex scalar) [270, 271, 323] are in tension with cosmological observables. The reason is that in the cosmological standard model, BBN started at a temperature of about 1 MeV, and the predictions are well confirmed by the measured abundance of light elements; extra relativistic degrees of freedom, N_{eff}, during this evolutionary stage could affect the expansion of the Universe and thus change the temperature at which BBN begins,

which would alter the predicted values for the abundance of light elements.

If the particles were never in chemical equilibrium with the SM (which is a necessary condition for freeze-in production), the number density is much smaller than the equilibrium number density, and the contribution to $N_{\rm eff}$ is negligible. We will check this condition below when we compare the parameters needed for freeze-in production to the couplings that would keep the dark matter in chemical equilibrium with the SM bath.

Another constraint on the dark matter mass comes from the existence of small-scale structure. Below dark matter masses of 1 keV, fermionic dark matter cannot account for all of the dark matter in dwarf galaxies [38, 39] due to the Pauli principle. Moreover, when the first structures form, the process can be disturbed if (a large component of) the dark matter (either fermionic or bosonic) is too warm. The fast streaming of the particles would then 'wash out' the forming structures. For thermal relics this is the case if the mass is lighter than about 1 keV [324]. In general, the constraint depends on the momentum distribution of the dark sector, which is modified in the non-thermal case by the average momentum $\langle|\mathbf{p}|\rangle$ compared to the thermal momentum $\langle|\mathbf{p}|\rangle^{\rm eq}$ [324]

$$m_{\chi/\phi} \geq \frac{\langle|\mathbf{p}|\rangle}{\langle|\mathbf{p}|\rangle^{\rm eq}} \times 1 \text{ keV} \,. \tag{4.9}$$

While a detailed calculation of the resulting mass bound in our models is beyond the scope of this paper, we do not expect the result to differ significantly from 1 keV (see e.g. [308], which considered a model consisting of dark matter interacting with a very light dark photon and find only an $O(1)$ correction).

For the dark-photon portal, large values of α_D imply large self-interactions among the dark matter particles mediated by the dark photon. For dark photons with a mass near the dark matter mass, the self-interaction limit on α_D from observations of the Bullet cluster, $\sigma_{\rm SIDM}/m_\chi \lesssim 2$ cm^2/g [37], become very stringent for small masses. In particular, for $m' = 3m_\chi$, we need $\alpha_D < 0.5$ for dark matter masses below ∼20 MeV, while we need $\alpha_D \leq 10^{-6}$ for dark matter masses below ∼28 keV. We will see below that the stellar constraints disfavor dark matter interacting with a dark photon to constitute a dominant component of dark matter from freeze-in production for dark matter masses below approximately 15 keV for $\alpha_D = 10^{-6}$. Below, we will consider values for α_D ranging between 10^{-6} to 0.5. We note that for dark matter interacting through a dipole moment, the self-interaction limits are not relevant, since the couplings to the mediator – the photon in this case – are very small.

We note that the bounds from $N_{\rm eff}$, structure formation, and self-interactions may be evaded if the dark matter candidates constitute only a sub-component of the observed dark matter density. Laboratory bounds will be discussed in Sec. 4.5.

4.3 Production via Freeze-In

If the interaction between the dark sector and SM sector is sufficiently small, the dark sector was never in chemical equilibrium with the SM sector throughout the history of the Universe. Excluded from the thermal bath, the dark matter abundance today therefore cannot be set via the typical freeze-out mechanism. Still, as long as there is some small coupling between the SM and dark sector, SM particles in the thermal bath can annihilate to produce dark sector particles. This is called the freeze-in mechanism [277, 278], and here we consider the freeze-in production of dark matter interacting with a heavy dark photon mediator, an electric dipole moment, or a magnetic dipole moment, as discussed

in Sec. 4.2.

In general, the number density, n_a, of a particle species a produced within the thermal history of the Universe is derived from the Boltzmann equation

$$\frac{dn_a}{dt} + 3Hn_a = R(T) \,. \tag{4.10}$$

Here, $R(T)$ is the number of interactions per unit volume and per unit time in which the particle is produced,

$$R(T) = \int \Pi_i \Pi_f |\mathcal{M}_{i\to f}|^2 (2\pi)^4 \delta^{(4)}\left(\Sigma p_i - \Sigma p_f\right) , \tag{4.11}$$

where

$$\Pi_i = \prod_i \frac{g_i d^3 p_i}{(2\pi)^3 2E_i} f_i, \;\; \Pi_f = \prod_f \frac{d^3 p_f}{(2\pi)^3 2E_f}(1 \pm f_f) , \tag{4.12}$$

p and E are the momentum and energy, respectively, subscripts i and f correspond to initial and final particles, f is the distribution function, + and − correspond to bosons and fermions, respectively, and the final state includes the particle a. $R(T)$ for $2 \to 2$ processes is conventionally written as $n_i^2\langle\sigma v\rangle$, and for $1 \to 2$ processes it is written as $n_i\langle\Gamma\rangle$. The factor g_i accounts for the degrees of freedom in the initial state.

The yield Y from freeze-in is found by integrating [325]

$$\frac{\mathrm{d}Y}{\mathrm{d}T} = -2\frac{M_{\rm Pl}}{(2\pi)^2}\left(\frac{45}{\pi}\right)^{3/2}\frac{\tilde{g}}{g_s^*\sqrt{g^*}}\frac{R(T)}{T^6} \,. \tag{4.13}$$

Here, $M_{\rm Pl} \simeq 1.22 \times 10^{22}$ MeV is the Planck mass, $g^*(T)$ is the effective number of relativistic degrees of freedom at temperature T, $g_s^*(T)$ the entropic relativistic degrees of freedom, and $\tilde{g}(T) = \left(1 + \frac{T}{3}\frac{\mathrm{d}\ln(g_s^*)}{\mathrm{d}T}\right)$ (see e.g. [326]). The first factor of two in Eq. (4.13) accounts for the production of both particles and antiparticles.

For the production of light dark matter coupled to the SM via the dark photon, there are several processes: pair annihilation of the SM particles f with $\bar{f}$, plasmon decay, and Z-boson decay,

$$R(T)_{\text{dark photon}} = \sum_f n_f^2\langle\sigma v\rangle_{f\bar{f}\to \mathrm{DM}+\overline{\mathrm{DM}}} + n_{\gamma^\star}\langle\Gamma\rangle_{\gamma^\star\to \mathrm{DM}+\overline{\mathrm{DM}}} + n_Z\langle\Gamma\rangle_{Z\to \mathrm{DM}+\overline{\mathrm{DM}}} \,. \tag{4.14}$$

The contribution from Z-boson decay is important for $m_\chi \gtrsim 1$ GeV. For $m_\chi \lesssim 1$ GeV, which is our focus in this paper, the Z-boson decay contributes $O(10\%)$. For the production of light dark matter coupled to the SM via an electric or magnetic dipole moment, there are pair annihilation of the SM particles f with $\bar{f}$ and plasmon decay processes that contribute to the production rate

$$R(T)_{\text{EDM/MDM}} = \sum_f n_f^2\langle\sigma v\rangle_{f\bar{f}\to \mathrm{DM}+\overline{\mathrm{DM}}} + n_{\gamma^\star}\langle\Gamma\rangle_{\gamma^\star\to \mathrm{DM}+\overline{\mathrm{DM}}} \,. \tag{4.15}$$

We show relevant processes for a dark matter fermion coupled to a dark photon or with an electric or magnetic dipole moment in Fig. 4.1 (the case of a scalar dark matter particle coupled to a dark photon is similar).

We can estimate from dimensional analysis the temperature at which dark matter production via freeze-in is important. Since $R(T)$ has mass dimension 4, $R(T) \sim T^4$ for dimension-4 operators like

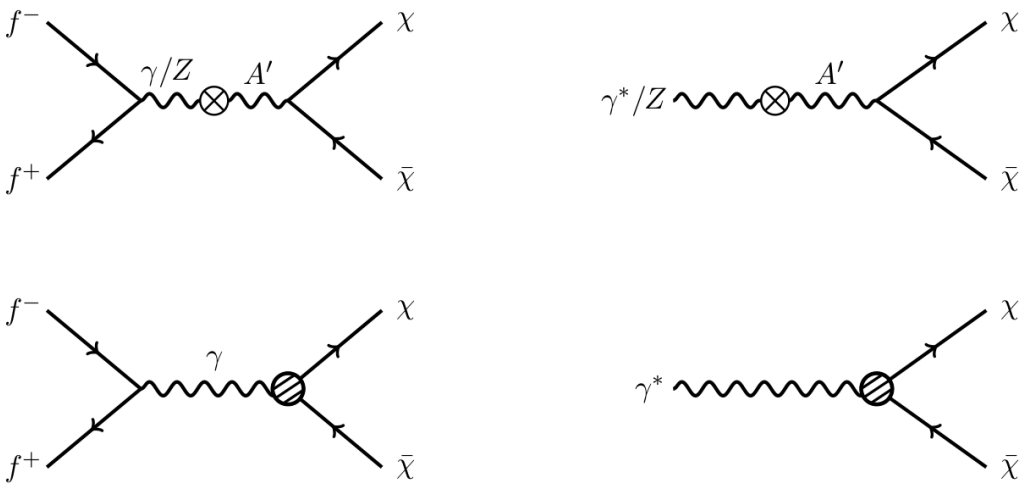

Figure 4.1: The dominant processes relevant for the production of dark matter interacting with a dark photon (upper diagrams) and dipole moments (lower diagrams) in the early Universe: pair annihilation (left) and plasmon/Z-boson decay (right).

the dark photon kinetic mixing term, and $R(T) \sim \frac{T^6}{\Lambda^2}$ for dimension-5 operators like the electric or magnetic dipole moment interactions. For the dark photon case, this then implies that $\frac{dY}{dT} \sim T^{-2}$, and freeze-in production is dominant at low temperature and is not sensitive to the reheating temperature. It is thus said to be infrared-dominated. In contrast, for the dipole moment case, $\frac{dY}{dT} \sim T^0$, so processes at all temperatures are relevant, up to the reheating scale, which therefore determines the relic abundance.

For the infrared dominated dark photon case, the precise process that dominates the freeze-in production depends on the dark matter mass. If the dark matter is heavier than the electron mass, pair annihilation dominates over plasmon decays (both longitudinal and transverse plasmons). Transverse plasmon decays occur at higher temperatures than the annihilation process, as the plasma frequency has to fulfill $2m_\chi \lesssim \omega_p \approx T/10$. The plasmon production process thus becomes inefficient for $T \lesssim 20m_\chi$, while the pair annihilation process is still very efficient. For dark matter masses above the electron mass, the dominant contributions are expected from those SM particles that are lighter than the dark matter and freeze out only after the freeze-in production has been completed. For example, for $m_e \lesssim m_\chi \lesssim m_\mu$, the dark matter freeze-in production is dominated by electron-positron pair annihilation. On the other hand, for dark matter masses below the electron mass, the pair annihilation process quickly becomes inefficient, and the decay of (transverse) plasmons yields sizable contributions to the number density. The longitudinal plasmon modes are always suppressed compared to the transverse plasmon modes for infrared dominated production due to lack of available phase space.

For the production of dark matter with an electric or magnetic dipole moment, which is determined by the reheating scale, decays of the longitudinal plasmon mode become relevant for large dark matter masses. The reason is that at high temperatures the maximal possible value of the longitudinal wave vector is sufficiently large to provide enough phase space for the decay into a dark matter pair.

We now consider the two production processes—pair annihilation and plasmon decay—in more detail below. For the subdominant Z-boson decay contribution, we provide detailed formulae in App. 4.B. Matching the dark matter density to the observed relic abundance today $\Omega_{\rm DM}h^2 = 0.11$ [19],

will allow us to find the value of the kinetic mixing factor, ϵ, or the electric or magnetic dipole moment, d_χ or μ_χ, that gives the right relic abundance.

4.3.1 Pair Annihilation

For dark matter masses above ∼1 MeV, the freeze-in production is dominated by contributions from annihilation into the dark sector. The rate to produce the dark matter particle f in a thermal bath of temperature T can then be derived from [325, 327]

$$n_f^2 \langle \sigma v \rangle_{\text{prod}} = \frac{g_i g_j T}{32(2\pi)^6} \int \mathrm{d}s \, \sqrt{s} K_1\left(\frac{\sqrt{s}}{T}\right) \sqrt{1 - \frac{4m_{\chi/\phi}^2}{s}} \sqrt{1 - \frac{4m_f^2}{s}} \int \mathrm{d}\Omega \, |\mathcal{M}|^2 \ , \tag{4.16}$$

where m_f is the mass of particle f, $K_n(x)$ is the modified Bessel function of the second kind, and s is the usual Mandelstam variable. $g_i = g_j = 2$ account for the degrees of freedom of the incoming fermions. Here $|\mathcal{M}^2|$ is averaged over initial state spins and summed over final state spins.We can now consider several cases:

- If the dark matter is a fermion interacting with a dark photon, the integrated matrix element of the annihilation of SM fermions $f + \bar{f}$ with charge q_f in units of e and mass m_f is given by [325]

$$\int \mathrm{d}\Omega \, |\mathcal{M}|^2 = \frac{16\pi}{3} (\epsilon e q_f g_D)^2 \left(1 + \frac{2m_f^2}{s}\right)\left(1 + \frac{2m_\chi^2}{s}\right) \frac{s^2}{(s - m'^2)^2 + m'^2 \Gamma_{A'}^2} \ , \tag{4.17}$$

  with the total width of the dark photon given by [325][1]

$$\Gamma_{A'} = \frac{m'}{12\pi} \left[g_D^2 \left(1 + \frac{2m_\chi^2}{m'^2}\right) \sqrt{1 - \frac{4m_\chi^2}{m'^2}} + \sum_f (\epsilon e q_f)^2 \left(1 + \frac{2m_f^2}{m'^2}\right) \sqrt{1 - \frac{4m_f^2}{m'^2}} \right] . \tag{4.18}$$

  These formulae do not include A'-Z-mixing, but we show the full formulae that include this mixing in App. 4.B and also use them in our code. In the second term of Eq. (4.18), the sum is over all fermions that are lighter than the dark photon. If $m' < 2m_e$, only the first term contributes. In our calculations, we drop the second term, which is a reasonable approximation as long as $\alpha_D = g_D^2/4\pi \gg \alpha\epsilon^2$. For Eq. (4.17), the major contribution comes from electron-positron annihilations, since the freeze-in is dominated by the lowest temperatures.

- If the dark matter is a boson interacting with a dark photon, the integrated matrix element is

$$\int \mathrm{d}\Omega \, |\mathcal{M}|^2 = \frac{4\pi}{3} (\epsilon e q_f g_D)^2 \left(1 + \frac{2m_f^2}{s}\right)\left(1 - \frac{4m_\phi^2}{s}\right) \frac{s^2}{(s - m'^2)^2 + m'^2 \Gamma_{A'}^2} \ , \tag{4.19}$$

[1] We correct the result given in [325] by a factor of 1/3 to account for the average over the three polarization modes.

and the total width of the dark photon is

$$\Gamma_{A'} = \frac{m'}{12\pi}\left[\frac{g_D^2}{4}\left(1-\frac{4m_\phi^2}{m'^2}\right)^{3/2} + \sum_f (\epsilon e q_f)^2\left(1+\frac{2m_f^2}{m'^2}\right)\sqrt{1-\frac{4m_f^2}{m'^2}}\right]. \tag{4.20}$$

Again, the second term accounts for the dark photon decays to SM particles, and the first term accounts for the decay to dark matter particles. A factor of $1/3$ appears from averaging over the dark photon polarizations. We again drop the second term in our calculations.

- For the case of dark matter with an electric or magnetic dipole moment, the integrated matrix elements are

$$\int \mathrm{d}\Omega \left|\mathcal{M}^{\mathrm{EDM}}\right|^2 = d_\chi^2 \frac{32\pi^2\alpha}{3}\frac{(s+2m_f^2)(s-4m_\chi^2)}{s} \tag{4.21}$$

$$\int \mathrm{d}\Omega \left|\mathcal{M}^{\mathrm{MDM}}\right|^2 = \mu_\chi^2 \frac{32\pi^2\alpha}{3}\frac{(s+2m_f^2)(s+8m_\chi^2)}{s}, \tag{4.22}$$

respectively.

With these expressions, Eq. (4.16) can be used to derive the number density averaged interaction rate that enters Eq. (4.13) to yield the relic abundance.

4.3.2 Plasmon decay

Another important production process for dark matter comes from the decay of plasmons in the thermal plasma of the early Universe. In a thermal plasma, the interaction of the photon with charged particles, most dominantly electrons, leads to an effective mass for the photon, which depends on the electron density and temperature of the thermal bath (see App. 4.A). At finite temperature, the photon propagator gets renormalized. The additional term acts like a self-energy of the photon, making it effectively massive. These quasi-massive states are called plasmons. The pole of the photon propagator determines the dispersion relations, which are then modified in comparison to the vacuum case. The properties of plasmons differ significantly from photons propagating in vacuum: they move slower than the speed of light and there is a longitudinal mode in addition to the transverse modes. We will refer to the different modes as 'longitudinal' or 'transverse' plasmons.

The plasmon production and decay includes all electromagnetic processes where on-shell photons are produced. One thus has to be careful to avoid double counting diagrams that contribute with an on-shell photon. However, here there is no such danger for the annihilation process; the intermediate photon cannot be on-shell, which can be seen by cutting the diagram (see Fig. 4.1) in the middle. If the photon were on-shell, the inverse process of the right-hand-side would correspond to a plasmon that decays to an electron-positron pair. This process is kinematically not allowed for plasmons, since the charged SM particles receive corrections to their mass and are too heavy. Thus, in the early Universe, the decay of plasmons and the annihilation of SM particles are two distinct processes that can be treated separately.

The decay of plasmons is an important production mechanisms for neutrinos in stellar objects [306]. Similarly, the plasmons can decay into particles from a dark sector. This process is relevant in the

early Universe as well as in stellar objects. In the following, unless stated otherwise, we follow the notation and conventions of [306].

We now want to derive the production rates of dark matter from plasmon decay. In general, the thermally averaged rate is given by

$$n_{\gamma^\star}\langle\Gamma\rangle_{\gamma^\star\to \mathrm{DM}+\overline{\mathrm{DM}}} = \sum_{\mathrm{pol}}\int \frac{\mathrm{d}^3k}{(2\pi)^3 2\omega_{\mathrm{pol}}(k)}\frac{\mathrm{d}^3p_{\mathrm{DM}}}{(2\pi)^3 2E_{\mathrm{DM}}}\frac{\mathrm{d}^3p_{\overline{\mathrm{DM}}}}{(2\pi)^3 2E_{\overline{\mathrm{DM}}}} \\ f(\omega_{\mathrm{pol}})(2\pi)^4\delta^{(4)}\left(K - P_{\mathrm{DM}} - P_{\overline{\mathrm{DM}}}\right)|\mathcal{M}_{\mathrm{pol}}|^2_{\gamma^\star\to \mathrm{DM}+\overline{\mathrm{DM}}}\,. \tag{4.23}$$

Here, $K = (\omega,\vec{k})$ is the four momentum of the plasmon and $P_{\mathrm{DM}}, P_{\overline{\mathrm{DM}}}$ are the four momenta of the outgoing dark matter particles. The sum over the polarizations 'pol' includes one longitudinal and two transverse modes. The distribution function of the plasmons is a Bose-Einstein distribution $f = g_{\mathrm{pol}}/(\exp(\omega_{\mathrm{pol}}/T) - 1)$, where $g_T = 2$ and $g_L = 1$. In the following subsections, we give the expressions for the matrix element in Eq. (4.23) for the models considered in this paper. The two processes indicated by the expressions in Eq. (4.16) and Eq. (4.23) together then give the total production rate of the freeze-in process that appears in Eq. (4.13), which gives the final dark matter yield. It turns out that for dark matter interacting with a dark photon mediator, the decay of the longitudinal mode contributes only at the percent level compared to the contribution from the transverse mode. However, for the dipole moment models, the contribution from the longitudinal mode can dominate.

Dark photon + fermion dark matter

At low energies, the mixing term in Eq. (4.1) becomes the mixing between the photon and the dark photon. For particles coupled to the SM sector via a dark photon, it is useful to transform the kinetic mixing term to the interaction basis

$$\frac{1}{2}\epsilon F^{\mu\nu}F'_{\mu\nu} \to A^\mu \epsilon K^2 A'_\mu\,, \tag{4.24}$$

such that the mixing vertex can be seen to be ϵK^2. The matrix element for the top right Feynman diagram of Fig. 4.1 can then be written as

$$i\mathcal{M}_{\mathrm{pol}} = \tilde{\epsilon}^\mu_{\mathrm{pol}}\epsilon K^2 \frac{-\eta_{\mu\nu} + \frac{K_\mu K_\nu}{m'^2}}{K^2 - m'^2 + im'\Gamma_A + \Pi_D}\bar{u}_\chi(-ig_D\gamma^\nu)v_{\bar{\chi}}\,. \tag{4.25}$$

The polarization index runs over the longitudinal and the two transverse polarizations. The self-energy of the dark photon in a dark matter plasma, Π_D, can be neglected if the dark matter particles do not thermalize.[2] The dispersion relations defining the photon self-energy as well as the definitions for the dressed polarization vectors $\tilde{\epsilon}^\mu$ and the renormalization factors therein can be found in App. 4.A.

[2] This is a good approximation in our case, since the coupling is sufficiently small to guarantee free streaming in stellar objects (as is relevant for deriving the lower boundary of the stellar constraints) and sufficiently small to avoid chemical equilibrium in the early Universe (as is relevant for freeze-in production). At large couplings, free-streaming in the stellar objects is not guaranteed, but there is still a constraint, see the discussion in Sec. 4.4.4.

In summary, we find for the squared matrix elements [315]

$$\left|\mathcal{M}_T^\chi\right|^2 = 8\pi\alpha_D\epsilon^2 Z_T \frac{K^4[K^2 - 2p_\chi^2\sin^2\theta]}{(K^2 - m'^2)^2 + (m'\Gamma_{A'})^2}\,, \tag{4.26}$$

$$\left|\mathcal{M}_L^\chi\right|^2 = 8\pi\alpha_D\epsilon^2 Z_L \frac{K^4[K^2 - 4(P_\chi^\mu\epsilon_{L\mu})^2]}{(K^2 - m'^2)^2 + (m'\Gamma_{A'})^2}\,, \tag{4.27}$$

where the width $\Gamma_{A'}$ is given in Eq. (4.18), and θ is the angle between the incoming photon and outgoing χ. We denote the dark matter four vector as P^μ and the absolute value of its momentum three-vector as p_χ. The longitudinal polarization tensor of the dark photon is given by $\epsilon_{L\mu} = (\frac{k}{\sqrt{K^2}}, \frac{\omega_L}{\sqrt{K^2}}\frac{\vec{k}}{k})$. With this definition, $\epsilon_L^\mu k_\mu = 0$ and $\epsilon_L^\mu\epsilon_{L\mu} = -1$. For the matrix element of the transverse modes, we averaged over the initial spins. Hence, here and in the following, $|\mathcal{M}_T^\chi|^2$ describes the matrix element for one transverse polarization mode, so in the sum in Eq. (4.23) it enters twice. We refer the reader to App. 4.A for more details.

Dark photon + scalar dark matter

For the plasmon decay to a pair of complex scalars via the dark photon, the only thing that changes from the fermion case discussed above is the last part of Eq. (4.25);

$$i\mathcal{M}_{\rm pol} = \tilde{\epsilon}_{\rm pol}^\mu\epsilon K^2 \frac{-\eta_{\mu\nu} + \frac{k_\mu k_\nu}{m'^2}}{K^2 - m'^2 + im'\Gamma_A + \Pi_D}\left(-ig_D(P_\chi - P_{\bar{\chi}})\right)^\nu\,. \tag{4.28}$$

Proceeding as before we find for the squared matrix elements

$$\left|\mathcal{M}_T^\phi\right|^2 = 8\pi\alpha_D\epsilon^2 Z_T \frac{K^4 p_\phi^2\sin^2\theta}{(K^2 - m'^2)^2 + (m'\Gamma_{A'})^2}\,, \tag{4.29}$$

$$\left|\mathcal{M}_L^\phi\right|^2 = 16\pi\alpha_D\epsilon^2 Z_L \frac{K^4(P_\phi^\mu\epsilon_{L\mu})^2}{(K^2 - m'^2)^2 + (m'\Gamma_{A'})^2}\,, \tag{4.30}$$

with the width $\Gamma_{A'}$ given in Eq. (4.20) and the same notation for other parameters as in Sec. 4.3.2.

Dark matter with an electric or magnetic dipole moment

Next we look at fermion dark matter with an electric or magnetic dipole moment. We find for the squared amplitudes of the plasmon decay for dark matter with an electric dipole moment

$$\left|\mathcal{M}_T^{\rm EDM}\right|^2 = 4Z_T K^2 d_\chi^2 p_\chi^2\sin^2\theta\,, \tag{4.31}$$

$$\left|\mathcal{M}_L^{\rm EDM}\right|^2 = 8Z_L d_\chi^2\left(E_\chi k - p_\chi\omega_L\cos\theta\right)^2\,, \tag{4.32}$$

while for dark matter with a magnetic dipole moment, we find

$$\left|\mathcal{M}_T^{\rm MDM}\right|^2 = 4Z_T K^2\mu_\chi^2\left[p_\chi^2\sin^2\theta + 2m_\chi^2\right]\,, \tag{4.33}$$

$$\left|\mathcal{M}_L^{\rm MDM}\right|^2 = 8Z_L\mu_\chi^2\left[\left(E_\chi k - p_\chi\omega_L\cos\theta\right)^2 + K^2 m_\chi^2\right]\,. \tag{4.34}$$

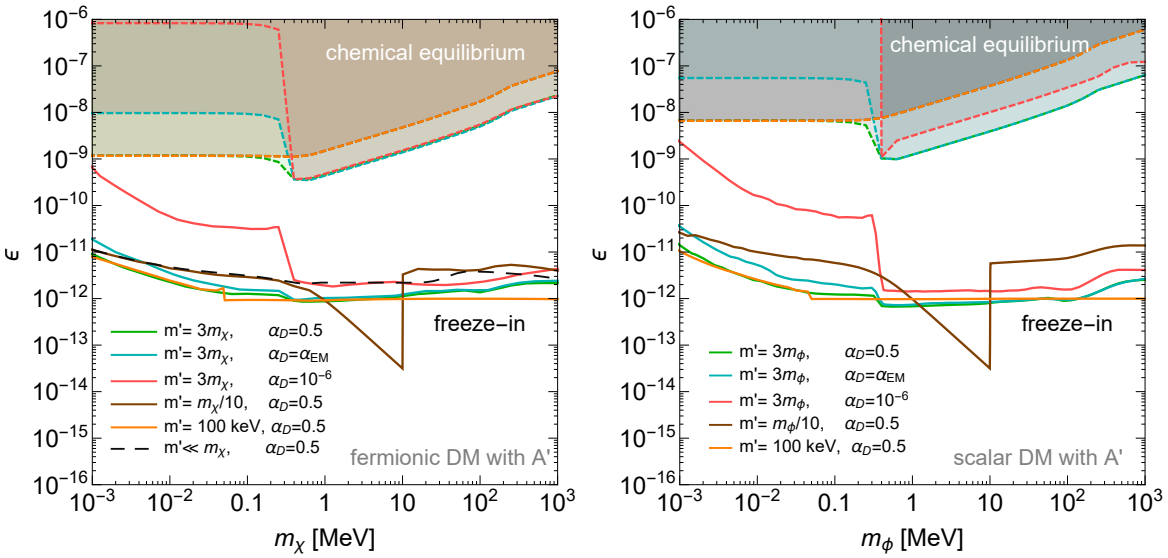

Figure 4.2: Solid lines show the values of ϵ for which the correct dark matter relic abundance is obtained in a model with fermionic (left) and scalar (right) dark matter from freeze-in through a dark photon. We show various choices for the dark-matter-to-dark-photon mass ratio and dark-photon couplings α_D. For $m' < 2m_{\chi/\phi}$ and $m' < 2m_e$, the dark photon can make up the relic abundance, rather than the fermion χ or scalar ϕ (see text for details). For parameters above these 'freeze-in lines', too much dark matter is produced in the early Universe. Above the dashed lines, the dark matter and SM sector are in chemical equilibrium. Below the chemical equilibrium lines the model is safe from constraints on the number of relativistic degrees of freedom in the early Universe.

Here, we used the notations as in Sec. 4.3.2.

4.3.3 Results

Dark photon + fermion dark matter

In Fig. 4.2 (left), we show the values of ϵ needed to obtain the correct relic abundance from freeze-in for the dark photon portal for a fermionic dark matter candidate. We consider six different scenarios. We see that the value of ϵ that yields the correct relic abundance through the freeze-in mechanism does not depend very strongly on the model parameters and mass ratios.

We first discuss the case for which the dark photon can decay to dark matter, and choose $m' = 3m_\chi$. We show lines corresponding to three different values of α_D, namely $\alpha_D = 0.5$, $\alpha_D = \alpha_{\rm EM} \simeq 1/137$, and $\alpha_D = 10^{-6}$. The latter value satisfies the self-interaction bound down to dark matter masses of ~28 keV, below which production via freeze-in is constrained from stellar cooling, see Sec. 4.4.

From the matrix element for the annihilation Eq. (4.17) or the plasmon decay Eq. (4.25), we see that far off the resonance, where the decay width is negligible, the production rate is proportional to $\alpha_D\epsilon^2$. In contrast, close to the resonance, the coupling α_D, which appears also in the decay width, divides out. In the early Universe, a range of temperatures is scanned, so the production always gets large contributions from the resonance at some point. It is for this reason that the scaling of ϵ between the different lines is less than a factor of $1/\sqrt{\alpha_D}$.

If the dark matter is heavier than electrons, it is mainly produced through the annihilation pro-

cess, which rapidly becomes inefficient when the temperature drops below the mass of a dark matter pair. The production from plasmon decays is subdominant, since the plasma frequency, which is the measure for the available phase space of the decay, is much lower than the temperature, $\omega_p \approx T/10$. So the plasmon process contributes less than the annihilation process, since the freeze-in production of dark-photon-mediated dark matter particles is infrared dominated and the plasmon decay process stops at larger temperatures than the annihilation process.

In contrast, for dark matter masses below the electron mass, the dominant contribution comes from plasmon decays. Again, thanks to the infrared domination, the main production happens at late times and stops when the production of dark matter is kinematically forbidden. If this occurs after electrons freeze out, the annihilation process does not contribute anymore. However, plasmon decays can still occur until the plasma frequency $\omega_p \approx T/10$ falls below twice the dark matter mass.

We also present two cases where the dark photon is (partly) lighter than twice the dark matter mass. In this case, the dark photons can make up the entire dark matter abundance for $m' < 2m_e$. This scenario is studied in [307], and we find that it does not receive significant corrections from the presence of heavier particles in the dark sector. However, we briefly discuss the composition of the dark relics in these scenarios. The small kink in the orange line ($m' = 100$ keV) in Fig. 4.2 marks the transition when the dark fermions become heavier than the dark photons. While the dark photons are efficiently produced in the early Universe for all dark fermion masses, they rapidly decay to the dark fermions for dark fermion masses below the kink. On the other hand, for dark fermion masses above the kink, the dark photons are very long-lived and constitute the dark relics. In the same figure, the brown line shows the case where the dark matter is always lighter than the dark photon ($m' = m_\chi/10$). At dark photon masses below ~100 keV, only a small number of dark photons is produced directly, such that their initial relic abundance is small. Thus, most of the dark relics that are frozen-in are dark fermions, which may then annihilate into dark photons. However, above roughly $m' \sim 100$ keV and below $m' = 2m_e$, the direct freeze-in production of dark photons becomes sizable compared to dark fermions, and they can constitute the dark relics. For $m' > 2m_e$, the dark photon is short-lived and decays rapidly into electron positron pairs. This causes the big kink in the brown line in Fig. 4.2.

Irrespective of the component that is most dominantly produced by the freeze-in mechanism (dark fermions or dark photons), processes like dark photon annihilation into dark fermions or vice versa could allow for a change in the relative abundance of the two species after freeze-in. This will only occur if the dark gauge coupling is large enough and the two species achieve chemical equilibrium in the dark sector. Although these transitions do not change the total energy in the dark sector, this has important implications for direct and indirect dark matter searches. We leave further investigation of this effect to future work.

Finally, we show the values of ϵ needed for the ultralight dark photon mediator case [280, 281, 308, 318]. We see that these values are similar to the other cases, especially (at low dark matter masses) the case with $m' = m_\chi/10$.

When ϵ is smaller than the values indicated by the solid curves in Fig. 4.2, the relic abundance of χ-particles and/or dark photons is less than the observed dark matter relic abundance, so that they form a subdominant dark matter component. Above the freeze-in line, too much dark matter would have been produced through freeze-in, and the Universe would be overclosed. We also show the lines indicating the coupling at which the dark matter would attain chemical equilibrium with the SM bath. This happens if the interaction rate $\Gamma = n_\chi^{\mathrm{eq}} \langle \sigma v \rangle$ for the annihilation process is at any time bigger than the Hubble rate $H = \frac{\pi \sqrt{g_{\mathrm{eff}}}}{\sqrt{90} M_{\mathrm{Pl}}} T^2$. For the interaction rate, the annihilation into electrons is the most relevant process, i.e., the one that gives the most stringent constraint, and the rate is given by

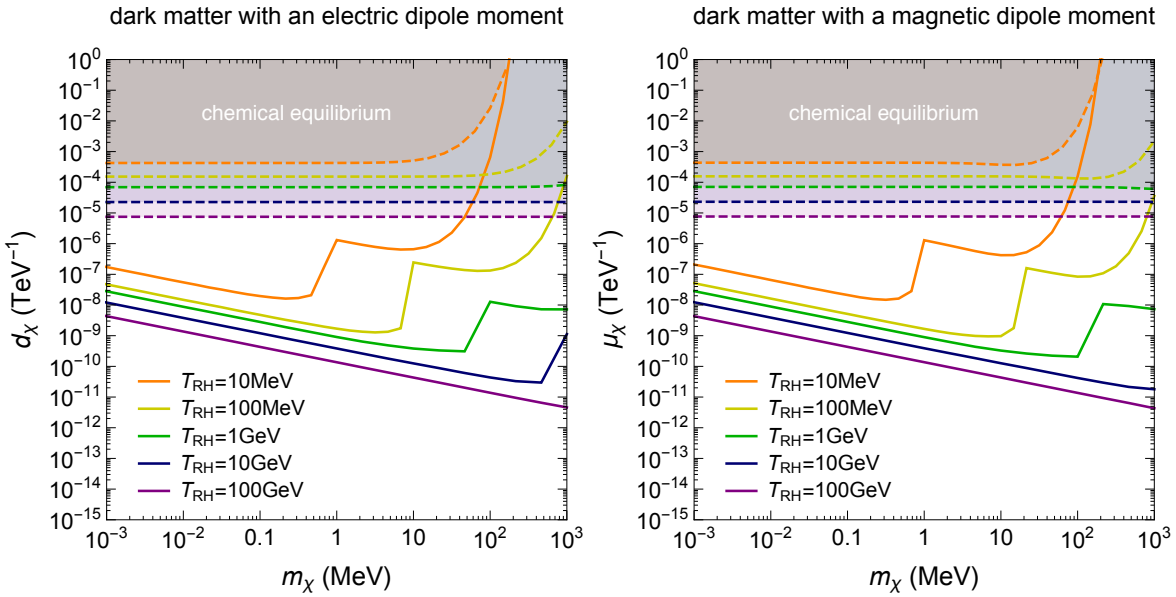

Figure 4.3: Solid lines in the left (right) plot show the values of the electric (magnetic) dipole moment needed to obtain the correct relic abundance from freeze-in for electric (magnetic) dipole dark matter for different reheating temperatures. For parameters above these 'freeze-in lines', too much dark matter is produced in the early Universe. Above the dashed lines, the dark matter and SM sector are in chemical equilibrium, so that this parameter region is not compatible with any form of freeze-in production. Below the chemical equilibrium lines the model is safe from constraints on the number of relativistic degrees of freedom in the early Universe.

Eq. (4.16) divided by the equilibrium number density [327]

$$n_i^{\rm eq} = \frac{g_i}{2\pi^2} m_i^2 T K_2\left(\frac{m_i}{T}\right) . \tag{4.35}$$

Here, g_i is the number of degrees of freedom of the particle species; for a Dirac fermion or a complex scalar, $g_i = 4$. Chemical equilibrium would of course spoil the freeze-in mechanism, and it is thus important to check that the freeze-in line does not get too close to the coupling that allows for chemical equilibration. In Fig. 4.2 (left), we see that for the dark photon portal dark matter this requirement is fulfilled.

Dark photon + scalar dark matter

The ϵ values needed to obtain the correct relic abundance from freeze-in for scalar dark matter coupled to a dark photon are shown with solid lines in Fig. 4.2 (right). We also show with dashed lines the ϵ values above which chemical equilibrium with the SM is reached. We find that the results for scalar dark matter look very similar to the fermion dark matter scenario. Thus, below we will usually consider only the latter case, but we emphasize that our results are approximately applicable to scalar dark matter as well.

Dark matter with an Electric or Magnetic Dipole Moment

The values of the electric (magnetic) dipole moment needed to obtain the correct relic abundance from freeze-in for electric (magnetic) dipole dark matter are shown for different reheating temperatures in the left (right) plot of Fig. 4.3. Above the lines, too much dark matter is produced in the early Universe, whereas below the lines the relic abundance is lower than the observed amount of dark matter. Towards larger values of m_χ, the production is dominated by the annihilation of SM particles. For reheating temperatures, T_{RH}, with $m_\chi \lesssim T_{\mathrm{RH}}/20$, the production from plasmon decay dominates, giving rise to the kink in the freeze-in lines at this mass scale. The position of the kink is caused by the fact that the plasma frequency, which is a good estimate for the available phase space in the plasmon decay, is roughly $T_{\mathrm{RH}}/10$ and the process starts at the reheating epoch (due to the high energy tail of the thermal distribution, the kink is near masses of $T_{\mathrm{RH}}/10$ rather than $T_{\mathrm{RH}}/20$).

Dark matter with mass above the reheating temperature cannot be produced efficiently in the early Universe and thus large values of the electric or magnetic dipole moments are needed. However, these values become so large for increasing dark matter masses that the freeze-in line intersects with the chemical equilibrium line, so that for even larger dark matter masses, the observed relic abundance cannot be obtained from freeze-in for any value of the dipole moment.

4.4 Stellar Constraints

For dark matter masses below ∼100 keV, the models under consideration can be constrained from stellar cooling arguments [66]. In some stages of stellar evolution the energy loss into a dark sector is severely constrained from astrophysical observations of globular clusters and the Sun. We will briefly review these arguments and then discuss the resulting limits.

4.4.1 Critical Stages of Stellar Evolution

A globular cluster is a star cluster with a particularly high density of stars. It is tightly gravitationally bound and has a spherical shape. Typically, it is a satellite of a galaxy and most likely it was formed within the star formation process of the parent galaxy. Low mass stars in globular clusters can be used to constrain particle physics properties by the stars' characteristic properties of helium ignition and burning.

To understand the origin of the constraints, it is useful to look at the Hertzsprung-Russel-diagram (HRD) of the globular cluster. Each single star is presented by a point in the plane spanned by the absolute brightness (in magnitudes) and the spectral classes. Note that the latter is correlated with the surface temperature, increasing from the right to the left. Within its lifetime, a star moves through the diagram, starting on the so-called 'main sequence', which is the diagonal from the lower right to the upper left corner. In this stage, it is burning hydrogen to helium in the core. Once the core is transformed into helium, the fusion process moves outwards, building a shell around the core. At this stage, the star becomes a red giant (RG), increasing its magnitude and moving to the red giant branch in the HRD. Depending on the mass of the star, it continues burning helium and eventually heavier elements in the horizontal branch or as a super giant. In its final stage, it becomes either a white dwarf, which is found in the lower left corner of the HRD (faint and hot), or a neutron star or black hole, which are not depicted, since they have no brightness.

Helium Ignition in Red Giants

For low mass stars ($0.5M_\odot \lesssim M \lesssim 2.3M_\odot$) helium ignition starts once the core has accumulated to roughly $0.5M_\odot$. At this stage of stellar evolution the star has reached the tip of the red giant branch. An extra source of cooling would delay helium ignition. The resulting heavier core would imply longer hydrogen burning in the shell and thus a brighter red giant. From the magnitude of the tip of the red giant branch one can thus constrain unknown elementary processes that would enhance the cooling of the star.

Simulations have shown that an extra energy loss of $\lesssim 10$ erg g^{-1}s^{-1} [66] is consistent with observations. The core density of the red giant is on average 2×10^5 g/cm^3 and varies only within a factor of order one. The electrons are degenerate. The temperature is 10^8 K and the electron concentration is $Y_e = 0.5$.

Lifetime on the Horizontal Branch

Once the star is burning helium, it moves to the so-called 'horizontal branch' (HB) in the HRD. The stars have a core mass of roughly $0.5M_\odot$. The stars on the HB differ only in the mass of their hydrogen shell, and hence they have different surface temperatures (or spectral classes) but a similar magnitude; this is why in the HRD they lie on a horizontal line. A globular cluster has hundreds of thousands of stars. This allows one to determine the lifetime of a star on the HB from the ratio of the number of stars on the HB to the number of stars on the red giant branch. It agrees with the prediction from the stellar standard models within 10%. However, an exotic contribution to cooling would result in a faster fuel consumption and has been constrained to be smaller than 10 erg g^{-1}s^{-1} [66]. The temperature and electron concentration are the same as for the red giants discussed in Sec. 4.4.1, but the density is slightly smaller, 0.6×10^4 g/cm^3. In this case, the electrons are not degenerate.

4.4.2 Solar Luminosity

Another constraint can be deduced directly from the minimal lifetime of the Sun. An extra efficient hydrogen burning mechanism would result in faster fuel consumption, reducing the Sun's overall lifetime. Observations of the Sun's age today suggest that the energy emitted via the dark sector should not exceed the 'normal' solar luminosity, $L_\odot = 3.84 \times 10^{33}$ erg/s. We take the temperature and density profile of the Sun from the model BS2005 [328]. The temperature in the core of the Sun reaches only $\sim 10^7$ K, which corresponds to roughly 1 keV.

4.4.3 Dark Matter Production Mechanisms In Stars

The energy-loss rate or luminosity per unit volume in stellar objects can be written as

$$\frac{\mathrm{d}L_\chi}{\mathrm{d}V} = \int \Pi_i \Pi_f E_{\mathrm{out}} |\mathcal{M}_{i\to f}|^2 (2\pi)^4 \delta^{(4)} \left(\Sigma P_i - \Sigma P_f\right). \tag{4.36}$$

Here, we use the same notation as in Eq. (4.11), and E_{out} is the energy sum of outgoing dark sector particles.

The electron-photon plasma inside stars gives rise to several production channels of light dark matter particles. The core temperature of the stellar objects discussed above reaches up to ~10 keV. In this energy regime, the dominant production channel for light dark matter particles is plasmon

decay. Additionally, for dark matter masses above the plasma frequency, where the plasmon decay is kinematically suppressed, the production via Compton-like processes is relevant. In principle, the production through bremsstrahlung could also be possible, but at these low temperatures it is always suppressed as it requires high-energy electrons, which are not very abundant at keV temperatures. In the following, we will discuss the plasmon decay and the Compton-like processes. The total luminosity will then be given by

$$\frac{\mathrm{d}L_\chi}{\mathrm{d}V} = \frac{\mathrm{d}L_\chi^{\mathrm{plasmon}}}{\mathrm{d}V} + \frac{\mathrm{d}L_\chi^{\mathrm{Compton}}}{\mathrm{d}V} \,. \tag{4.37}$$

We note that these processes for the dark matter models with an electric and a magnetic dipole moment have been calculated in detail recently in [316], which appeared during the last stages of completing our work.

Plasmon Decays

As discussed in Sec. 4.3.2, the continuous interaction of photons with the free electrons in the plasma gives rise to quasi-massive longitudinal and transverse modes of the photon. The dispersion relations in the plasma (see Eqs. (4.55) and (4.56) in App. 4.A), allow decays to massive particles like neutrinos or dark matter. An estimate of the maximum dark matter mass that can be produced from plasmon decays is given by the plasma frequency ω_p (see Eq. (4.53)), which reaches roughly 0.3 keV in the solar core, 1.6 keV in stars on the horizontal branch, and 8.6 keV in red giants before helium ignition.

For plasmon decays, Eq. (4.36) can be written as [315]

$$\frac{\mathrm{d}L_\chi^{\mathrm{plasmon}}}{\mathrm{d}V} = \int \frac{\mathrm{d}^3k}{(2\pi)^3}\left(\frac{2\omega_T\Gamma_T}{e^{\omega_T/T}-1} + \frac{\omega_L\Gamma_L}{e^{\omega_L/T}-1}\right) . \tag{4.38}$$

The form of this formula is simple to understand: the total energy carried away in the dark sector is given by the energy of the decaying plasmon $\omega_{T,L}$ and the rate with which it decays, $\Gamma_{T,L}$. The factor of two in the numerator accounts for the two transverse modes and the denominator comes from the Bose-Einstein-distribution that is obeyed by the photons in the star of temperature T. The plasmon decay rate to the dark sector is given by

$$\Gamma_{T,L} = \frac{1}{2\omega_{T,L}}\int \frac{\mathrm{d}^3p_{\mathrm{DM}}}{(2\pi)^3 2E_{\mathrm{DM}}}\frac{\mathrm{d}^3p_{\overline{\mathrm{DM}}}}{(2\pi)^3 2E_{\overline{\mathrm{DM}}}}(2\pi)^4\delta^4\left(K - P_{\mathrm{DM}} - P_{\overline{\mathrm{DM}}}\right)\left|\mathcal{M}_{T,L}\right|^2 \tag{4.39}$$

$$= \frac{1}{16\pi\omega_{T,L}}\int \mathrm{d}\cos\theta \frac{p_{\mathrm{DM}}^2}{E_{\mathrm{DM}}E_{\overline{\mathrm{DM}}}}\left(\frac{\mathrm{d}g(k,\theta)}{\mathrm{d}p_{\mathrm{DM}}}\right)^{-1}\left|\mathcal{M}_{T,L}\right|^2 \,, \tag{4.40}$$

where again θ is the angle between the incoming photon and outgoing dark matter, and $K_{T,L} = (\omega_{T,L},\vec{k})$ is the four-vector of the transverse or longitudinal plasmon, respectively.

Also, $E_{\overline{\mathrm{DM}}} = \sqrt{k^2 + m_{\mathrm{DM}}^2 + p_{\mathrm{DM}}^2 - 2kp_{\mathrm{DM}}\cos\theta}$, and p_{DM} is given by the solution of $g(k,\theta) = 0$ with

$$g(k,\theta) = \omega(k) - \sqrt{p_{\mathrm{DM}}^2 + m_{\mathrm{DM}}^2} - \sqrt{k^2 + p_{\mathrm{DM}}^2 - 2kp_{\mathrm{DM}}\sin\theta + m_{\mathrm{DM}}^2} \,. \tag{4.41}$$

The difference between the rate derived here compared to the freeze-in rate Eq. (4.23) is only the

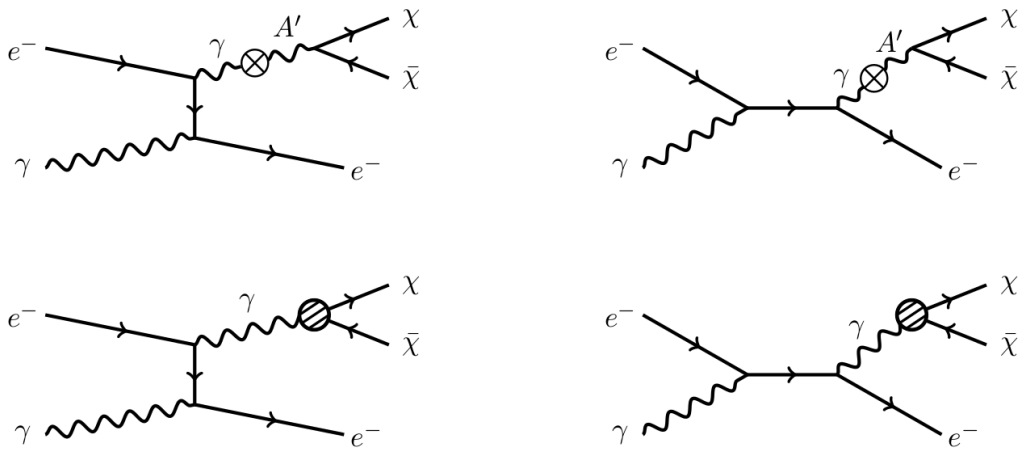

Figure 4.4: The diagrams contributing to the Compton-like process of producing dark matter in stars. An incoming photon scatters off an electron, and the outgoing photon can produce dark matter either through mixing with the dark photon (top two diagrams) or through the electric or magnetic dipole moment (bottom two diagrams).

factor of the energy $\omega_{T/L}$ in Eq. (4.38). To derive the stellar constraints, we are interested in the energy that is taken away from the star, i.e., the energy of the decaying plasmon. For the freeze-in production in the early Universe, the relevant quantity is the number of particles that go into the dark sector.

The only model-dependent quantity that enters into the computation is the matrix element in Eq. (4.39). These are given in Sec. 4.3.2 for the models discussed in this paper.

Compton-like processes

In a Compton-like process, a photon scatters off an electron, and the outgoing photon can produce a pair of dark matter particles, as depicted in Fig. 4.4. For these processes, we can ignore the thermal plasma effects because these processes are relevant only for dark matter masses above the plasma frequency.

Since we ignore thermal effects here, we can use Lorentz invariance for the amplitude and final-state phase space. The energy loss rate Eq. (4.36) from the Compton process is found to be

$$\frac{\mathrm{d}L_\chi^{\mathrm{Compton}}}{\mathrm{d}V} = \frac{1}{(2\pi)^8}\int \mathrm{d}\omega \mathrm{d}p_e \mathrm{d}\cos\theta\, f_\gamma f_e E_{\mathrm{out}} \frac{\omega p_e^2}{4E_e} \frac{1}{16\sqrt{\lambda(s,0,m_e^2)}} \int \frac{\mathrm{d}t_1 \mathrm{d}s_2 \mathrm{d}t_2 \mathrm{d}s_1}{\sqrt{-\Delta_4}} \sum |\mathcal{M}|^2 \ . \quad (4.42)$$

Here,

$$f_\gamma = \frac{2}{e^{\omega/T}-1},\ f_e = n_e\left(\frac{2\pi}{m_e T}\right)^{3/2} e^{-\frac{p_e^2}{2m_e T}},\ \ s = m_e^2 + 2\sqrt{m_e^2+p_e^2} - 2\omega p_e\cos\theta, \quad (4.43)$$

ω is the energy of the incoming photon, E_e (p_e) is the energy (momentum) of the incoming electron, θ is the angle between the incoming particles, and n_e is the number density of electrons. Also, we use the approximation $E_{\mathrm{out}} \sim \sqrt{s_2}$ to have Lorentz invariance; this assumption gives conservative results,

since $\sqrt{s_2}$ is always smaller than $E_2 + E_3$. The invariants s_1, s_2, t_1, t_2 are defined in App. 4.C, where we also give the definitions of $\lambda(x,y,z)$, the Gram determinant of the four independent four-vectors Δ_4, and more details on the derivation, which follows [329]. The matrix elements that enter Eq. (4.42) for the different cases are given in App. 4.C.

The stellar properties that enter the total energy loss rate, L_χ, are the temperature T and the total number of electrons. The latter is determined by the density ρ, the volume V, and the electron fraction Y_e. Since the core temperature, core mass, and the electron concentration of the red giant and horizontal branch stars are the same, the loss rates for the red giant and horizontal branch stars are also the same $L_{\rm HB}^{\rm Compton} = L_{\rm RG}^{\rm Compton}$. Moreover, since the constraint on the energy emission in both horizontal branch stars and red giants is the same, 10 erg $\rm g^{-1}s^{-1}$, the constraint on dark matter emission in the Compton-like regime is the same as well. For the Sun, the analysis is computationally more expensive, as a complex temperature dependence should be taken into account, resulting in an additional integration variable. Since the Sun has comparable mass to the globular cluster stars but a lower temperature, the loss rate due to Compton-like scattering is strictly weaker. Hence, in the solar constraints we present below, we include only the contribution from the plasmon decay, with the knowledge that the parameter space accessible with Compton-like scattering is already disfavored.

4.4.4 Results

The total dark luminosity is found by integrating Eq. (4.38) and Eq. (4.42) over the volume of the star and summing the two contributions. If the density and temperature profile is non-trivial, like in the solar case, all quantities depend on the radius, which has to be taken into account for the spatial integration. The constraint on ϵ is found by requiring that the dark luminosity does not exceed the limits discussed in Secs. 4.4.1 and 4.4.2.

In Fig. 4.5, we show the stellar constraints for the dark photon portal dark matter for $m' = 3m_\chi$ and for $\alpha_D = 0.5$ (solid lines) and $\alpha_D = 10^{-6}$ (dashed lines). The yellow, brown, and red contours show the constraints from the Sun (labeled 'SUN'), the lifetime on the horizontal branch ('HB'), and the non-delay of helium ignition in red giants ('RG'), respectively. The plasma frequency in red giant stars is the highest, hence it can probe the largest dark matter masses. When the plasma frequency equals the dark photon mass, the propagator in the cross section is on resonance. The production is enhanced at this parameter point, and the constraint is thus particularly strong. This is seen in the spike-like features in the stellar constraints. While we show the results for a dark matter fermion only, we again note that the bounds on scalar dark matter coupled to a dark photon will be very similar.

For the dark-photon-mediated dark matter, we compare in Fig. 4.5 the stellar constraints to the freeze-in lines (in green), which are also shown in Fig. 4.2. We find that dark matter that is entirely produced from this mechanism is ruled out below ~35 keV for $\alpha_D = 0.5$, and below ~50 keV for $\alpha_D = 10^{-6}$. Note that the areas between the respective freeze-in and freeze-out lines (blue) are forbidden in this model, as an overabundance of dark matter would have been produced, overclosing the Universe. Additional decay modes (of the dark photon) beyond the ones assumed in the minimal model setup discussed here, or slight model variations, could open up some of this parameter region (see, e.g., [283–295]).

Note that we have not derived the constraints from the cooling of white dwarfs. In the high-mass regime where the Compton-like processes dominate, it is not competitive with the other stellar cooling constraints as the white dwarfs have a much lower temperature than red giant stars. However, due to the high density, they have a high plasma frequency of ~23 keV. Thus, a small fraction of the

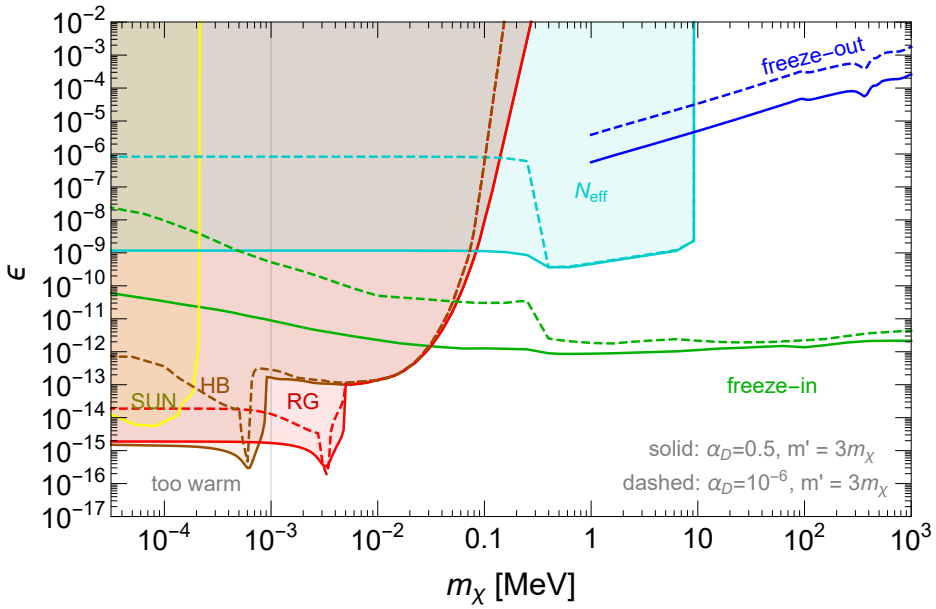

Figure 4.5: Stellar cooling constraints derived in this work on Dirac fermion dark matter interacting with a dark photon with dark photon masses $m' = 3m_\chi$ and $\alpha_D = 0.5$ ($\alpha_D = 10^{-6}$) for the solid (dashed) lines. The cooling constraints are derived for the Sun (yellow), stars on the horizontal branch (brown), and red giants (red). The constraint from the Sun includes only the production from the plasmon decay. In green, we show the parameters for which freeze-in production provides the entire dark matter relic abundance (see also Fig. 4.2); above the line too much dark matter would have been produced. In blue, we show the parameters for which thermal freeze-out production provides the entire dark matter relic abundance. Above the cyan lines, the dark sector was in chemical equilibrium with the SM bath and is constrained below $m_\chi = 9.4$ MeV by $N_{\rm eff}$. Below ~1 keV dark matter is constrained from structure formation. Other relevant constraints and some projections from terrestrial searches are shown in Fig. 4.7. The bounds on scalar dark matter coupling to a dark photon (not shown) are similar.

parameter space on the right-hand-side of the red giant tip can in principle be excluded additionally (see e.g. [311], where this was shown for dark photon dark matter).

The stellar constraints for dark matter with a dipole moment are shown in Fig. 4.6, together with the freeze-in lines. The left (right) plot shows the limits for dark matter with an electric (magnetic) dipole moment, respectively. The limits from the red giants are always stronger than the ones from the horizontal branch stars. The limit from the Sun is even weaker and not shown. No resonant production occurs due to the absence of a mediator in that mass range. We find that for dark matter with a dipole moment, the freeze-in lines are so low that they are barely constrained from stellar cooling arguments. We show also the freeze-out parameters from [301], as well as the LEP limit from [322].

The stellar constraints do not have upper boundaries, unlike the supernova 1987A constraints [66, 315]. Consider first the supernova 1987A constraint. In this case, the lower boundary of the constrained region is set by the requirement of producing a sufficient number of dark sector particles to carry away more energy than that carried away by neutrinos, which are believed to dominate the energy loss. This would drastically change the cooling of the proto-neutron star, in conflict with observations. The upper boundary of the constrained region arises from a sufficient number of dark sector

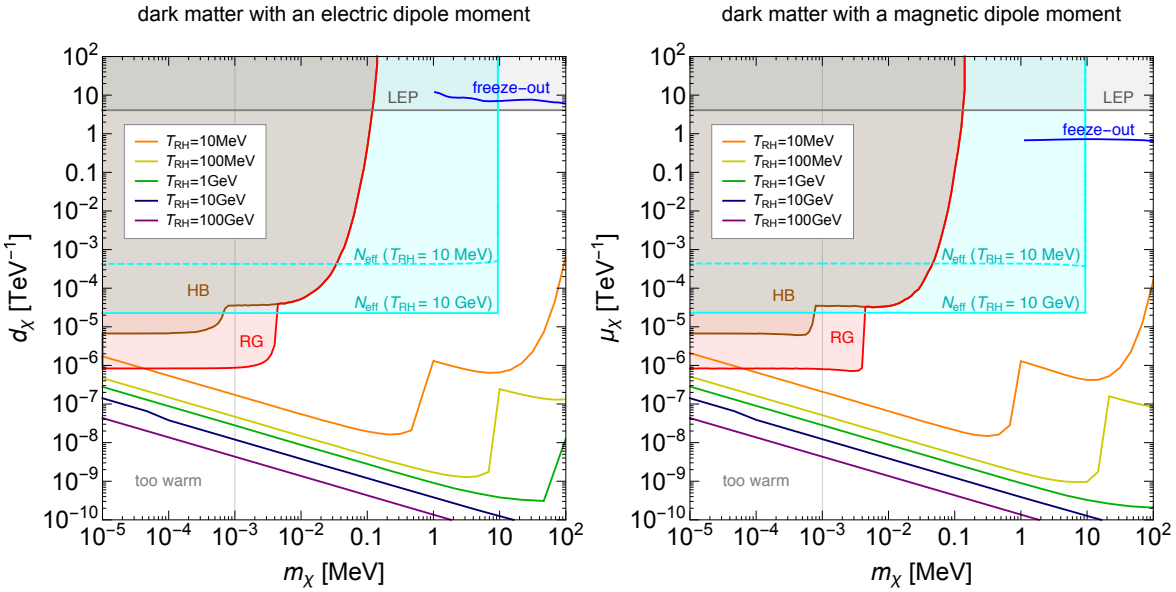

Figure 4.6: Stellar cooling constraints derived in this work on dark matter with an electric dipole moment (left) or a magnetic dipole moment (right), from stars on the horizontal branch (brown) and red giants (red). We also show lines for different reheating temperatures along which freeze-in production provides the entire dark matter relic abundance (see also Fig. 4.3); above the line too much dark matter would have been produced. Above the cyan lines, the dark sector was in chemical equilibrium with the SM bath and is constrained below $m_\chi = 9.4$ MeV by $N_{\rm eff}$. Below ~ 1 keV dark matter is constrained from structure formation. Above the gray line the models are constrained from LEP data. The blue curve shows the parameters needed to obtain the correct relic abundance from thermal freeze-out.

particles becoming trapped, thermalizing with the matter inside the proto-neutron star, and failing to carry away sufficient energy. Roughly speaking, if the dark sector particles couple more strongly than neutrinos to the matter inside the proto-neutron star (mostly protons, neutrons, and electrons), the dark sector particles are unable to carry away enough energy, and there is no constraint. This is why there is no supernova 1987A constraint up to arbitrarily high couplings. However, in the case of stellar cooling, the photon dominates the energy loss of the stars. Since it is impossible for the dark sector particles considered in this paper to have stronger couplings to photons than SM particles, the dark sector particles will always carry away more energy than the photon. Moreover, the criteria used for the stellar cooling bounds is that the dark sector particles must carry away *less* than a fraction of the energy carried away by photons. Thus, only if the dark sector particles interact more strongly than photons, would they fail to carry away sufficient energy. Therefore, there is no upper boundary for the stellar cooling constraints.

4.5 Potential Reach of Terrestrial Searches

The freeze-in dark matter models discussed in this paper are challenging to detect in the laboratory with direct-detection and accelerator-based experiments. This is not surprising, given the small required couplings. Nevertheless, we illustrate this challenge in Fig. 4.7 for a 'heavy' dark photon mediator with $m' = 3m_\chi$ and $\alpha_D = 0.5$ (unless otherwise indicated), and in Fig. 4.8 for dark matter

interacting with an electric or magnetic dipole moment. We parameterize as usual the reference dark-matter-electron scattering cross section, $\overline{\sigma}_e$, and form factor for the dark matter, $|F_{\rm DM}(q)|^2$, as [280, 318]

$$\overline{|\mathcal{M}_{\rm free}(\vec{q})|^2} \equiv \overline{|\mathcal{M}_{\rm free}(\alpha m_e)|^2} \times |F_{\rm DM}(q)|^2 \tag{4.44}$$

$$\overline{\sigma}_e \equiv \frac{\mu_{\chi e}^2 \overline{|\mathcal{M}_{\rm free}(\alpha m_e)|^2}}{16\pi m_\chi^2 m_e^2}, \tag{4.45}$$

where $\overline{|\mathcal{M}_{\rm free}|^2}$ is the absolute value squared of the elastic dark-matter-(free)-electron matrix element and q is the magnitude of the three-momentum lost by the dark matter when it scatters off the electron. For each of these models, we can derive $\bar{\sigma}_e$ to be

$$\overline{\sigma}_e^{A'} = \frac{16\pi\alpha\alpha_D\epsilon^2\mu_{\chi e}^2}{(\alpha^2 m_e^2 + m'^2)^2} \tag{4.46}$$

$$\overline{\sigma}_e^{\rm EDM} = \frac{4 d_\chi^2 \mu_{\chi e}^2}{\alpha m_e^2} \tag{4.47}$$

$$\overline{\sigma}_e^{\rm MDM} = \frac{\alpha\mu_\chi^2\mu_{\chi e}^2}{m_e^2 m_\chi}\left(m_\chi - 2m_e + \frac{4m_\chi^2 v_{\rm rel}^2}{\alpha^2}\right) \simeq \frac{5\alpha\mu_\chi^2\mu_{\chi e}^2}{m_e^2} \quad (m_\chi \gg m_e, v_{\rm rel} \simeq \alpha)\,, \tag{4.48}$$

where $\mu_{\chi e}$ is the reduced mass between the electron and χ, and $v_{\rm rel}$ is the relative velocity between the incoming dark matter and the incoming electron.

A dark photon mediator can be classified as 'heavy' and give $F_{\rm DM} = 1$ once its mass is above the typical momentum transfer, $q_{\rm typ}$, which varies for different targets. For example, for direct-detection experiments with semiconductor or noble liquid targets, $q_{\rm typ} \equiv \mu_{\chi,e} v_{\rm rel} \simeq \alpha m_e$ [318]. So for dark photon masses above a few keV (which is enforced by the stellar constraints), we have $F_{\rm DM} = 1$. Dark matter interacting with an electric dipole moment has the form factor

$$F_{\rm DM} = \alpha m_e / q \qquad \text{(EDM)}\,. \tag{4.49}$$

The form factor for dark matter interacting with a magnetic dipole moment is more complicated,

$$F_{\rm DM}^2(q) \simeq \frac{1}{(5m_\chi - 2m_e)}\left((m_\chi - 2m_e) + \frac{4m_e^2 m_\chi v_{\rm rel}^2}{q^2}\right) \qquad \text{(MDM)}\,, \tag{4.50}$$

$$\simeq \frac{1}{5} + \frac{4\alpha^2 m_e^2}{5q^2} \qquad m_\chi \gg m_e, v_{\rm rel} \simeq \alpha\,, \tag{4.51}$$

which is a combination of $F_{\rm DM} = 1$ and $F_{\rm DM} = \alpha m_e/q$. In deriving this form factor, we find an explicit dependence on the relative velocity between the incoming dark matter and the incoming electron in the free $2 \to 2$ (dark-matter-electron to dark-matter-electron) scattering. A precise calculation of the crystal form factor defined in [318] would need to take this into account. However, here we approximate $v_{\rm rel} \simeq \alpha$ and calculate the direct-detection bounds and direct-detection projections using

$$\overline{\sigma}_e^{\rm MDM} \simeq 5\left(\sigma_{F_{\rm DM}=1}^{-1} + \frac{4\alpha^2 m_e^2}{q^2}\sigma_{F_{\rm DM}=\alpha m_e/q}^{-1}\right)^{-1}. \tag{4.52}$$

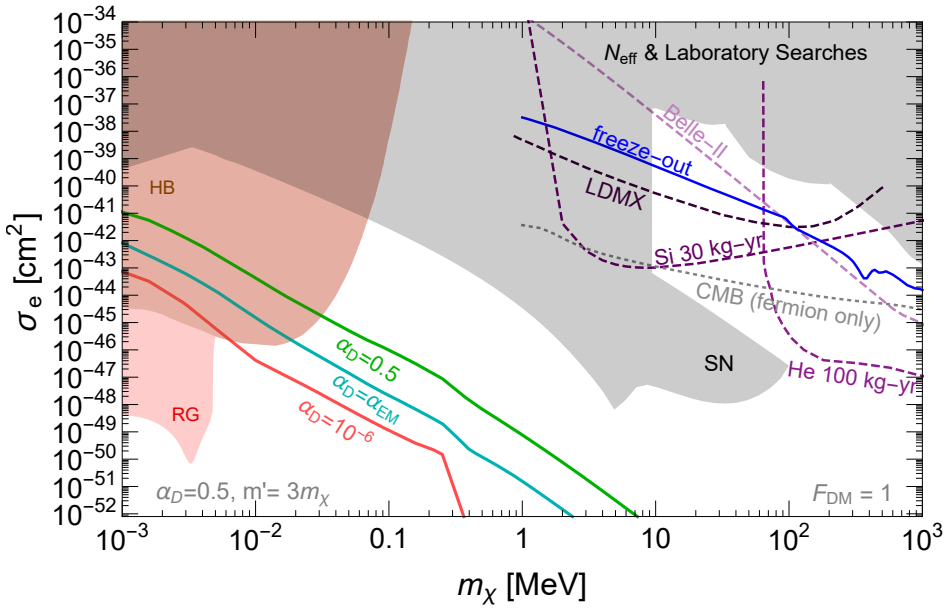

Figure 4.7: Solid lines in green, cyan, and red show the values of the dark-matter-electron-scattering cross section for which the correct dark matter relic abundance is obtained from freeze-in for Dirac fermion dark matter coupled to a dark photon, for various choices of the dark-photon couplings α_D (see Fig. 4.2). Red and brown-shaded regions show the stellar constraints from red giant and horizontal branch stars (see Fig. 4.5). Dashed lines show the potential reach of laboratory experiments. The gray shaded regions are excluded from the number of effective relativistic degrees of freedom (see Fig. 4.5), supernova 1987A, and existing laboratory constraints. The dotted line shows the CMB constraint, which excludes the freeze-out line (blue) when the dark matter particle is a Dirac fermion. Projections and constraints for dark matter that is a scalar particle are similar, except with a much weaker CMB bound. If not stated otherwise, the model parameters are $m' = 3m_\chi$ and $\alpha_D = 0.5$. See text for details.

Finally, to convert nuclear recoil cross section sensitivities to $\overline{\sigma}_e$, we follow [330].

We show in Fig. 4.7 and in Fig. 4.8 the sensitivity (when available in the literature) for a few future planned direct-detection and fixed-target experiments or proposals: a silicon detector with a 30-kg-year exposure and single-electron threshold (using, for example, Skipper-CCDs [318, 331]), a superfluid helium detector with a 1 kg-year exposure and 10 eV phonon energy threshold [332], an electron-beam fixed-target experiment searching for missing momentum (LDMX, from Fig. 5 in [333]), and an electron-positron collider searching for missing energy (Belle-II) [334] (the latter two do not have sensitivity to dipole moment dark matter in the range of parameters shown in the plot [304]). In Fig. 4.7, we also show in gray the bound from $N_{\rm eff}$ (also seen in Fig. 4.5) as well as current laboratory bounds from direct-detection and accelerator-based probes, including XENON10/100/1T, DarkSide-50, DAMIC-SNOLAB, SENSEI, SuperCDMS, E137, LSND, and BaBar [334–344]. In Fig. 4.8, we show in gray the bound from $N_{\rm eff}$ (also seen in Fig. 4.6) as well as the direct-detection bounds from [341, 344]. At low couplings, the limit reaching to ~100 MeV is from supernova 1987A (from [315] for the dark photon portal, and from [316] for dark matter coupled to an electric or magnetic dipole moment); we find that the couplings that are probed by the supernova bound lie between the freeze-in and the freeze-out line. The CMB (dotted gray line) sets a strong constraint for Dirac fermion dark matter, but is easily avoided, for example, for scalar dark matter [345, 346]. The

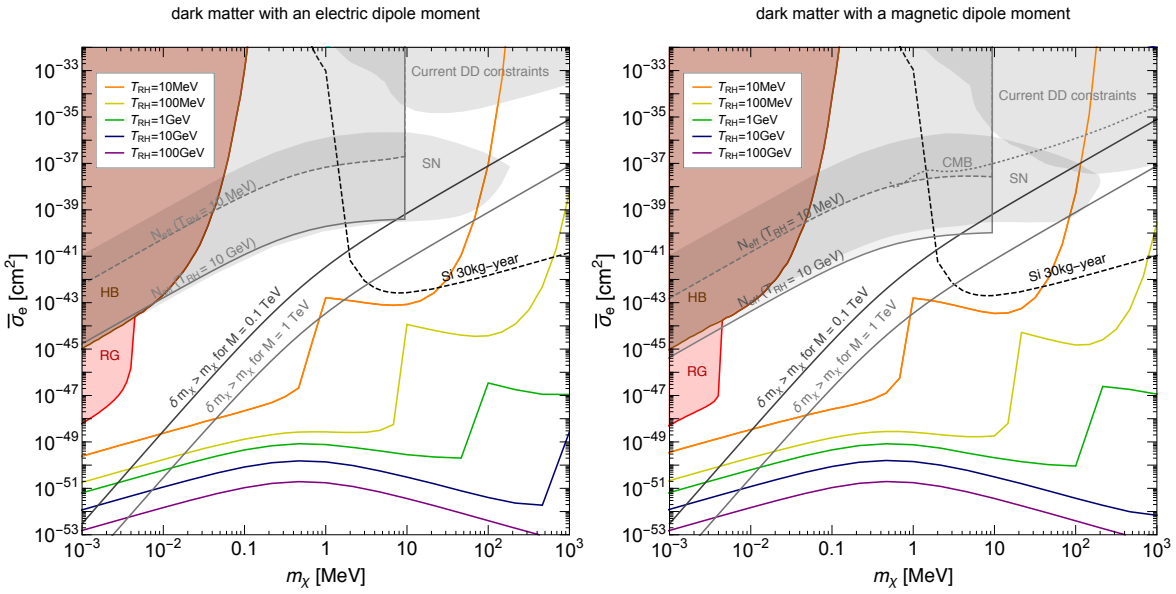

Figure 4.8: Solid colored lines show the values of the dark-matter-electron-scattering cross section for which the correct dark matter relic abundance is obtained from freeze-in for dark matter interacting with an electric (left) or magnetic (right) dipole moment, for various reheating temperatures (see Fig. 4.3). Red and brown-shaded regions show the stellar constraints from red giant and horizontal branch stars (see Fig. 4.6). The dashed line shows the potential reach of a direct-detection experiment using Skipper-CCDs for a 30 kg-year exposure. The gray shaded areas are excluded from the number of effective relativistic degrees of freedom (see Fig. 4.6), direct detection searches, and supernova 1987A. For the right plot, the region above the dotted line is excluded from the CMB. The freeze-in line for $T_{\rm RH} = 10$ MeV (orange) stops at the coupling where dark matter would thermalize with the SM sector. See text for details.

freeze-out line in Fig. 4.7 is almost independent of the dark photon mass as long as the dark photon mass is sufficiently far away from $2m_\chi$, so we just present the line for the benchmark case $m' = 3m_\chi$ and $\alpha_D = 0.5$ (although see [347]). We repeat the freeze-in lines from Figs. 4.2 and 4.3 as well as the stellar cooling and other bounds from Figs. 4.5 and 4.6. As expected, the freeze-in parameters are typically too small to be probed by laboratory searches in the near future. However, interestingly, we see that the freeze-in targets for dark matter interacting with an electric or magnetic dipole moment *can* be probed for low reheating temperatures with upcoming direct-detection experiments.

Since the dark matter models with an electric or magnetic dipole moment are dimension 5 operators, one can ask how these are UV completed. As discussed in Sec. 4.2, one simple possibility is to imagine charged scalars and fermions of a common mass M generating the dipole moment operators. In Fig. 4.8, we show the resulting upper bound on the cross section $\overline{\sigma}_e$ on this simple UV completion, derived from the upper bound on d_χ or μ_χ from Eq. (4.8): the black (gray) solid line corresponds to cross sections above which the corrections to the dark matter mass is larger than the tree-level dark matter mass for M at the scale of 100 GeV (1 TeV). Of course, different UV completions may allow for higher cross sections. We do not consider this further in this paper.

4.6 Conclusions

In this work, we discussed the freeze-in production of dark matter in the keV-to-GeV mass range as well as the constraints from stellar cooling. We considered two distinct scenarios: fermionic and bosonic dark matter that is coupled to the SM through kinetic mixing between the photon and a dark photon, as well as fermionic dark matter interacting with SM photons through an electric or magnetic dipole moment.

When the dark matter interactions with SM particles are small, the dark sector is not in thermal equilibrium with the SM in the early Universe, and dark matter production can occur through freeze-in from fermion-antifermion annihilation and from the decay of plasmons. The latter dominates for sub-MeV masses and pushes the couplings needed to obtain the observed relic abundance from freeze-in to very small values. For the dark photon portal models, the production in the early Universe is infrared dominated. In contrast, the dark matter models with a dipole moment are described by dimension-five operators, so that the freeze-in production occurs at all temperatures. Consequently, the freeze-in parameters depend on the reheating temperature. Moreover, the production from longitudinal plasmon modes becomes more important at higher reheating temperatures. We also checked that the dark matter does not thermalize with the SM thermal bath, such that the bounds from BBN and $N_{\rm eff}$, which usually constrain dark matter with masses in the sub-MeV-range, are avoided.

In addition to deriving the freeze-in production, we also calculated the stellar cooling constraints, and find that the strongest limits are from the non-delay of helium ignition at the red giant tip. This bound excludes freeze-in production of dark photon portal dark matter with masses below 35 keV (50 keV) for a dark gauge coupling of $\alpha_D = 0.5$ ($\alpha_D = 10^{-6}$). For dark matter with an electric or magnetic dipole moment, the production in the early Universe is so efficient that the freeze-in parameters lie below the stellar constraints, making these scenarios especially hard to probe.

Finally, we discussed the potential to probe these models in laboratory experiments. In the case of dark matter coupled via a dark photon, some part of the parameter space that can be probed by future experiments is already ruled out by the red giant constraint. Towards larger dark matter masses, the freeze-in lines are too low to be probed in the foreseeable future, but present potential targets for future, very ambitious, experiments. However, for dark matter with an electric or magnetic dipole moment, and for dark matter masses above the reheating temperature, the freeze-in production in the early Universe is suppressed; relatively large couplings are required to then obtain the correct relic abundance, so that these scenarios can be partially probed with upcoming direct-detection experiments.

4.A Properties Of Photons In A Thermal Plasma

In a plasma, electrons can move freely and thus affect the propagation of electromagnetic waves. They become a combination of coherent vibrations of not only the electromagnetic field, but also the electron density. Quantization leads to a spin-1 field with one longitudinal and two transverse polarization modes. We review the material needed to derive our results in this paper, following [306].

The effectively massive photon modes are caused by a modified dispersion relation for the photon in a plasma. For a photon in vacuum, the relation between its frequency ω and wave vector $\vec{k}$ is simply given by $\omega^2 = k^2$. For plasmons, this relation is subject to modifications depending on the electron density n_e and temperature T. The modified dispersion relations give rise to a non-zero phase-space $\omega^2 - k^2$ allowing for decays to massive particles. Note that in principle free protons and nuclei could

also contribute to the plasma effect. However, they are much heavier than the electrons and thus more inert, so their contribution turns out to be negligible.

A characteristic quantity of a plasma is its plasma frequency

$$\omega_p^2 = \frac{4\alpha}{\pi}\int_0^\infty \mathrm{d}p\frac{p^2}{E}\left(1-\frac{v^2}{3}\right)(n_e(E)+\bar{n}_e(E)) \ . \tag{4.53}$$

It is in general a function of the temperature T, as the electron (positron) density follows the Fermi distribution $n_{e/\bar{e}} = [e^{(E\mp\mu)/T}+1]^{-1}$ with the chemical potential μ. For the explicit computation it is helpful to replace $v = \frac{p}{E}$. Defining

$$\omega_1^2 = \frac{4\alpha}{\pi}\int_0^\infty \mathrm{d}p\frac{p^2}{E}\left(\frac{5}{3}v^2-v^4\right)(n_e(E)+\bar{n}_e(E)) \ , \tag{4.54}$$

allows the definition of the quantity $v_\star = \omega_1/\omega_p$, which intuitively is the typical electron velocity. With these ingredients, the general dispersion relations valid at all temperatures and densities up to first order in the electromagnetic fine structure constant α are given by [306]

$$\omega_T^2 = k^2+\omega_p^2\frac{3\omega_T^2}{2v_\star^2k^2}\left(1-\frac{\omega_T^2-v_\star^2k^2}{\omega_T^2}\frac{\omega_T}{2v_\star k}\ln\left(\frac{\omega_T+v_\star k}{\omega_T-v_\star k}\right)\right), \quad 0\le k<\infty \ , \tag{4.55}$$

$$\omega_L^2 = \omega_p^2\frac{3\omega_L^2}{v_\star^2k^2}\left(\frac{\omega_L}{2v_\star k}\ln\left(\frac{\omega_L+v_\star k}{\omega_L-v_\star k}\right)-1\right), \quad 0\le k<k_{\max} \ . \tag{4.56}$$

The transverse mode satisfies $\omega_T > k$ for all values of k. In contrast, the dispersion relation for the longitudinal mode can cross the light cone if k becomes larger than ω_L. This prevents the longitudinal plasmon from propagating and constrains the longitudinal wave vector to a maximal value

$$k_{\max} = \frac{4\alpha}{\pi}\int_0^\infty \mathrm{d}p\frac{p^2}{E}\left(\frac{1}{v}\ln\left(\frac{1+v}{1-v}\right)-1\right)(n_e(E)+\bar{n}_e(E)) \tag{4.57}$$

$$= \left[\frac{3}{v_\star^2}\left(\frac{1}{2v_\star}\ln\left(\frac{1+v_\star}{1-v_\star}\right)-1\right)\right]^{1/2}\omega_p \ . \tag{4.58}$$

The renormalization of the propagator determines the propagation of plasmons. However, when interactions are considered it is useful to change from the mass to the interaction basis. The coupling to the electromagnetic current then gets renormalized. With the conventions applied in this work, the renormalization factors are [306, 316]

$$Z_T(k) = \frac{2\omega_T^2(\omega_T^2-v_\star^2k^2)}{3\omega_p^2\omega_T^2+(\omega_T^2+k^2)(\omega_T^2-v_\star^2k^2)-2\omega_T^2(\omega_T^2-k^2)} \ , \tag{4.59}$$

$$Z_L(k) = \frac{2(\omega_L^2-v_\star^2k^2)}{3\omega_p^2-(\omega_L^2-v_\star^2k^2)}\frac{\omega_L^2}{\omega_L^2-k^2} \ , \tag{4.60}$$

such that the dressed polarization vectors are [316]

$$\tilde{\epsilon}_T^\mu = \sqrt{Z_T}\epsilon_T^\mu \ , \qquad \tilde{\epsilon}_L^\mu = \sqrt{Z_L}\epsilon_L^\mu \ . \tag{4.61}$$

We now want to discuss specific limits that are helpful for our numerical implementation of the calculations. In general, as $k \to 0$ the frequencies $\omega_{t/l}$ approach the plasma frequency. For large wave numbers $k \gg T$ and small electron density, the situation of the vacuum is restored, $\omega_T \to k$ and the longitudinal mode disappears.

In the **relativistic limit**, $T \gg m_e$ or $\mu \gg m_e$, Eqs. (4.55) and (4.56) simplify as $v_\star = 1$ and $k_{\max} \to \infty$. The plasma frequency reduces to

$$\omega^2_{p,\text{rel.}} = \frac{4\alpha}{3\pi}\left(\mu^2 + \frac{\pi^2 T^2}{3}\right) . \tag{4.62}$$

In the **degenerate limit**, $T \ll \mu - m_e$, the plasma frequency can be expressed in terms of the Fermi momentum p_F

$$\omega^2_{p,\text{deg.}} = \frac{4\alpha}{3\pi} p_F^2 v_F \; ; \quad p_F = \left(3\pi^2 n_e\right)^{1/3} . \tag{4.63}$$

In the dispersion relations, $v_\star$ can be replaced by the Fermi velocity $v_F = \frac{p_F}{E_F}$ with the Fermi energy $E_F = \sqrt{p_F^2 + m_e^2}$.

In the **classical limit**, the electrons are non-relativistic and non-degenerate, $T \ll m_e - \mu$. The plasma frequency is given by

$$\omega^2_{p,\text{cl.}} = \frac{4\pi\alpha n_e}{m_e}\left(1 - \frac{5}{2}\frac{T}{m_e}\right) , \tag{4.64}$$

and the dispersion relations reduce to

$$\omega_T^2 = k^2 + \omega_p^2\left(1 + \frac{k^2}{\omega_T^2}\frac{T}{m_e}\right) , \quad 0 \le k < \infty \tag{4.65}$$

$$\omega_L^2 = \omega_p^2\left(1 + 3\frac{k^2}{\omega_L^2}\frac{T}{m_e}\right) , \quad 0 \le k < \omega_p\sqrt{1 + 3T/m_e} . \tag{4.66}$$

Most contributions to the freeze-in for the dark photon portal comes from late stages of the thermal history of the early Universe. For dark matter masses below the electron mass, the classical limit is important as production occurs partly when the electrons are non-relativistic. At temperatures of tens of keV, the lepton asymmetry becomes important, such that the sum of the electron and positron number densities is given by

$$n_e^{\text{non-rel.}} = 4\left(\frac{m_e T}{2\pi}\right)^{3/2} \exp\left(-\frac{m_e}{T}\right) + \eta_B n_\gamma . \tag{4.67}$$

In the last term, $\eta_B \approx 6 \times 10^{-10}$ is the baryon to photon ratio and $n_\gamma = 2\zeta_3 T^3/\pi^2$ is the photon number density with the Riemann zeta function value $\zeta_3 \approx 1.2$. Since the baryon number density seems to coincide with the number density of electrons, the last term accounts for the asymmetry.

4.B Inclusion of $A' - Z$ Mixing In Freeze-In Calculations

The mixing term between the dark photon and the hypercharge gauge boson in the Lagrangian reads

$$\mathcal{L} \supset -\frac{\epsilon}{2\cos\theta_W} F'_{\mu\nu} B^{\mu\nu} \,. \tag{4.68}$$

After the electroweak symmetry breaking, this term can be written with gauge boson mass eigenstates,

$$\mathcal{L} \supset -\frac{\epsilon}{2} F'_{\mu\nu} F^{\mu\nu} - \frac{\epsilon \tan\theta_W}{2} F'_{\mu\nu} Z^{\mu\nu} \,, \tag{4.69}$$

where $Z_{\mu\nu}$ is the field strength of the Z boson. The second term is negligible at low energies, but can be relevant for energies larger than the GeV scale. In this work, we mainly focus on the sub-GeV scale, so the contribution from Z-mixing is less than $O(10\%)$. However, we include the contribution from Z-mixing in our calculations, and briefly summarize the relevant formulae in this appendix. For the Z-mixing contribution, we ignore plasma effects because the effects do not open a new production channel, and the correction is not significant. Also, we do not include Z-mixing for the stellar bounds, as the temperature of the stellar objects are very small compared to the Z-boson mass.

4.B.1 Z-Boson Decay

The last term in Eq. (4.14) describes the contribution from the Z-boson decay to a dark matter pair, which dominates for 10 GeV $\lesssim m_{\rm DM} < m_Z/2$. The term for the case of fermionic dark matter χ can be written as

$$n_Z \langle\Gamma\rangle_{Z\to\chi\bar{\chi}} = \frac{g_Z m_Z^2 T}{2\pi^2} \Gamma_{Z\to\chi\bar{\chi}} K_1\left(\frac{m_Z}{T}\right) \,, \tag{4.70}$$

where $g_Z = 3$ is the degrees of freedom of the Z boson, and

$$\Gamma_{Z\to\chi\bar{\chi}} = \frac{1}{3}\alpha_D \epsilon^2 \tan^2\theta_W m_Z \left(1 + 2\frac{m_\chi^2}{m_Z^2}\right)\sqrt{1 - 4\frac{m_\chi^2}{m_Z^2}} \,. \tag{4.71}$$

4.B.2 Annihilation through the Z boson

In Eq. (4.17), we only show the amplitude for production through the photon. Here, we show the full amplitude with the Z-boson in the CM frame:

$$\begin{aligned}
\int d\Omega\, |\mathcal{M}|^2 =& \frac{16\pi}{3} \frac{(\epsilon e q_f g_D)^2 (s + 2m_f^2)(s + 2m_\chi^2)}{(s - m'^2)^2 + m'^2\Gamma_{A'}^2} \\
&+ \frac{4\pi}{3} \frac{(\epsilon \tan\theta_W g_Z g_D)^2 s^2 (s + 2m_\chi^2)\left[\left(C_V^f\right)^2\left(s + 2m_f^2\right) + \left(C_A^f\right)^2\left(s - 4m_f^2\right)\right]}{\left((s - m'^2)^2 + m'^2\Gamma_{A'}^2\right)\left((s - m_Z^2)^2 + m_Z^2\Gamma_Z^2\right)} \\
&+ \frac{16\pi}{3} \frac{(\epsilon^2 \tan\theta_W e q_f g_Z C_V^f g_D^2) s (s + 2m_\chi^2)(s + 2m_f^2)(s - m_Z^2)}{\left((s - m'^2)^2 + m'^2\Gamma_{A'}^2\right)\left((s - m_Z^2)^2 + m_Z^2\Gamma_Z^2\right)} \,,
\end{aligned} \tag{4.72}$$

where θ_W is the weak mixing angle, $g_Z = \frac{e}{\cos\theta_W \sin\theta_W}$, $C_V^f = T_{3,f} - 2q_f \sin^2\theta$, $C_A^f = T_{3,f}$, $\Gamma_Z \simeq 2.5$ GeV is the decay width of the Z-boson and $T_{3,f}$ is the weak isospin of the incoming fermion.

4.C Compton-like Processes

In the Compton-like process $a + b \to 1 + 2 + 3$ we have an incoming photon and electron, a and b, respectively, and an outgoing electron and dark matter pair, labeled 1, 2, and 3. For the evaluation of the phase space, which is derived following [329], it is useful to define the following invariants

$$s = (P_a + P_b)^2 = (P_1 + P_2 + P_3)^2 \tag{4.73}$$
$$s1 = (P_1 + P_2)^2 = (P_a + P_b - P_3)^2 \tag{4.74}$$
$$s2 = (P_2 + P_3)^2 = (P_a + P_b - P_1)^2 \tag{4.75}$$
$$t1 = (P_a - P_1)^2 = (P_2 + P_3 - P_b)^2 \tag{4.76}$$
$$t2 = (P_b - P_3)^2 = (P_1 + P_2 - P_a)^2 \,. \tag{4.77}$$

In terms of these variables the three body phase space reduces to

$$\int \frac{\mathrm{d}^3 p_1}{(2\pi)^3 2E_1} \frac{\mathrm{d}^3 p_2}{(2\pi)^3 2E_2} \frac{\mathrm{d}^3 p_3}{(2\pi)^3 2E_3} (2\pi)^4 \delta^{(4)}(P_a + P_b - P_1 - P_2 - P_3) = \frac{1}{2^9 \pi^4} \frac{1}{\lambda^{1/2}(s, m_a^2, m_b^2)} \int \frac{\mathrm{d}t_1 \mathrm{d}s_2 \mathrm{d}t_2 \mathrm{d}s_1}{(-\Delta_4)^{1/2}} \,. \tag{4.78}$$

In this expression, $\lambda(x,y,z) = x^2 + y^2 + z^2 - 2xy - 2xz - 2yz$ and Δ_4 is the Gram determinant of any of the four independent four-vectors. In our case it can be expressed as

$$\Delta_4 = -\frac{1}{16} \begin{vmatrix} 0 & m_\chi^2 & s_2 & t_1 & m_e^2 & 1 \\ m_\chi^2 & 0 & m_\chi^2 & t_2 & s_1 & 1 \\ s_2 & m_\chi^2 & 0 & m_e^2 & s & 1 \\ t_1 & t_2 & m_e^2 & 0 & 0 & 1 \\ m_e^2 & s_1 & s & 0 & 0 & 1 \\ 1 & 1 & 1 & 1 & 1 & 0 \end{vmatrix} \,. \tag{4.79}$$

The boundary of the integrals is fixed by the requirement $\Delta_4 < 0$, restricting the phase space to the physically allowed region.

For the different models considered in this work, the squared matrix elements averaged over the initial states and summed over all final states are given by

$$\begin{aligned} \sum |\mathcal{M}|^2 = {} & \frac{e^4}{4(t_1 - m_e^2)^2} \mathrm{Tr}\left[(\not{P}_1 + m_e)\gamma^\mu(\not{P}_1 - \not{P}_a + m_e)\gamma^\nu(\not{P}_b + m_e)\gamma^\beta(\not{P}_1 - \not{P}_a + m_e)\gamma_\mu\right] X_{\nu\beta} \\ & + \frac{e^4}{4(s - m_e^2)^2} \mathrm{Tr}\left[(\not{P}_1 + m_e)\gamma^\nu(\not{P}_a + \not{P}_b + m_e)\gamma^\mu(\not{P}_b + m_e)\gamma_\mu(\not{P}_a + \not{P}_b + m_e)\gamma^\beta\right] X_{\nu\beta} \\ & + \frac{e^4}{2(t_1 - m_e^2)(s - m_e^2)} \mathrm{Tr}\left[(\not{P}_1 + m_e)\gamma^\mu(\not{P}_1 - \not{P}_a + m_e)\gamma^\nu(\not{P}_b + m_e)\gamma_\mu(\not{P}_a + \not{P}_b + m_e)\gamma^\beta\right] X_{\nu\beta} \end{aligned} \tag{4.80}$$

with X:

$$X_{\nu\beta} = \begin{cases} (\epsilon g_D)^2 \frac{-\eta_{\nu\rho}+K_\nu K_\rho/m'^2}{K^2-m'^2+m'\Gamma_{A'}} \frac{-\eta_{\beta\sigma}+K_\beta K_\sigma/m'^2}{K^2-m'^2+m'\Gamma_{A'}} \operatorname{Tr}\left[(\not{P}_2 + m_\chi)\gamma^\rho(\not{P}_3 - m_\chi)\gamma^\sigma\right] , & \text{dark photon + fermion} \\ (\epsilon g_D)^2 \frac{-\eta_{\nu\rho}+K_\nu K_\rho/m'^2}{K^2-m'^2+m'\Gamma_{A'}} \frac{-\eta_{\beta\sigma}+K_\beta K_\sigma/m'^2}{K^2-m'^2+m'\Gamma_{A'}} (P_2 - P_3)^\rho (P_2 - P_3)^\sigma , & \text{dark photon + scalar} \\ \frac{d_\chi^2}{K^4} \operatorname{Tr}\left[(\not{P}_2 + m_\chi)\gamma^5(\not{K}\gamma^\nu - K^\nu)(\not{P}_3 - m_\chi)(\gamma^\beta \not{K} - K^\beta)\gamma^5\right] , & \text{dark matter with EDM} \\ \frac{\mu_\chi^2}{K^4} \operatorname{Tr}\left[(\not{P}_2 + m_\chi)(\not{K}\gamma^\nu - K^\nu)(\not{P}_3 - m_\chi)(\gamma^\beta \not{K} - K^\beta)\right] , & \text{dark matter with MDM} \end{cases} \tag{4.81}$$

with $K = P_2 + P_3$ the four-vector of the intermediate (dark) photon. The traces can easily be evaluated using FeynCalc [348, 349] and expressed in terms of the invariant variables s, s_1, s_2, t_1, and t_2.

CHAPTER 5

Conclusion

In this work, we have studied different aspects of astrophysics and cosmology that are relevant for indirect and direct dark matter searches. To begin with, in Chap. 2, we investigated a claimed excess in the cosmic ray antiproton spectrum. Thereby, we focused on the systematic uncertainties that underlie cosmic ray propagation and the background determination. Cosmic ray anti-matter and other nuclei, that are not produced in stellar objects, come from secondary production due to cosmic ray nuclei scattering on interstellar matter. We described cosmic ray propagation within a two-zone diffusion model, and used secondary to primary ratios and positron data to narrow down the parameter space. A modification of the force-field method allowed us to describe charge-sign dependent effects of solar modulation that are relevant for the interpretation of low energy cosmic ray data. Another source of uncertainties are the secondary production cross sections that we have improved by bringing together data from various experiments. Still, nuclear cross sections are measured with precision only up to a few GeV, and so new experimental data are urgently required. In our final analysis, we have developed a method to take the uncertainties of the parameters as well as their correlations into account. This allowed us to robustly constrain even subdominant dark matter signals through their spectral properties. For a standard NFW dark matter profile, we are able to exclude thermal WIMPs that annihilate into bottom quarks upto masses of 570 GeV. While we confirmed a reported excess in the antiproton spectrum that is compatible with dark matter of mass around 80 GeV, its local (global) significance only reaches $2.2\,\sigma$ ($1.1\,\sigma$) in our analysis.

However, our analysis cannot capture one of the biggest systematic uncertainties of indirect dark matter searches: the question about the propagation model itself. Homogeneous diffusion models are a self-consistent framework that aim to fit the locally observed cosmic ray data into a simple global picture of galactic cosmic rays. These models consider cosmic ray transport on multi-kpc scales, covering the entire galactic cosmic ray halo which is taken to be in a time-independent steady-state. However, the local interstellar medium, on distance scales below $\sim$ 1 kpc, is not at all in steady-state equilibrium; rather it changes due to supernova shock waves and the formation and collision of clouds, on timescales ranging from 10^4 to 10^7 years. Global diffusion models assume that the relativistic cosmic rays form a stationary and near-homogeneous ambient density distribution that hangs in the background of the turbulent interstellar medium, without being affected by it. Still, these models seem to give suitable descriptions for stable cosmic ray nuclei. However, these particle species – that are used to calibrate the parameters of the model – are not sensitive to the propagation time scale. This is not the case for electrons and positrons: due to synchrotron radiation and Compton scattering, they loose energy – the longer they stay within the propagation region, the more the loss. The case is similar for radioactive cosmic nuclei; if the decay time is of the order of the propagation time, measurements can help to resolve the degeneracy. So far, the only available limit (from the measurement of Be/B) constrains the propagation time to roughly 10 Myr at a rigidity of $\mathcal{R} \sim 10$ GV [15]. Towards

higher energies, measurements are difficult since it is hard to find purely secondary radioactive cosmic nuclei with a suitable lifetime. In addition, the nuclear production cross sections are not measured with the required precision. Fortunately, the cosmic ray electron and positron spectra may actually carry important information about the particles' residence time in the galaxy.

In Chap. 3, we investigated the origin of the high energy $e^- + e^+$ spectrum, and found that different interpretations differ in the corresponding escape time at TeV energies. On the one hand, within typical homogeneous diffusion models, cosmic rays spend tens of Myr within the galactic halo, leaving and returning to the galactic disc multiple times. Accordingly, $e^\pm$ are strongly affected by energy losses, and thus there is a commonly expressed opinion in the literature that cosmic-ray e^+ come from a primary source which could be dark matter or pulsars. We have noted some new evidence to the contrary– namely, that e^+ are of purely secondary origin. We have shown that recent measurements of the total $e^- + e^+$ flux at $E \gtrsim 3$ TeV are in good agreement with the predicted flux of secondary $e^- + e^+$ that one would obtain if radiative energy losses during cosmic ray propagation do not play an important role. If the agreement is not accidental, then the requirement of small radiative losses implies a short propagation time for high energy cosmic rays: $t_{\rm esc} \lesssim 10^5$ yr at $\mathcal{R} \gtrsim 3$ TV. Such short propagation history suggests that recent, near-by source(s) dominate the cosmic rays at these energies. We checked this hypothesis with various astrophysical measurements, and found that short escape time together with the measured grammage implies that high energy secondary cosmic rays must originate from an overdense region with $\langle n_{\rm ISM} \rangle \approx (3.5 \pm 1.5)$ cm^{-3} at $\mathcal{R} = 3$ TV. To the contrary, it is observed that the next 50 to 100 pc around the solar system are occupied by the local bubble, which has a very low density. However, if, for example, the local bubble was formed through a supernova explosion in a molecular cloud, there may actually be sufficiently dense regions at its edge. Starlight extinction maps support this hypothesis, but further clarification is required. As a proof of concept, we have presented a leaky box and a diffusion model with rigidity dependent propagation volume that can describe these scenarios, i.e., the positrons from secondary origin together with the cosmic ray nuclei.

We conclude that the answer to the positron puzzle has important implications for the general understanding of cosmic rays. Either, the measured e^+ are secondary up to some TeV, and then all TeV cosmic rays are of recent and local origin. In this case, the indirect detection of dark matter signals is limited to $\gamma-$ray analyses since the charged cosmic rays that may be produced in the galactic halo from dark matter annihilation or decay would hardly reach our detectors. Or, high energy e^+ come from an extra primary source and cosmic rays may propagate in the galactic halo for a long time and long distances. In this case, signals from dark matter can potentially be explored and constrained. e^+ measurements up to a few TeV can help to clarify the picture: if the data keep following the upper bound discussed in Sec. 3.2 (see Fig. 3.1), it would support the secondary interpretation.

In the last part of this work, Chap. 4, we addressed the dark matter problem from a different perspective. We considered different dark matter models that have a feeble interaction with light. Firstly, we looked at a dark fermion or scalar coupled to the visible sector through a massive, kinetically mixed dark photon. We further considered the case where a dark matter fermion has an electric or magnetic dipole moment, where these effective operators can be induced through the couplings to some heavy, charged particles. For masses below a few MeV and couplings sufficiently large such that chemical equilibrium was attained at some point in the thermal history of the universe, these models are typically excluded by the number of relativistic degrees of freedom during big bang nucleosynthesis. However, for very small couplings, the dark matter can be produced out of equilibrium through standard model particles that decay or annihilate into the dark sector. This process is known

as the 'freeze-in' mechanism and allows for dark matter masses down to $\sim$ 1 keV. We have derived the parameters that reproduce the observed relic dark matter abundance. We have also computed constraints from the cooling of red giant stars, horizontal branch stars, and the Sun, carefully evaluating the thermal processes as well as the Compton scattering that dominates for masses above the plasma frequency. The strongest limits arise from the cooling argument for the red giant stars. They exclude the freeze-in scenario with the dark photon mediator below some tens of keV, depending on the value of the dark gauge coupling constant. For dark matter with an electric or magnetic dipole moment, the parameters needed for the freeze-in production are smaller than the ones constrained from stellar cooling losses. However, in this case, the freeze-in parameters for masses larger than the reheating temperature can potentially be probed by future direct detection experiments.

Overall, we have seen that the question about the nature of dark matter can be addressed from various perspectives. Future measurements of nuclear cross sections, precision measurements of the electron and positron spectrum at TeV energies, astronomical observations of photons over a broad range of frequencies, and upcoming direct detection experiments may illuminate the discussion.

Bibliography

[1] A. Cuoco, M. Krämer and M. Korsmeier.
"Novel dark matter constraints from antiprotons in the light of AMS-02". In: (2016).
arXiv: 1610.03071 [astro-ph.HE] (cit. on pp. 1, 11, 13, 14, 43, 46, 47).

[2] R. J. A. Lambourne, S. Serjeant and M. H. Jones, eds.
An Introduction to Galaxies and Cosmology. Cambridge University Press, 2015.
ISBN: 9781107492615.
URL: http://www.cambridge.org/academic/subjects/astronomy/astrophysics/introduction-galaxies-and-cosmology-1?format=PB&isbn=9781107492615
(cit. on p. 2).

[3] S. Gillessen et al. "An Update on Monitoring Stellar Orbits in the Galactic Center".
In: *The Astrophysical Journal* 837.1 (2017), p. 30. ISSN: 1538-4357.
DOI: 10.3847/1538-4357/aa5c41.
URL: http://dx.doi.org/10.3847/1538-4357/aa5c41 (cit. on p. 2).

[4] W. Reis and W. J. B. Corradi.
"Mapping the interface between the Local and Loop I bubbles using Stromgren photometry".
In: *Astron. Astrophys.* 486 (2008), p. 471. DOI: 10.1051/0004-6361:20077946.
arXiv: 0805.2542 [astro-ph] (cit. on pp. 2, 55).

[5] R. Lallement et al.
"3D maps of the local ISM from inversion of individual color excess measurements".
In: *Astron. Astrophys.* 561 (2014), A91. DOI: 10.1051/0004-6361/201322032.
arXiv: 1309.6100 [astro-ph.GA] (cit. on pp. 2, 55, 64).

[6] P. Frisch and V. V. Dwarkadas. "Effect of Supernovae on the Local Interstellar Material".
In: (2018). arXiv: 1801.06223 [astro-ph.SR] (cit. on pp. 2, 55, 57–59).

[7] J. P. Williams, L. Blitz and C. F. McKee.
"The structure and evolution of molecular clouds: from clumps to cores to the imf".
In: (1999). arXiv: astro-ph/9902246 [astro-ph] (cit. on p. 2).

[8] V. Ginzburg et al. "Astrophysics of cosmic rays". In: (1990). Ed. by V. Ginzburg
(cit. on pp. 3, 4, 6, 58).

[9] E. Fermi. "On the Origin of the Cosmic Radiation".
In: *Phys. Rev.* 75 (1949), pp. 1169–1174. DOI: 10.1103/PhysRev.75.1169 (cit. on p. 3).

[10] R. Diesing and D. Caprioli. "Spectrum of Electrons Accelerated in Supernova Remnants".
In: *Phys. Rev. Lett.* 123.7 (2019), p. 071101. DOI: 10.1103/PhysRevLett.123.071101.
arXiv: 1905.07414 [astro-ph.HE] (cit. on p. 3).

[11] W. R. Webber and T. L. Villa.
"A Comparison of the Galactic Cosmic Ray Electron and Proton Intensities From 1 MeV/nuc to 1 TeV/nuc Using Voyager and Higher Energy Magnetic Spectrometer Measurements Are There Differences in the Source Spectra of These Particles?" In: (2018). arXiv: 1806.02808 [physics.space-ph] (cit. on p. 3).

[12] A. U. Abeysekara et al. "Extended gamma-ray sources around pulsars constrain the origin of the positron flux at Earth". In: *Science* 358.6365 (2017), pp. 911–914. DOI: 10.1126/science.aan4880. arXiv: 1711.06223 [astro-ph.HE] (cit. on pp. 3, 41, 55, 56, 62).

[13] F. Aharonian et al. "Probing the "Sea" of Galactic Cosmic Rays with Fermi-LAT". In: (2018). arXiv: 1811.12118 [astro-ph.HE] (cit. on pp. 4, 57, 58).

[14] K. Blum.
"Cosmic ray propagation time scales: lessons from radioactive nuclei and positron data". In: *JCAP* 1111 (2011), p. 037. DOI: 10.1088/1475-7516/2011/11/037. arXiv: 1010.2836 [astro-ph.HE] (cit. on pp. 5, 53).

[15] K. Blum, R. Sato and E. Waxman. "Cosmic-ray Antimatter". In: (2017). arXiv: 1709.06507 [astro-ph.HE] (cit. on pp. 6, 41, 55, 61, 97).

[16] M. Wolleben. "A New Model For The Loop-I (The North Polar Spur) Region". In: *Astrophys. J.* 664 (2007), pp. 349–356. DOI: 10.1086/518711. arXiv: 0704.0276 [astro-ph] (cit. on pp. 6, 58).

[17] M. Ackermann et al.
"The Fermi Galactic Center GeV Excess and Implications for Dark Matter". In: *Astrophys. J.* 840.1 (2017), p. 43. DOI: 10.3847/1538-4357/aa6cab. arXiv: 1704.03910 [astro-ph.HE] (cit. on pp. 6, 49).

[18] A. Fraknoi and S. Wolff. *Astronomy (The Textbook)*. Oct. 2016. ISBN: 978-1-938168-28-4 (cit. on p. 6).

[19] M. e. a. Tanabashi. "Review of Particle Physics". In: *Phys. Rev. D* 98 (3 2018), p. 030001. DOI: 10.1103/PhysRevD.98.030001.
URL: https://link.aps.org/doi/10.1103/PhysRevD.98.030001 (cit. on pp. 7, 72).

[20] K. Garrett and G. Duda. "Dark Matter: A Primer". In: *Adv. Astron.* 2011 (2011), p. 968283. DOI: 10.1155/2011/968283. arXiv: 1006.2483 [hep-ph] (cit. on pp. 7, 10).

[21] J. de Swart, G. Bertone and J. van Dongen. "How Dark Matter Came to Matter". In: (2017). [Nature Astron.1,0059(2017)].
DOI: 10.1038/s41550017-0059,10.1038/s41550-017-0059.
arXiv: 1703.00013 [astro-ph.CO] (cit. on p. 7).

[22] J. C. Kapteyn.
"First Attempt at a Theory of the Arrangement and Motion of the Sidereal System". In: *Astrophys. J.* 55 (1922), pp. 302–328. DOI: 10.1086/142670 (cit. on p. 7).

[23] J. H. Oort. "The force exerted by the stellar system in the direction perpendicular to the galactic plane and some related problems".
In: *Bulletin of the A. Inst. of the Netherlands* 6 (1932), p. 249 (cit. on p. 7).

[24] M. S. Roberts and R. N. Whitehurst.
"The rotation curve and geometry of M31 at large galactocentric distances."
In: *Astrophys. J.* 201 (Oct. 1975), pp. 327–346. DOI: 10.1086/153889 (cit. on p. 7).

[25] F. Zwicky. "Die Rotverschiebung von extragalaktischen Nebeln".
In: *Helv. Phys. Acta* 6 (1933). [Gen. Rel. Grav.41,207(2009)], pp. 110–127.
DOI: 10.1007/s10714-008-0707-4 (cit. on p. 7).

[26] A. N. Taylor et al. "Gravitational Lens Magnification and the Mass of Abell 1689".
In: *Astrophys. J.* 501.2 (1998), pp. 539–553. DOI: 10.1086/305827.
arXiv: astro-ph/9801158 [astro-ph] (cit. on p. 8).

[27] X.-P. Wu et al.
"A comparison of different cluster mass estimates: consistency or discrepancy?"
In: *Monthly Notices of the Roy. Astron. Soc.* 301.3 (1998), pp. 861–871.
DOI: 10.1046/j.1365-8711.1998.02055.x. arXiv: astro-ph/9808179 [astro-ph]
(cit. on p. 8).

[28] P. Natarajan et al. "Mapping substructure in the HST Frontier Fields cluster lenses and in cosmological simulations". In: *Mon. Not. Roy. Astron. Soc.* 468.2 (2017), pp. 1962–1980.
DOI: 10.1093/mnras/stw3385. arXiv: 1702.04348 [astro-ph.GA] (cit. on p. 8).

[29] D. Clowe et al. "A direct empirical proof of the existence of dark matter".
In: *Astrophys. J.* 648 (2006), pp. L109–L113. DOI: 10.1086/508162.
arXiv: astro-ph/0608407 [astro-ph] (cit. on p. 8).

[30] A. A. Penzias and R. W. Wilson.
"A Measurement of excess antenna temperature at 4080-Mc/s".
In: *Astrophys. J.* 142 (1965), pp. 419–421. DOI: 10.1086/148307 (cit. on p. 8).

[31] G. F. Smoot et al.
"Structure in the COBE differential microwave radiometer first year maps".
In: *Astrophys. J.* 396 (1992), pp. L1–L5. DOI: 10.1086/186504 (cit. on p. 8).

[32] M. Milgrom. "A Modification of the Newtonian dynamics as a possible alternative to the hidden mass hypothesis". In: *Astrophys. J.* 270 (1983), pp. 365–370. DOI: 10.1086/161130
(cit. on p. 8).

[33] R. B. Tully and J. R. Fisher. "A New method of determining distances to galaxies".
In: *Astron. Astrophys.* 54 (1977), pp. 661–673 (cit. on p. 8).

[34] S. S. McGaugh et al. "The Baryonic Tully-Fisher relation".
In: *Astrophys. J.* 533 (2000), pp. L99–L102. DOI: 10.1086/312628.
arXiv: astro-ph/0003001 [astro-ph] (cit. on p. 8).

[35] B. Famaey and S. McGaugh. "Modified Newtonian Dynamics (MOND): Observational Phenomenology and Relativistic Extensions". In: *Living Rev. Rel.* 15 (2012), p. 10.
DOI: 10.12942/lrr-2012-10. arXiv: 1112.3960 [astro-ph.CO] (cit. on p. 8).

[36] S. McGaugh, F. Lelli and J. Schombert.
"Radial Acceleration Relation in Rotationally Supported Galaxies".
In: *Phys. Rev. Lett.* 117.20 (2016), p. 201101. DOI: 10.1103/PhysRevLett.117.201101.
arXiv: 1609.05917 [astro-ph.GA] (cit. on p. 8).

[37] A. Robertson, R. Massey and V. Eke.
"What does the Bullet Cluster tell us about self-interacting dark matter?"
In: *Mon. Not. Roy. Astron. Soc.* 465.1 (2017), pp. 569–587. DOI: 10.1093/mnras/stw2670.
arXiv: 1605.04307 [astro-ph.CO] (cit. on pp. 9, 70).

[38] S. Tremaine and J. E. Gunn. "Dynamical Role of Light Neutral Leptons in Cosmology".
In: *Phys. Rev. Lett.* 42 (1979). [,66(1979)], pp. 407–410.
DOI: 10.1103/PhysRevLett.42.407 (cit. on pp. 9, 70).

[39] A. Boyarsky, O. Ruchayskiy and D. Iakubovskyi.
"A Lower bound on the mass of Dark Matter particles". In: *JCAP* 0903 (2009), p. 005.
DOI: 10.1088/1475-7516/2009/03/005. arXiv: 0808.3902 [hep-ph] (cit. on pp. 9, 70).

[40] J. F. Navarro, C. S. Frenk and S. D. M. White. "The Structure of cold dark matter halos".
In: *Astrophys. J.* 462 (1996), pp. 563–575. DOI: 10.1086/177173.
arXiv: astro-ph/9508025 [astro-ph] (cit. on pp. 9, 33).

[41] M. Davis et al.
"The Evolution of Large Scale Structure in a Universe Dominated by Cold Dark Matter".
In: *Astrophys. J.* 292 (1985). [,105(1985)], pp. 371–394. DOI: 10.1086/163168
(cit. on p. 9).

[42] R. A. Alpher, J. W. Follin and R. C. Herman.
"Physical Conditions in the Initial Stages of the Expanding Universe".
In: *Phys. Rev.* 92 (1953), pp. 1347–1361. DOI: 10.1103/PhysRev.92.1347 (cit. on p. 9).

[43] M. Pospelov and J. Pradler. "Big Bang Nucleosynthesis as a Probe of New Physics".
In: *Ann. Rev. Nucl. Part. Sci.* 60 (2010), pp. 539–568.
DOI: 10.1146/annurev.nucl.012809.104521. arXiv: 1011.1054 [hep-ph]
(cit. on p. 9).

[44] N. Aghanim et al. "Planck 2018 results. VI. Cosmological parameters". In: (2018).
arXiv: 1807.06209 [astro-ph.CO] (cit. on p. 9).

[45] C. Alcock et al. "The MACHO project LMC microlensing results from the first two years and the nature of the galactic dark halo". In: *Astrophys. J.* 486 (1997), pp. 697–726.
DOI: 10.1086/304535. arXiv: astro-ph/9606165 [astro-ph] (cit. on p. 9).

[46] H. Niikura et al. "Microlensing constraints on primordial black holes with Subaru/HSC Andromeda observations". In: *Nat. Astron.* 3.6 (2019), pp. 524–534.
DOI: 10.1038/s41550-019-0723-1. arXiv: 1701.02151 [astro-ph.CO] (cit. on p. 10).

[47] J. Lesgourgues and S. Pastor. "Neutrino mass from Cosmology".
In: *Adv. High Energy Phys.* 2012 (2012), p. 608515. DOI: 10.1155/2012/608515.
arXiv: 1212.6154 [hep-ph] (cit. on p. 10).

[48] S. Dodelson and L. M. Widrow. "Sterile-neutrinos as dark matter".
In: *Phys. Rev. Lett.* 72 (1994), pp. 17–20. DOI: 10.1103/PhysRevLett.72.17.
arXiv: hep-ph/9303287 [hep-ph] (cit. on p. 10).

[49] G. Jungman, M. Kamionkowski and K. Griest. "Supersymmetric dark matter".
In: *Phys. Rept.* 267 (1996), pp. 195–373. DOI: 10.1016/0370-1573(95)00058-5.
arXiv: hep-ph/9506380 [hep-ph] (cit. on p. 10).

[50] D. J. E. Marsh. "Axion Cosmology". In: *Phys. Rept.* 643 (2016), pp. 1–79. DOI: 10.1016/j.physrep.2016.06.005. arXiv: 1510.07633 [astro-ph.CO] (cit. on p. 10).

[51] F. Wilczek. "Problem of Strong P and T Invariance in the Presence of Instantons". In: *Phys. Rev. Lett.* 40 (1978), pp. 279–282. DOI: 10.1103/PhysRevLett.40.279 (cit. on p. 10).

[52] S. Weinberg. "A New Light Boson?" In: *Phys. Rev. Lett.* 40 (1978), pp. 223–226. DOI: 10.1103/PhysRevLett.40.223 (cit. on p. 10).

[53] M. Dine, W. Fischler and M. Srednicki. "A Simple Solution to the Strong CP Problem with a Harmless Axion". In: *Phys. Lett.* 104B (1981), pp. 199–202. DOI: 10.1016/0370-2693(81)90590-6 (cit. on p. 10).

[54] J. Preskill, M. B. Wise and F. Wilczek. "Cosmology of the Invisible Axion". In: *Phys. Lett.* 120B (1983), pp. 127–132. DOI: 10.1016/0370-2693(83)90637-8 (cit. on p. 10).

[55] J. A. Frieman et al. "Cosmology with ultralight pseudo Nambu-Goldstone bosons". In: *Phys. Rev. Lett.* 75 (1995), pp. 2077–2080. DOI: 10.1103/PhysRevLett.75.2077. arXiv: astro-ph/9505060 [astro-ph] (cit. on p. 10).

[56] L. Hui et al. "Ultralight scalars as cosmological dark matter". In: *Phys. Rev.* D95.4 (2017), p. 043541. DOI: 10.1103/PhysRevD.95.043541. arXiv: 1610.08297 [astro-ph.CO] (cit. on p. 10).

[57] A. V. Kravtsov et al. "The Cores of dark matter dominated galaxies: Theory versus observations". In: *Astrophys. J.* 502 (1998), p. 48. DOI: 10.1086/305884. arXiv: astro-ph/9708176 [astro-ph] (cit. on p. 10).

[58] B. Holdom. "Two U(1)'s and Epsilon Charge Shifts". In: *Phys. Lett.* 166B (1986), pp. 196–198. DOI: 10.1016/0370-2693(86)91377-8 (cit. on pp. 10, 67, 68).

[59] P. Galison and A. Manohar. "TWO Z's OR NOT TWO Z's?" In: *Phys. Lett.* 136B (1984), pp. 279–283. DOI: 10.1016/0370-2693(84)91161-4 (cit. on pp. 10, 67).

[60] B. Patt and F. Wilczek. "Higgs-field portal into hidden sectors". In: (2006). arXiv: hep-ph/0605188 [hep-ph] (cit. on p. 10).

[61] S. Profumo, L. Giani and O. F. Piattella. "An Introduction to Particle Dark Matter". In: *Universe* 5.10 (2019), p. 213. DOI: 10.3390/universe5100213. arXiv: 1910.05610 [hep-ph] (cit. on p. 10).

[62] D. Hooper and L. Goodenough. "Dark Matter Annihilation in The Galactic Center As Seen by the Fermi Gamma Ray Space Telescope". In: *Phys. Lett.* B697 (2011), pp. 412–428. DOI: 10.1016/j.physletb.2011.02.029. arXiv: 1010.2752 [hep-ph] (cit. on p. 11).

[63] E. Carlson, T. Linden and S. Profumo.
"Improved Cosmic-Ray Injection Models and the Galactic Center Gamma-Ray Excess".
In: *Phys. Rev.* D94.6 (2016), p. 063504. DOI: 10.1103/PhysRevD.94.063504.
arXiv: 1603.06584 [astro-ph.HE] (cit. on p. 11).

[64] T. Braine et al.
"Extended Search for the Invisible Axion with the Axion Dark Matter Experiment".
In: (2019). arXiv: 1910.08638 [hep-ex] (cit. on p. 11).

[65] O. Moreno. "The Light Dark Matter eXperiment (LDMX)".
In: *PoS* ICHEP2018 (2019), p. 395. DOI: 10.22323/1.340.0395 (cit. on p. 11).

[66] G. G. Raffelt. *Stars as laboratories for fundamental physics*. 1996. ISBN: 9780226702728.
URL: http://wwwth.mpp.mpg.de/members/raffelt/mypapers/199613.pdf
(cit. on pp. 11, 68, 80, 81, 85).

[67] A. Reinert and M. W. Winkler.
"A Precision Search for WIMPs with Charged Cosmic Rays".
In: *JCAP* 1801.01 (2018), p. 055. DOI: 10.1088/1475-7516/2018/01/055.
arXiv: 1712.00002 [astro-ph.HE] (cit. on p. 13).

[68] O. Adriani et al.
"An anomalous positron abundance in cosmic rays with energies 1.5-100 GeV".
In: *Nature* 458 (2009), pp. 607–609. DOI: 10.1038/nature07942.
arXiv: 0810.4995 [astro-ph] (cit. on pp. 13, 41, 51).

[69] A. A. Abdo et al. "Constraints on Cosmological Dark Matter Annihilation from the Fermi-LAT Isotropic Diffuse Gamma-Ray Measurement". In: *JCAP* 1004 (2010), p. 014.
DOI: 10.1088/1475-7516/2010/04/014. arXiv: 1002.4415 [astro-ph.CO]
(cit. on pp. 13, 41).

[70] M. Ackermann et al. "Constraining Dark Matter Models from a Combined Analysis of Milky Way Satellites with the Fermi Large Area Telescope".
In: *Phys. Rev. Lett.* 107 (2011), p. 241302. DOI: 10.1103/PhysRevLett.107.241302.
arXiv: 1108.3546 [astro-ph.HE] (cit. on pp. 13, 41).

[71] S. Galli et al.
"CMB constraints on Dark Matter models with large annihilation cross-section".
In: *Phys. Rev.* D80 (2009), p. 023505. DOI: 10.1103/PhysRevD.80.023505.
arXiv: 0905.0003 [astro-ph.CO] (cit. on pp. 13, 41).

[72] T. R. Slatyer, N. Padmanabhan and D. P. Finkbeiner. "CMB Constraints on WIMP Annihilation: Energy Absorption During the Recombination Epoch".
In: *Phys. Rev.* D80 (2009), p. 043526. DOI: 10.1103/PhysRevD.80.043526.
arXiv: 0906.1197 [astro-ph.CO] (cit. on pp. 13, 41).

[73] G. Huetsi, A. Hektor and M. Raidal. "Constraints on leptonically annihilating Dark Matter from reionization and extragalactic gamma background".
In: *Astron. Astrophys.* 505 (2009), pp. 999–1005. DOI: 10.1051/0004-6361/200912760.
arXiv: 0906.4550 [astro-ph.CO] (cit. on pp. 13, 41).

[74] M. Boudaud et al. “The pinching method for Galactic cosmic ray positrons: implications in the light of precision measurements”. In: *Astron. Astrophys.* 605 (2017), A17. DOI: 10.1051/0004-6361/201630321. arXiv: 1612.03924 [astro-ph.HE] (cit. on pp. 13, 14, 16, 42).

[75] S. Ting. In: *AMS Days at CERN* (2015) (cit. on pp. 13, 38).

[76] R. Kappl, A. Reinert and M. W. Winkler. “AMS-02 Antiprotons Reloaded”. In: *JCAP* 1510.10 (2015), p. 034. DOI: 10.1088/1475-7516/2015/10/034. arXiv: 1506.04145 [astro-ph.HE] (cit. on p. 13).

[77] G. Giesen et al. “AMS-02 antiprotons, at last! Secondary astrophysical component and immediate implications for Dark Matter”. In: (2015). arXiv: 1504.04276 [astro-ph.HE] (cit. on p. 13).

[78] C. Evoli, D. Gaggero and D. Grasso. “Secondary antiprotons as a Galactic Dark Matter probe”. In: (2015). arXiv: 1504.05175 [astro-ph.HE] (cit. on p. 13).

[79] M. Kachelriess, I. V. Moskalenko and S. S. Ostapchenko. “New calculation of antiproton production by cosmic ray protons and nuclei”. In: *Astrophys.J.* 803.2 (2015), p. 54. DOI: 10.1088/0004-637X/803/2/54. arXiv: 1502.04158 [astro-ph.HE] (cit. on pp. 13, 38).

[80] M. W. Winkler. “Cosmic Ray Antiprotons at High Energies”. In: *JCAP* 1702.02 (2017), p. 048. DOI: 10.1088/1475-7516/2017/02/048. arXiv: 1701.04866 [hep-ph] (cit. on pp. 13, 14, 25–28, 30, 38).

[81] M. J. Boschini et al. “Solution of heliospheric propagation: unveiling the local interstellar spectra of cosmic ray species”. In: *Astrophys. J.* 840.2 (2017), p. 115. DOI: 10.3847/1538-4357/aa6e4f. arXiv: 1704.06337 [astro-ph.HE] (cit. on p. 13).

[82] M. Aguilar et al. “Electron and Positron Fluxes in Primary Cosmic Rays Measured with the Alpha Magnetic Spectrometer on the International Space Station”. In: *Phys. Rev. Lett.* 113 (2014), p. 121102. DOI: 10.1103/PhysRevLett.113.121102 (cit. on p. 13).

[83] M. Aguilar et al. “Precision Measurement of the Boron to Carbon Flux Ratio in Cosmic Rays from 1.9 GV to 2.6 TV with the Alpha Magnetic Spectrometer on the International Space Station”. In: *Phys. Rev. Lett.* 117.23 (2016), p. 231102. DOI: 10.1103/PhysRevLett.117.231102 (cit. on pp. 13, 14).

[84] M. Aguilar et al. “Antiproton Flux, Antiproton-to-Proton Flux Ratio, and Properties of Elementary Particle Fluxes in Primary Cosmic Rays Measured with the Alpha Magnetic Spectrometer on the International Space Station”. In: *Phys. Rev. Lett.* 117.9 (2016), p. 091103. DOI: 10.1103/PhysRevLett.117.091103 (cit. on pp. 13, 14, 19, 38).

[85] M.-Y. Cui et al. “A possible dark matter annihilation signal in the AMS-02 antiproton data”. In: (2016). arXiv: 1610.03840 [astro-ph.HE] (cit. on pp. 13, 14, 43, 46, 47).

[86] D. Maurin et al.
"Cosmic rays below z=30 in a diffusion model: new constraints on propagation parameters".
In: *Astrophys.J.* 555 (2001), pp. 585–596. DOI: 10.1086/321496.
arXiv: astro-ph/0101231 [astro-ph] (cit. on pp. 14–16, 42).

[87] F. Donato et al. "Anti-protons from spallations of cosmic rays on interstellar matter".
In: *Astrophys.J.* 563 (2001), pp. 172–184. DOI: 10.1086/323684.
arXiv: astro-ph/0103150 [astro-ph] (cit. on pp. 14–16).

[88] D. Maurin et al. "Galactic cosmic ray nuclei as a tool for astroparticle physics". In: (2002).
arXiv: astro-ph/0212111 [astro-ph] (cit. on pp. 14, 15, 32).

[89] O. Adriani et al. "Measurement of the flux of primary cosmic ray antiprotons with energies of 60-MeV to 350-GeV in the PAMELA experiment".
In: *JETP Lett.* 96 (2013), pp. 621–627. DOI: 10.1134/S002136401222002X
(cit. on pp. 14, 19, 38).

[90] I. V. Moskalenko and A. W. Strong.
"Production and propagation of cosmic ray positrons and electrons".
In: *Astrophys. J.* 493 (1998), pp. 694–707. DOI: 10.1086/305152.
arXiv: astro-ph/9710124 [astro-ph] (cit. on p. 14).

[91] A. Strong and I. Moskalenko. "Propagation of cosmic-ray nucleons in the galaxy".
In: *Astrophys.J.* 509 (1998), pp. 212–228. DOI: 10.1086/306470.
arXiv: astro-ph/9807150 [astro-ph] (cit. on pp. 14, 15).

[92] A. W. Strong and I. V. Moskalenko.
"New developments in the galprop cr propagation model".
In: *ICRC 2001, Proceedings* (2001), pp. 1942–1945.
arXiv: astro-ph/0106504 [astro-ph] (cit. on p. 14).

[93] C. Evoli et al.
"Cosmic-Ray Nuclei, Antiprotons and Gamma-rays in the Galaxy: a New Diffusion Model".
In: *JCAP* 0810 (2008), p. 018. DOI: 10.1088/1475-7516/2008/10/018.
arXiv: 0807.4730 [astro-ph] (cit. on p. 14).

[94] C. Evoli et al.
"Cosmic-ray propagation with DRAGON2: II. Nuclear interactions with the interstellar gas".
In: (2017). arXiv: 1711.09616 [astro-ph.HE] (cit. on p. 14).

[95] V. S. Ptuskin et al.
"Transport of relativistic nucleons in a galactic wind driven by cosmic rays".
In: *Astron. Astrophys.* 321 (1997), p. 434 (cit. on p. 15).

[96] T. Delahaye et al. "Galactic secondary positron flux at the Earth".
In: *Astron.Astrophys.* 501 (2009), pp. 821–833. DOI: 10.1051/0004-6361/200811130.
arXiv: 0809.5268 [astro-ph] (cit. on pp. 15, 16, 29).

[97] R. Tripathi, J. Wilson and F. Cucinotta.
"Medium modified nucleon nucleon cross-sections in a nucleus".
In: *Nucl.Instrum.Meth.* B152 (1999), pp. 425–431.
DOI: 10.1016/S0168-583X(99)00181-0 (cit. on p. 15).

[98] R. K. Tripathi, F. A. Cucinotta and J. W. Wilson.
"Accurate universal parameterization of absorption cross sections III – light systems".
In: *Nucl. Instrum. Meth.* B155 (1999), 349–356 (cit. on p. 15).

[99] R. Protheroe. "Cosmic Ray Anti-protons in the Closed Galaxy Model".
In: *Astrophys.J.* 251 (1981), pp. 387–392. DOI: 10.1086/159473 (cit. on p. 15).

[100] L. Tan and L. Ng. "Calculation Of The Equilibrium Anti-Proton Spectrum".
In: *J.Phys.* G9 (1983), pp. 227–242. DOI: 10.1088/0305-4616/9/2/015 (cit. on p. 15).

[101] R. Kappl and M. W. Winkler. "Dark Matter after BESS-Polar II".
In: *Phys.Rev.* D85 (2012), p. 123522. DOI: 10.1103/PhysRevD.85.123522.
arXiv: 1110.4376 [hep-ph] (cit. on p. 15).

[102] A. Putze, L. Derome and D. Maurin. "A Markov Chain Monte Carlo technique to sample transport and source parameters of Galactic cosmic rays: II. Results for the diffusion model combining B/C and radioactive nuclei". In: *Astron.Astrophys.* 516 (2010), A66.
DOI: 10.1051/0004-6361/201014010. arXiv: 1001.0551 [astro-ph.HE] (cit. on p. 16).

[103] A. Barrau et al. "Anti-protons from primordial black holes".
In: *Astron. Astrophys.* 388 (2002), p. 676. DOI: 10.1051/0004-6361:20020313.
arXiv: astro-ph/0112486 [astro-ph] (cit. on p. 16).

[104] F. Donato et al. "Antiprotons in cosmic rays from neutralino annihilation".
In: *Phys. Rev.* D69 (2004), p. 063501. DOI: 10.1103/PhysRevD.69.063501.
arXiv: astro-ph/0306207 [astro-ph] (cit. on p. 16).

[105] L. Gleeson and W. Axford. "Solar Modulation of Galactic Cosmic Rays".
In: *Astrophys.J.* 154 (1968), p. 1011. DOI: 10.1086/149822 (cit. on p. 17).

[106] J. Kota. "Drift - the Essential Process in Losing Energy".
In: *International Cosmic Ray Conference* 3 (1979), p. 13 (cit. on p. 17).

[107] J. R. Jokipii and B. Thomas. "Effects of drift on the transport of cosmic rays. IV - Modulation by a wavy interplanetary current sheet".
In: *Astrophys. J.* 243 (1981), pp. 1115–1122. DOI: 10.1086/158675 (cit. on p. 17).

[108] X. Sun et al.
"On Polar Magnetic Field Reversal and Surface Flux Transport During Solar Cycle 24".
In: *Astrophys. J.* 798 (2015), p. 114. DOI: 10.1088/0004-637X/798/2/114.
arXiv: 1410.8867 [astro-ph.SR] (cit. on p. 17).

[109] O. Adriani et al. "Time Dependence of the Electron and Positron Components of the Cosmic Radiation Measured by the PAMELA Experiment between July 2006 and December 2015".
In: *Phys. Rev. Lett.* 116.24 (2016), p. 241105. DOI: 10.1103/PhysRevLett.116.241105.
arXiv: 1606.08626 [astro-ph.HE] (cit. on pp. 17, 19).

[110] I. Cholis, D. Hooper and T. Linden.
"A Predictive Analytic Model for the Solar Modulation of Cosmic Rays".
In: *Phys. Rev.* D93.4 (2016), p. 043016. DOI: 10.1103/PhysRevD.93.043016.
arXiv: 1511.01507 [astro-ph.SR] (cit. on p. 17).

[111] E. E. Vos and M. S. Potgieter.
"New Modeling of Galactic Proton Modulation during the Minimum of Solar Cycle 23/24".
In: *Astrophys. J.* 815 (2015), p. 119. DOI: 10.1088/0004-637X/815/2/119 (cit. on p. 18).

[112] A. Ghelfi et al.
"Non-parametric determination of H and He interstellar fluxes from cosmic-ray data".
In: *Astron. Astrophys.* 591 (2016). [Erratum: Astron. Astrophys. 605 (2017)], A94.
DOI: 10.1051/0004-6361/201527852,10.1051/0004-6361/201527852e.
arXiv: 1511.08650 [astro-ph.HE] (cit. on p. 18).

[113] C. Corti et al. "Solar Modulation of the Local Interstellar Spectrum with Voyager 1, AMS-02, PAMELA, and BESS". In: *Astrophys. J.* 829.1 (2016), p. 8.
DOI: 10.3847/0004-637X/829/1/8. arXiv: 1511.08790 [astro-ph.HE] (cit. on p. 18).

[114] E. C. Stone et al. "Voyager 1 Observes Low-Energy Galactic Cosmic Rays in a Region Depleted of Heliospheric Ions". In: *Science* 341 (2013), pp. 150–153.
DOI: 10.1126/science.1236408 (cit. on p. 18).

[115] M. Aguilar.
"Precision Measurement of the Proton Flux in Primary Cosmic Rays from Rigidity 1 GV to 1.8 TV with the Alpha Magnetic Spectrometer on the International Space Station".
In: *Phys.Rev.Lett.* 114.17 (2015), p. 171103. DOI: 10.1103/PhysRevLett.114.171103 (cit. on pp. 18, 19, 29).

[116] M. J. Boschini et al. "Propagation of Cosmic Rays in Heliosphere: the HelMod Model".
In: (2017). arXiv: 1704.03733 [astro-ph.SR] (cit. on p. 18).

[117] O. Adriani et al. "Time dependence of the proton flux measured by PAMELA during the July 2006 - December 2009 solar minimum". In: *Astrophys. J.* 765 (2013), p. 91.
DOI: 10.1088/0004-637X/765/2/91. arXiv: 1301.4108 [astro-ph.HE] (cit. on p. 19).

[118] W. R. Webber et al. "Updated Formula for Calculating Partial Cross Sections for Nuclear Reactions of Nuclei with Z <= 28 and E > 150 MeV Nucleon^{-1} in Hydrogen Targets".
In: *Astrophys. J. Suppl. Series* 144 (2003), p. 153. DOI: 10.1086/344051
(cit. on pp. 19, 20, 24, 32).

[119] R. Silberberg and C. H. Tsao. "Partial Cross-Sections in High-Energy Nuclear Reactions, and Astrophysical Applications. I. Targets With z <= 28."
In: *Astrophys. J. Suppl.* 25 (1973), pp. 315–333. DOI: 10.1086/190271 (cit. on p. 20).

[120] R. Silberberg, C. Tsao and A. Barghouty.
"Updated Partial Cross Sections of Proton-Nucleus Reactions".
In: *Astrophys.J.* 501.2 (1998), pp. 911–919. DOI: 10.1086/305862 (cit. on p. 20).

[121] I. V. Moskalenko and S. G. Mashnik.
"Evaluation of production cross sections of Li, Be, B in CR".
In: *ICRC 2003, Proceedings* (2003), p. 1969. arXiv: astro-ph/0306367 [astro-ph]
(cit. on p. 20).

[122] S. M. Read and V. E. Viola. "Excitation functions for A >= 6 fragments formed in 1 H- and 4 He-induced reactions on light nuclei".
In: *Atom. Data Nucl. Data Tabl.* 31 (1984), pp. 359–397.
DOI: 10.1016/0092-640X(84)90009-3 (cit. on p. 20).

[123] Y. Génolini et al.
"Indications for a high-rigidity break in the cosmic-ray diffusion coefficient". In: (2017).
arXiv: 1706.09812 [astro-ph.HE] (cit. on pp. 21, 29, 34, 36).

[124] D. Bodansky, W. W. Jacobs and D. L. Oberg.
"On the production of lithium, beryllium, and boron at low energies".
In: *Astrophys. J.* 202 (1975), p. 222. DOI: 10.1086/153967 (cit. on pp. 21, 22).

[125] R. Bodemann et al.
"Production of residual nuclei by proton-induced reactions on C, N, O, Mg, AI and Si".
In: *Nucl. Instrum. Meth.B* 82 (1993), p. 9 (cit. on pp. 21, 22).

[126] C. Brechtmann, W. Heinrich and E. V. Benton.
"Fragmentation Cross-sections of ^{28}Si at 14.5-GeV/nucleon".
In: *Phys. Rev.* C39 (1989), pp. 2222–2226. DOI: 10.1103/PhysRevC.39.2222
(cit. on p. 22).

[127] C. N. Davids, H. Laumer and S. M. Austin. "Production of the Light Elements Lithium, Beryllium, and Boron by Proton Spallation of C12". In: *Phys. Rev.* C1 (1970), pp. 270–275. DOI: 10.1103/PhysRevC.1.270 (cit. on pp. 21, 22).

[128] M. Epherre et al.
"Comparison between the evaporation and the break-up models of nuclear de-excitation".
In: *Nucl. Phys.* A139 (1969), pp. 545–553. DOI: 10.1016/0375-9474(69)90278-4
(cit. on p. 22).

[129] P. Fontes. "B-10 and B-11 Production Cross-Sections in C-12 Spallation by Protons and alpha Particles: Application to Cosmic Ray Propagation".
In: *Phys. Rev.* C15 (1977), pp. 2159–2168. DOI: 10.1103/PhysRevC.15.2159
(cit. on pp. 22, 24).

[130] P. Fontes et al. "Production cross-sections of lithium and beryllium isotopes in c-12 by high-energy protons and alpha particles". In: *Nucl. Phys.* A165 (1971), pp. 405–414.
DOI: 10.1016/0375-9474(71)90769-X (cit. on p. 22).

[131] P. S. Goel. "Production Rate of 10-Be from Oxygen Spallation".
In: *Nature* 223 (1969), p. 1263 (cit. on p. 22).

[132] M. Jung et al. "Cross Sections of Li, Be, and B Emitted in 125-MeV p and 90-MeV alpha-Particle Interactions with C and N-Application to Nucleosynthesis".
In: *Phys. Rev.* C1 (1970), pp. 435–444. DOI: 10.1103/PhysRevC.1.435 (cit. on p. 22).

[133] A. Korejwo et al. "The measurement of isotopic cross-sections of C-12 beam fragmentation on liquid hydrogen at 3.66-GeV/nucleon". In: *J. Phys.* G26 (2000), pp. 1171–1186.
DOI: 10.1088/0954-3899/26/8/306 (cit. on pp. 22, 24).

[134] A. Korejwo et al. "Isotopic cross-sections of C-12 fragmentation on hydrogen measured at 1.87-GeV/nucleon and 2.69-GeV/nucleon". In: *J. Phys.* G28 (2002), pp. 1199–1208.
DOI: 10.1088/0954-3899/28/6/304 (cit. on pp. 22, 24).

[135] H. Laumer, S. M. Austin and L. M. Panggabean. "Production of the light elements lithium, beryllium, and boron by proton-induced spallation of O-16".
In: *Phys. Rev.* C10 (1974), pp. 1045–1049. DOI: 10.1103/PhysRevC.10.1045
(cit. on p. 22).

[136] H. Laumer et al. "Production of the Light Elements Lithium, Beryllium, and Boron by Proton-Induced Spallation of N-14". In: *Phys. Rev.* C8 (1973), pp. 483–491.
DOI: 10.1103/PhysRevC.8.483 (cit. on p. 22).

[137] P. J. Lindstrom et al. “Isotope Production Cross-Sections from the Fragmentation of O-16 and C-12 at Relativistic Energies”. In: *LBL-3650* (1975) (cit. on p. 22).

[138] R. A. Moyle et al.
“Nucleosynthesis of Li, Be, and B: contributions from the p+ O-16 reaction at 50-90 MeV”.
In: *Phys. Rev.* C19 (1979), pp. 631–640. DOI: 10.1103/PhysRevC.19.631 (cit. on p. 22).

[139] D. l. Olson et al. “FACTORIZATION OF FRAGMENT PRODUCTION CROSS-SECTIONS IN RELATIVISTIC HEAVY ION COLLISIONS”.
In: *Phys. Rev.* C28 (1983), pp. 1602–1613. DOI: 10.1103/PhysRevC.28.1602 (cit. on p. 22).

[140] G. M. Raisbeck and F. Yiou. “Cross sections for the spallation production of Be-10 in targets of N, Mg, and Si and their astrophysical applications”.
In: *Phys. Rev.* C9 (1974), pp. 1385–1395. DOI: 10.1103/PhysRevC.9.1385 (cit. on p. 22).

[141] G. M. Raisbeck and F. Yiou. “Cross section for b-11(p,2p)be-10 at 150 and 600 mev - implications for cosmic ray studies”. In: *Phys. Rev. Lett.* 27 (1971), pp. 875–877.
DOI: 10.1103/PhysRevLett.27.875 (cit. on p. 22).

[142] C. T. Roche et al. “Li, Be, and B production in reactions of 45-100 MeV protons with C:12 Astrophysical implications”. In: *Phys. Rev.* C14 (1976), pp. 410–418.
DOI: 10.1103/PhysRevC.14.410 (cit. on pp. 21, 22).

[143] T. Schiekel et al. “Nuclide production by proton-induced reactions on elements (6 <= Z <= 29) in the energy range from 200 MeV to 400 MeV”.
In: *Nucl. Instrum. Meth.B* 114 (1996), p. 91 (cit. on p. 22).

[144] W. R. Webber, J. C. Kish and D. A. Schrier. “Individual charge changing fragmentation cross-sections of relativistic nuclei in hydrogen, helium, and carbon targets”.
In: *Phys. Rev.* C41, 533 (1990), pp. 533–546. DOI: 10.1103/PhysRevC.41.533 (cit. on pp. 21, 22, 24, 25).

[145] W. R. Webber, J. C. Kish and D. A. Schrier. “Individual isotopic fragmentation cross-sections of relativistic nuclei in hydrogen, helium, and carbon targets”.
In: *Phys. Rev.* C41, 547 (1990), pp. 547–565. DOI: 10.1103/PhysRevC.41.547 (cit. on pp. 21, 22).

[146] W. R. Webber et al. “Production Cross Sections of Fragments from Beams of 400-650 MeV per Nucleon 9Be,11B,12C,14N,15N,16O,20Ne,22Ne,56Fe, and 58Ni Nuclei Interacting in a Liquid Hydrogen Target. II. Isotopic Cross Sections of Fragments”.
In: *Astrophys. J.* 508 (1998), p. 949 (cit. on p. 22).

[147] F. Yiou, C. Seide and R. Bernas. “Formation cross sections of lithium, beryllium, and boron isotopes produced by the spallation of oxygen by high-energy protons”.
In: *J. of Geophys. Research* 74 (1969), p. 2447 (cit. on p. 22).

[148] C. Zeitlin et al. “Fragmentation cross sections of Si-28 at beam energies from 290-A-MeV to 1200-A-MeV”. In: *Nucl. Phys.* A784 (2007), pp. 341–367.
DOI: 10.1016/j.nuclphysa.2006.10.088 (cit. on pp. 21, 22, 24).

[149] C. Zeitlin et al.
"Fragmentation of 14-N, 16-O, 20-Ne, and 24-Mg Nuclei at 290 to 1000 MeV/nucleon".
In: *Phys. Rev.* C83 (2011), p. 034909. DOI: 10.1103/PhysRevC.83.034909.
arXiv: 1102.2848 [nucl-ex] (cit. on pp. 21, 22).

[150] C. Zeitlin et al.
"Fragmentation cross-sections of 600-MeV/nucleon Ne-20 on elemental targets".
In: *Phys. Rev.* C64 (2001), p. 024902. DOI: 10.1103/PhysRevC.64.024902
(cit. on pp. 21, 22).

[151] R. Gupta and A. Kumar.
"Fragmentation cross-section of 600 A MeV Si-14+ ions in thick polyethylene target".
In: *Europ. Phys. J.* A49 (2013), p. 98. DOI: 10.1140/epja/i2013-13098-3 (cit. on p. 21).

[152] P. Ferrando et al. "Measurement of ^{12}C, ^{16}O, and ^{56}Fe Charge Changing Cross-sections in Helium at High-energy, Comparison With Cross-sections in Hydrogen, and Application to Cosmic Ray Propagation". In: *Phys.Rev.* C37 (1988), pp. 1490–1501.
DOI: 10.1103/PhysRevC.37.1490 (cit. on pp. 24, 25).

[153] R. Kappl and M. W. Winkler. "The Cosmic Ray Antiproton Background for AMS-02".
In: *JCAP* 1409 (2014), p. 051. DOI: 10.1088/1475-7516/2014/09/051.
arXiv: 1408.0299 [hep-ph] (cit. on pp. 25, 26, 28).

[154] L. Tan and L. Ng. "Parametrization Of Anti-p Invariant Cross-Section In P P Collisions Using A New Scaling Variable". In: *Phys.Rev.* D26 (1982), pp. 1179–1182.
DOI: 10.1103/PhysRevD.26.1179 (cit. on pp. 26, 27).

[155] M. di Mauro et al.
"New evaluation of the antiproton production cross section for cosmic ray studies".
In: *Phys.Rev.* D90.8 (2014), p. 085017. DOI: 10.1103/PhysRevD.90.085017.
arXiv: 1408.0288 [hep-ph] (cit. on pp. 26, 27).

[156] M. Antinucci et al. "Multiplicities of charged particles up to ISR energies".
In: *Lett.Nuovo Cim.* 6 (1973), pp. 121–128. DOI: 10.1007/BF02827250 (cit. on p. 27).

[157] B. I. Abelev et al. "Systematic Measurements of Identified Particle Spectra in pp, d^+ Au and Au+Au Collisions from STAR". In: *Phys. Rev.* C79 (2009), p. 034909.
DOI: 10.1103/PhysRevC.79.034909. arXiv: 0808.2041 [nucl-ex] (cit. on p. 27).

[158] T. Anticic et al. "Inclusive production of protons, anti-protons and neutrons in p+p collisions at 158-GeV/c beam momentum". In: *Eur.Phys.J.* C65 (2010), pp. 9–63.
DOI: 10.1140/epjc/s10052-009-1172-2. arXiv: 0904.2708 [hep-ex] (cit. on p. 27).

[159] A. Adare et al.
"Identified charged hadron production in $p + p$ collisions at $\sqrt{s} = 200$ and 62.4 GeV".
In: *Phys. Rev.* C83 (2011), p. 064903. DOI: 10.1103/PhysRevC.83.064903.
arXiv: 1102.0753 [nucl-ex] (cit. on p. 27).

[160] K. Aamodt et al. "Production of pions, kaons and protons in pp collisions at $\sqrt{s} = 900$ GeV with ALICE at the LHC". In: *Eur. Phys. J.* C71 (2011), p. 1655.
DOI: 10.1140/epjc/s10052-011-1655-9. arXiv: 1101.4110 [hep-ex] (cit. on p. 27).

[161] S. Chatrchyan et al. "Study of the inclusive production of charged pions, kaons, and protons in pp collisions at $\sqrt{s}$ = 0.9, 2.76, and 7 TeV". In: *Eur. Phys. J.* C72 (2012), p. 2164. DOI: 10.1140/epjc/s10052-012-2164-1. arXiv: 1207.4724 [hep-ex] (cit. on p. 27).

[162] B. Baatar et al. "Inclusive production of protons, anti-protons, neutrons, deuterons and tritons in p+C collisions at 158 GeV/c beam momentum". In: *Eur.Phys.J.* C73 (2013), p. 2364. DOI: 10.1140/epjc/s10052-013-2364-3. arXiv: 1207.6520 [hep-ex] (cit. on pp. 26, 28).

[163] "Measurement of antiproton production in pHe collisions at $\sqrt{s_{\mathrm{NN}}}$ = 110 GeV". In: *LHCb-CONF-2017-002* (2017) (cit. on p. 28).

[164] G. D. Badhwar and S. A. Stephens. "Secondary positrons and electrons in the cosmic radiation". In: *ICRC, Conference Papers* 1 (1977), pp. 398–403 (cit. on p. 29).

[165] L. Tan and L. Ng. "Parametrization Of Hadron Inclusive Cross-Sections In P P Collisions Extended To Very Low-Energies". In: *J.Phys.* G9 (1983), pp. 1289–1308. DOI: 10.1088/0305-4616/9/10/015 (cit. on p. 29).

[166] K. Blum, R. Sato and M. Takimoto. "e^+ and $\bar{p}$ production in pp collisions and the cosmic-ray $e^+/\bar{p}$ flux ratio". In: (2017). arXiv: 1709.04953 [astro-ph.HE] (cit. on pp. 29, 53, 62, 63).

[167] T. Kamae et al. "Parameterization of Gamma, e+/- and Neutrino Spectra Produced by p-p Interaction in Astronomical Environment". In: *Astrophys.J.* 647 (2006), pp. 692–708. DOI: 10.1086/513602,10.1086/505189. arXiv: astro-ph/0605581 [astro-ph] (cit. on pp. 29, 42).

[168] N. Tomassetti. "Inhomogeneous diffusion model for recent data on high-energy cosmic rays". In: *PoS* ICRC2015 (2016), p. 551. arXiv: 1510.09214 [astro-ph.HE] (cit. on p. 29).

[169] M. Aguilar et al. "Precision Measurement of the Helium Flux in Primary Cosmic Rays of Rigidities 1.9 GV to 3 TV with the Alpha Magnetic Spectrometer on the International Space Station". In: *Phys. Rev. Lett.* 115.21 (2015), p. 211101. DOI: 10.1103/PhysRevLett.115.211101 (cit. on p. 29).

[170] Q. Yan. "CR nuclei measurements with AMS-02: latest results and perspectives". In: *Talk at XSCRC2017, CERN* (2017) (cit. on p. 29).

[171] J. J. Engelmann et al. "Charge composition and energy spectra of cosmic-ray nuclei for elements from Be to NI - Results from HEAO-3-C2". In: *Astrophys. J.* 233 (1990), pp. 96–111 (cit. on p. 30).

[172] M. Cirelli et al. "PPPC 4 DM ID: A Poor Particle Physicist Cookbook for Dark Matter Indirect Detection". In: *JCAP* 1103 (2011). [Erratum: JCAP 1210 (2012)], p. 051. DOI: 10.1088/1475-7516/2012/10/E01,10.1088/1475-7516/2011/03/051. arXiv: 1012.4515 [hep-ph] (cit. on p. 33).

[173] M. Drees, M. Kakizaki and S. Kulkarni.
"The Thermal Abundance of Semi-Relativistic Relics".
In: *Phys. Rev.* D80 (2009), p. 043505. DOI: 10.1103/PhysRevD.80.043505.
arXiv: 0904.3046 [hep-ph] (cit. on p. 33).

[174] M. Laine and Y. Schroder. "Quark mass thresholds in QCD thermodynamics".
In: *Phys. Rev.* D73 (2006), p. 085009. DOI: 10.1103/PhysRevD.73.085009.
arXiv: hep-ph/0603048 [hep-ph] (cit. on p. 33).

[175] R. Catena and P. Ullio. "A novel determination of the local dark matter density".
In: *JCAP* 1008 (2010), p. 004. DOI: 10.1088/1475-7516/2010/08/004.
arXiv: 0907.0018 [astro-ph.CO] (cit. on p. 33).

[176] P. Salucci et al. "The dark matter density at the Sun's location".
In: *Astron. Astrophys.* 523 (2010), A83. DOI: 10.1051/0004-6361/201014385.
arXiv: 1003.3101 [astro-ph.GA] (cit. on p. 33).

[177] M. Pato, F. Iocco and G. Bertone.
"Dynamical constraints on the dark matter distribution in the Milky Way".
In: *JCAP* 1512.12 (2015), p. 001. DOI: 10.1088/1475-7516/2015/12/001.
arXiv: 1504.06324 [astro-ph.GA] (cit. on p. 33).

[178] P. J. McMillan. "The mass distribution and gravitational potential of the Milky Way ".
In: *Mon. Not. Roy. Astron. Soc.* 465 (2017), p. 76. arXiv: 1608.00971 [astro-ph.GA]
(cit. on p. 33).

[179] J. Guedes et al.
"Forming Realistic Late-Type Spirals in a LCDM Universe: The Eris Simulation".
In: *Astrophys. J.* 742 (2011), p. 76. DOI: 10.1088/0004-637X/742/2/76.
arXiv: 1103.6030 [astro-ph.CO] (cit. on p. 33).

[180] S. Roca-Fàbrega et al. "GARROTXA Cosmological Simulations of Milky Way-sized
Galaxies: General Properties, Hot Gas Distribution, and Missing Baryons".
In: *Astrophys. J.* 824.2 (2016), p. 94. DOI: 10.3847/0004-637X/824/2/94.
arXiv: 1504.06261 [astro-ph.GA] (cit. on p. 33).

[181] Q. Zhu et al. "Baryonic impact on the dark matter distribution in Milky Way-sized galaxies
and their satellites". In: *Mon. Not. Roy. Astron. Soc.* 458.2 (2016), pp. 1559–1580.
DOI: 10.1093/mnras/stw374. arXiv: 1506.05537 [astro-ph.CO] (cit. on p. 33).

[182] M. Schaller et al.
"Dark matter annihilation radiation in hydrodynamic simulations of Milky Way haloes".
In: *Mon. Not. Roy. Astron. Soc.* 455.4 (2016), pp. 4442–4451.
DOI: 10.1093/mnras/stv2667. arXiv: 1509.02166 [astro-ph.CO] (cit. on p. 33).

[183] P. Mollitor, E. Nezri and R. Teyssier.
"Baryonic and dark matter distribution in cosmological simulations of spiral galaxies".
In: *Mon. Not. Roy. Astron. Soc.* 447.2 (2015), pp. 1353–1369.
DOI: 10.1093/mnras/stu2466. arXiv: 1405.4318 [astro-ph.GA] (cit. on p. 33).

[184] P. D. Serpico. "Possible physics scenarios behind cosmic-ray "anomalies"".
In: *PoS* ICRC2015 (2016), p. 009. arXiv: 1509.04233 [astro-ph.HE] (cit. on p. 34).

[185] V. Ptuskin, V. Zirakashvili and E.-S. Seo.
"Spectra of Cosmic Ray Protons and Helium Produced in Supernova Remnants".
In: *Astrophys. J.* 763 (2013), p. 47. DOI: 10.1088/0004-637X/763/1/47.
arXiv: 1212.0381 [astro-ph.HE] (cit. on p. 34).

[186] Y. Ohira, N. Kawanaka and K. Ioka. "Cosmic-ray hardenings in light of AMS-02 data".
In: *Phys. Rev.* D93.8 (2016), p. 083001. DOI: 10.1103/PhysRevD.93.083001.
arXiv: 1506.01196 [astro-ph.HE] (cit. on p. 34).

[187] P. Blasi, E. Amato and P. D. Serpico.
"Spectral breaks as a signature of cosmic ray induced turbulence in the Galaxy".
In: *Phys.Rev.Lett.* 109 (2012), p. 061101. DOI: 10.1103/PhysRevLett.109.061101.
arXiv: 1207.3706 [astro-ph.HE] (cit. on p. 34).

[188] N. Tomassetti. "Origin of the Cosmic-Ray Spectral Hardening".
In: *Astrophys.J.* 752 (2012), p. L13. DOI: 10.1088/2041-8205/752/1/L13.
arXiv: 1204.4492 [astro-ph.HE] (cit. on p. 34).

[189] S. Thoudam and J. R. Horandel.
"Nearby supernova remnants and the cosmic-ray spectral hardening at high energies".
In: *Mon. Not. Roy. Astron. Soc.* 421 (2012), p. 1209.
DOI: 10.1111/j.1365-2966.2011.20385.x. arXiv: 1112.3020 [astro-ph.HE]
(cit. on p. 35).

[190] G. Bernard et al. "No More Anomaly in the TeV Cosmic Ray Proton and Helium Spectra".
In: *Astron.Astrophys.* 555 (2013), A48. DOI: 10.1051/0004-6361/201321202.
arXiv: 1207.4670 [astro-ph.HE] (cit. on p. 35).

[191] N. Tomassetti. "Origin of the Proton-to-Helium Ratio Anomaly in Cosmic Rays".
In: *Astrophys. J.* 815 (2015), p. L1. DOI: 10.1088/2041-8205/815/1/L1.
arXiv: 1511.04460 [astro-ph.HE] (cit. on p. 35).

[192] M. Kachelrieß, A. Neronov and D. V. Semikoz.
"Cosmic ray signatures of a 2-3 Myr old local supernova". In: (2017).
arXiv: 1710.02321 [astro-ph.HE] (cit. on p. 35).

[193] P. Blasi and E. Amato. "Diffusive propagation of cosmic rays from supernova remnants in the Galaxy. II: anisotropy". In: *JCAP* 1201 (2012), p. 011.
DOI: 10.1088/1475-7516/2012/01/011. arXiv: 1105.4529 [astro-ph.HE]
(cit. on pp. 35, 36).

[194] P. Salati et al. "The proton and helium anomalies in the light of the Myriad model".
In: *RICAP16, Proceedings* (2016). DOI: 10.1051/epjconf/201713602006.
arXiv: 1611.06154 [astro-ph.HE] (cit. on p. 35).

[195] M. Aguilar et al.
"Observation of New Properties of Secondary Cosmic Rays Lithium, Beryllium, and Boron by the Alpha Magnetic Spectrometer on the International Space Station".
In: *Phys. Rev. Lett.* 120.2 (2018), p. 021101. DOI: 10.1103/PhysRevLett.120.021101
(cit. on pp. 36, 53, 60, 63).

[196] R. H. Kraichnan. "Inertial-Range Spectrum of Hydromagnetic Turbulence".
In: *Phys. Fluids* 8 (1965), pp. 1385–1387. DOI: 10.1063/1.1761412 (cit. on p. 36).

[197] A. Kolmogorov. "The Local Structure of Turbulence in Incompressible Viscous Fluid for Very Large Reynolds' Numbers".
In: *Akademiia Nauk SSSR Doklady* 30 (1941), pp. 301–305 (cit. on p. 36).

[198] K. Hamaguchi, T. Moroi and K. Nakayama.
"AMS-02 Antiprotons from Annihilating or Decaying Dark Matter". In: (2015).
arXiv: 1504.05937 [hep-ph] (cit. on p. 38).

[199] S.-J. Lin et al. "Implications for dark matter annihilation from the AMS-02 $\bar{p}/p$ ratio".
In: (2015). arXiv: 1504.07230 [hep-ph] (cit. on p. 38).

[200] Y.-H. Chen, K. Cheung and P.-Y. Tseng. "Dark Matter with Multi-Annihilation Channels and AMS-02 Positron Excess and Antiproton". In: (2015). arXiv: 1505.00134 [hep-ph] (cit. on p. 38).

[201] B. Katz, K. Blum and E. Waxman.
"What can we really learn from positron flux 'anomalies'?"
In: *Mon. Not. Roy. Astron. Soc.* 405 (2010), p. 1458.
DOI: 10.1111/j.1365-2966.2010.16568.x. arXiv: 0907.1686 [astro-ph.HE]
(cit. on pp. 41, 51, 53, 60, 63).

[202] K. Blum, B. Katz and E. Waxman.
"AMS-02 Results Support the Secondary Origin of Cosmic Ray Positrons".
In: *Phys. Rev. Lett.* 111.21 (2013), p. 211101. DOI: 10.1103/PhysRevLett.111.211101.
arXiv: 1305.1324 [astro-ph.HE] (cit. on pp. 41, 51, 52, 55).

[203] P. Lipari. "Interpretation of the cosmic ray positron and antiproton fluxes".
In: *Phys. Rev.* D95.6 (2017), p. 063009. DOI: 10.1103/PhysRevD.95.063009.
arXiv: 1608.02018 [astro-ph.HE] (cit. on p. 41).

[204] R. Cowsik, B. Burch and T. Madziwa-Nussinov.
"The origin of the spectral intensities of cosmic-ray positrons".
In: *Astrophys. J.* 786 (2014), p. 124. DOI: 10.1088/0004-637X/786/2/124.
arXiv: 1305.1242 [astro-ph.HE] (cit. on pp. 41, 59).

[205] R. Kappl and A. Reinert.
"Secondary Cosmic Positrons in an Inhomogeneous Diffusion Model".
In: *Phys. Dark Univ.* 16 (2017), pp. 71–80. DOI: 10.1016/j.dark.2017.04.007.
arXiv: 1609.01300 [astro-ph.HE] (cit. on p. 41).

[206] P. Blasi. "The origin of the positron excess in cosmic rays".
In: *Phys. Rev. Lett.* 103 (2009), p. 051104. DOI: 10.1103/PhysRevLett.103.051104.
arXiv: 0903.2794 [astro-ph.HE] (cit. on p. 41).

[207] P. Mertsch and S. Sarkar.
"Testing astrophysical models for the PAMELA positron excess with cosmic ray nuclei".
In: *Phys. Rev. Lett.* 103 (2009), p. 081104. DOI: 10.1103/PhysRevLett.103.081104.
arXiv: 0905.3152 [astro-ph.HE] (cit. on p. 41).

[208] P. Mertsch and S. Sarkar.
"AMS-02 data confront acceleration of cosmic ray secondaries in nearby sources".
In: *Phys. Rev.* D90 (2014), p. 061301. DOI: 10.1103/PhysRevD.90.061301.
arXiv: 1402.0855 [astro-ph.HE] (cit. on p. 41).

[209] F. A. Aharonian, A. M. Atoyan and H. J. Volk. “High energy electrons and positrons in cosmic rays as an indicator of the existence of a nearby cosmic tevatron”. In: *Astron. Astrophys.* 294 (1995), pp. L41–L44 (cit. on p. 41).

[210] D. Hooper, P. Blasi and P. D. Serpico. “Pulsars as the Sources of High Energy Cosmic Ray Positrons”. In: *JCAP* 0901 (2009), p. 025. DOI: 10.1088/1475-7516/2009/01/025. arXiv: 0810.1527 [astro-ph] (cit. on pp. 41, 51).

[211] J. Lavalle, D. Maurin and A. Putze. “Direct constraints on diffusion models from cosmic-ray positron data: Excluding the MIN model for dark matter searches”. In: (2014). arXiv: 1407.2540 [astro-ph.HE] (cit. on p. 42).

[212] M. Ackermann et al. “Fermi-LAT Observations of the Diffuse Gamma-Ray Emission: Implications for Cosmic Rays and the Interstellar Medium”. In: *Astrophys. J.* 750 (2012), p. 3. DOI: 10.1088/0004-637X/750/1/3. arXiv: 1202.4039 [astro-ph.HE] (cit. on p. 43).

[213] T. Bringmann, F. Donato and R. A. Lineros. “Radio data and synchrotron emission in consistent cosmic ray models”. In: *JCAP* 1201 (2012), p. 049. DOI: 10.1088/1475-7516/2012/01/049. arXiv: 1106.4821 [astro-ph.GA] (cit. on p. 43).

[214] G. Di Bernardo et al. “Cosmic Ray Electrons, Positrons and the Synchrotron emission of the Galaxy: consistent analysis and implications”. In: *JCAP* 1303 (2013), p. 036. DOI: 10.1088/1475-7516/2013/03/036. arXiv: 1210.4546 [astro-ph.HE] (cit. on p. 43).

[215] E. Orlando and A. Strong. “Galactic synchrotron emission with cosmic ray propagation models”. In: *Mon. Not. Roy. Astron. Soc.* 436 (2013), p. 2127. DOI: 10.1093/mnras/stt1718. arXiv: 1309.2947 [astro-ph.GA] (cit. on p. 43).

[216] R. B. Davies. “Hypothesis testing when a nuisance parameter is present only under the alternative”. In: *Biometrika* 74 (1987), pp. 33–43. DOI: 10.1093/biomet/74.1.33 (cit. on p. 43).

[217] E. Gross and O. Vitells. “Trial factors or the look elsewhere effect in high energy physics”. In: *Eur. Phys. J.* C70 (2010), pp. 525–530. DOI: 10.1140/epjc/s10052-010-1470-8. arXiv: 1005.1891 [physics.data-an] (cit. on p. 43).

[218] M. Korsmeier, F. Donato and N. Fornengo. “Prospects to verify a possible dark matter hint in cosmic antiprotons with antideuterons and antihelium”. In: (2017). arXiv: 1711.08465 [astro-ph.HE] (cit. on p. 46).

[219] F. C. Jones et al. “The modified weighted slab technique: models and results”. In: *Astrophys. J.* 547 (2001), p. 264. DOI: 10.1086/318358. arXiv: astro-ph/0007293 [astro-ph] (cit. on p. 46).

[220] V. S. Ptuskin et al. “Dissipation of magnetohydrodynamic waves on energetic particles: impact on interstellar turbulence and cosmic ray transport”. In: *Astrophys. J.* 642 (2006), pp. 902–916. DOI: 10.1086/501117. arXiv: astro-ph/0510335 [astro-ph] (cit. on p. 46).

[221] L. Goodenough and D. Hooper. "Possible Evidence For Dark Matter Annihilation In The Inner Milky Way From The Fermi Gamma Ray Space Telescope". In: (2009). arXiv: 0910.2998 [hep-ph] (cit. on p. 47).

[222] M. E. Krauss et al. "Soft Gamma Rays from Heavy WIMPs". In: *Phys. Dark Univ.* 14 (2016), pp. 29–34. DOI: 10.1016/j.dark.2016.08.004. arXiv: 1605.05327 [hep-ph] (cit. on p. 47).

[223] A. Cuoco et al. "Probing dark matter annihilation in the Galaxy with antiprotons and gamma rays". In: *JCAP* 1710.10 (2017), p. 053. DOI: 10.1088/1475-7516/2017/10/053. arXiv: 1704.08258 [astro-ph.HE] (cit. on p. 49).

[224] R. Bartels, S. Krishnamurthy and C. Weniger. "Strong support for the millisecond pulsar origin of the Galactic center GeV excess". In: *Phys. Rev. Lett.* 116.5 (2016), p. 051102. DOI: 10.1103/PhysRevLett.116.051102. arXiv: 1506.05104 [astro-ph.HE] (cit. on p. 49).

[225] S. K. Lee et al. "Evidence for Unresolved γ-Ray Point Sources in the Inner Galaxy". In: *Phys. Rev. Lett.* 116.5 (2016), p. 051103. DOI: 10.1103/PhysRevLett.116.051103. arXiv: 1506.05124 [astro-ph.HE] (cit. on p. 49).

[226] M. Ajello et al. "Characterizing the population of pulsars in the inner Galaxy with the Fermi Large Area Telescope". In: *Submitted to: Astrophys. J.* (2017). arXiv: 1705.00009 [astro-ph.HE] (cit. on p. 49).

[227] M. Ackermann et al. "Searching for Dark Matter Annihilation from Milky Way Dwarf Spheroidal Galaxies with Six Years of Fermi Large Area Telescope Data". In: *Phys. Rev. Lett.* 115.23 (2015), p. 231301. DOI: 10.1103/PhysRevLett.115.231301. arXiv: 1503.02641 [astro-ph.HE] (cit. on p. 49).

[228] A. Albert et al. "Searching for Dark Matter Annihilation in Recently Discovered Milky Way Satellites with Fermi-LAT". In: *Astrophys. J.* 834.2 (2017), p. 110. DOI: 10.3847/1538-4357/834/2/110. arXiv: 1611.03184 [astro-ph.HE] (cit. on p. 49).

[229] K. Blum and A. Reinert. "Cosmic ray e at high energy". In: *EPJ Web Conf.* 208 (2019), p. 04001. DOI: 10.1051/epjconf/201920804001 (cit. on p. 51).

[230] M. Aguilar et al. "Precision Measurement of the $(e^+ + e^-)$ Flux in Primary Cosmic Rays from 0.5 GeV to 1 TeV with the Alpha Magnetic Spectrometer on the International Space Station". In: *Phys. Rev. Lett.* 113 (2014), p. 221102. DOI: 10.1103/PhysRevLett.113.221102 (cit. on p. 51).

[231] G. Ambrosi et al. "Direct detection of a break in the teraelectronvolt cosmic-ray spectrum of electrons and positrons". In: *Nature* 552 (2017), pp. 63–66. DOI: 10.1038/nature24475. arXiv: 1711.10981 [astro-ph.HE] (cit. on p. 51).

[232] O. Adriani et al. “Energy Spectrum of Cosmic-Ray Electron and Positron from 10 GeV to 3 TeV Observed with the Calorimetric Electron Telescope on the International Space Station”. In: *Phys. Rev. Lett.* 119.18 (2017), p. 181101. DOI: 10.1103/PhysRevLett.119.181101. arXiv: 1712.01711 [astro-ph.HE] (cit. on p. 51).

[233] O. Adriani et al. “Extended Measurement of the Cosmic-Ray Electron and Positron Spectrum from 11 GeV to 4.8 TeV with the Calorimetric Electron Telescope on the International Space Station”. In: *Phys. Rev. Lett.* 120.26 (2018), p. 261102. DOI: 10.1103/PhysRevLett.120.261102. arXiv: 1806.09728 [astro-ph.HE] (cit. on p. 51).

[234] S. Abdollahi et al. “Cosmic-ray electron-positron spectrum from 7 GeV to 2 TeV with the Fermi Large Area Telescope”. In: *Phys. Rev.* D95.8 (2017), p. 082007. DOI: 10.1103/PhysRevD.95.082007. arXiv: 1704.07195 [astro-ph.HE] (cit. on p. 51).

[235] F. Aharonian et al. “The energy spectrum of cosmic-ray electrons at TeV energies”. In: *Phys. Rev. Lett.* 101 (2008), p. 261104. DOI: 10.1103/PhysRevLett.101.261104. arXiv: 0811.3894 [astro-ph] (cit. on p. 51).

[236] F. Aharonian et al. “Probing the ATIC peak in the cosmic-ray electron spectrum with H.E.S.S”. In: *Astron. Astrophys.* 508 (2009), p. 561. DOI: 10.1051/0004-6361/200913323. arXiv: 0905.0105 [astro-ph.HE] (cit. on p. 51).

[237] A. Archer et al. “Measurement of Cosmic-ray Electrons at TeV Energies by VERITAS”. In: *Phys. Rev.* D98.6 (2018), p. 062004. DOI: 10.1103/PhysRevD.98.062004. arXiv: 1808.10028 [astro-ph.HE] (cit. on p. 51).

[238] A. K. Mallot. “The energy spectrum of cosmic electrons measured with the MAGIC telescopes”. PhD thesis. DESY, 2017. DOI: 10.18452/17698,10.3204/PUBDB-2017-11591 (cit. on p. 51).

[239] L. Bergstrom, T. Bringmann and J. Edsjo. “New Positron Spectral Features from Supersymmetric Dark Matter - a Way to Explain the PAMELA Data?” In: *Phys. Rev.* D78 (2008), p. 103520. DOI: 10.1103/PhysRevD.78.103520. arXiv: 0808.3725 [astro-ph] (cit. on p. 51).

[240] I. Cholis et al. “High Energy Positrons From Annihilating Dark Matter”. In: *Phys. Rev.* D80 (2009), p. 123511. DOI: 10.1103/PhysRevD.80.123511. arXiv: 0809.1683 [hep-ph] (cit. on p. 51).

[241] V. Barger et al. “PAMELA and dark matter”. In: *Phys. Lett.* B672 (2009), pp. 141–146. DOI: 10.1016/j.physletb.2009.01.016. arXiv: 0809.0162 [hep-ph] (cit. on p. 51).

[242] M. Cirelli and A. Strumia. “Minimal Dark Matter predictions and the PAMELA positron excess”. In: *PoS* IDM2008 (2008), p. 089. arXiv: 0808.3867 [astro-ph] (cit. on p. 51).

[243] A. M. Atoyan, F. A. Aharonian and H. J. Völk. “Electrons and positrons in the galactic cosmic rays”. In: *Phys. Rev. D* 52 (6 1995), pp. 3265–3275. DOI: 10.1103/PhysRevD.52.3265. URL: https://link.aps.org/doi/10.1103/PhysRevD.52.3265 (cit. on p. 51).

[244] A. Boulares.
"The nature of the cosmic-ray electron spectrum, and supernova remnant contributions".
In: *Astrophys. J.* 342 (July 1989), pp. 807–813. DOI: 10.1086/167637 (cit. on p. 51).

[245] S. Profumo. "Dissecting cosmic-ray electron-positron data with Occam's Razor: the role of known Pulsars". In: *Central Eur. J. Phys.* 10 (2011), pp. 1–31.
DOI: 10.2478/s11534-011-0099-z. arXiv: 0812.4457 [astro-ph] (cit. on p. 51).

[246] A. W. Strong, I. V. Moskalenko and V. S. Ptuskin.
"Cosmic-ray propagation and interactions in the Galaxy".
In: *Ann.Rev.Nucl.Part.Sci.* 57 (2007), pp. 285–327.
DOI: 10.1146/annurev.nucl.57.090506.123011.
arXiv: astro-ph/0701517 [astro-ph] (cit. on p. 53).

[247] W. R. Webber and A. Soutoul. "A Study of the Surviving Fraction of the Cosmic-Ray Radioactive Decay Isotopes ^10Be, ^26Al, ^36Cl and ^54Mn as a Function of Energy Using the Charge Ratios Be/B, Al/Mg, Cl/Ar, and Mn/Fe Measured on HEAO3".
In: *Astrophys. J.* 506 (Oct. 1998), pp. 335–340. DOI: 10.1086/306224 (cit. on p. 53).

[248] G. R. Blumenthal and R. J. Gould. "Bremsstrahlung, synchrotron radiation, and compton scattering of high-energy electrons traversing dilute gases".
In: *Rev. Mod. Phys.* 42 (1970), pp. 237–270. DOI: 10.1103/RevModPhys.42.237
(cit. on pp. 53, 54).

[249] C. C. Popescu et al. "A radiation transfer model for the Milky-Way: I. Radiation fields and application to High Energy Astrophysics".
In: *Mon. Not. Roy. Astron. Soc.* 470.3 (2017), pp. 2539–2558.
DOI: 10.1093/mnras/stx1282. arXiv: 1705.06652 [astro-ph.GA] (cit. on pp. 53, 54).

[250] T. A. Porter, G. Johannesson and I. V. Moskalenko.
"High-Energy Gamma Rays from the Milky Way: Three-Dimensional Spatial Models for the Cosmic-Ray and Radiation Field Densities in the Interstellar Medium".
In: *Astrophys. J.* 846.1 (2017), p. 67. DOI: 10.3847/1538-4357/aa844d.
arXiv: 1708.00816 [astro-ph.HE] (cit. on pp. 53, 54).

[251] R. Schlickeiser and J. Ruppel.
"Klein-Nishina steps in the energy spectrum of galactic cosmic ray electrons".
In: *New J. Phys.* 12 (2010), p. 033044. DOI: 10.1088/1367-2630/12/3/033044.
arXiv: 0908.2183 [astro-ph.HE] (cit. on p. 54).

[252] S. Redfield and R. E. Falcon.
"The Structure of the Local Interstellar Medium V: Electron Densities".
In: *Astrophys. J.* 673 (2008), p. 283. DOI: 10.1086/524002.
arXiv: 0804.1802 [astro-ph] (cit. on p. 55).

[253] R. N. Manchester et al. "The Australia Telescope National Facility pulsar catalogue".
In: *Astron. J.* 129 (2005), p. 1993. DOI: 10.1086/428488.
arXiv: astro-ph/0412641 [astro-ph] (cit. on p. 55).

[254] H. Abdalla et al. "Particle Transport within the Pulsar Wind Nebula HESS J1825-137".
In: *Astron. Astrophys.* 621 (2019), A116. DOI: 10.1051/0004-6361/201834335.
arXiv: 1810.12676 [astro-ph.HE] (cit. on pp. 55, 56).

[255] G. Giacinti, M. Kachelriess and D. V. Semikoz.
"Reconciling cosmic ray diffusion with Galactic magnetic field models".
In: *JCAP* 1807.07 (2018), p. 051. DOI: 10.1088/1475-7516/2018/07/051.
arXiv: 1710.08205 [astro-ph.HE] (cit. on p. 56).

[256] S. M. Adams et al. "Observing the Next Galactic Supernova".
In: *Astrophys. J.* 778 (2013), p. 164. DOI: 10.1088/0004-637X/778/2/164.
arXiv: 1306.0559 [astro-ph.HE] (cit. on p. 57).

[257] R. D. Abrahams and T. A. D. Paglione.
"High-latitude, Transluscent Molecular Clouds as Probes of Local Cosmic Rays".
In: *Astrophys. J.* 805.1 (2015), p. 50. DOI: 10.1088/0004-637X/805/1/50.
arXiv: 1503.05100 [astro-ph.HE] (cit. on p. 57).

[258] P. A. R. Ade et al. "Planck intermediate results. XXVIII. Interstellar gas and dust in the Chamaeleon clouds as seen by Fermi LAT and Planck".
In: *Astron. Astrophys.* 582 (2015), A31. DOI: 10.1051/0004-6361/201424955.
arXiv: 1409.3268 [astro-ph.HE] (cit. on p. 57).

[259] R.-z. Yang.
"Investigation of cosmic ray penetration with wavelet cross-correlation analysis".
In: *Astron. Astrophys.* 592 (2016), A53. DOI: 10.1051/0004-6361/201628520.
arXiv: 1606.00270 [astro-ph.HE] (cit. on p. 57).

[260] F. Acero et al. "Development of the Model of Galactic Interstellar Emission for Standard Point-Source Analysis of Fermi Large Area Telescope Data".
In: *Astrophys. J. Suppl.* 223.2 (2016), p. 26. DOI: 10.3847/0067-0049/223/2/26.
arXiv: 1602.07246 [astro-ph.HE] (cit. on p. 58).

[261] R. Yang, F. Aharonian and C. Evoli.
"Radial distribution of the diffuse gamma-ray emissivity in the Galactic disk".
In: *Phys. Rev.* D93.12 (2016), p. 123007. DOI: 10.1103/PhysRevD.93.123007.
arXiv: 1602.04710 [astro-ph.HE] (cit. on p. 58).

[262] D. P. Cox and B. W. Smith. "Large-Scale Effects of Supernova Remnants on the Galaxy: Generation and Maintenance of a Hot Network of Tunnels".
In: *Astrophysical Journal* 189 (May 1974), p. L105. DOI: 10.1086/181476 (cit. on p. 58).

[263] L. Tibaldo et al. "Fermi-LAT Observations of High- and Intermediate-Velocity Clouds: Tracing Cosmic Rays in the Halo of the Milky Way". In: *Astrophys. J.* 807.2 (2015), p. 161. DOI: 10.1088/0004-637X/807/2/161. arXiv: 1505.04223 [astro-ph.HE] (cit. on p. 58).

[264] M. Di Mauro, S. Manconi and F. Donato.
"Evidences of low-diffusion bubbles around Galactic pulsars". In: (2019).
arXiv: 1908.03216 [astro-ph.HE] (cit. on p. 59).

[265] M. Kachelrieß, A. Neronov and D. V. Semikoz. "Signatures of a two million year old supernova in the spectra of cosmic ray protons, antiprotons and positrons".
In: *Phys. Rev. Lett.* 115.18 (2015), p. 181103. DOI: 10.1103/PhysRevLett.115.181103.
arXiv: 1504.06472 [astro-ph.HE] (cit. on pp. 59, 64).

[266] Y. Yoon et al. "Cosmic-Ray Proton and Helium Spectra from the First CREAM Flight". In: *Astrophys.J.* 728 (2011), p. 122. DOI: 10.1088/0004-637X/728/2/122. arXiv: 1102.2575 [astro-ph.HE] (cit. on p. 64).

[267] H. P. Dembinski et al. "Data-driven model of the cosmic-ray flux and mass composition from 10 GeV to 10^{11} GeV". In: *PoS* ICRC2017 (2018), p. 533. DOI: 10.22323/1.301.0533. arXiv: 1711.11432 [astro-ph.HE] (cit. on p. 64).

[268] J. H. Chang, R. Essig and A. Reinert. "Light(ly)-coupled Dark Matter in the keV Range: Freeze-In and Constraints". In: (2019). arXiv: 1911.03389 [hep-ph] (cit. on p. 67).

[269] P. D. Serpico and G. G. Raffelt. "MeV-mass dark matter and primordial nucleosynthesis". In: *Physical Review D* 70.4 (2004). ISSN: 1550-2368. DOI: 10.1103/physrevd.70.043526. URL: http://dx.doi.org/10.1103/PhysRevD.70.043526 (cit. on p. 67).

[270] C. Boehm, M. J. Dolan and C. McCabe. "A Lower Bound on the Mass of Cold Thermal Dark Matter from Planck". In: *JCAP* 1308 (2013), p. 041. DOI: 10.1088/1475-7516/2013/08/041. arXiv: 1303.6270 [hep-ph] (cit. on pp. 67, 69).

[271] D. Green and S. Rajendran. "The Cosmology of Sub-MeV Dark Matter". In: *JHEP* 10 (2017), p. 013. DOI: 10.1007/JHEP10(2017)013. arXiv: 1701.08750 [hep-ph] (cit. on pp. 67, 69).

[272] K. Griest and M. Kamionkowski. "Unitarity Limits on the Mass and Radius of Dark Matter Particles". In: *Phys. Rev. Lett.* 64 (1990), p. 615. DOI: 10.1103/PhysRevLett.64.615 (cit. on p. 67).

[273] C. Boehm and P. Fayet. "Scalar dark matter candidates". In: *Nucl. Phys.* B683 (2004), pp. 219–263. DOI: 10.1016/j.nuclphysb.2004.01.015. arXiv: hep-ph/0305261 [hep-ph] (cit. on p. 67).

[274] J. L. Feng and J. Kumar. "The WIMPless Miracle: Dark-Matter Particles without Weak-Scale Masses or Weak Interactions". In: *Phys. Rev. Lett.* 101 (2008), p. 231301. DOI: 10.1103/PhysRevLett.101.231301. arXiv: 0803.4196 [hep-ph] (cit. on p. 67).

[275] D. Hooper and K. M. Zurek. "A Natural Supersymmetric Model with MeV Dark Matter". In: *Phys. Rev.* D77 (2008), p. 087302. DOI: 10.1103/PhysRevD.77.087302. arXiv: 0801.3686 [hep-ph] (cit. on p. 67).

[276] D. E. Kaplan, M. A. Luty and K. M. Zurek. "Asymmetric Dark Matter". In: *Phys. Rev.* D79 (2009), p. 115016. DOI: 10.1103/PhysRevD.79.115016. arXiv: 0901.4117 [hep-ph] (cit. on p. 67).

[277] J. McDonald. "Thermally generated gauge singlet scalars as selfinteracting dark matter". In: *Phys. Rev. Lett.* 88 (2002), p. 091304. DOI: 10.1103/PhysRevLett.88.091304. arXiv: hep-ph/0106249 [hep-ph] (cit. on pp. 67, 70).

[278] L. J. Hall et al. "Freeze-In Production of FIMP Dark Matter". In: *JHEP* 03 (2010), p. 080. DOI: 10.1007/JHEP03(2010)080. arXiv: 0911.1120 [hep-ph] (cit. on pp. 67, 70).

[279] R. Essig et al. "On the Origin of Light Dark Matter Species". In: *Submitted to: Physical Review D* (2010). arXiv: 1004.0691 [hep-ph] (cit. on p. 67).

[280] R. Essig, J. Mardon and T. Volansky. "Direct Detection of Sub-GeV Dark Matter". In: *Phys. Rev.* D85 (2012), p. 076007. DOI: 10.1103/PhysRevD.85.076007. arXiv: 1108.5383 [hep-ph] (cit. on pp. 67, 78, 87).

[281] X. Chu, T. Hambye and M. H. G. Tytgat. "The Four Basic Ways of Creating Dark Matter Through a Portal". In: *JCAP* 1205 (2012), p. 034. DOI: 10.1088/1475-7516/2012/05/034. arXiv: 1112.0493 [hep-ph] (cit. on pp. 67, 78).

[282] A. Falkowski, J. T. Ruderman and T. Volansky. "Asymmetric Dark Matter from Leptogenesis". In: *JHEP* 05 (2011), p. 106. DOI: 10.1007/JHEP05(2011)106. arXiv: 1101.4936 [hep-ph] (cit. on p. 67).

[283] Y. Hochberg et al. "Mechanism for Thermal Relic Dark Matter of Strongly Interacting Massive Particles". In: *Phys. Rev. Lett.* 113 (2014), p. 171301. DOI: 10.1103/PhysRevLett.113.171301. arXiv: 1402.5143 [hep-ph] (cit. on pp. 67, 84).

[284] E. Kuflik et al. "Elastically Decoupling Dark Matter". In: *Phys. Rev. Lett.* 116.22 (2016), p. 221302. DOI: 10.1103/PhysRevLett.116.221302. arXiv: 1512.04545 [hep-ph] (cit. on pp. 67, 84).

[285] E. Izaguirre et al. "Analyzing the Discovery Potential for Light Dark Matter". In: *Phys. Rev. Lett.* 115.25 (2015), p. 251301. DOI: 10.1103/PhysRevLett.115.251301. arXiv: 1505.00011 [hep-ph] (cit. on pp. 67, 84).

[286] R. T. D'Agnolo and J. T. Ruderman. "Light Dark Matter from Forbidden Channels". In: *Phys. Rev. Lett.* 115.6 (2015), p. 061301. DOI: 10.1103/PhysRevLett.115.061301. arXiv: 1505.07107 [hep-ph] (cit. on pp. 67, 84).

[287] D. Pappadopulo, J. T. Ruderman and G. Trevisan. "Dark matter freeze-out in a nonrelativistic sector". In: *Phys. Rev.* D94.3 (2016), p. 035005. DOI: 10.1103/PhysRevD.94.035005. arXiv: 1602.04219 [hep-ph] (cit. on pp. 67, 84).

[288] M. Farina et al. "Phases of Cannibal Dark Matter". In: *JHEP* 12 (2016), p. 039. DOI: 10.1007/JHEP12(2016)039. arXiv: 1607.03108 [hep-ph] (cit. on pp. 67, 84).

[289] R. T. D'Agnolo, D. Pappadopulo and J. T. Ruderman. "Fourth Exception in the Calculation of Relic Abundances". In: *Phys. Rev. Lett.* 119.6 (2017), p. 061102. DOI: 10.1103/PhysRevLett.119.061102. arXiv: 1705.08450 [hep-ph] (cit. on pp. 67, 84).

[290] R. T. D'Agnolo et al. "Exponentially Light Dark Matter from Coannihilation". In: *JHEP* 08 (2018), p. 079. DOI: 10.1007/JHEP08(2018)079. arXiv: 1803.02901 [hep-ph] (cit. on pp. 67, 84).

[291] R. T. D'Agnolo et al. "Thermal Relic Targets with Exponentially Small Couplings". In: (2019). arXiv: 1906.09269 [hep-ph] (cit. on pp. 67, 84).

[292] T. Hambye et al. "Dark matter from dark photons: a taxonomy of dark matter production". In: (2019). arXiv: 1908.09864 [hep-ph] (cit. on pp. 67, 84).

[293] S. Heeba and F. Kahlhoefer. "Probing the freeze-in mechanism in dark matter models with $U(1)'$ gauge extensions". In: (2019). arXiv: 1908.09834 [hep-ph] (cit. on pp. 67, 84).

[294] M. Battaglieri et al.
"US Cosmic Visions: New Ideas in Dark Matter 2017: Community Report". In: *U.S. Cosmic Visions: New Ideas in Dark Matter College Park, MD, USA, March 23-25, 2017*. 2017. arXiv: 1707.04591 [hep-ph]. URL: http://lss.fnal.gov/archive/2017/conf/fermilab-conf-17-282-ae-ppd-t.pdf (cit. on pp. 67, 84).

[295] J. A. Evans, C. Gaidau and J. Shelton. "Leak-in Dark Matter". In: (2019). arXiv: 1909.04671 [hep-ph] (cit. on pp. 67, 84).

[296] S. Koren and R. McGehee. "Freeze-Twin Dark Matter". In: (2019). arXiv: 1908.03559 [hep-ph] (cit. on p. 67).

[297] N. Arkani-Hamed et al. "A Theory of Dark Matter". In: *Phys. Rev.* D79 (2009), p. 015014. DOI: 10.1103/PhysRevD.79.015014. arXiv: 0810.0713 [hep-ph] (cit. on p. 67).

[298] M. Pospelov and A. Ritz. "Astrophysical Signatures of Secluded Dark Matter". In: *Phys. Lett.* B671 (2009), pp. 391–397. DOI: 10.1016/j.physletb.2008.12.012. arXiv: 0810.1502 [hep-ph] (cit. on p. 67).

[299] J. Bagnasco, M. Dine and S. D. Thomas. "Detecting technibaryon dark matter". In: *Phys. Lett.* B320 (1994), pp. 99–104. DOI: 10.1016/0370-2693(94)90830-3. arXiv: hep-ph/9310290 [hep-ph] (cit. on p. 67).

[300] M. Pospelov and T. ter Veldhuis.
"Direct and indirect limits on the electromagnetic form-factors of WIMPs". In: *Phys. Lett.* B480 (2000), pp. 181–186. DOI: 10.1016/S0370-2693(00)00358-0. arXiv: hep-ph/0003010 [hep-ph] (cit. on p. 67).

[301] K. Sigurdson et al. "Dark-matter electric and magnetic dipole moments". In: *Phys. Rev.* D70 (2004). [Erratum: Phys. Rev.D73,089903(2006)], p. 083501. DOI: 10.1103/PhysRevD.70.083501,10.1103/PhysRevD.73.089903. arXiv: astro-ph/0406355 [astro-ph] (cit. on pp. 67, 85).

[302] T. Banks, J.-F. Fortin and S. Thomas.
"Direct Detection of Dark Matter Electromagnetic Dipole Moments". In: (2010). arXiv: 1007.5515 [hep-ph] (cit. on p. 67).

[303] P. W. Graham et al. "Semiconductor Probes of Light Dark Matter". In: *Phys. Dark Univ.* 1 (2012), pp. 32–49. DOI: 10.1016/j.dark.2012.09.001. arXiv: 1203.2531 [hep-ph] (cit. on pp. 67, 69).

[304] X. Chu, J. Pradler and L. Semmelrock.
"Light dark states with electromagnetic form factors". In: *Phys. Rev.* D99.1 (2019), p. 015040. DOI: 10.1103/PhysRevD.99.015040. arXiv: 1811.04095 [hep-ph] (cit. on pp. 67, 88).

[305] F. Elahi, C. Kolda and J. Unwin. "UltraViolet Freeze-in". In: *JHEP* 03 (2015), p. 048. DOI: 10.1007/JHEP03(2015)048. arXiv: 1410.6157 [hep-ph] (cit. on p. 67).

[306] E. Braaten and D. Segel.
"Neutrino energy loss from the plasma process at all temperatures and densities". In: *Phys. Rev.* D48 (1993), pp. 1478–1491. DOI: 10.1103/PhysRevD.48.1478. arXiv: hep-ph/9302213 [hep-ph] (cit. on pp. 67, 74, 75, 90, 91).

[307] J. Redondo and M. Postma. "Massive hidden photons as lukewarm dark matter". In: *JCAP* 0902 (2009), p. 005. DOI: 10.1088/1475-7516/2009/02/005. arXiv: 0811.0326 [hep-ph] (cit. on pp. 67, 68, 78).

[308] C. Dvorkin, T. Lin and K. Schutz. "Making dark matter out of light: freeze-in from plasma effects". In: (2019). arXiv: 1902.08623 [hep-ph] (cit. on pp. 67, 70, 78).

[309] J. Redondo. "Helioscope Bounds on Hidden Sector Photons". In: *JCAP* 0807 (2008), p. 008. DOI: 10.1088/1475-7516/2008/07/008. arXiv: 0801.1527 [hep-ph] (cit. on p. 68).

[310] H. An, M. Pospelov and J. Pradler. "New stellar constraints on dark photons". In: *Phys. Lett.* B725 (2013), pp. 190–195. DOI: 10.1016/j.physletb.2013.07.008. arXiv: 1302.3884 [hep-ph] (cit. on p. 68).

[311] H. Vogel and J. Redondo. "Dark Radiation constraints on minicharged particles in models with a hidden photon". In: *JCAP* 1402 (2014), p. 029. DOI: 10.1088/1475-7516/2014/02/029. arXiv: 1311.2600 [hep-ph] (cit. on pp. 68, 85).

[312] J. Redondo and G. Raffelt. "Solar constraints on hidden photons re-visited". In: *JCAP* 1308 (2013), p. 034. DOI: 10.1088/1475-7516/2013/08/034. arXiv: 1305.2920 [hep-ph] (cit. on p. 68).

[313] J. H. Chang, R. Essig and S. D. McDermott. "Revisiting Supernova 1987A Constraints on Dark Photons". In: *JHEP* 01 (2017), p. 107. DOI: 10.1007/JHEP01(2017)107. arXiv: 1611.03864 [hep-ph] (cit. on p. 68).

[314] S. Knapen, T. Lin and K. M. Zurek. "Light Dark Matter: Models and Constraints". In: *Phys. Rev.* D96.11 (2017), p. 115021. DOI: 10.1103/PhysRevD.96.115021. arXiv: 1709.07882 [hep-ph] (cit. on p. 68).

[315] J. H. Chang, R. Essig and S. D. McDermott. "Supernova 1987A Constraints on Sub-GeV Dark Sectors, Millicharged Particles, the QCD Axion, and an Axion-like Particle". In: *JHEP* 09 (2018), p. 051. DOI: 10.1007/JHEP09(2018)051. arXiv: 1803.00993 [hep-ph] (cit. on pp. 68, 76, 82, 85, 88).

[316] X. Chu et al. "Stellar probes of dark sector-photon interactions". In: *Phys. Rev.* D100.8 (2019), p. 083002. DOI: 10.1103/PhysRevD.100.083002. arXiv: 1908.00553 [hep-ph] (cit. on pp. 68, 82, 88, 91).

[317] S. Davidson, S. Hannestad and G. Raffelt. "Updated bounds on millicharged particles". In: *JHEP* 05 (2000), p. 003. DOI: 10.1088/1126-6708/2000/05/003. arXiv: hep-ph/0001179 [hep-ph] (cit. on p. 68).

[318] R. Essig et al. "Direct Detection of sub-GeV Dark Matter with Semiconductor Targets". In: *JHEP* 05 (2016), p. 046. DOI: 10.1007/JHEP05(2016)046. arXiv: 1509.01598 [hep-ph] (cit. on pp. 68, 78, 87, 88).

[319] Y. Hochberg et al. "Detecting Superlight Dark Matter with Fermi-Degenerate Materials". In: *JHEP* 08 (2016), p. 057. DOI: 10.1007/JHEP08(2016)057. arXiv: 1512.04533 [hep-ph] (cit. on p. 68).

[320] M. Tanabashi et al. "Review of Particle Physics". In: *Phys. Rev.* D98.3 (2018), p. 030001. DOI: 10.1103/PhysRevD.98.030001 (cit. on p. 69).

[321] D. Egana-Ugrinovic, M. Low and J. T. Ruderman. "Charged Fermions Below 100 GeV". In: *JHEP* 05 (2018), p. 012. DOI: 10.1007/JHEP05(2018)012. arXiv: 1801.05432 [hep-ph] (cit. on p. 69).

[322] J.-F. Fortin and T. M. P. Tait. "Collider Constraints on Dipole-Interacting Dark Matter". In: *Phys. Rev.* D85 (2012), p. 063506. DOI: 10.1103/PhysRevD.85.063506. arXiv: 1103.3289 [hep-ph] (cit. on pp. 69, 85).

[323] N. Sabti et al. "Refined Bounds on MeV-scale Thermal Dark Sectors from BBN and the CMB". In: (2019). arXiv: 1910.01649 [hep-ph] (cit. on p. 69).

[324] V. A. Rubakov and D. S. Gorbunov. *Introduction to the Theory of the Early Universe*. Singapore: World Scientific, 2017. ISBN: 9789813209879, 9789813209886, 9789813220058. DOI: 10.1142/10447. URL: http://www.DESY.eblib.com/patron/FullRecord.aspx?p=737614 (cit. on p. 70).

[325] M. Dutra et al. "MeV Dark Matter Complementarity and the Dark Photon Portal". In: *JCAP* 1803 (2018), p. 037. DOI: 10.1088/1475-7516/2018/03/037. arXiv: 1801.05447 [hep-ph] (cit. on pp. 71, 73).

[326] L. Husdal. "On Effective Degrees of Freedom in the Early Universe". In: *Galaxies* 4.4 (2016), p. 78. DOI: 10.3390/galaxies4040078. arXiv: 1609.04979 [astro-ph.CO] (cit. on p. 71).

[327] P. Gondolo and G. Gelmini. "Cosmic abundances of stable particles: Improved analysis". In: *Nucl. Phys.* B360 (1991), pp. 145–179. DOI: 10.1016/0550-3213(91)90438-4 (cit. on pp. 73, 79).

[328] J. N. Bahcall, A. M. Serenelli and S. Basu. "New solar opacities, abundances, helioseismology, and neutrino fluxes". In: *Astrophys. J.* 621 (2005), pp. L85–L88. DOI: 10.1086/428929. arXiv: astro-ph/0412440 [astro-ph] (cit. on p. 81).

[329] E. Byckling and K. Kajantie. *Particle kinematics*. 1973 (cit. on pp. 84, 94).

[330] R. Essig et al. "Direct Detection of Spin-(In)dependent Nuclear Scattering of Sub-GeV Dark Matter Using Molecular Excitations". In: (2019). arXiv: 1907.07682 [hep-ph] (cit. on p. 88).

[331] J. Tiffenberg et al. "Single-electron and single-photon sensitivity with a silicon Skipper CCD". In: *Phys. Rev. Lett.* 119.13 (2017), p. 131802. DOI: 10.1103/PhysRevLett.119.131802. arXiv: 1706.00028 [physics.ins-det] (cit. on p. 88).

[332] S. A. Hertel et al. "A Path to the Direct Detection of sub-GeV Dark Matter Using Calorimetric Readout of a Superfluid ^{4}He Target". In: (2018). arXiv: 1810.06283 [physics.ins-det] (cit. on p. 88).

[333] T. Akesson et al. "Light Dark Matter eXperiment (LDMX)". In: (2018). arXiv: 1808.05219 [hep-ex] (cit. on p. 88).

[334] R. Essig et al. “Constraining Light Dark Matter with Low-Energy e^+e^- Colliders”. In: *JHEP* 11 (2013), p. 167. DOI: 10.1007/JHEP11(2013)167. arXiv: 1309.5084 [hep-ph] (cit. on p. 88).

[335] R. Essig et al. “First Direct Detection Limits on sub-GeV Dark Matter from XENON10”. In: *Phys. Rev. Lett.* 109 (2012), p. 021301. DOI: 10.1103/PhysRevLett.109.021301. arXiv: 1206.2644 [astro-ph.CO] (cit. on p. 88).

[336] B. Batell, R. Essig and Z. Surujon. “Strong Constraints on Sub-GeV Dark Sectors from SLAC Beam Dump E137”. In: *Phys. Rev. Lett.* 113.17 (2014), p. 171802. DOI: 10.1103/PhysRevLett.113.171802. arXiv: 1406.2698 [hep-ph] (cit. on p. 88).

[337] M. Crisler et al. “SENSEI: First Direct-Detection Constraints on sub-GeV Dark Matter from a Surface Run”. In: *Phys. Rev. Lett.* 121.6 (2018), p. 061803. DOI: 10.1103/PhysRevLett.121.061803. arXiv: 1804.00088 [hep-ex] (cit. on p. 88).

[338] R. Agnese et al. “First Dark Matter Constraints from a SuperCDMS Single-Charge Sensitive Detector”. In: *Phys. Rev. Lett.* 121.5 (2018). [erratum: Phys. Rev. Lett.122,no.6,069901(2019)], p. 051301. DOI: 10.1103/PhysRevLett.122.069901,10.1103/PhysRevLett.121.051301. arXiv: 1804.10697 [hep-ex] (cit. on p. 88).

[339] O. Abramoff et al. “SENSEI: Direct-Detection Constraints on Sub-GeV Dark Matter from a Shallow Underground Run Using a Prototype Skipper-CCD”. In: *Phys. Rev. Lett.* 122.16 (2019), p. 161801. DOI: 10.1103/PhysRevLett.122.161801. arXiv: 1901.10478 [hep-ex] (cit. on p. 88).

[340] P. Agnes et al. “Constraints on Sub-GeV Dark-Matter-Electron Scattering from the DarkSide-50 Experiment”. In: *Phys. Rev. Lett.* 121.11 (2018), p. 111303. DOI: 10.1103/PhysRevLett.121.111303. arXiv: 1802.06998 [astro-ph.CO] (cit. on p. 88).

[341] R. Essig, T. Volansky and T.-T. Yu. “New Constraints and Prospects for sub-GeV Dark Matter Scattering off Electrons in Xenon”. In: *Phys. Rev.* D96.4 (2017), p. 043017. DOI: 10.1103/PhysRevD.96.043017. arXiv: 1703.00910 [hep-ph] (cit. on p. 88).

[342] A. H. Abdelhameed et al. “First results from the CRESST-III low-mass dark matter program”. In: (2019). arXiv: 1904.00498 [astro-ph.CO] (cit. on p. 88).

[343] E. Aprile et al. “Light Dark Matter Search with Ionization Signals in XENON1T”. In: (2019). arXiv: 1907.11485 [hep-ex] (cit. on p. 88).

[344] A. Aguilar-Arevalo et al. “Constraints on Light Dark Matter Particles Interacting with Electrons from DAMIC at SNOLAB”. In: *Phys. Rev. Lett.* 123.18 (2019), p. 181802. DOI: 10.1103/PhysRevLett.123.181802. arXiv: 1907.12628 [astro-ph.CO] (cit. on p. 88).

[345] M. S. Madhavacheril, N. Sehgal and T. R. Slatyer.
"Current Dark Matter Annihilation Constraints from CMB and Low-Redshift Data".
In: *Phys. Rev.* D89 (2014), p. 103508. DOI: 10.1103/PhysRevD.89.103508.
arXiv: 1310.3815 [astro-ph.CO] (cit. on p. 88).

[346] H. Liu, T. R. Slatyer and J. Zavala.
"Contributions to cosmic reionization from dark matter annihilation and decay".
In: *Phys. Rev.* D94.6 (2016), p. 063507. DOI: 10.1103/PhysRevD.94.063507.
arXiv: 1604.02457 [astro-ph.CO] (cit. on p. 88).

[347] J. L. Feng and J. Smolinsky.
"Impact of a resonance on thermal targets for invisible dark photon searches".
In: *Phys. Rev.* D96.9 (2017), p. 095022. DOI: 10.1103/PhysRevD.96.095022.
arXiv: 1707.03835 [hep-ph] (cit. on p. 89).

[348] R. Mertig, M. Bohm and A. Denner.
"FEYN CALC: Computer algebraic calculation of Feynman amplitudes".
In: *Comput. Phys. Commun.* 64 (1991), pp. 345–359.
DOI: 10.1016/0010-4655(91)90130-D (cit. on p. 95).

[349] V. Shtabovenko, R. Mertig and F. Orellana. "New Developments in FeynCalc 9.0".
In: *Comput. Phys. Commun.* 207 (2016), pp. 432–444. DOI: 10.1016/j.cpc.2016.06.008.
arXiv: 1601.01167 [hep-ph] (cit. on p. 95).

List of Figures

List of Tables